PARTICLE ACCELERATION AND DETECTION

P. Lecoq
A. Annenkov
A. Gektin
M. Korzhik
C. Pedrini

Inorganic Scintillators for Detector Systems

Physical Principles and Crystal Engineering

Springer

Inorganic Scintillators for Detector Systems

Particle Acceleration and Detection

springer.com

The series *Particle Acceleration and Detection* is devoted to monograph texts dealing with all aspects of particle acceleration and detection research and advanced teaching. The scope also includes topics such as beam physics and instrumentation as well as applications. Presentations should strongly emphasise the underlying physical and engineering sciences. Of particular interest are

- contributions which relate fundamental research to new applications beyond the immediate realm of the original field of research
- contributions which connect fundamental research in the aforementioned fields to fundamental research in related physical or engineering sciences
- concise accounts of newly emerging important topics that are embedded in a broader framework in order to provide quick but readable access of very new material to a larger audience

The books forming this collection will be of importance for graduate students and active researchers alike.

Paul Lecoq Alexander Annenkov Alexander Gektin
Mikhail Korzhik Christian Pedrini

Inorganic Scintillators for Detector Systems

Physical Principles and Crystal Engineering

With 125 Figures

Springer

Paul Lecoq
CERN, European Organization for
Nuclear Research
1211 Geneva 23
Switzerland
E-mail: paul.lecoq@cern.ch

Mikhail Korzhik
Institute of Nuclear Problems
Bobruiskaya ul. 11
220050 Minsk
Belarus
E-mail: mikhail.korjik@cern.ch

Alexander Annenkov
Bogoroditsk Techno Chemical Plant
301801 Bogoroditsk
Tula Region
Russian Federation
E-mail: annenkov@btcp.tdn.ru

Christian Pedrini
Université Lyon 1
LPCML, 4MR 5620 CNRS
Bât. A. Kastler
10 rue Ampère
Domaine Scientifique de la Doua
69622 Villeurbanne Cedex
France
E-mail: pedrini@pcml.univ-lyon1.fr

Alexander Gektin
Institute for Scintillation Materials
Lenin Avenue 60
310001 Kharkov
Ukraine
E-mail: gektin@isc.kharkov.com

Library of Congress Control Number: 2005933613

ISSN 1611-1052

ISBN-10 3-540-27766-8 Springer Berlin Heidelberg New York
ISBN-13 978-3-540-27766-8 Springer Berlin Heidelberg New York

Springer is a part of Springer Science+Business Media
springer.com

Printed in The Netherlands

Typesetting: by the authors and TechBooks using a Springer LaTeX macro package
Cover design: *design & production* GmbH, Heidelberg

Printed on acid-free paper SPIN: 10988435 54/TechBooks 5 4 3 2 1 0

Preface

The last two decades have seen a spectacular increase of interest for inorganic scintillators. This has been to a large part a consequence of the visibility given to this field by several large crystal-based detectors in particle physics. To answer the very challenging requirements for these experiments (huge data rates, linearity of response over a large dynamic range, harsh radiation environment, impressive crystal quantities to be produced in a short time period and at an affordable cost, etc...) an effort of coordination was needed. Several groups of experts working in different aspects of material science have combined their efforts in international and multidisciplinary collaborations to better understand the fundamental mechanisms underlying the scintillation process and its efficiency. Similarly, the stability of the scintillation properties and the role of color centers has been extensively studied to develop radiation hard scintillators. Dedicated conferences on inorganic scintillators have seen an increasing participation from different communities of users outside the domain of high-energy physics. This includes nuclear physics, astrophysics, security systems, industrial applications, and medical imaging. This last domain in particular is growing very fast since a few years at the point that the volume of scintillating crystals to be produced for positron emission tomography (PET) is going to exceed the one for high-energy physics. As more and more crystal producers are also attending these conferences, a very fruitful synergy was progressively built up among scientific experts, technologists, and end users. This aspect of a multidisciplinary collaboration is essential to help people design and build detectors of ever-increasing performance through the choice, optimization or development of the best scintillator, and a thorough investigation of the technologies to produce the crystals of the highest quality.

The idea for this book was born during one of the conferences of the SCINT cycle (eight conferences since the first one in Chamonix, France, in September 1992). It appears that the progress in understanding scintillation process and in material sciences in general opens new ways to answer the challenging requirements of an increasing number of customers. Whereas until recently the only possibility was to scan scintillator databases to select, among the few which are available, the one having reasonable properties, very often at the price of important compromises, the dream of engineering

scintillators closely matching the user's requirements is becoming every day more realistic. This is why we have deliberately taken the end user's viewpoint. This book does not follow an academic scenario, starting from theoretical considerations, describing the different scintillation mechanisms in a didactic way, and concluding with a few examples. Several authors have already published excellent monographs of that sort. We have chosen instead a more pragmatic approach trying to answer practical problems and insisting on limiting factors which are not only of theoretical nature but also related to technological difficulties, production yield, and cost.

This book is therefore a practical guide for people, scientists, and engineers who intend to develop a detector using inorganic scintillators for basic research, medical imaging, or industrial applications. It will also interest students and teachers to get an overall picture of a field in rapid expansion. Its multidisciplinary approach is a good illustration of how modern challenges are met. It does not address organic and liquid scintillators.

The introduction defines the vocabulary and describes the different classes of scintillators. Definitions of *luminescence*, *scintillation*, and *phosphorescence* are given. The main parameters of interest for scintillating materials are described with a short and comprehensive definition for each of them.

The following chapter reviews the user's requirements for the different applications. Starting from the problem to be solved in domains as different as fundamental physics, medical imaging, security systems, oil well logging, and other industrial applications, it explains how these requirements influence the development of new scintillators.

The chapter on scintillation mechanism in inorganic scintillators is treated in a practical way. The point is to show how to answer high light yield, short decay time, good energy resolution, etc... as requested by users. The fundamental mechanisms are of course explained, but a particular emphasis is put on the description of factors limiting these performances in good-quality crystals.

In the next section the influence of crystal defects and their role in the degradation of the scintillator performance is thoroughly studied. In particular, problems of nonlinearity of the scintillator response and radiation damage are discussed.

At this stage it is important to address the problems of crystal engineering. This is the subject of the next chapter where the reader will get familiar with the most frequently used technologies of crystal growth and their limitations. The mechanical processing and different methods to optimize the light collection are also discussed in this part.

Finally, two examples of recently developed scintillators are given as an illustration of the approach proposed in this book. The first one describes the huge effort on Lead Tungstate (PWO) for the largest electromagnetic calorimeter ever built in high-energy physics. The second one concerns the

development of the Lutetium Aluminum perovskite (LuAP) for medical imaging devices.

The authors hope through their work to contribute to the development of this very active domain of material sciences, to help the people interested in the use of inorganic scintillators, and to promote education in this field.

Acknowledgments

The authors express their warm thanks to all their colleagues who contributed a lot with their research to the development of new scintillation materials. Special thanks go to the members of the Crystal Clear Collaboration, the CMS Collaboration at CERN, the CERN management, the ISTC Foundation, the different National Science Funding Agencies for their support to this research. We are also very grateful to Dr. S. Sytova for her efficient technical support for assembling the book. Finally the authors express their gratitude to Dr. A. Fedorov, Dr. O. Missevitch, Dr. A. Hofstaetter, Dr. R. Novotny, Dr. M. Kirm, Dr. P. Dorenbos, Dr. A. Belsky, Prof. A. Vasil'ev, and Prof. V. Mikhailin for collaborative research and fruitful discussions at the preparation of this book.

August 2005 *Paul Lecoq*

Contents

1 Scintillation and Inorganic Scintillators

Abstract. This chapter introduces the basic definitions and gives the minimum necessary information about the phenomenon of scintillation and the mechanisms which have to be taken into account for the development of scintillation materials. It starts with an historical brief and describes the sequence of the processes leading to scintillation in a dielectric medium. Definitions are then given of the parameters related to the physical process of light production in the medium and not dependent on the shape, surface state and optical quality of the scintillator block. After a survey of scintillation mechanisms it is shown that several self activated scintillators show better scintillation properties when they are doped by appropriate ions. A description is given of the most important activators with a discussion about the conditions for the activator to be efficient in a host matrix. As an example the electron energy level structure of Ce^{3+} and Pr^{3+} ions is described. It is shown that these two ions are good activators with a bright and fast scintillation in many compounds. Several approaches to classify scintillation materials are discussed. This chapter is concluded with a list of the scintillation materials developed so far and of their most important properties.

1.1 The Phenomenon of Scintillation

What is a scintillator?

For a long time the answer to this apparently simple question did not find a clear and unambiguous formulation.

Scintillators have played a major role in the development of modern physics. The visual observation of scintillation on a zinc sulfide screen has allowed E. Rutherford to observe α particles, an event which can be considered as the starting point of modern nuclear physics. Till the end of the Second World War, zinc sulfide and calcium tungstate were among the most popular particle detectors found in nuclear physics laboratories. The intensive development of atomic projects in the postwar period stimulated the development of new ionizing-radiation – detecting technique, including scintillation counters. With the development of experimental physics, and in particular with the occurrence of the photoelectric multipliers, it became clear that scintillating materials are ideal devices to detect elementary particles and to measure their parameters [1–3]. In a rather short time (1947–51) it has been discovered that scintillation can be observed in various organic and

inorganic crystalline media [4–7], as well as in fluids [8–11], gases [12, 13], and polymeric compounds [14]. At the same time the still most widely used scintillating crystalline material NaI (Tl) [15] has been discovered.

Kallmann [5] has made an attempt to specify the essential parameters of scintillation materials. He made, in particular, the distinction between

(a) the physical light output, which corresponds to the fraction of the absorbed ionizing radiation energy which is transformed into light, and
(b) the technical light output, which is the amount of light actually collected at the extremity of a scintillation element, taking into account all factors of light collection and absorption in the medium.

He defined scintillation as flashes of light in phosphorus. In the Physical Encyclopedia [16], scintillation is defined as "the short light flashes originating in a scintillator under the effect of ionizing radiation." Fünfer and Neuert [17] defined scintillation as "the phenomenon of luminescence in transparent solids, fluids or gases, originating at the propagation of the ionizing radiation through them."

One shall remark that all these definitions of scintillation have some shortcomings. First of all, they are restricted to the phenomenology of light production under excitation by ionizing radiation but they do not consider the mechanism of energy transfer and conversion into light. From this point of view, Cherenkov radiators [18] could be considered as scintillators, which is fundamentally incorrect. A second limitation results from the confusion between scintillation and luminescence, which is at the origin of a semantic imprecision between scintillators and luminophores. Although for the end user "there is no difference between a scintillator and a fluorescent lamp," according to A. Lempicki, there is nevertheless an important difference in the mode of excitation and energy relaxation.

The mechanism of luminescence, which is exploited in fluorescent lamps and in lasers, results from the radiative relaxation of an active ion of the material after the direct excitation between its fundamental state and excited energy levels by an electrostatic discharge or a pulse of light. On the other hand the origin of the scintillation is the energy loss of ionizing radiation through matter.

Electrons and γ quanta lose energy when traversing a medium by the three fundamental mechanisms of electromagnetic interactions:

(a) photoabsorption,
(b) Compton scattering, and
(c) electron–positron pair formation.

The interaction cross section through each of these mechanisms is energy dependent [19], photoabsorption and Compton scattering being dominant at low and medium energy and pair formation at high energy with an onset at 1.02 MeV, the mass energy of an electron–positron pair at rest. Neutral particles and charged hadrons lose energy mainly through direct interactions with

nuclei or ionization of atoms for charged particles. Knock-on electrons or γ or β decay from the relaxation of nuclei excited by neutron or neutrino capture will then lose energy through the standard electromagnetic interactions described above. As long as the energy of particles is high enough for multiple scattering and electron–positron pair creation, their energy is progressively distributed to a number of secondary particles of lower energy which form an electromagnetic shower. Below the threshold of electron–positron pair creation, electrons will continue to lose energy through Compton scattering. In the case of an ordered material like a crystal, another mechanism takes place at this stage. The electrons in the keV range from the shower will start to couple with the electrons and atoms of the lattice. They will excite the electrons from the occupied electronic states of the material (valence or deeper bound states) at different levels in the conduction band. At each of these interactions, an electron–hole pair is created. If the energy of the electron is high enough to reach the ionization threshold, we have then free carriers which will move randomly in the crystal until they are trapped by a defect or recombine on a luminescent center. In the case the ionization threshold is not reached the electron and hole will cool their energy by coupling to the lattice vibration modes until they reach the top of the valence band for the hole and the bottom of the conduction band for the electron. They can also be bound and form an exciton whose energy is in general slightly smaller than the bandgap energy. At this stage the probability is maximum for a coupling to luminescent centers through either an energy or a charge transfer mechanism.

For a material to be a scintillator it must contain luminescent centers. They are either extrinsic, generally doping ions, or intrinsic, i.e. molecular systems of the lattice or of defects of the lattice which possess a radiative transition between an excited and a lower energy state. Moreover, the energy levels involved in the radiative transition must be contained in the forbidden energy band, to avoid reabsorption of the emitted light or photo-ionization of the center.

In a way, a *scintillator* can be therefore defined as a wavelength shifter. It converts the energy (or wavelength) of an incident particle or energetic photon (UV, X-ray, or gamma-ray) into a number of photons of much lower energy (or longer wavelength) in the visible or near visible range, which can be easily detected with current photomultipliers, photodiodes, or avalanche photodiodes.

In contrast to Cherenkov radiation, scintillation occurs as the result of a chain of processes which are characterized by different time constants. This is well described by Vasiliev [20] and will be discussed in details in Chap. 4, taking into account the existence of thresholds of "hot" electrons and holes inelastic interactions. Four essential phases are distinguished and listed in Table 1.1.

Table 1.1. The sequence of processes leading to scintillation in a medium

Phase	Characteristic Time, s
1 *Energy conversion:* Initial energy release with formation of "hot" electrons and holes	$\tau_1 = 10^{-18} - 10^{-9}$
2 *Thermalization:* Inelastic processes of interaction of "hot" electrons and holes and their thermalization	$\tau_2 = 10^{-16} - 10^{-12}$
3 *Transfer to luminescent centers:* Formation of excitonic states and groups of excited luminescent centers	$\tau_3 = 10^{-12} - 10^{-8}$
4 *Light emission:* Relaxation of excited luminescent centers and emission of scintillation light	$\tau_4 > 10^{-10}$

The initial energy release in a medium occurs in a wide time range; however, its duration cannot be smaller than $2R/c$, where $R \sim 10^{-10}$ m is the order of atomic radius and c is the light speed. It also cannot exceed the transit time of the particle or γ-quantum in the scintillator and, for crystalline inorganic compounds, is restricted to a few nanoseconds. It must be noticed at this stage that the transfer to the detecting medium of at least a fraction of the energy of a particle does not necessarily require the transit of that particle through the medium. The transverse electrical field associated with a relativistic particle traveling close to the surface of a dielectric inorganic scintillator can in fact penetrate the medium and therefore interact with the electrostatic field of the crystal. This phenomenon could be exploited for the monitoring of intense particles beams near a flat surface or through nanotubes [21].

The "hot" electrons and holes inelastic scattering processes and their thermalization are rather fast in heavy crystals generally used as scintillating materials which are characterized by a high density of electronic states.

The formation of excitonic states and the transfer of their excitation to luminescent centers occur with characteristic time constants which are generally in the picosecond range.

At the end of the process the relaxation of the excited luminescent centers and the corresponding light emission is characterized by time constants distributed in a wide time range which are determined by the quantum wavefunction characteristics of the different levels involved in the transitions.

It must be noticed here that the excitation of the scintillation by a charged particle does not necessarily require direct impact of the particle with the electrons and nuclei of the scintillation medium. Energy is transferred from the particle to the scintillation through the electromagnetic field associated to the particle. It is therefore possible to excite the luminescence of a scintillator by a relativistic particle (the transverse extention of the electromagnetic wave is larger in this case) travelling very close to its surface without penetrating it.

Therefore, *scintillation* is a luminescence induced by ionizing radiation in transparent, dielectric media.

This complex sequence of phenomena characterizes the scintillation process, contrary to the photoluminescence which results from the direct excitation of the luminescent centers.

The kinetics is therefore more complex in many cases, contrary to what can be observed in gases, condensed gases, fluids, and their vapors. In such media the atoms of the gas or molecules of organic dyes or anionic complexes of rare-earth ions can be considered to some extent as free with almost no interaction with other particles of the medium. The luminescence decay time is therefore equal to the radiating decay time τ_r of luminescent centers excited states. It means that all the light quanta have been emitted after a few τ_r. On the other hand, crystalline compounds are characterized by a noncontinuous electronic energy distribution with an energy gap $E_g \gg kT$, separating a filled valence electronic band from higher energy and generally not populated levels forming the conduction band. The width of the forbidden band between the valence and the conduction band determines if the material is a semiconductor ($<$ 2–3 eV) or an insulator ($>$3 eV, typically $\geq$4 eV).

For a given material, a plurality of luminescent centers, whose radiating levels are localized in the forbidden zone, can coexist and interfere with each other. Some of these luminescent centers are cations or anionic complexes of the lattice or doping ions such as Ce^{3+} specifically introduced at the crystal growth. Some others are generated by the interaction of the ionizing radiation with the medium. Such induced centers play an important role in the scintillation as they can sensitize or quench luminescence or act as electron or hole donors for existing radiating centers via a secondary excitation process. In practice this secondary excitation is generated not only by direct Coulomb interaction but also by thermoactivation or electron tunneling from matrix host defects which trap electrical carriers produced by the incident particle. The kinetics of primary and secondary excitation processes are different. If we define ω_{int} as the frequency of interaction between primary and secondary luminescent centers in the medium, we can distinguish different cases, depending on how the mean time between interactions compares with the time of formation of primary excited luminescent centers τ_3 and with their radiating decay time τ_r.

For

$$1/\omega_{int} \sim \tau_3 \ll \tau_r \ , \tag{1.1}$$

the kinetics of the direct scintillation will dominate, characterized by a very fast rise time followed by a single exponential decay, the signature of the radiative relaxation of the luminescent center.

If on the other hand

$$1/\omega_{int} \gg \tau_r \quad \text{and} \quad 1/\omega_{int} \gg \tau_3 \ , \tag{1.2}$$

which is frequently the case in real materials, the direct scintillation is accompanied by a phosphorescence which results from the delayed decay of the secondary luminescent centers. The interaction of luminescent centers between themselves or with charge carriers traps leads to a more complex kinetics with generally longer rise time and strong nonexponential decay with long tails in some cases. As a measure of the contribution of phosphorescence in scintillation, the afterglow parameter is used. *Afterglow* is the amplitude of the luminescence signal, excited by ionizing radiation and measured after a fixed time, for example $10 \cdot \tau_{\mathrm{r}}$.

Scintillation is characterized by several parameters. Some of them depend on the shape, surface state, and optical quality of the scintillator block. We list here those which are related to the physical process of light production in the medium.

1.1.1 Scintillation Yield

Following [22,23] we define the quantum yield or the light yield of scintillation Y as the amount of light quanta emitted by a scintillator per unit energy deposited by ionizing radiation in the medium. Thus,

$$Y = \prod_i y_i \ , \tag{1.3}$$

where y_i are the yields of the processes given in Table 1.1.

The yields of the first two processes have been analyzed by the authors [24–29]. The models show approximately the same limiting yields [23] but their experimental measurement is not easy as it is difficult in practice to decouple these processes from luminescence quenching in real crystalline materials. A phenomenological approach leads to the following formulation:

$$y_1 \cdot y_2 = \frac{E_\gamma}{\beta \cdot E_{\mathrm{g}}} \ ,$$

where $\beta \cdot E_{\mathrm{g}}$ is the mean energy necessary for the formation of one thermalized electron–hole pair in a medium with a forbidden zone of width E_{g} and E_γ is the absorbed energy.

The yield of the formation of radiating centers S is defined by the efficiency of the energy transfer of thermalized pairs to the excited states of luminescent centers.

Finally we define Q as the quantum yield of the intracenter luminescence. Hence,

$$Y = \frac{E_\gamma}{\beta \cdot E_{\mathrm{g}}} S \cdot Q \tag{1.4}$$

and the energy efficiency of scintillation Y_{e} is

$$Y_{\mathrm{e}} = \frac{E_f}{\beta \cdot E_{\mathrm{g}}} S \cdot Q \ , \tag{1.5}$$

where E_f is the average energy of scintillation photons. There is therefore a clear advantage of having a host with a small bandgap. In this case however, the risk of photo-ionization of the activator increases if its ground or excited states are too close to the valence or conduction bands respectively. The density of traps in the forbidden band also increases which generally reduces the scintillator yield. P. Dorenbos [146] has calculated a maximum theoretical scintillator yield of 140,000 photons/sec in an ideal Ce^{3+} doped scintillator with a small bandgap, just large enough to host the Ce^{3+} optimal transition.

These expressions become more complex if we take into account additional mechanisms of energy losses, for instance surface losses in a medium [30, 31], and the structure of the density of states in the valence and in the conduction bands [20].

1.1.2 Kinetics of Scintillations

The kinetics of scintillation $I(t)$ is defined as the law of the variation in time of the scintillation light intensity and its magnitude $I = \int I(t)\,dt$ is proportional to Y. It is related to the time variation of the population of the excited states of the luminescent centers. For a simple process, with only one radiating center and no interaction between luminescent centers and traps, the decay is exponential and characterized by a time constant τ_{sc}, the time after which the amplitude has decreased by a factor e. For two independent radiating centers the same description with two exponentials is also valid. But in real cases the situation is very often more complex, involving energy transfer between centers and quenching mechanisms, and the resulting light emission is strongly nonexponential. It is nevertheless a common practice to describe this complex emission curve by a series of exponentials with different time constants. This has in most of the cases no physical justification but simplifies the calculations.

1.1.3 Radioluminescence Spectrum

This is the wavelength (or frequency or energy) distribution of the scintillation light when the medium is excited by ionizing radiation. It is generally composed of a series of emission bands which are each characterized by their maximum λ_{sc} or ν_{sc} and half-width $\Delta\lambda_{sc}(\Delta\nu_{sc})$ at a given temperature. Radioluminescence is also called cathodoluminescence in reference to the first observations of scintillation at the cathode of an electron gun.

1.1.4 Photoluminescence Spectrum

This is the wavelength (or frequency or energy) distribution of the scintillation light when the medium is excited by photons of energy below the ionization energy of the atoms. This information combined with the structure of the excitation spectrum, generally up to a few tens of eV, is very

useful to determine the energy levels involved in the excitation and relaxation mechanisms. On the other hand, one has to be very careful not to draw too rapid conclusions about the properties of the scintillator on the basis of the photoluminescence spectrum only which does not reflect at all the mechanisms of energy transfer and thermalization in the medium. This error is frequently made and leads to several misinterpretations. In the most dramatic case we can find materials with a good photoluminescent yield when excited in the UV range but with no light emitted under gamma-rays excitation. A typical example is given by the tungstate group which exhibits good scintillation properties in some host matrices ($CaWO_4$, $CdWO_4$, $PbWO_4$) and no scintillation at all in some other compounds ($BaWO_4$).

1.2 Survey of Scintillation Mechanisms

As already explained, the mechanisms of excitation of the luminescent centers in a scintillator as well as their properties are strongly influenced by the surrounding medium, particularly if this is a solid, and even more in the case of a crystal with a regular structure. Fundamental aspects of this phenomenon will be discussed in details in Chap. 4. Here we give a survey of scintillation mechanisms. The coupling between the lattice and the luminescent center is essential in the way the energy is transferred between them in both directions. In particular the conditions of localization and delocalization of excitations are strongly affected by the positions of the luminescent centers energy levels relative to the valence and conduction bands formed by the orbitals of the lattice atoms. This is well illustrated for instance by the modifications of the luminescent properties of activating ions such as Ce^{3+} depending on the type of ligand and on the strength and the symmetry of the crystalline field in different host materials.

Electrons and holes produced by ionizing radiation have several ways to be involved in the scintillation process after their thermalization:

1. $e + h \rightarrow h\,\nu$,
2. $e + h \rightarrow ex \rightarrow h\,\nu$,
3. $e + h + A \rightarrow ex + A \rightarrow A^{*} \rightarrow A + h\,\nu$,
4. $e + h + A \rightarrow A^{1+} + e \rightarrow A^{*} \rightarrow A + h\,\nu$,
5. $e + h + A \rightarrow (A^{1-})^{*} + h \rightarrow A + h\,\nu$,
6. $A \rightarrow A^{*} \rightarrow A + h\,\nu$

The simplest emission process (1) is the result of the direct radiative recombination of free thermalized electrons in the conduction band with holes from the valence band or from deeper electronic shells. Usually the ionizing radiation produces deep holes in the lattice which are progressively converted into holes of smaller energy through a succession of Auger conversions. Similarly hot electrons from the first interaction are cooled down to the bottom of the

conduction band by inelastic interactions. In most of the cases the recombination takes place when the energy of the electron and hole has sufficiently decreased so that they bind to each other, creating an exciton with an energy slightly smaller than the bandgap.

However, for certain configurations of the valence and core atomic electron bands the Auger conversion cannot take place and the electron recombines directly with a deep hole, giving rise to a fast UV emission [32–34]. Such kind of radiating recombination is called cross-luminescence and it is observed in some wide band gap fluoride and chloride crystals.

Thermalized carriers can also be bound in some places of the lattice, for instance, in the vicinity of a specific atom or a structural defect (2). They are called autolocalized excitons (*ex*) and their radius, small or large, depends on the electrostatic field in this configuration. In many inorganic compounds these excitons have a radiative decay channel [35]. The luminescence of free excitons or bound excitons is generally absent in complex compounds and has been observed so far only in simple oxides [36, 139].

Under certain conditions in the presence of impurity centers or activating ions A the exciton luminescence is efficiently quenched, causing thus a sensitization of the luminescence of the activating ions A(3). In this case the excitation of radiative centers results from an energy transfer from excited matrix states.

The process competing to the formation of excitons is the direct capture of free thermalized carriers, electrons (4) or holes (5) by activating ions A with the subsequent formation of their excited state A^*. The cross section for electron or hole capture depends on the nature of the activating ion and on the structure of the local electrostatic field in its vicinity. In contrast to the previous case the excitation of radiating centers is now the result of a charge transfer mechanism from excited matrix states.

Finally the direct excitation of activating centers by ionizing radiation (6) provides an important contribution to the scintillation in the case of heavy doped or self-activated scintillators. A typical example is cerium fluoride (CeF_3).

Besides these mechanisms, an intrazone luminescence caused by radiating transitions of hot electrons and holes from the conduction and valence bands has also been reported [37]. This luminescence is distributed in a wide spectral region and characterized by a low yield, independent of the temperature, of typically 10^{-3}–5×10^{-6} eV/eV in $NaNO_3$ and $BaMgAl_{10}O_{17}$ crystals. The decay time τ_{sc} is very fast, of the order of a few nanoseconds only.

The efficiency of activated scintillators is strongly dependent on the ratio of the bandgap in the crystal to the energy of the activator radiating state as well as on the relative position of its ground and excited states to the top of valence band and to the bottom of the conduction band, respectively. The first requirement for an activator with an excited state energy E_r to be efficient in a host matrix with a bandgap E_g is

$$E_{\mathrm{g}} \geq E_{\mathrm{r}} \,. \tag{1.6}$$

This condition prevents the reabsorption of the luminescence in the medium, at least if the crystal is free from impurities or structural defects having energy levels in the bandgap.

Another condition to avoid the delocalization of electrons in the conduction band from the activator excited state is related to the energy gap ΔE between the radiating level of the doping ion and the bottom of the conduction band.

Thus,

$$\Delta E \leq 0, \quad \text{the scintillation yield } Y = 0 \,, \tag{1.7}$$

$$\Delta E > 0, \quad \text{the scintillation yield } Y \geq 0 \,. \tag{1.8}$$

Moreover, if

$$\Delta E \gg kT \quad \text{or} \quad \tau_{\mathrm{r}} \ll \tau_{\mathrm{d}} \,, \tag{1.9}$$

where the delocalization time $\tau_{\mathrm{d}} \approx (1/S)\exp(-\Delta E/kT)$, with S is the frequency factor, k is the Boltzman constant, and T is the temperature, the scintillation yield is not strongly dependent on the temperature. In the reverse case, one can anticipate a reduction of the scintillation yield when the temperature increases (temperature quenching).

The energy gap between the ground state of the activating ion and the top of the valence band plays also an essential role in the hole capture by the activator through the mechanism (4). In the case of a ground state localization in the valence band, the hole remains delocalized and its trapping never occurs. If on the other hand the activator ground state lies too high above the valence band, the probability of hole capture by the radiating center is low, resulting in a poor efficiency of the scintillator.

The characteristic decay time for the direct electron–hole recombination (1) does not exceed a few nanoseconds if the final state involves a core atomic band. If on the other hand there is a participation of the valence band in the direct or excitonic recombination (1,2), the scintillation, as a rule, is characterized by slowly decaying kinetics due to radiating recombination process with characteristic time constants in the μs–ms region. The fact that some self-activated scintillators, like $PbWO_4$ [38], exhibit a fast room temperature scintillation in the nanosecond range is only the consequence of a luminescence-quenching mechanism competing with the radiative relaxation of the excitation. In this case the decay is nonexponential, which is a common signature of temperature-quenched scintillators.

In the case of radiating transitions in the simple model of the dipole electrical transition the lifetime of the activator luminescence (radiant time) is defined by the well-known formula:

$$\tau_{\mathrm{r}} \sim 1/(\nu^3 \langle \Psi_A \,|d|\, \Psi_A^* \rangle^2) \tag{1.10}$$

where $\langle \Psi_A | d | \Psi_A^* \rangle$ is the operator of the dipole electrical transition between the excited and ground states of the activating ion and ν is the frequency of the transition. The general expression is given in [39]:

$$\tau_{\mathrm{r}} = \frac{1.5 \times 10^5 \lambda^2}{f \frac{1}{9}(n^2+2)^2 \, n} \, , \tag{1.11}$$

where f is oscillator strength, λ is averaged wavelength of transition equal to $1/\nu$, and n is index of refraction of the medium.

When the requirements (1.8) and (1.9) are satisfied and in the absence of quenching mechanisms the radiating time is close to the radiant time. Figure 1.1 shows the room temperature radiant (τ_{r}) and scintillation (τ_{sc}) time of the interconfiguration $5d \rightarrow 4f$ transition of the Ce^{3+} ion in different crystals as a function of the frequency ν of the peak of the luminescence. GSO and YSO have two different coordinations of Ce^{3+} with different maxima and kinetics of the luminescence. The luminescence decay time correlates well with a square-law dependence of the radiating time with the frequency of the peak of the luminescence band.

On the other hand, the values for the scintillation decay time τ_{sc} are in some cases very different from the intracenter-excited luminescence radiating

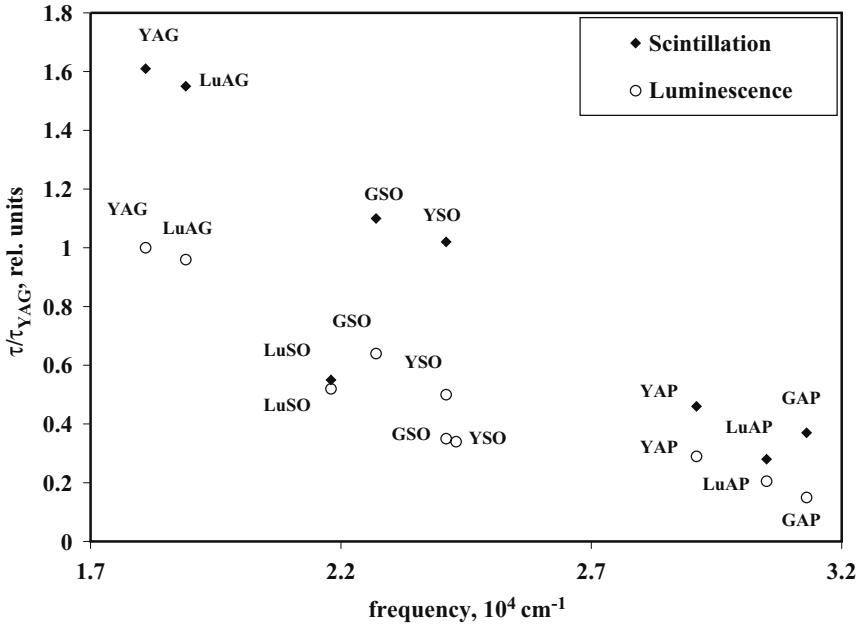

Fig. 1.1. Luminescent decay time τ_{r} of the interconfiguration $5d \rightarrow 4f$ transition of the Ce^{3+} ion and scintillation decay time τ_{sc} versus frequency ν of the luminescence band maximum at room temperature. Data are taken from [42–48]

time. This is caused by the time needed to transfer the energy to the radiating centers through the different mechanisms described in this paragraph. If this transfer occurs preferentially through the energy transfer mechanism, the decay time of scintillation is closer to the radiating time of the activator. This is explained within the Förster–Dexter model [40, 41] describing the sensitization of activating ions by randomly distributed donors in the crystal. According to the model the luminescence kinetics in a dipole approximation is described by the expression

$$I(t) = I_0 \exp[-(t/\tau_\mathrm{r}) + 4\sqrt{t}\pi^{3/2} N_\mathrm{a} (C_\mathrm{DA})^{1/2}/3 + \bar{w}t] \,, \tag{1.12}$$

where N_a is the concentration of activators, C_DA is a parameter of donor–acceptor dipole–dipole interaction, and $\bar{\omega}$ the rate of migration-restricted energy transfer. For a large migration rate $\bar{\omega}$ and interaction probability C_DA, the rise time of the scintillation is fast and the scintillation kinetics approaches the intracenter-excited luminescence kinetics.

For the direct recombination of thermalized electrical carriers as well as for the excitonic emission according to the processes (1) and (2), the peak emission of the scintillation correlates with the band-gap value. The set of possible radiating states is in this case limited to excited levels of metallic ions of the host matrix, polaronic or excitonic states, or shallow traps. All these states are located near the bottom of the conduction band. As the relaxation involves energy levels situated at the top of the valence band, the energy of the transition is generally close to the bandgap energy. However, the interaction of the electrostatic field of the lattice with the radiating center, which is in practice different for the excited and the ground state, introduces a modification of the orbital configurations through vibronic interactions [49]. This effect results in a shift of the luminescence band maximum to longer wavelength (the Stockes shift). Figure 1.2 shows the wavelength of the scintillation band maximum of various undoped scintillation crystals versus their respective bandgap energy.

In doped crystals the luminescence properties of the doping ions can be predicted by the effect of the crystalline field for ions of the iron group [50,51] and for the rare-earth ions in the frame of the model described in [52]. It has been shown that for a given crystalline matrix the energy difference between the first excited state $4f^{n-1}5d$ and the ground state configuration $4f^n$ is given by

$$\Delta_{fd} = \Delta^0_{fd} - \sigma_2 S_\mathrm{host} \tag{1.13}$$

where Δ^0_{fd} is the energy difference between the first excited state $4f^{n-1}5d$ and the ground state configuration $4f^n$ of a free ion, and S_host is the parameter defined by the specificity of the matrix host,

$$\sigma_2 = [\langle 4f^{n-1}5d \left| r^2 \right| 4f^{n-1}5d\rangle - \langle 4f^n \left| r^2 \right| 4f^n\rangle] \sum_i \alpha_i Z_i e^2/R_i^6 \,, \tag{1.14}$$

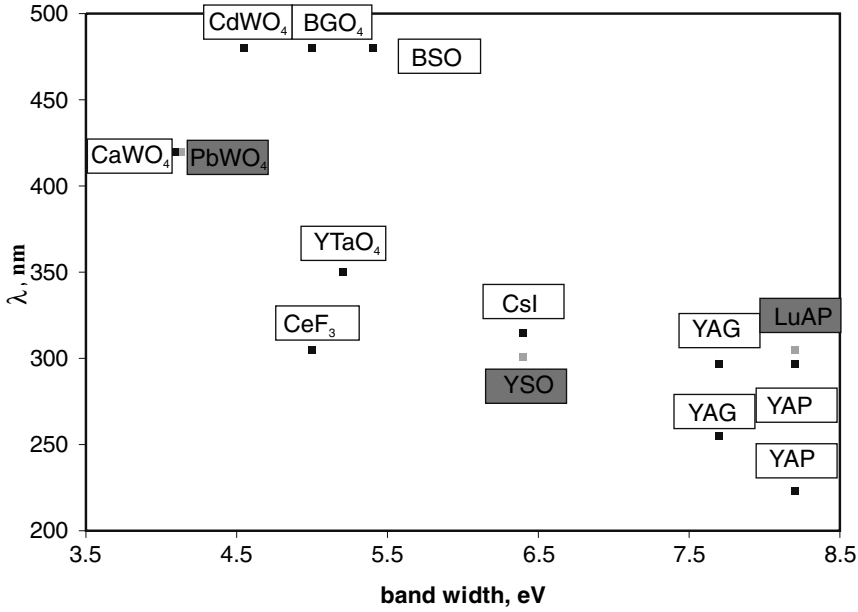

Fig. 1.2. Luminescence band maxima of various undoped scintillation crystals versus band gap. The data from [55–57] have been used

where Z_i is the quantity of ligands with polarizability α_i and distance R_i from the doping ion. Using this expression, the authors of reference [53] have shown that the energy of the first excited state $4f^{n-1}5d$ of any trivalent rare-earth ion of the Lanthanide family scales with the one of the Ce^{3+} ion and is equal to

$$\Delta_{fd}(Ln^{3+}) = C\Delta_{fd}(Ce^{3+}) + B\,, \tag{1.15}$$

where B and C are independent of the crystal parameters constants. The decrease of this energy for a given crystalline compound is about the same for all rare-earth ions because σ_2 is about the same for all lanthanides and S_{host} depends only on lattice parameters of the compound.

The surveyed model has found convincing confirmation in the analysis of spectroscopic parameters of trivalent rare-earth ions in more than 300 various compounds [54,58,59]. The basic conclusion concerning interconfiguration optical transitions in trivalent rare-earth ions is that the effects of the crystalline matrix and of the activator ion on the parameters of the optical transition are independent. Thus, knowing the energy of one allowed interconfiguration transition of any of the rare-earth ions, for example Ce^{3+} in a given matrix, it is possible to calculate similar transitions for another Lanthanide ions in the same crystalline compound.

1.3 Scintillation-Radiating Centers

We will consider here the different impurity ions which can activate a scintillator. Several self-activated scintillators show better scintillation properties when they are doped by appropriate ions. As explained in the previous paragraph, there are some conditions to be met for the activator to be efficient in a host matrix. These conditions are related to the position of the activator energy levels involved in the luminescence relative to the conduction and valence bands of the matrix. More generally the two basic practical requirements are the stability of the charge states of the luminescent center in the host and the high-quantum yield of the intracenter luminescence. They limit the number of centers to be considered and exclude, for instance, point structure defects associated to the substitution of a host matrix ion by an activator ion with a different valence state (nonisovalent doping), however, do not guarantee an efficient scintillation yield through the activation of the specific centers of a crystal.

1.3.1 Ions of the Iron Group

Radiating transitions in these ions arise between the Stark components of the $3d^n$ electronic configurations. As the $3d^n$ shell is the outer shell for the light ions of this group, the effect of the crystalline field is stronger than the spin–orbit interaction. The peak position of the luminescence band is therefore rather sensitive to the strength of the crystalline field created by the coordination of the ligands. The energies of the Stark components of the terms of the $3d^n$ configurations depend on the strength of the crystalline field. They are described by the Tanabe–Sugano diagrams [50] and discussed explicitly in the literature [60].

The lightest ion of the iron group is the titanium. Its trivalent ion Ti^{3+}has the $3d^1$ electronic configuration and is localized in an octahedral oxygen coordination. Its wide luminescence band with a maximum of 790 nm is observed in the garnet $Y_3Al_5O_{12}$. In the yttrium perovskite crystal $YAlO_3$ the Ti^{3+} ion has a luminescence band with a maximum at 610 nm and a mono-exponential kinetics with $\tau_r = 3\,\mu s$. Figure 1.3 compares the radioluminescence spectra of BGO and $YAlO_3$:Ti^{3+} (0.2 at. %). The room temperature light yield of Ti^{3+} doped crystal is 30% higher than that of BGO. Al_2O_3:Ti^{3+} crystal codoped with Ca has also an intense luminescence in the near IR with a maximum at 780 nm and a decay time $\tau_r = 4.3\,\mu s$. It has a high scintillation yield [61] and is optimally combined with semiconductor photo-detectors with high sensitivity in the IR region [62].

Ion of vanadium V^+ ($3d^4$) shows an IR luminescence in narrow band gap compounds [63]. The oxide compounds doped with vanadium ions of other valence states V^{2+} ($3d^3$), V^{3+}($3d^2$), V^{4+}($3d^1$) do not show an intense radioluminescence in the visible region at room temperature. Alcali-vanadates,

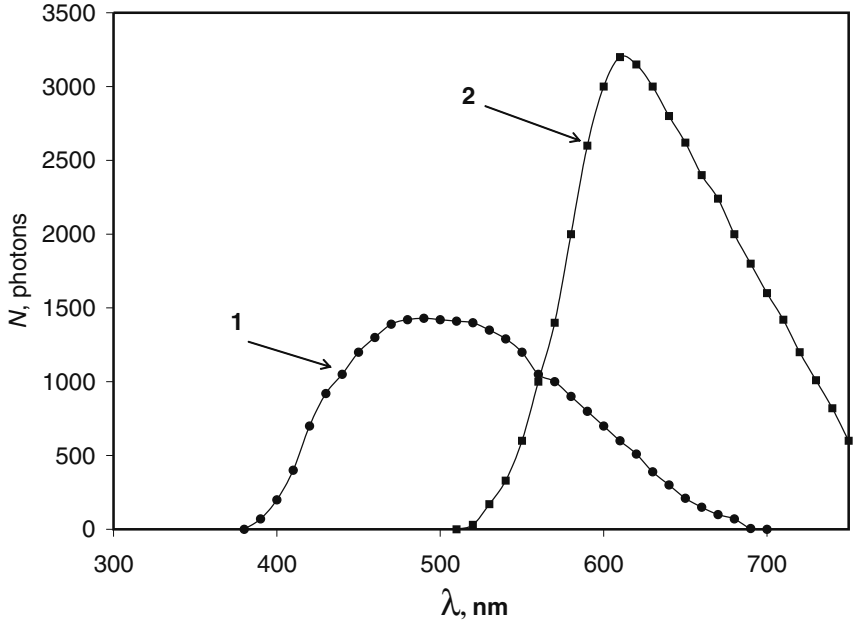

Fig. 1.3. Radioluminescence spectra of BGO (1) and $YAlO_3$:Ti (2) crystals at $T = 300\,K$

where the vanadium ion is in its maximum oxidation state V^{5+}, have an intense cathodoluminescence and are used as luminophore. Double vanadates also exhibit an intense photoluminescence. The luminescence kinetics of double vanadates has a decay time of the order of tens of microseconds at room temperature.

Another well-known activating ion, Cr^{3+} ($3d^3$), can exhibit a narrow luminescence band at 694 nm due to the $^2E \rightarrow {}^4A_2$ transition, or a wide band in the near-IR region related to the $^4T_2 \rightarrow {}^4A_2$ transition [64], depending on the crystalline field strength in the position of its localization. While crystalline field is weak, the ^{2}E term is lower than the $^4T_2$ term and causes luminescence properties of the material like in ruby. In strong crystalline field in oxygen octahedron, like in emerald, $^4T_2$ level becomes lower showing wide luminescence band. As the $^2E \rightarrow {}^4A_2$ transition is a spin-forbidden transition, the decay kinetics constant is large, of the order of milliseconds. On the other hand, the wide band decays with a characteristic time constant in the microsecond range. $Cr^{4+}(3d^2)$ ion also emits IR luminescence with a decay time constant in the microsecond range in some oxygen compounds [65].

Divalent manganese $Mn^{2+}(3d^5)$ has a strong green luminescence in many compounds with long decay times (milliseconds) because of a spin-forbidden transfer $^4T_1 \rightarrow {}^6A_1$. For instance, Zn_2SiO_4:Mn is one of the best known phosphors [66], which was applied in the first color TVs and is also used in

modern plasma panels. In this compound the Mn^{2+} ion has an intense green luminescence with a maximum near 520 nm and τ_r of about 25 ms.

The trivalent ion of iron $Fe^{3+}(3d^5)$ localized in tetrahedral oxygen coordination is also responsible for a slowly decaying IR luminescence [67]. Its $^4T_1 \rightarrow {}^6A_1$ luminescence can be either directly excited through intracenter transitions or due via a charge transfer process: $O^{2-} \rightarrow Fe^{3+}$ [68]. Iron-doped YAG, $Y_3Al_5O_{12}$:Fe, has radioluminescence spectrum with a peak at 810 nm and a scintillation yield of about 1,000 ph MeV^{-1} at room temperature. The Ni^{2+}-doped crystals also show an intense IR radioluminescence when excited by an electron beam at room temperature [69].

A general drawback of the $3d^n$ ions as activating ions in inorganic scintillator is related to their heterovalence which means that they can change their valence state under ionizing radiation. The localization of their luminescence in the near IR region and the relatively slow decay time of the luminescence are also limiting factors for several applications. It seems that from this group only the Ti^{3+} ion can be considered as a prospective activator if it is in a rather strong crystalline field environment. Apparently, rare-earth aluminium perovskite and some hafnium and zirconium compounds are good host candidates from this point of view.

1.3.2 Ions With s^2 Outer Shell (Mercury-Like Ions)

Ions with s^2 outer shell form a large class of luminescent centers. They are easily introduced into various crystalline compounds which find wide application as phosphors for fluorescent lamps and various fluorescent transducers [70,71]. Ga^+, Ge^{2+}, Se^{4+} with $4s^2$ outer shell; In^+, Sn^{2+}, Sb^{3+}, Te^{4+} with $5s^2$ shell; Hg, Tl^+, Pb^{2+}, Bi^{3+} with $6s^2$ are all in this class. These ions have an intense interconfiguration transition $s^2 \rightarrow sp$ in the vacuum ultraviolet (VUV) range. However the associated luminescence is not observed due to quenching by underlying excited terms $^1P_1$, $^3P_2$, $^3P_1$, $^3P_0$ of s^2-configuration. The intraconfiguration luminescence $^3P_0 \rightarrow {}^1S_0$ is characterized by a large Stokes shift in many compounds and, hence, has strong temperature quenching [72]. The radiant decay time is of the order of hundreds of microseconds at low temperatures but is reduced by three orders of magnitudes (hundreds of nanoseconds) at room temperature by temperature quenching. Moreover the spin–orbit interaction mixes singlet and triplet excited states, reducing further more τ_r in heavy $6s^2$ ions as it is observed for Tl^+, Pb^{2+}, Bi^{3+} ions in an alcali halide and oxide compounds. Ions of s^2 type have played a prominent role in inorganic scintillators development. The discovery of the most widely applied scintillation crystal NaI (Tl) [15] became possible because of the numerous studies of the luminescent properties of the Tl^+ ion in alcali halides. Moreover the first heavy scintillator, BGO, is also the result of systematic investigations of the Bi^{3+} ion in various oxide compounds.

1.3.3 Ion of Molybdenum

Mo doping ion in crystals of tungsten compounds is considered to be a characteristic luminescent center. The Mo impurity substitutes to the tungsten ion in the matrix and forms an anionic complex MoO_4^{2-}, which has a large cross section for electron capture. The properties of the MoO_4^{2-} center and its influence on scintillation parameters of lead tungstate crystal are described in [73, 74].

1.3.4 Uranium Anionic Complexes

Another well-investigated luminescent center is the anionic complex $UO_2{}^{2+}$, which shows a bright green–yellow luminescence in a variety of the crystalline compounds grown from saturated solution [75]. There have been several mentions in the past of a fast luminescence kinetics (nanoseconds) of uranium compounds [76]; however, the majority of the observed uranium doped compounds have a luminescent band with a characteristic decay constant in the microsecond range. Recently it has been shown [77] that the uranyl ion U^{4+} in the $LiYF_4$ crystal has a strong interconfiguration luminescence band $6d5f \rightarrow 5f^2$ in the 240–360-nm region at room temperature. The fast component of the decay $\tau_r = 15$–19 ns dominates in the kinetics. The luminescent properties of the U^{4+} ion have some similarities with those of the Pr^{3+} ion described below.

1.3.5 Rare-Earth Ions

Rare-earth ions are the most frequently used activating luminescent ions. Intraconfiguration luminescent transitions $4f^n \rightarrow 4f^n$ of trivalent ions Pr, Nd, Sm, Eu, Gd, Tb, Dy, Ho, Er, Tm, Yb are widely used in fluorescent lamps, cathode tubes, and lasers [78]. Slow and bright scintillation in the IR region with $\tau_{sc} = 1.9$ ms has been reported in $Y_3Al_5O_{12}$ crystal doped with trivalent ytterbium [79]. The general trend today is to look for fast scintillators. Fast-decaying scintillation in inorganic compounds can be obtained when they are activated by rare-earth ions with the transition $4f^{n-1}5d \rightarrow f^n$. Interconfiguration transitions in trivalent rare-earth ions are allowed both on spin and on parity. They are therefore fast with a decay time constant of $\tau_r = 5$–100 ns. Such trivalent ions are restricted to five rare-earth elements: Ce^{3+} ($4f^1$), Pr^{3+} ($4f^2$), Nd^{3+} ($4f^3$), Er^{3+} ($4f^{11}$), and Tm^{3+} ($4f^{12}$). However the interconfiguration luminescence of Nd^{3+}, Er^{3+}, Tm^{3+} is localized in the region higher than 45,000 cm^{-1} and observed in fluorides only [80]. Moreover, for these three ions there is a strong quenching of this interconfiguration luminescence due to a nonradiating transfer on numerous underlying f levels.

Practically, only two ions, Ce^{3+} and Pr^{3+}, are therefore acceptable activators with a bright and fast scintillation in many compounds. However, the praseodymium ion has, though to a lesser degree, the same problem as

the neodymium ion – a quenching due to nonradiating transitions on lower f levels. Let us consider in more detail the energy-level scheme of trivalent praseodymium ions in a typical fluoride crystal, LaF_3 and in two oxides namely garnet and oxyorthosilicate. They are compared in Fig. 1.4. Contrary to the oxide compounds, the $^1S_0$ level of the f configuration lays below the Stark components of the $5d$ level in fluorides, causing the complete quenching of $4f5d \rightarrow f^2$ Pr^{3+} ion luminescence [81, 82].

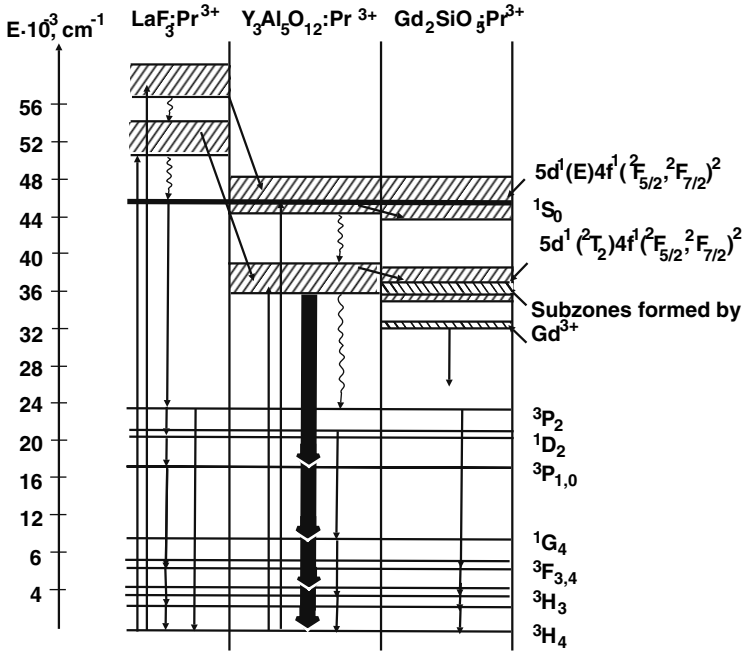

Fig. 1.4. The position of d and f configuration energy levels of Pr^{3+} ion in some crystalline compounds

However, the interconfiguration luminescence is observed as two overlapped wide unstructured bands in many oxide compounds at room temperature for which the host matrix ions do not have energy levels in the forbidden band (for instance, Y, Lu). This is not the case for gadolinium (Gd) where a nonradiative transfer to the subzones formed by the lower excited states $\{^6I_J, ^6P_J, J = 7/2\}$ of Gd^{3+} ions quenches the luminescence.

Ce^{3+} ions have a rather simple structure of energy levels which is shown in Fig. 1.5 according to the data from [83]. The basic $4f$ configuration of the Ce^{3+} ion consists of two spin–orbit components $^2F_{7/2,5/2}$, with an energy difference $\sim$2,400 cm^{-1} As the effect of the crystalline field for the f-orbital of a rare-earth ion is much weaker than the spin–orbit coupling this energy

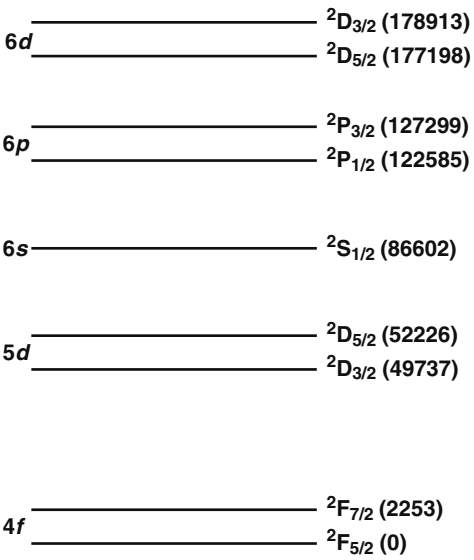

Fig. 1.5. Energy-level structure of free Ce^{3+} ion. Energy levels are given in cm^{-1}

gap between the components $^2F_{7/2,5/2}$ is approximately the same in many compounds. In contrast, the $5d$-orbital is strongly influenced by the ligands.

The influence of the type of ligand (nepheloxetic effect) appears as a decrease of the difference between the d and f energy levels from the free ion value following the sequence of ligands: F^-, Cl^-, Br^-, I^-. The average difference in fluorides is $\sim$45,000 cm^{-1}, in chlorides $\sim$37,000 cm^{-1}, in bromides $\sim$35,000 cm^{-1}, and in iodides $\sim$31,000 cm^{-1} [59]. Oxygen compounds have a mean difference of about 40,000 cm^{-1}; however, one can distinguish several groups as a function of the type of matrix creating the oxy-anionic complex [59] as is shown in Table 1.2.

Table 1.2. Mean energy difference between d and f configurations of Ce^{3+} ion in oxide compounds in different matrices with an oxy-anionic complex

Anionic Group	SO_4^{2-}	CO_3^{2-}	PO_4^{3-}	BO_3^{3-}	SiO_4^{4-}	AlO_6^{9-}, AlO_4^{5-}
Energy difference (cm^{-1})	43,000	42,000	41,500	40,000	39,000	37,000

The mean luminescence maximum of the $4f^0 5d^1 \rightarrow 4f^1$ transition decreases following the same sequence of ligands: fluorides $\sim$35,000 cm^{-1}, chlorides $\sim$28,000 cm^{-1}, bromides $\sim$26,000 cm^{-1}, oxides $\sim$24,000 cm^{-1}, and sulfides $\sim$18,000 cm^{-1} [84]. The next upper $6s$ configuration is not subject to

a strong influence of the nepheloxetic effect as the $6d$ configuration is mixed with levels of $6s$ and $6p$ configurations.

Only the $5d$ first excited configuration and its Stark components appear in the forbidden zone in the majority of oxides with the oxy-complexes mentioned before. The symmetry of the ligand polyhedron and the coordination of the Ce^{3+} ion determine the level of the Stark decomposition of the $5d$ configuration. Two sets of bands with maxima at 21,830, 29,400 cm^{-1} and at 38,300, 44,400, 48,780 cm^{-1} are observed in absorption and excitation spectra of $Y_3Al_5O_{12}$ where the Ce^{3+} ion is localized in an eightfold oxygen site with a local symmetry D_2. They correspond to the transitions to the doublet E and to the triplet $^3T_1$ of the $5d$ configuration [85–87]. A separation of the doublet components is also found in $LuBO_3$ with vaterite structure where the Ce^{3+} ion is localized in a position with point symmetry D_{2d}, and components of the doublet have maxima near 27,400 and 29,000 cm^{-1} [88]. In a less visible way the doublet was also found in phosphates YPO_4, $LuPO_4$ [89–91] with absorption and excitation bands around 31,000 and 40,000 cm^{-1} have been measured. The localization of the Ce^{3+} ion is C_1 in rare-earth perovskites and an inverse disposition of the triplet and the doublet was observed in absorption and luminescence excitation spectra. For example, the three components of the triplet are seen in $YAlO_3$ at 33,300, 34,500, 36,360 cm^{-1}, and the two components of the doublet have their maximum at 41,900 and 45,500 cm^{-1}, respectively [92, 93].

The Ce^{3+} is localized in the crystalline structure with a ligand coordination number going from 7 up to 12, leading to a large variation of the crystalline field. Therefore, the five components of the Ce^{3+} ion $5d$ configuration decomposition are observed in various compounds in a wide spectral interval between 50,000 and 17,000 cm^{-1}. The maximum of the corresponding luminescence also varies in a wide range from 35,000 up to 15,000 cm^{-1}.

As the averaged energy difference between the ground and first excited states of Ce^{3+} exceeds 10,000 cm^{-1} in the majority of hosts the luminescence quantum yield for an intracenter excitation is close to 1 at room temperature and up to rather high temperature. For example, the temperature luminescence quenching starts at 500 K in $YAlO_3$:Ce^{3+} [94] only.

Besides the trivalent rare-earth ions discussed here, the divalent Eu^{2+} ion is also subject to a bright interconfiguration luminescence; however, it has a relatively slow kinetics with τ_r about 1 µs [95]. The intense 440 nm $4f^6 5d^1 \rightarrow 4f^7$ luminescence band of the Eu^{2+} ion is found in crystals with a structure of the type MAl_2O_4 (M = Co, Sr) [96]. There is a phosphorescence due to the decay of electron centers and the subsequent excitation of Eu^{2+} ion that makes impossible their application as fast scintillators.

The candidates of choice to design fast-doped scintillators within the rare-earth ions family are therefore the trivalent ions of Ce and Pr.

1.4 Classification of Inorganic Scintillation Materials

Since the discovery of sodium iodide by Hofstadter in 1949, alcali-halide crystals have been the most widely used scintillators in numerous applications ranging from detectors for physics research to industrial and medical imaging devices. But the limits of these crystals, especially in experimental high energy and nuclear physics, became apparent with the development of fast response photodetectors, electronics and acquisition systems in the beginning of the eighties. On the other hand, the fast development of crystallographic production technology as well as the large research effort in the field of laser media based on oxide and fluoride crystalline materials boosted the development of high-temperature production technology of crystals. Luminescent crystalline oxide and fluoride of high quality became available in large quantities. This has led to the discovery of a number of new prospective scintillation materials. With the increase of the number of known inorganic scintillators, several approaches to classify them have been developed. Here we will discuss several classifications of the scintillators and give a list of the developed to date scintillation materials and their properties because many of them will be quoted in chapters bellow.

1.4.1 Classification Based on the User's Requirements

Such a classification would help the end user to quickly identify the best scintillating material for a given application. In this case the parameters of choice are the density, the photo-fraction, the light yield, the decay time, and more generally the scintillation performance in the low – ($E < 10\,\mathrm{MeV}$) or in the high – ($E > 10$ MeV) energy domain. Physicochemical and engineering parameters are also important as well as the conditions of the production as they have a direct impact on the price.

1.4.2 Classification Based on Scintillation Mechanisms

Lempicki [23] has suggested to divide scintillators into two categories: extrinsic and stoichiometric. As the cross-luminescence can be observed in crystals, irrespective of the presence of impurities and stoichiometric composition, it is more comprehensive to introduce three classes, namely, *activated scintillators* on the basis of crystalline compounds doped with activating ions; *self-activated scintillators* where radiating centers are ions, anionic complexes, and various excitonic states from the matrix itself; and *cross-luminescent scintillators*.

Some authors have suggested a classification based on the different types of excitons [97]. However, such an approach mixes in one-class materials very different from each other, like NaI (Tl) and $YAlO_3$:Ce, BGO and CsI.

1.4.3 Classification Based on Structural Types of Crystals

Such a classification involves only the crystallographic structure of the scintillator. This approach has allowed to predict and to produce a number of new scintillation crystals, for example, scintillators with garnet, perovskite, oxyorthosilicate, pirosilicate structure doped with cerium and praseodymium ions. Such classification is rather convenient for material scientists but of little interest for end users.

1.4.4 Classification Based on Specific Features of Materials

It has been frequently reported [29] that compounds with wide bandgap can be considered good candidates for scintillation. This is related to the development of Ce^{3+}-doped scintillation materials. On the other hand, the presence of a wide bandgap is not a necessary condition for scintillation occurrence. It increases only the potential spectral domain of the scintillation as it makes the material transparent in a wider spectral rage.

1.4.5 Combined Classification

We would like to propose here a combined classification taking into account the physicochemical properties of a material, for example, a specific anion of the matrix, with the different mechanisms of scintillation. Following this approach, we can distinguish the two important classes of halides (F, Cl, Br, I) and oxydes. Additional classes of compounds are also related to anions sulfur S, phosphorus P, and selenium Se. Each class is divided into groups which involve different mechanisms of scintillation. A further partition inside each group is based on the structural peculiarities of the compounds and of the different types of luminescent centers.

The proposed classification is oriented on one hand to the user and allows without specific knowledge to spot the potential of a class or group on the basis of given operational parameters. On the other hand, it allows the researchers to identify a set of compounds for future development on the basis of the mechanisms of scintillation. This attempt for a classification of scintillation inorganic crystalline compounds known to the present time and some of their physical and scintillation parameters are shown in Table 1.3. To scintillation parameters we insert in the table density ρ, effective charge Z_{eff}, and absorption length X_0 of the crystalline compounds.

Among the crystals listed in the table fluorides have the largest bandgap $E_g > 7$ eV. This is a condition for a possible observation of cross-luminescence. The best known representative of fluoride cross-luminescent scintillators is BaF_2, with a reasonable light yield. Another interesting cross-luminescent material is CsF with a decay time $\tau_{sc} \sim 2{-}4$ ns, and a luminescence peak at 390 nm. Among the self-activated fluorides CeF_3 has been considered as a good candidate for electromagnetic calorimetry at colliders.

Table 1.3. Inorganic scintillation compounds and their essential properties

Scintillator	ρ ($g\,cm^{-3}$)	Z_{eff}/photo absorp. coeff., 511 keV, cm^{-1}/ X_0, cm	Y ph MeV^{-1}	τ_{sc} (ns)	λ_{max} (nm)	Reference
Fluorides						
Cross-luminescent materials						
$LiBaF_3$	5.2	49.3/0.079/2.11	1,400	0.8	190, 230	98
$KMgF_3$	3.2	14.3/0.0007/8.38	1,400	1.3	140–190	98
$KCaF_3$	3	16.7/0.001/7.65	1,400	2	140–190	98
KYF_4	3.6	30.2/0.011/4.55	1,000	1.9	170	98
$BaLu_2F_8$	6.94	63/0.22/1.25	870	1+slow	313	99, 102
BaF_2	4.88	52.7/0.085/2.03	1,430 9,950	0.6 620	220 310	100
CsF	4.64	53.2/0.086/2.69	1,900	2-4	390	103
RbF	3.6	34.6/0.016/3.6	1,700	1.3	203, 234	98
Self-activated materials						
CeF_3	6.16	53.3/0.11/1.77	4,500	30	330	104, 128
Activated						
BaY_2F_8:Ce	4.97	44/0.04/2.5	980	45+slow	329	99, 102
$BaLu_2F_8$:Ce	6.94	63/0.22/1.35	400	35+slow	330	99, 102
CaF_2:Eu	3.18	16.4/0.045/3.72	21,500	940	435	101
LaF_3:Ce	5.9	50.8/0.09/1.69	2,200	26.5	290, 340	130
LuF_3:Ce	8.3	61.1/0.31/1.1	8,000	23+slow	310	130
Chlorides						
Cross-luminescent materials						
$CsCaCl_3$	2.9	43.6/0.03/4.1	1,400	1	250, 305	98
Self-activated materials						
Cs_2LiYCl_6	3.31	44.5/0.04/5.85	6,535 (1 µs) 22,420 (10 µs)	6,600	305	134
$Cs_2NaCeCl_6$	3,25	50.1/0.047/3.22	11,000	1,000	376	99
Activated materials						
Li_3YCl_6:Ce	2.45	27.4/0.027/8.17	3,305 (1 µs) 6,185 (10 µs)	250 2,300	360, 385	134

(*continue*)

Table 1.3. Cont.

Scintillator	ρ ($g\,cm^{-3}$)	Z_{eff}/photo absorp. coeff., 511 keV, cm^{-1}/ X_0, cm	Y ph MeV_1	τ_{sc} (ns)	λ_{max} (nm)	Reference
$LaCl_3$:Ce	3.86		17,000 (0.5 μs) 40,000 (10 μs)	20,330, 2,200	337, 358	130, 133
$CeCl_3$:Ce	3.9	48.4/0.06/2.02	28,000	23	360	122, 133
$LuCl_3$:Ce	4.	61/0.12/1.98	1,300 (0.5 μs) 5700 (10 μs)	50, 250–350, 4,000	374, 400	130 135 133
K_2LaCl_5:Ce	2.89	44.1/0.025/4.5	25,000	1,000	348	99
$RbGd_2Cl_7$:Ce	3.74	53.9/0.069/2.75	43,000	1,000	370	99
Cs_2LiYCl_6:Ce	3.31	44.5/0.04/5.85	9,565 (1 μs) 18,400 (10 μs)	600 6,000	372, 400	134
$Cs_2NaLaCl_6$:Ce	3.2	49.7/0.045/3.3	5,400	1,000	368	99
$Cs_2NaLuCl_6$:Ce	3.71	56.5/0.079/2.61	5,200	1,000	373	99
Cs_3LuCl_6:Ce	3.79	56.7/0.083/2.27	4,400	1,000	375	99
$Cs_3Lu_2Cl_9$:Ce	4.01	58.6/0.097/2.46	650	100,000	409	99
Bromides						
Cross-luminescent materials have not be found						
Self-activated materials have not be found						
Activated materials						
$LaBr_3$:Ce	5.29	46.9/0.065/1.64	61,000	17-35		145
$LuBr_3$:Ce	5.17	63/0.17/1.29	10,000 (0.5 μs) 24,000 (10 MKS)	32,450–550, 5,000	408, 408	130 133
$RbGd_2Br_7$:Ce	4.8	50.6/0.070/2.03	54,700	66	420	99
Cs_2LiYBr_6:Ce	4.15	45.2/0.046/2.15	25,000	72+slow	388	145
K_2LaBr_5:Ce	3.9	42.8/0.035/2.3	40,000	100	359	145
$RbLu_2Br_7$:Ce	4.8	53.6/0.099/1.92	30,000	80+slow	420	130
Iodides						
Cross-luminescent materials have not be found						
Self-activated materials						
CsI	4.51	54/0.09/2.43	16,800	10	310	101
CaI_2	3.96	51.1/0.065/2.29	86,000	550	410	105
HgI_2	6.38	68.8/0.27/1.13	6,000	2,100	580	106
Activated materials						
NaI:Tl	3.67	50.8/0.058/2.56	43,000	230	415	107
CsI:Tl	4.51	54/0.09/2.43	51,800	1,000	560	101
CsI:Na	4.51	54/0.09/2.43	38,500	630	420	101

Table 1.3. Cont.

Scintillator	ρ ($g\,cm^{-3}$)	Z_{eff}/photo absorp. coeff., 511 keV, cm^{-1}/ X_0, cm	Y ph MeV_1	τ_{sc} (ns)	λ_{max} (nm)	Reference
LaI_3:Ce	5.6	54.2/0.12/1.52	200–300	1–2	452, 502	140
LuI_3:Ce	5.6	60.4/0.17/1.35	50,000	31(69%) 400(15%) 3,000(16%) + slow	475, 520	141
K_2LaI_5:Ce	4.4	52.5/0.084/1.91	57,000	24	401	145
CaI_2:Eu		50.6/0.065/2.29	86,000	790	470	105
LiI:Eu	4.08	40.8/0.073/2.73	12,900	1,400	470	101
Sulfides						
Cross-luminescent materials have not be found						
Self-activated materials have not be found						
Activated materials						
CdS:Te	4.8	48/0.051/2.15	17,000	270+slow	640 580	108
Gd_2O_2S:Pr,Ce,F	7.34	61.1/0.214/1.13	40,000	2,100	580	109
Lu_2S_3:Ce	6.2	66.7/0.241/1.25	28,000	32	592	110
$PbSO_4$	6.1-6.4	70.4/0.34/1.3	5,500	1.8, 19 95	340, 380	142 143
Oxides						
Cross-luminescent materials have not be found						
Self-activated materials						
BeO	2.86	8.1/0.0003/7.3	6,500	18	250	123, 125
Y_2O_3	5.04	36/0.019/3.02	15,480	28	370	125
$Y_3Al_5O_{12}$	4.55	30.1/0.014/3.6	11,610	100	260	125
$YAlO_3$	5.35	32/0.02/4.1	9,000	2, 60,2000	308	55, 127
$LuAlO_3$	8.34	64.9/0.29/1.1	13,000	2, 70, 2500	310	
$(Y_{0.3}$-$Lu_{0.7})AlO_3$	7.1	60/0.21/1.3	13,000	2, 70, 3000	310	
Sc_2SiO_5	3.2	16.8/0.0007/10.98	10,600	15	320	124
$NaZrSiO_5$	4.3	30/0.013/3.72	5,600	110, 580	290, 520	124
Lu_3(Al-$Sc)_5O_{12}$	6.7	62.9/0.2/1.41	22,500	610	270	112
$CaMoO_4$: La, Nb		35.2/0.02/1.97	7,500	18,000	530	This book
$CdWO_4$	7.9	64.2/0.262/1.21	19 700	2,000	495	111
$ZnWO_4$	7.87	62.5/0.266/1.19	21,500	22,000	480	121
$CaWO_4$	6.1	63.8/0.221/1.50	6,000	6,00	430	122
$PbWO_4$	8.28	75.6/0.485/0.89	100	6	420	129
$Bi_3Si_4O_{12}$	7.12	74.4/1.15	1,200	100	480	124
$Bi_3Ge_4O_{12}$	7.13	75.2/0.336/1.12	8,200	300	505	111
Activated materials						
LiLuSiO4: Ce	5.61	63.4/0.178/1.68	23,000	41+slow	405	99
$Rb_3Lu(PO_4)_2$:Ce	4.7	49.6/0.077/2.4	30,000	34+slow	420	110
$K_3Lu(PO_4)_2$:Ce	4	51/0.072/3.13	50,000	37+slow	410	110
$Gd_3Sc_2Al_3O_{12}$:Ce	5.56	55.5/0.11/1.93	1,100	108	550	99
$Y_3Al_5O_{12}$:Ce	4.55	32.6/0.017/3.28	11,000	70	550	122

(*continue*)

Table 1.3. Cont.

Scintillator	ρ ($g\,cm^{-3}$)	Z_{eff}/photo absorp. coeff., 511 keV, cm^{-1}/ X_0, cm	Y ph MeV_1	τ_{sc} (ns)	λ_{max} (nm)	Reference
$Y_3Al_5O_{12}$:Pr	4.55	32.6/0.017/3.28	9,250	23.4	310, 380	119
$Lu_3Al_5O_{12}$:Ce	6.7	62.9/0.205/1.41	14,000	100	520	131
Lu_3(Al-Sc)$_3O_{12}$:Pr	6.7		10,000	610	320, 370	112
$YAlO_3$:Ce	5.35	32/0.019/2.2	16,200	30	347	114
$YAlO_3$:Pr	5.35	32//0.019/2.2	7,050	13.3	260, 295	113
($Y_{0.3}$-$Lu_{0.7}$) AlO_3:Ce	7.1	60/0.21/1.3	13,000	18/80/450	375	118
$GdAlO_3$:Ce	7.15	56.2/0.17/1.34	9,000	4/180	335, 358	116, 117
$LuAlO_3$:Ce	8.34	64.9/0.29/1.1	11,400	16/80/520	375	115
Y_2SiO_5:Ce	4.45	35/0.014/3.23	9,200	42	420	126
Y_2SiO_5:Pr	4.45	35/0.014/3.23	4,580	6.5, 33	270, 305	119
$Lu_2Si_2O_7$:Pr	6.23	64.4/0.21/1.39	6,000	15	260, 300	144
Gd_2SiO_5:Ce	6.71	59.4/0.175/1.36	12,500	60, 600	430	107, 120
Lu_2SiO_5:Ce	7.4	66/0.28/1.1	27,000	40	420	126
$Lu_2Si_2O_7$:Ce	6.23	64.4/0.21/1.39	30,000	30	380	132
$La_2Be_2O_5$:Ce		51.5/0.14/1.62	4,300	65	470	124
$LuBO_3$:Ce	7.4	64.5/0.28/1.32	26,000	39	410	110
$Li_6Gd(BO_3)_3$:Ce	3.5	47.9/0.051/4.13	17,000		390	110

Remark. The properties of the scintillating materials listed in the table are at room temperature.

However, its relatively small radiation length X_o ia a major drawback for very large detectors which need to be as compact as possible (see the next chapter). Among the rare-earth ion-doped crystals, CaF_2:Eu and to some extent LuF_3:Ce have a high-light yield, comparable to oxyde crystals. But only LuF_3:Ce has a fast component of the scintillation. Till now, no more effective scintillation cross-luminescent materials have been found among fluorides. A limiting property of fluorides, with the exception of LuF_3 and $BaLu_2F_8$, is their rather low density which restricts their application to low-energy particles and γ-quanta detection.

Chlorides and bromides are characterized by a smaller value of the band-gap E_g and no cross-luminescence at the exception of $CsCaCl_3$ [136]. On the other hand, several high-light yield scintillators have been found in these classes of materials such as $RbGd_2Cl_7$:Ce, $LaCl_3$:Ce, $LuBr_3$:Ce, $RbGd_2Br_7$:Ce [137]. Similar to fluorides, chlorides and bromides have a relatively low density.

Iodides of alkali elements are till now the most frequently used scintillation materials. They are rather light, but are among the brightest known scintillators when doped with Thallium for iodides or in the case of isovalent

substitution of Cs by Na. Their decay time is in the range of hundreds of nanoseconds. Undoped CsI has about the same radiation length as BaF_2 and its scintillation is rather fast. It is therefore a good candidate for high-flux particle physics when a very high density is not mandatory. LiI compound is also a promising scintillation material to detect neutrons.

Sulfides, besides their historical role with ZnS being the first scintillator used for the discovery of α particles, are again at the center of brisk discussions, because of the nice properties of fast and bright red scintillation of Lu_2S_3 doped with Ce^{3+} ions.

Scintillators based on oxide compounds have several advantages. First of all, in an oxygen environment, they are much more stable than halides and particularly fluoride crystals. Thus the majority of oxide single crystals which are potentially applicable as scintillators are rugged, not hygroscopic and chemically inert. Oxygen compounds can have a very high density of 7–10 $\mathrm{g\,cm^{-3}}$ and open new perspectives for detection systems for high-energy γ-quanta.

References

1. Broser VI, Kallmann H (1947) Uber die Anregung von Leuchtstoffen durch schnelle Korpuskularteilchen I. Z Naturforschg 2a:439–440
2. Marshall FH, Coltman JW (1947) The photo-multiplier radiation detector. Phys Rev 72:528
3. Coltman JW, Marshall FH (1947) Some characteristics of the photo-multiplier radiation detector. Phys Rev 72:528
4. Moon RJ (1948) Inorganic crystals for the detection of high energy particles and quanta. Phys Rev 73:1210
5. Kallmann H (1949) Quantitative measurements with scintillation counters. Phys Rev 75:623–626
6. Collins GB, Hoyt RC (1948) Detection of beta-rays by scintillations. Phys Rev 73:1259–1260
7. Bell PR (1948) The use of anthrance as a scintillation counter. Phys Rev 73:1405–1406
8. Kallmann H (1950) Scintillation counting with solutions. Proc Phys Soc (London) Letters to the Editor, pp 621–622
9. Kallmann H, Furst M (1950) Fluorescence of solutions bombarded with high energy radiation (energy transport in liquids). Phys Rev 79:857–870
10. Kallmann H, Furst M (1951) Fluorescence of solutions bombarded with high energy radiation (energy transport in liquids). Part II. Phys Rev 81:853–864
11. Kallmann H, Furst M (1951) High energy induced fluorescence in organic liquid solutions (energy transport in liquids). Part III. Phys Rev 85:816–825
12. Reynolds GT (1950) Noble gas scintillation under electron excitation. Nucleonics 6:488–489
13. Swank RK (1954) Recent advances in theory of scintillation phosphors. Nucleonics 12:14–22
14. Schorr MG, Torney FL (1950) Solid non-crystalline scintillation phosphors. Proc Phys Soc (London) Letters to the Editor, pp 474–475

15. Hofstadter R (1949) The detection of gamma-rays with thallium-activated sodium iodide crystals. Phys Rev 75:796–810
16. Ed A.M. Prokhorov (1998) (In Russian) Physics Encyclopedia Big Russian Encyclopedia, 5:41
17. Fünfer E, Neuert H (1959) Zalhrohre und szcintillationszzäler. Verlag G. Braun, Karlsruhe
18. Cherenkov PA (1934) A visible radiation of pure liquids under γ-radiation. Doclady AN USSR 2:451 (in Russian)
19. Klienknecht K (1987) Detektoren fur Teilchenstrahlung. BG Teubner, Stuttgart
20. Vasiliev A (2000) Relaxation of hot electronic excitations in scintillators:account for scattering, track effects, complicated electronic structure. In: Mikhailin VV (ed) Proc of the Fifth Int Conf on Inorganic Scintillators and Their Applications, SCINT99. Moscow State University, Moscow, pp 43–52
21. Khruchinski A, Korzhik M, Lecoq P (2002) The phenomenon of scintillation in solids. Nucl Instr Meth Phys Res A486:381–384
22. Rodnyi P, Dorenbos P, van Eijk CWE (1995) Energy loss in inorganic scintillators. Phys Stat Sol (b) 187:15–29
23. Lempicki A (1995) The physics of inorganic scintillators. J Appl Spectroscopy 62:209
24. Robbins DJ (1980) On predicting of maximum efficiency of phosphor systems excited by ionizing radiation. J Electrochem Soc 127:2694–2702
25. Van Roosbroeck W (1965) Theory of the yield and Fano factor of electron–hole pairs generated in semiconductors by high-energy particles. Phys Rev A139:1702–1716
26. Lempicki A, Wojtowicz AJ, Berman E (1993) Fundamental limits of scintillator performance. Nucl Instr Meth Phys Res A333:304–1311
27. Rodnyi PA (1997) Physical processes in inorganic scintillators. CRC Press
28. Wojtowicz AJ, Berman E, Lempicki A (1992) Stoichiometric cerium compounds as scintillators, II CeP_5O_{14}. IEEE Trans Nucl Sci NS-39:1542–1548
29. Nikl M (2000) Wide band gap scintillation materials: progress in the technology and material understanding. Phys Stat Sol (a) 178:595–620
30. Becker J, Belski AN, Boutett D et al. (1993) Relaxation of electronic excitations in wide bandgup insulators. In: De Notaristefani F, Lecoq P, Scneegans M (eds) Heavy scintillators for scientific and industrial applications. Frontieres, pp 118–125
31. Vasil'ev AN (1993) Final stages of inelastic electron scattering: influence of scintillation efficiency. In: De Notaristefani F, Lecoq P, Scneegans M (eds) Heavy scintillators for scientific and industrial applications. Frontieres, pp 126–129
32. Ershow N, Zacharov NG, Rodny PA (1982) Spectral-kinetic study of the intrinsic-luminescence characteristics of a fluorite-type crystal. Optica Spectroskopy 53:89–93 (in Russian)
33. Gudovskikh VA, Ershow NN, Krasilnikov SB et al. (1982) Emission of Singlet and Triplet Excitons in Fluorite-Type Crystals under X-ray Excitation. Optics Spectroscopy 53:910–916 (in Russian)
34. Jansons JL, Krumiens V, Rachko ZA et al. (1987) Luminescence due to radiative transitions between valence band and upper core band in ionic crystals (Crosluminescence). Phys Stat Sol (b) 144:835–844

35. Murk V, Namozov B, Yaroshevich N (1995) Complex oxides: electron excitation and their relaxation. Radiat Measure 24:371–374
36. Lushchik A, Murk M, Lushchik Ch et al. (2000) Luminescence of free and self trapped excitons in wide-gap oxides. J Luminescence 87–89:232–234
37. Luschik A, Savkin F, Tokbergenov I (2003) Electron and hole intraband luminescence in complex metal oxides. J Luminescence 102–103:44–47
38. Lecoq P, Dafinei I, Auffray E et al. (1994) Lead tungstate ($PbWO_4$) scintillators for LHC EM-calorimetry. Preprint CERN-PPE/94-225, CMS TN/94-308, December 1994
39. Henderson B, Imbusch GF (1989) Optical spectroscopy of inorganic solids. Clarendon, Oxford
40. Förster TZs (1949) Experimentelle und theoretische untersuchung des zwischenmolekularen ubergangs von elektronenanregungsenergie. Naturforsch 1049 4a:321–332
41. Voronko YuK, Mamedov TG, Osiko VV et al. (1976) Luminescence quenching in garnets doped with trivalent RE JETP 12:478–496 (in Russian)
42. Baryshevsky VG, Drobyshev GYu, Fedorov AA et al. (1992) Rare-earth aluminum perovskite scintillators. In: De Notaristefani F, Lecoq P, Scneegans M (eds) Heavy scintillators for scientific and industrial applications. Frontieres, pp 195–200
43. Dorenbos P, Visser R, van Eijk CWE et al. (1993) Scintillation properties of some Ce^{3+} and Pr^{3+} doped inorganic crystals. In: IEEE NS Symposium, Orlando, USA, 1992 Conference record l:281–285
44. Korzhik M (2000) Scintillators on a base of oxide crystals, inorganic scintillators and their applications In: Mikhailin VV (ed) Proc of the Fifth Int Conf on Inorganic Scintillators and Their Applications, SCINT99. Moscow State University, Moscow, pp 97–105
45. Smirnova SA, Kazakova LI, A Fyodorov AA et al. (1994) Fast and heavy $GdAlO_3$:Ce Scintillators. J Luminescence 60–61:960–962
46. Dijardin C, Pedrini C, Blanc W et al. (1998) Optical and scintillation properties of large LuAlO:Ce^{3+} crystals. J Phys: Condens Matter 10:3061–3073
47. Suzuki H, Tambrello TA, Melcher CL et al. (1992) UV and gamma-ray excited luminescence of Ce doped rear-earth oxyortosilicates. Nucl Instr Meth Phys Res A320:263–272
48. Van Eijk NWE (2001) Inorganic-scintillator development. Nucl Instr Meth Phys Res A460:1–14
49. Bersuker IV, Polinger VZ (1983) Vibronic interaction. Nauka, Moscow (in Russian)
50. Tanabe Y, Sugano SJ (1954) On the absorption spectra of complex ions II. Phys Soc Jap 9:753–766; 9:766–779
51. Vansovski SV (ed) (1969) The theory of crystalline field and optical spectra of impurity ions with notfilled 3d shell. Nauka, Moscow (in Russian)
52. Morrison CA (1980) Host dependence of the rare-earth ion energy separation $4f^N - 4f^{N-1}$ nl. J Chem Phys 72:1001–1002
53. Bettinelli M, Moncorge R (2001) Correlation between the 5d-level position of Ce^{3+} and of the other Ln^{3+} ions in solids. J Luminescence 92:287–289
54. Dorenbos P (2000) The $4f^n \leftrightarrow 4f^{n-1}5d$ transitions of the trivalent lanthanides in halogenises and chalcogenides. J Luminescence 91:91–106
55. Korzhik M, Trower WP (1995) Origin of scintillation in cerium doped oxide crystals. Appl Phys Lett 66:2327–2328

56. Murk V, Kuznetsov A, Namosov B et al. (1994) Relaxation of electronic excitations in YAG and YAP crystals. Nucl Instr Meth Phys Res B91:327–330
57. Bartham RH, Lempicki A (1996) Efficiency of electron–hole pair production in scintillators. J Luminescence 68:225–240
58. Dorenbos P (2001) 5d-level energies of Ce^{3+} and the crystalline environment III. Oxides containing ionic complexes. Phys Rev B 64:125117–1–125117-12
59. Dorenbos P (2002) 5d-level energies of Ce^{3+} and the crystalline environment IV, Aluminates and. simple. Oxides. J Luminescence 99:283–302
60. Balhausen D (1964) Introduction in a ligand fuield theory. Mir, Moscow (in Russian)
61. Krivonosov E, Litvinov LA, Ryzhikov VD (1997) Scintillator based on Al_2O_3. Functional Materials 4:602–604
62. Globus ME, Grinev BV (2000) Inorganic scintillators. New and traditional materials. Akta, Kharkov (in Russian)
63. Goetz G, Pohl UW, Schulz H-J et al. (1994) Spectroscopic detection of the V^+ (d^4) acceptor state im zinc selenide and zinc sulfide. J Luminescence 60–61:16–20
64. McDonagh CJ, Glinn TJ, Imbush GF et al. (1994) Luminescent properties of Cr^{3+} doped $LaSr_2Ga_{11}O_{20}$. J Luminescence 60–61:154–157
65. Baryshevsky VG, Korzhik MV, Kimaev AV (1990) Laser based on a forsterite doped with chromium with tunable wavelenght in niar IR range. J Appl Spectroscopy 53:7–9
66. Bratkar VB, Omanwar SK, Moharil S (2002) Combustion synthesis of the Zn_2SiO_4:Mn Phosphor. Phys Stat Sol (a) 1991:272–276
67. Korzhik MV (1990) Influence of trivalen iron ion on spectroscopic and laser properties YAG:Nd and alumosilicate glasses doped with trivalen rare earth ions. Ph.D. Thesis, Belarussian State University (in Russian)
68. Korzhik MV, Zotov NI, Livshits MG et al. (1988) On the origin of charge transfer transitions $O^{2-} \rightarrow Fe^{3+}$ in doped garnet crystals. J Appl Spectroscopy 48:972–975 (in Russian)
69. Walker G, Kamaluddin B, Glinn TJ et al. (1994) Luminescence of Ni^{2+} centers in forsterite (Mg_2SiO_4). J Luminescence 60–6:123–126
70. Butler KH (1980) Fluorescent lamp phosphors:technology and theory. Pensilvania State University Press, University Park
71. Blasse G, Grabmaier C (1994) Luminescent materials. Springer-Verlag, Berlin
72. Van Den Brand-Folkerts HF (1996) Luminesece of the lead ion in the solids. Thesis, Utrecht
73. Bohm M, Borisevich AE, Drobychev GYu (1997) Influence of Mo impurity on the spectroscopic and scintillation properties of $PbWO_4$ crystals. LAPP Preprint, LAPP-EXP-97 13 December 1997
74. Annenkov A, Bohm M, Borisevich A et al. (2000) Thermally stimulated luminescence properties of lead tungstae crystals, inorganic scintillators and their application In: Mikhailin VV (ed) Proc of the Fifth Int Conf on Inorganic Scintillators and Their Applications, SCINT99. Moscow State University, Moscow, pp 619–626
75. Volodko LV, Komiak AI, Ymreiko DS (1981) Uranium compounds (spectra and strucutre). Belarussian State University, Minsk, pp 1–620
76. Gaviola E, Pringsheim P (1927) Fluorescence of the uranium salts. Z Phys 43:384–386

77. Kirm M, Krupa JS, Makhov VN et al. (2003) 6d5f and 5f^2 configurations of U^{4+} doped into $LiYF_4$ and YF_3 crystals. J Luminescence 104:85–92
78. Shionoya S, Yen WM (1998) Phosphor handbook. Boca Raton, FL, CRS Press, New York
79. Antonini P, Belogubov S, Bressi G et al. (2002) Infrared scintillation of Yb (10%):YAG crystal. Nucl Instr Meth Phys Res A486:799–802
80. Van Pieterson L, Reid MF, Wegh RT et al. (2001) $4f^n \leftrightarrow 4\ f^{n-1}5d$ transitions of the trivalent lanthanides: experiment and theory. J Luminescence 94–95:79–83
81. Loh E (1965) $^1S_0$ level of Pr^{3+} in crystals of fluorides. Phys Rev A 140:1463–1466
82. Caspers HH, Rast HE, Buchanan RA (1965) Energy levels of Pr^{3+} in LaF_3. J Chem Phys 43:2124–2128
83. Eliashevich MA (1953) Rare earth spectra. Nauka, Moscow (in Russian)
84. Dorenbos P (2002) Light output and energy resolution of Ce^{3+} doped scintillators. Nucl Instr Meth Phys Res A486:208–213
85. Autrata R, Schauer P, Kvapil J et al. (1978) A single crystal of YAG—New fast scintillator in SEM. Phys E 11:707–711
86. Presioza (1995) Co YAP:Ce, YAG:Ce scintillators data sheet, Turnov, Czech Republik
87. Tomiki T, Koohatsu T, Shimabukuro H et al. (1992) Ce^{3+} centers in $Y_3Al_5O_{12}$ (YAG) single crystals II. Phys Soc Japan 61:2382–2387
88. Zhang L (1998) Elaboration et propriétés de luminescence et de scintillation de matériaux denses à base de lutécium dopés aux ions cérium et praséodyme. Ph.D. Thesis, l: Universite Claude Bernard-Luon I, France
89. Karanjikar NP, Naik RC (1988) X-ray excited optical luminescence of Ce^{3+} in YPO_4 and location of 5d levels. Solid State Comm 65:1419–1422
90. Ropp RC (1968) Phosphors based on rare earth phosphates. I. Spectral properties of some rare earth phosphates. J Electrochem Soc 115:841–845
91. Williams GM, Edelstein N, Boatner LA et al. (1989) Anomalously small 4f–5d oscillator strengths and 4f–4f electronic Raman scattering cross sections for Ce^{3+} in crystals of $LuPO_4$. Phys Rev B 40:4143–4152
92. Baryshevski VG, Davidchenko AG, Korzhik MV et al. (1990) Fast scitillation crystals for detectors of ionizing radiation. JETP Letters 16:75–78
93. Weber MJ (1973) Optical spectra of Ce^{3+} fluorescence in $YAlO_3$. J Appl Phys 44:3205–3208
94. Lyu LJ, Hamilton DS (1991) Radiative and non-radiative relaxation measurements in Ce^{3+} doped crystals. J Luminescence 48–49:251–254
95. Hoshina T (1980) 5d $\geq$ 4f radiative transition probabilities of Ce^{3+} and Eu^{2+} in crystals. J Phys Soc Jpn 48:1261–1268
96. Aitasalo T, Holsa J, Jungner H et al. (2001) Mechanism of persistent luminescence in Eu^{2+}/RE^{3+} doped alkaline earth aluminates. J Luminescernce 94–95:59–63
97. Belski AN (2000) Localization and interaction of electronic excitations are created by Renthen synchrotron radiation in inorganic scintillators. Ph.D. Thesis, Moscow State University (in Russian)
98. Van Eijk CWE, Andriessen J et al. (1993) Experimental and theoretical studies of cross luminescence In: De Notaristefani F, Lecoq P, Scneegans M (eds) Heavy scintillators for scientific and industrial applications. Frontieres, pp 161–166

99. Van't Spijker JC (1999) Luminescence and scintillation of Ce^{3+} doped inorganic materials for gamma-ray detection. Thesis, Delft University Press
100. Optical crystals Merck Ltd catalog (1992)
101. Scintillation detectors Crismatec Saint Gobain Catalog (1992)
102. Van't Spijker JC, Dorenbos P, van Eijk CWE et al. (1999) Luminescence and scintillation properties of BaY_2F_8:Ce^{3+}, $BaLu_2F_8$ and $BaLu_2F_8$:Ce^{3+}. J Luminescence 85:11–19
103. Moszunski M, Allemand R, Laval M et al. (1983). Recent progress in fast timing with CsF scintillators in application to time—Of-flight positron tomography in medicine. Nucl Instr Meth Phys Res 205:239–249
104. Wojtowich AJ, Balcerzuk M, Berman E et al. (1994) Optical spectroscopy and scintillation mechanisms of $Ce_xLa_{1-x}F_3$. Phys Rev B49:14880–14895
105. Hofstadter R, O'Dell EW, Schmidt CT (1964) CaI_2 and CaI_2 (Eu) scintillation crystals. Rev Sci Instrum 35:246–247
106. Shulgin B, Gorkunova SI, Petrov VL et al. (1996) Some scintillation properties of HgI_2 single crystals. In: Dorenbos P, van Eijk CWE (eds). Inorganic scintillators and their application. Delft University Press, pp 459–461
107. Sakai E (1987) Recent measurements on scintillator–photodetector systems. IEEE Trans Nucl Sci NS-34:418–422
108. Scotanus P, Dorenbos P, Ryzikov VD (1992) Detection of CdS (Te) and ZnS (Tl) scintillation light with silicon photodieds. IEEE Trans Nucl Sci 39:546–550
109. Grabmaier BC, Rossner W, Berthold T (1996) Phosphors in X-ray computed tomography and for the γ-ray Anger camera In: Dorenbos P, van Eijk CWE (eds). Inorganic scintillators and their application. Delft University Press, pp 29–35
110. Van Eijk CWE (1997) New scintillators, new light sensors, new applications. In: Yin Zhiwen, Feng Xiqi, Li Peijun, Xue Zhilin (eds). Proc Int Conf on Inorganic Scintillators and Their Applications, SCINT'97. CAS, Shanghai Branch Press, Shanghai, pp 5–12
111. Holl I, Lorenz E, Mageras G (1988) A measurement of light yield of common inorganic scintillators. IEEE Trans Nucl Sci 35:105–109
112. Dorenbos P, de Haas JTM, van Eijk CWE et al. (1996) Scintillation properties of Pr^{3+} doped $Lu_3Al_{5-x}Sc_xO_{12}$ crystals, inorganic scintillators and their application. In: Dorenbos P, van Eijk CWE (eds). Inorganic scintillators and their application. Delft University Press, pp 365–367
113. Baryshevski VG, Zuevski RF, Korzhik MV et al. (1991) Fast scintillator $YAlO_3$:Pr. JETP Letters 17:82–85 (in Russian)
114. Baryshevsky VG, Korzhik MV, Moroz VI et al. (1991) $YAlO_3$:Ce-fast-acting scintillators for detection of ionizing radiation. Nucl Instr Meth Phys Res B58:291–293
115. Moszunski A, Wolski D, Ludziejewski T et al. (1997) Properties of the new LUAP:Ce scintillator. Nucl Instr Meth Phys Res A385:123–131
116. Dorenbos P, Visser R, van Eijk CWE et al. (1993) Fast scintillating crystals for the detectors of ionizing radiation. IEEE Trans Nucl Sci 40:388–394
117. Dorenbos P, Bougrine E, de Haas JTM et al. (1995) Scintillation properties of $GdAlO_3$:Ce crystals. Radiation Effects Defects Solids 135:321–324
118. Trower WP, Korzhik MV, Fedorov AA et al. (1995) Cerium-doped lutetium-based single crystal scintillators. Inorganic scintillators and their applications.

In: Dorenbos P, van Eijk CWE (eds). Inorganic scintillators and their application. Delft University Press, pp 355–358
119. Dorenbos P, Marsman M, van Eijk CWE et al. (1995) Scintillation properties of Y_2SiO_5:Pr crystals. Radiation Effects Defects Solids 135:325–327
120. Baryshevski VG, Livshits MG, Korzhik MV et al. (1991) Scintillation properties of $Gd_2SiO_5:Ce^{3+}$ crystals. Proseddings AN BSSR 4:114–117 (in Russian)
121. Stavisski YuJa, Shopar AV (1962) Scintillation caunter with crystal CaF_2. IET 5–6:177–178 (in Russian)
122. Derenzo SE, Moses WW (1993) Experimental efforts and results in finding new heavy scintillators. In: De Notaristefani F, Lecoq P, Scneegans M (eds). Heavy scintillators for scientific and industrial applications. Frontieres, pp 125–136
123. Shulgin BV, Kruzalov AV, Ogorodnikov IN (1988) Scintillation properties of BeO single crystals. J Appl Spectroscopy 49:286–291 (in Russian)
124. Shulgin B (1991) Fast inorganic scintillators. In: Proc Int Symp Luminescent detectors and transformers of ionizing radiation (Lumdetr'91). Riga, Latvia A3
125. Ogorodnikov IN, Kruzhalov A, Ivanov VYu (1995) Mechanizms of fast UV scintillations in oxyde crystals with self trapped excitons. In: Dorenbos P, van Eijk CWE (eds). Inorganic scintillators and their application. Delft University Press, pp 216–219
126. Melcher CL, Schweitzer JS, Peterson CA et al. (1995) Crystal growth and scintillation properties of the rare earth oxyorthosilicates. In: Dorenbos P, van Eijk CWE (eds). Inorganic scintillators and their application. Delft University Press, pp 309–316
127. Dorenbos P Private (1995) communication
128. Auffray E (1998) Etudes des mecanismes de scintillation et des modificatios sous irradiation des proprietés du fluorure de cerium en vus de son utilisation en calorimetrie electromagnetique de haute resolution. Thèse de doctorat de l'université Paris VI, specialité:Physique des solides. Paris
129. Annenkov AA, Korzhik M, Lecoq P (2002) Lead tungstate scintillation material. Nucl Instr Meth Phys Res A490:30–50
130. Guillot-Noel O, von Loef ED, Dorenbos P et al. (2000) Luminescence and scintillation properties of Ce^{3+} activited trihalides compounds. In: Mikhailin VV (ed) Proc of the Fifth Int Conf on Inorganic Scintillators and Their Applications, SCINT99. Moscow State University, Moscow, pp 282–287
131. Dorenbos P, Bougrine E (2002) (Private communication) Unpublished data
132. Van Eijk CWE. (1999) Some recent developemts in inorganic–scintillator research. In: Ronda CR, Shea LE, Srivastava AM (eds) Proc Eight Int Symp of Electrochemical Soc. 1999
133. Guillot-Noel O, de Haas JTM, Dorenbos P et al. (1999) Optical and scintillation properties of cerium-doped $LaCl_3$, $LuBr_3$, $LuCl_3$. J Luminescence 85:21–35
134. Van't Spijker JC, Dorenbos P, van Eijk CWE et al. (1999) Optical and scintillation properties pure and of Ce^{3+} doped $CsLiYCl_6$ and $Li_3YCl_6:Ce^{3+}$ crystals. J Luminescence 85:299–305
135. Van't Spijker JC, Dorenbos P, van Eijk CWE et al. (1999) Scintillation and luminescence properties of Ce^{3+} doped K_2LaCl_5. J Luminescence 85:1–10
136. Vasil'chenko VG, Zhmurova ZI, Krivandina EA et al. (2000) New optical multicomponent single-crystal materials based on heavy metal fluorides. IET 43:46–52 (in Russian)

137. Van Spijker JC, Frijns OW, Dorenbos P et al. (1997) $RbGd_2Cl_7:Ce^{3+}$ and $RbGd_2Br_7:Ce^{3+}$ new scintillators with a high light yield. In: Yin Zhiwen, Feng Xiqi, Li Peijun, Xue Zhilin (eds) Proc Int Conf on Inorganic Scintillators and Their Applications, SCINT'97. CAS, Shanghai Branch Press, Shanghai, pp 330–333
138. Shah KS, Glodo J, Klugerman M et al. (2003) LuI_3:Ce—A new scintillator for gamma ray spectroscopy. IEEE Conference Record, N27–7
139. Derenzo SE, Weber MJ, Klintenberg MK (2002) Temperature dependence of the fast, near-band-edge scintillation from CuI, HgI_2, PbI, ZnO:Ga, and CdS:In. Nucl Instr Meth Phys Res A486:214–219
140. Bessiere A, Doenbos P, van Eijk CWE, Kramer KW, Gudel HU, de mello Donega C, Meijrink A (2005) Luminescence and scintillation properties of the small band gup compound $LaI_3:Ce^{3+}$ To be published in Nucl. Instr. Meth. Phys. Res. A (NIMA 26260)
141. Glodo J, Shah KS, Klugerman M, Wong P, Higgins B, Dorenbos P (2005) Scintillation properties of LuI_3:Ce To be published in Nucl. Instr. Meth. Phys. Res. A (NIMA 26316)
142. Moses WW, Derenzo SE, Shichta PJ (1992) Scintillation properties of lead sulfate, IEEE trans. Nucl Sci, 39,5:1190–1194
143. Zadneprovsi BI, Kamenskikh IA, Kolobanov VN, Mikhailin VV, Spinkov IN, Kirm M (2004) Gel growth, luminescence and scintillation of PbSO4 crystals. Inorganic Materials 40,7:735–739
144. Pidol L, Viana B, Kahn-Harari A, Bessiere A, Dorenbos P (in press) Luminescence properties and scintillation mechaisms of Ce^{3+}, Pr^{3+}, and Nd^{3+} doped lutetium pyrosilicate. Nucl Instr Meth Phys Res A (NIMA 26281)
145. Van Loef (2003) Halide scintillators. Thesis, Delft University Press, p 125
146. Dorenbos P, Contribution to the SCINT05 conference on scintillators and their industrial applications, Alushta, Ukraine, Sept. 2005

2 How User's Requirements Influence the Development of a Scintillator

Abstract. In this chapter we discuss practical scintillation parameters which are relevant from a user's point of view for the pragmatic choice of an existing or the development of a new scintillator. They are density, operation speed, light yield, identification of particles, production capability, stability under ionizing radiation, durability of operational parameters. We describe five main domains of applications, each of them with its own list of requirements. Firstly, we consider high-energy physics (HEP) and particle detectors because last two decades have seen a new generation of HEP experiments emerging as a driving force for the development of new scintillators. Further, the spectrometry of low energy γ-quanta and nonlinearity of the scintillator response are described. The different medical imaging modalities and applications of scintillation materials in medical diagnostics are then considered. Finally, areas of scintillator applications in security systems as well as in space research and γ-ray astrophysics are discussed.

For a long time the choice of a scintillator has been limited to only a few which were used in a large range of applications. NaI(Tl) is the best example of a material, which, because of its exceptionally high light yield, has been considered as an acceptable compromise for the majority of applications in spite of its low density. However, through important progress in the understanding of fundamental mechanisms underlying scintillation properties as well as in the production technology, the large amount of materials available now and the possibility to tune some important properties give a larger flexibility and allow tailoring, to some extent, the performance of a scintillator to the specific requirements of different end users. Inorganic scintillation crystals are among the most popular ionizing radiation detectors. We consider here the most important inorganic scintillator parameters, which are relevant from a user's point of view for the choice of an existing or the development of a new scintillator.

1. High density. Scintillation inorganic materials, especially synthetic crystalline compounds, can reach a density $\rho > 8\ \mathrm{g\,cm^{-3}}$ and even more for lead tungstate crystal ($8.28\ \mathrm{g\,cm^{-3}}$ and for lutetium aluminum perovskite ($8.34\ \mathrm{g\,cm^{-3}}$). Moreover, high density reduces the material size of showers for high-energy γ-quanta and electrons as well as the range of Compton scattered photons for lower energy γ-rays. This allows a high segmentation of the detector and leads to a better spatial resolution. Finally high-density

materials have generally heavy ions in the lattice, which significantly increases the photo-fraction ($\sim Z^4$). This point is particularly important for some applications such as positron emission tomography [1]. This is also important to have a high stopping power for the electromagnetic component of the ionizing radiation in order to have a compact detector [2].

2. High operating speed. Crystalline scintillation materials cover a wide spectrum of scintillation decay times from a hundreds of picosecond as, for example BaF_2, up to millisecond or more such as Yb^{3+} and Tb^{3+} doped materials. The fastest ones can be used for high counting rates of γ-quanta and in systems where good time resolution is required. The precision of time measurement with a scintillation detector is proportional to $\sqrt{\tau_{sc}}$. Short scintillation decay time is therefore especially important for the measurement of short time intervals and for the operation in fast coincidence circuits.

The combination of high density and fast response of the scintillation detector gives a unique opportunity to detect rare events in particle physics particularly at high luminosity accelerators.

The very severe requirements imposed by high-energy physics detectors have been since a long time a driving force in the development of new heavy and fast scintillators.

3. Light yield. Inorganic crystalline scintillators can have a very high light yield Y as compared to other scintillation materials. Moreover, the room temperature specific light yield $S_{\tau\tau} = Y/\tau_{sc}$ (number of photons emitted in unit time) of some of them is even greater than the one of liquid xenon. As precision of timing measurements with scintillation detector is proportional to $1/\sqrt{S_\tau}$ and the energy resolution measured in the given time interval is proportional to $\sqrt{Y}$, a high light yield scintillator allows to achieve the best combination of energy and time resolution in a wide γ-quanta energy range. The search for scintillation material with a combination of high stopping power, fast time response, and good photo-absorption peak resolution was strongly motivated by the development of new express methods in well-logging.

4. Particles identification. A good feature of inorganic scintillators is that the scintillation detector response is proportional to the particle energy deposited in the material in a large energy range. However, the slope is different for charged particles, ions, and γ-quanta [3]. Therefore inorganic crystalline scintillators might be applied to identify particles and γ-quanta in fluxes of mixed interaction products.

5. Volume. The worldwide capacity of modern crystalline scintillator growing facilities allows production volume of up to several cubic meters in a relatively short time. It makes possible to build huge detectors and to study rare events resulting from interaction of the accelerated particles or from space origin. In comparison with Cherenkov and liquefied gas detectors, inorganic scintillators have incomparably greater values of specific light yield per unit volume of the material, which makes them rather attractive for space

experiments applications. On the other side, the same property allows, for example, to build very compact detectors for medical devices like intravenous and peroperative probes.

6. Parameters stability under ionizing radiation. Scintillation inorganic crystalline materials have in general a good stability of their parameters even in the presence of intense ionizing radiation environment. This property is crucially important for the measuring systems used in a space, well-logging, and high-energy physics experiments at high-luminosity accelerators. The high stability of the scintillation properties of inorganic materials under ionizing radiation is related to a high level of production technology, which guarantees the production of single crystals with a very low level of uncontrollable structural defects.

7. Durability of operational parameters. Similar to other crystalline materials having a high structural quality, scintillation crystals maintain their physical–chemical parameters for a long time. Although not addressed frequently, this point is of key importance for experiments having a long lifetime. This is caused by a high degree of internal symmetry in the material, which results in their high energetic stability. For this reason, several planned experiments in high-energy physics which have a duration from the design phase up to the data analysis of 10–15 years are using crystalline inorganic scintillators for their electromagnetic calorimeter.

However, it is generally impossible, in practice, to find a scintillator, which combines all these attractive properties. The choice of a material currently existing or to be developed will be therefore tailored to the user's requirements as a function of the priority given between the above-mentioned parameters. A large fraction of the scintillator market is driven by X-rays and γ-rays spectroscopy for a wide range of applications. The authors expect the reader to be introduced to general spectroscopy methods and techniques, which are anyway well described in many books. We consider here five main domains of applications, each of them with its own list of requirements:

- high-energy physics and particle detectors;
- spectrometry of low-energy γ-quanta;
- application in medical imaging;
- safety systems; and
- space application.

High-Energy Physics is a driving force in the development of new scintillation materials, because of the very challenging requirements of modern experiments as well as the large volumes of scintillators needed. As a recent example, the design and construction of new experiments to be installed at the Large Hadron Collider (LHC) at CERN have required a new detector component able to maintain a high stability of optical parameters under long-term exposure to ionizing radiation. In fact, at the beginning of the 1990s, the LHC programme initiated a variety of research and development projects to make

possible the design and construction of detectors with unprecedented performance. The lead tungstate $PbWO_4$ scintillator is the result of one of these successful projects. It is a good example of scintillator material engineering by a multidisciplinary community of material and technology scientists and high-energy physicists. Within 5 years, the crystal production technology has evolved from the production of a few samples to the mass production of more than 1 thousand of crystals with specified parameters per month. Currently, PWO crystal is used to build the Electromagnetic CALorimeter (ECAL) and the Photon Detector of the CMS and ALICE experiments at CERN, respectively. Recently, PWO scintillator has been selected as the basic material to build the ECAL of the proposed BTeV experiment at the Fermi National Accelerator Laboratory. It is also the most attractive candidate to build or upgrade several small setups for the intermediate energy region, where fast response and good energy resolution are required.

2.1 User's Requirements for High Energy Physics

2.1.1 Introduction

The discovery of α particles by Rutherford in 1899 was made possible because of the invention by Crookes a few years before of a device, called spinthariscope which made use of the scintillating properties of Lead Sulfide. Indeed, scintillators were already involved in what can be considered as the first High Energy Physics experiment, and that was the beginning of a long common story.

When Hofstadter [4] introduced in 1948 thallium-doped sodium iodide, NaI(Tl), he probably did not realize that it was going to be the most popular scintillator for the next 35 years. The best example of the high discovery potential of scintillators in High Energy Physics was first given by the NaI(Tl) Crystal Ball experiment at SLAC [5], which allowed to reconstruct the precise spectroscopy of charmonium particles (Fig. 2.1).

But in the last two decades, a new generation of HEP experiments has become a driving force for the development of new scintillators. This has started with bismuth germanate (BGO) for L3 [2] and cesium iodide (CsI either thallium doped or pure) for CleoII [6], Crystal Barrel [7], KTeV [8], Belle [9], and BaBar [10], which were already known but in small sizes and small quantities only. It became even more evident with barium fluoride (BaF_2) for TAPS [11] and GEM [12], cerium fluoride (CeF_3) as a candidate for CMS [13] and L3P [14], and finally lead tungstate ($PbWO_4$) for CMS [13] and Alice [15] at the CERN large hadron collider (LHC), which were essentially developed for HEP experiments. This chapter will describe how the difficult physics constraints and harsh experimental conditions impose very tight specifications to modern detectors. The size of the experiments and the high quantitative demand allowed organizing the R&D effort on a large scale. This has been

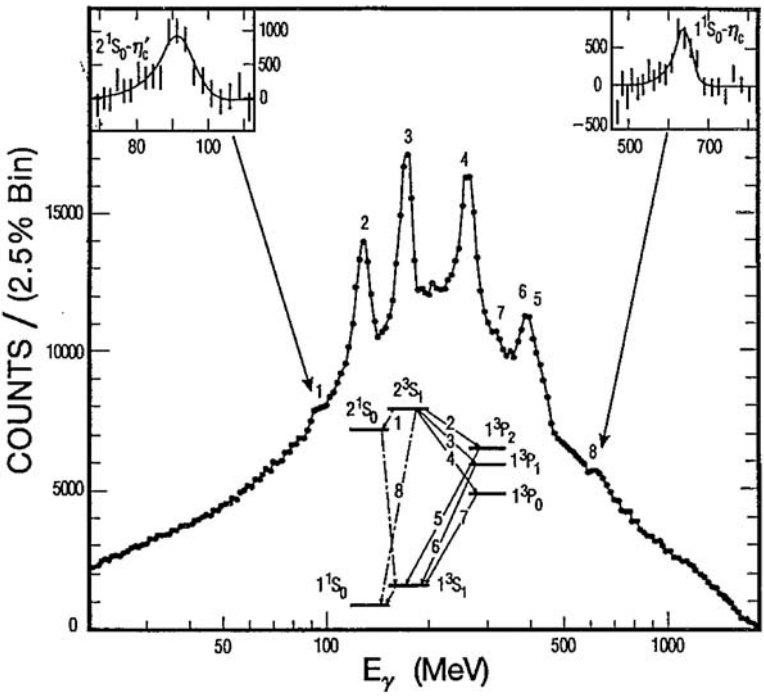

Fig. 2.1. Charmonium Spectroscopy with the Crystal Ball at SLAC [5]

particularly illustrated by the work of the Crystal Clear Collaboration [16], which was able to create a multidisciplinary effort to make the best use of cross-fertilization between different fields of expertise and industry to develop suitable scintillators at an industrial scale.

A better understanding of some basic mechanisms of energy relaxation, scintillation process, radiation damage is progressively being built through this common effort. The immediate consequence is to allow a much faster and much more efficient development of scintillators for other detectors in High Energy Physics, but also for other applications and particularly for industrial and medical imaging devices.

2.1.2 Physics Requirements for High Energy Physics Experiments

One of the main motivations for the construction of the CERN new proton–proton collider LHC is the study of the symmetry breaking mechanism, which is supposed to be responsible for the generation of the masses of the particles in the electroweak theory. One or several scalar bosons (the Higgs bosons) are involved in this mechanism and can be detected through their leptonic and $\gamma\gamma$-decay modes. The main argument, generally used to stress the high level of performance required for the detectors, is the detection of 2γ resulting

from the decay of the Standard Model Higgs boson, for which the measured width is completely dominated by the instrumental resolution below Higgs masses of $\approx$200 GeV c^{-2}. As this signal is associated with a very high background, generated by a combination of π° also decaying in 2γ, and the direct production of photons via the quark–quark, gluon–gluon, and higher order diagrams, the signal-to-noise ratio is dominated by the photon detector energy resolution.

Usually electron and photon energies are measured in detectors called calorimeters, where they are stopped, producing a shower of secondary particles. In sampling calorimeters, the photon energy is converted into high-density absorber plates, and a small fraction of the energy is measured in a sensitive medium interleaved with the absorption medium. In a homogeneous detector, on the other hand, the electron or photon showers are fully contained in the sensitive medium. The energy is then revealed by scintillation or Cherenkov light, both collected in highly transparent media or by ionization in conductive liquids, where charges are collected.

The mass resolution of a particle, which is detected through the two-photon decay channel, depends on the energy resolution and angular divergence θ [radian] of two quanta with energies $E_{\gamma 1}, E_{\gamma 2}$ [GeV] as

$$\frac{\delta_M}{M} = \frac{1}{2}\left[\frac{\delta_{E_{\gamma_1}}}{E_{\gamma_1}} \oplus \frac{\delta_{E_{\gamma_2}}}{E_{\gamma_2}} \oplus \frac{\delta\theta}{\tan(\theta/2)}\right] \tag{2.1}$$

Homogeneous detectors are well known to give an excellent energy resolution, which is usually parameterized in the following way:

$$\delta E\gamma/E\gamma = a/\sqrt{E} \oplus b \oplus c/E \tag{2.2}$$

where a is the statistical term (sampling or fluctuations of all sorts), b is the constant term, and c is the energy noise equivalent term.

High-precision calorimetry at the future proton–proton machines requires an energy resolution of the order of 0.5% for 100 GeV photons.

A homogeneous calorimeter is not limited by sampling fluctuations and an energy-dependent term of the resolution a as small as 2% has been currently achieved on several large size calorimeters. It is much more difficult to achieve a constant term b of $\approx$ 0.5%. On large systems such as the L3 BGO calorimeter at CERN, one recognizes usually three contributions to the constant term:

$$b^2 = b_L^2 \oplus b_F^2 \oplus b_C^2$$

The $b_L$term represents the fluctuations due to the energy leakage. The front leakage due to backscattered particles has a negligible contribution above a few GeV. Having sufficient material for full longitudinal energy containment can easily control the rear leakage. For the photon energies up to 100 GeV, at least 25 radiation lengths are necessary to maintain the leakage term within reasonable limits (one radiation length is the mean distance over which a

high-energy electron loses all but $1/e$ of its energy). The side leakage is more difficult to control. It is determined by the number of cells one has to sum up to reconstruct the energy with sufficient precision. On the other hand, this number is limited by the electronic noise and chiefly by the multiple event pileup at LHC if the shower spreads too much laterally. Low-noise electronics and high-density material will, of course, limit this contribution. A particular attention must be paid to all gaps, walls, and dead material in front, which may have an important contribution to the leakage term. All leakage contributions can be well reproduced by Monte-Carlo and a b_L term of $\approx$0.3% can be achieved with a crystal calorimeter.

The b_F term is associated to nonuniformity. They can result from non-homogenous active material, such as variation of doping concentration in nonintrinsic scintillators. Temperature gradient can be the dominant factor of nonuniformity when there is a strong dependence of the light yield with the temperature (lead tungstate, for instance, has a large temperature coefficient of $-1.9\%/^{\circ}\mathrm{C}$). Crystals such as cerium fluoride (CeF_3), with a temperature coefficient as small as $0.1\%/^{\circ}\mathrm{C}$ near room temperature, will be insensitive to this effect. Other sources of nonuniformity are associated to the light collection. Pointing geometry implies cells of pyramidal shape. The light-focusing effect in these cells, particularly if the refraction index of the medium is high, induces a strong nonuniformity; CeF_3, with an index of 1.6, is here again much better than BGO ($n = 2.15$) or PWO ($n = 2.3$). Finally, much attention should be paid to avoid large absorption of the light in the medium. This is perhaps the most important problem for crystals with an emission spectrum in the UV like BaF_2 and other cross-luminescent crystals, as well as for low-density materials because of the long path length of the photons to reach the photo-detector. For dense crystals with an emission spectrum in the visible, a b_{F} term as small as 0.25% can be obtained.

The last contribution b_{C} corresponds to the intercalibration errors. Frequent calibrations with an efficient monitoring system are necessary to maintain this contribution below 0.3%. The L3 BGO has proven that a well-designed fiber-monitoring system can maintain the intercalibration within 0.3% for long periods of time and more than 10,000 crystals. The high luminosity pp machines will also provide excellent means for a continuous calibration of the detector. At LHC, a rate of 10 Hz is expected for electron pairs from Z° decays in the central region, which should allow a weekly calibration with about 100 electrons per channel. If there is a good inner tracker, individual e^+ or e^- can be used (E/p matching) at a rate, which could be as high as 100 per channel and per day. Finally, one should be able to take advantage of the copious number of minimum ionizing particles for an almost continuous intercalibration control of all the channels. The CMS PWO calorimeter is aiming at a precision of 0.2% for the determination of intercalibration constants.

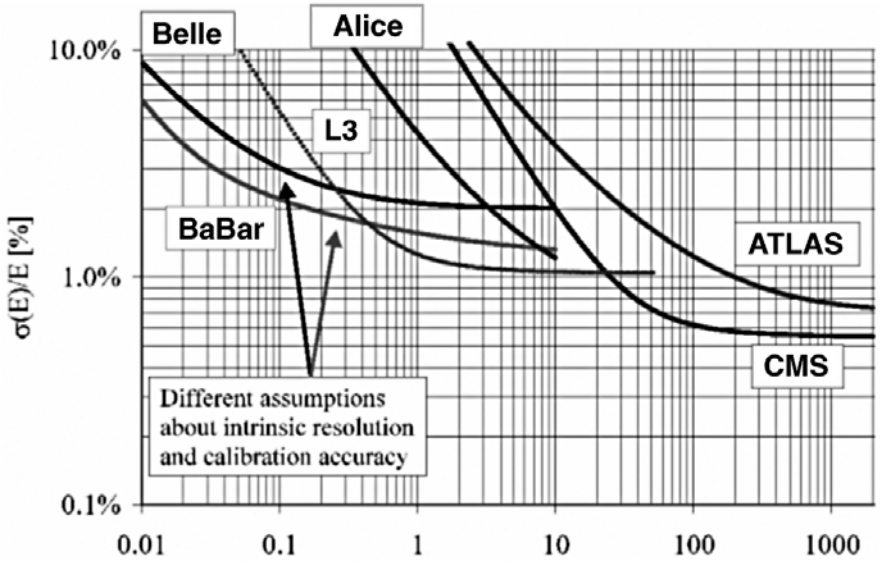

Fig. 2.2. Energy resolution of several HEP calorimeters (Courtesy of P. Denes, LBL)

Taking all these contributions together, it seems that a constant term $b = 0.5\%$, although difficult, is not out of reach for a well-designed homogeneous calorimeter. Figure 2.2 shows the energy resolution in the required energy range for several already-existing or proposed detectors.

2.1.3 Scintillator Requirements for High-Energy Physics Experiments

The criteria for the choice of the scintillator are based on the density, the scintillation properties, and the radiation hardness. The cost is also an important issue taking into consideration the very large volumes of several cubic meters considered for such detectors.

2.1.3.1 Density

The compactness of the calorimeter is essential to reduce the detector volume and cost. This is achieved by using high stopping power materials resulting in a small radiation length X_0. A high-density material ($\rho > 5\,\mathrm{g\,cm^{-3}}$) is therefore needed, but not necessarily with very high Z components as it is often quoted. The density should be preferably based on a high compactness of the crystal lattice (a large number of atoms per unit volume), keeping the atomic number of the components not too large to reduce the lateral shower size (Moliere radius: $R_\mathrm{M} \approx X_0\ (Z + 1.2)/37.74$). A small Moliere radius will

limit the contamination of the energy measurement by other particles from the same or other events (pileup) and help for the position reconstruction as well as for the π^0 rejection, which will be the dominant background at LHC. Finally, a compact material will reduce the lateral spread of the shower in a high-magnetic field.

2.1.3.2 Scintillation Properties

The pileup will impose severe constraints to the readout, particularly at LHC. It is, therefore, essential to collect as much signal as possible within one bunch crossing (25 ns), to keep a good signal-to-noise ratio in the electronics chain, and to reduce the fluctuations due to the timing jitter. Decay times of the order of the bunch crossing time or even less are necessary. Only optically allowed (interconfiguration) transitions (such as the transition $5d \rightarrow 4f$ for Ce^{3+}), cross-luminescence, which is intrinsically fast and temperature independent, and strongly quenched intrinsic luminescence can give rise to fast scintillations.

As the electromagnetic calorimeter is usually installed in a magnetic field, read out by photodiodes or avalanche photodiodes is desired. These photodetectors have a gain which is either 1 for PIN diodes or of a few hundreds in the case of avalanche photodiodes, which is significantly lower than photomultipliers. This implies a sufficient light yield (a few 100 $pe^- MeV^{-1}$ of deposited energy), and an emission wavelength above 250 to 300 nm, where the quantum efficiency of the photodiodes becomes high. A light emission in the visible spectrum will also ease the problems of light collection in long crystals.

The energy resolution of the calorimeter will strongly depend on all possible sources of nonuniformity. The light collection in a pointing geometry will introduce nonuniformity due to the focusing effect, which depends on the refractive index of the crystal. Fluoride crystals and glasses, with refractive index around 1.5, will limit this effect to a much smaller value (and therefore make it much easier to correct) than for the BGO (index 2.15) or PWO (index 2.3). The material can be intrinsically luminescent if it holds luminescent ions, or doped with a scintillating impurity. Intrinsic scintillators are generally preferred, as it is easier to control the light yield uniformity in long crystals. On the other hand, a controlled distribution of the doping could help correcting for the nonuniformity caused by the light collection in a pointing geometry. In addition, the scintillation yield should be as independent as possible from the temperature. Large temperature coefficients increase the complexity of the detector and of the software corrections, and temperature gradients between the front and back face of the crystals introduce nonuniformity affecting the constant term of the resolution.

2.1.3.3 Radiation Hardness

It is now well established that the most significant damage in the majority of inorganic scintillators results from the formation of color centers in the bulk of the material, which absorb part of the scintillation light on its path to the photo-detector [17]. More details are given in Chap. 5. A short radiation length will, therefore, reduce the total attenuation for a given damage. In addition, as most of the color centers absorb mostly in the UV (more precisely they involve traps which are in the vicinity of the fundamental absorption edge), large bandgap crystals emitting light in the visible are likely to be less severely damaged. Some surface effect may also occur but it is generally very small and saturates quickly with the dose.

The formation of color centers results from the trapping of electric charges by crystal structural defects or impurities and is therefore directly correlated with the quality of the raw material. A large effort should be made to purify the raw materials to the best quality. However, in some cases, a specific doping of the crystal has proved to be an efficient and economical way of significantly increasing the radiation hardness [18].

2.1.4 Cost Considerations

The factors building up the price of crystals must be identified and carefully analyzed. In some cases, the raw material of the desired purity can represent a substantial fraction of the cost. For this reason, crystals based on the rare lutetium have been discarded up to now for applications were tons of crystals are needed, although some of them are very fast cross-luminescent materials ($BaLu_2F_8$) or very efficient scintillators (LSO:Ce). Cerium is much more favorable, as it is the most common of the rare-earth components. The purification of cerium against the other rare-earth components may be difficult and expensive, but our first studies show that this is not a critical parameter. The growing technique and the crucible material are dominant parameters and crystals, which can be grown, for instance, by using the relatively cheap Bridgeman method in graphite crucibles, have obvious advantages. The cost of the energy plays also an important role, as a combination of the melting temperature and the pulling rate. From this point of view, the high melting point of GSO (>1900°C) and the high cleavage susceptibility of this matrix implying a low pulling rate (1 to 2 mm h^{-1}) may put some limits to the minimum obtainable price for such a crystal. On the other hand, the low melting point of PbF_2 (822°C) and $PbWO_4$ (1123°C) and the abundance of the raw material make them potentially low-cost materials. A high crystal density, directly limiting the total volume for a calorimeter, but also the crystal dimensions and consequently the furnace and crucible sizes will be a major parameter of the total cost for a crystal-based detector. Finally, the very good mechanical properties of $PbWO_4$ for instance, allow a high

Table 2.1. Scintillators used in HEP calorimeters (Courtesy of P. Denes)

	NaI(Tl)	BaF_2	CsI(Tl)	CeF_3	BGO $Bi_4Ge_3O_{12}$	PWO $PbWO_4$
Xo [cm]	2.59	2.03	1.86	1.66	1.12	0.92
ρ [g/cm^3]	3.67	4.89	4.53	6.16	7.13	8.2
τ [ns]	230	0.6 620	1050	30	340	15
λ [nm]	415	230 310	550	310 340	480	420
n@λ_{max}	1.85	1.56	1.80	1.68	2.15	2.3
LY [%NaI]	100	5 16	85	5	10	0.5

production yield of the mechanical processing, which will also reduce the final cost.

2.1.5 Crystal Calorimeters in the World

The continuous increase of the energy obtained in particle accelerators puts more and more emphasis on calorimetry as a tool to analyze the products of the collisions. As at the same time the proportion of interesting events is becoming smaller and smaller, the demand for high precision homogeneous calorimeters is continuously increasing. This is why, the last 20 years have seen a dramatic boost in the development of scintillators and associated readout techniques, directly related to a dozen of projects of impressive dimensions. The properties of the crystals used in these calorimeters are listed in Table 2.1, where some qualitative figures of merit are also indicated.

2.2 Spectrometry of Low-Energy γ-Quanta

2.2.1 Nonlinearity of Scintillator Response

The majority of scintillation materials combining at least two from a list of properties which make an "ideal scintillator," including high light yield, high density, fast response, and low price, can be used to detect low-energy ionizing radiation. This wide branch of detector applications includes devices

for research and medical diagnostics, geological and geophysical investigation, ecological monitoring, as well as devices of monitoring for technological processes and safety monitoring.

The linearity of the scintillation detector response with energy and a high resolution are crucial features for precision spectrometry. The proportionality between scintillator light yield and energy of ionizing radiation is based on the fundamental principle of electronic excitation multiplication in the scintillation crystal [19]. The first studies of scintillator properties [20, 21] have shown that their response is dependent on the type of ionizing radiation. Only for electrons they have shown a good linearity with energy up to 10 MeV. The linearity of the response of different scintillators to γ-quanta and electrons has been confirmed in many measurements performed in the region up to 100 GeV [3]. However, more detailed studies have shown a variation of the proportionality between light yield and energy for soft γ-quanta in the energy range below 1 MeV and especially near the K, L edges absorption of the heavy ions of the scintillator host matrix [22, 23].

The classical approximation of scintillator efficiency given in Chap. 2 does not imply an evident dependence of the scintillation yield on the absorbed electron or photon energy. However, this phenomenon is well known since the discovery of scintillation materials. The most commonly used scintillator NaI(Tl) was described in 1948 [4], 1 year later [24] it was observed that the light output of this material is not proportional to the energy released in the crystal for photon energies less than 1 MeV. This phenomenon is still under extensive investigation in many scintillators [22, 24–31].

The dependence of the scintillation efficiency on the electron energy is measured using the Compton coincidence technique [29] (the scintillator is excited by a monochromatic γ-source). A detailed description of the electron energy resolution measurement using the Compton coincidence technique is given in reference [30].

This nonlinearity has been observed in many halide and oxide scintillators [28]. Typical figure of signal response as a function of electron energy is shown in Fig. 2.3. The trends in alkali halides and oxides are opposite. In spite of the obvious influence of different matrix host elements on the low-energy response of both classes of scintillators, the opposite trends are still not clarified yet.

It was found that the nonlinearity curve is practically the same in similar compounds: silicates—YSO:Ce and LSO:Ce; garnets—YAG:Ce and LuAG:Ce [31]. Authors of reference [29] showed that for CsI(Tl) and CsI(Na) crystals the results are the same. On the other hand, the energy dependence of the response curve does not depend on the activator if its concentration is relatively small. It is obvious from these results that the crystal structure is the most important factor determining the response nonlinearity.

The nonlinearity of the light yield with the energy of the detected γ-quanta or electrons has a strong impact on the energy resolution. This

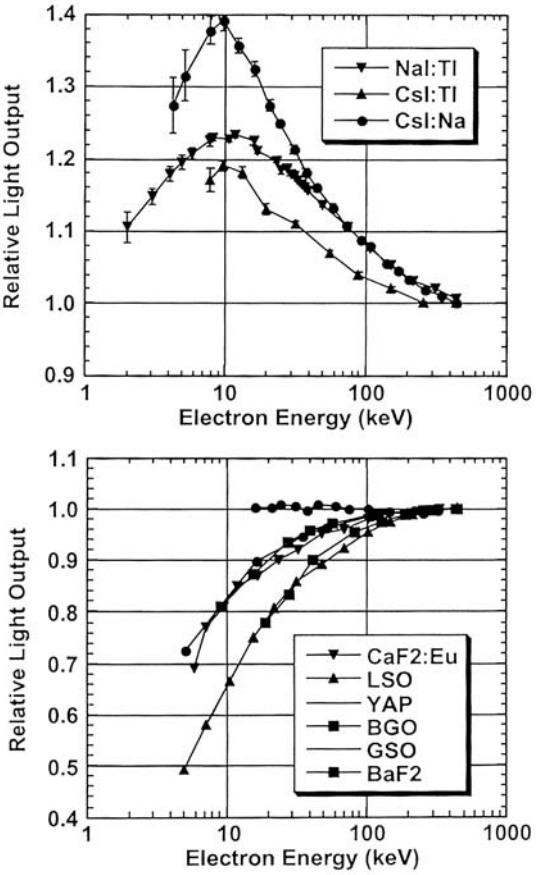

Fig. 2.3. Electron energy response (relative light output normalized to the value at 662 keV as a function of electron energy) for various scintillators [28]

intrinsic light yield nonproportionality (sometimes referred to as nonlinearity) is particularly effective at low energies. The best energy resolution in a scintillator can be achieved only when there is a combination of high absolute light yield, good matching of the scintillator emission spectrum with the photo-receiver sensitivity, and good proportionality to the energy of γ-quanta or electrons deposited in a crystal. The nonproportionality manifests itself as discontinuities of the light yield around the K- or L-edge of heavy atoms in most inorganic scintillators [30].

It is presently impossible to predict the response linearity of a given material, although it is certainly related to some nonradiative relaxation or quenching effects in the case of high ionization density. So far only $YAlO_3$: Ce(YAP), and to some extent ZnSe:Te [32], have a good energy resolution down to a few KeV.

There have been several studies to simulate the electron energy distribution produced in a scintillator by the interactions from incident photons. On the basis of Monte Carlo simulation results, electron energies were determined by considering Compton scattering, photoelectric absorption, and pair production interactions separately [29]. These simulations have shown good agreement with experiment at least for several materials such as NaI(Tl), CaF_2(Eu), and LSO. The comparison of these simulations with experimental data for electrons and photons interacting with LSO:Ce is shown in Fig. 2.4. The good match of the simulation and experimental data allows considering optimistically the theoretical prediction of nonproportionality in new materials.

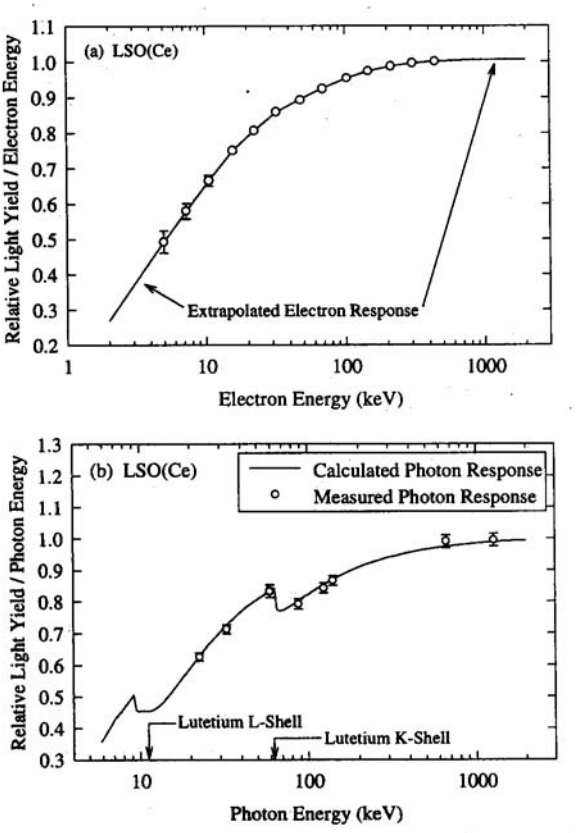

Fig. 2.4. (**a**) LSO:Ce electron response with low- and high-energy extrapolations. (**b**) Calculated photon response along with measured data for same crystal that was used to measure electron response in [30]

This effect has no practical implication for high-energy physics detectors but it is, on the other hand, of prime importance for high precision spectrometry in the medium energy range. The LSO:Ce crystal, which is a very successful material for medical imaging applications, has its advantage of a high light yield severely balanced by a poor linearity for energies below 1 MeV.

2.2.2 Spectrometric Properties of YAP:Ce Crystals

The YAP:Ce crystal is exceptionally linear in the low-energy range. This scintillation material has been discovered in the 1970s, however, large scale applications started a few years later with the development of the production technology of crystals with high light yield [33–42]. The comparison of scintillation and some physicochemical performances of $YAlO_3$:Ce and NaI(Tl) is shown in Table 2.2. The dependence of the linear attenuation factor L with energy and amplitude spectra of some soft γ-quanta is shown in Figs. 2.5 and 2.6. The unique detecting properties of YAP:Ce scintillator makes possible its wide use in Mössbauer spectroscopy which is one of the most powerful structural–analytical research techniques of condensed matter.

Table 2.2. The basic performances of crystal YAP:Ce in comparison with NaI(Tl)

Material	ρ(g cm^{-3})	$Z_{\text{eff.}}$	Y (%)	Refraction Index (n)	λ_{em} (nm)	τ_{sc} (ns)	Y temp. coeff at (% per °C)	Hardness (Moos)
NaI(Tl)	3.67	50	100	1.85	410	230	0.2–0.95	2
$YAlO_3$:Ce	5.55	36	40	1.94	347	28 ± 2	0.39	8.5

The efficiency of the transmittance Mössbauer spectroscopy is proportional to the count rate of the detector [43]. The fast scintillation time of YAP:Ce gives therefore a significant advantage on NaI(Tl) or even on cooled semi–conductors in spite of a worse energy resolution. YAP:Ce-based detector crystal of 0.35-mm thickness has allowed to increase by one order of magnitude the efficiency of measurements with a ^{57}Co (Rh) source of 2 GBq activity.

A distinctive feature of $YAlO_3$:Ce scintillator is the weak dependence of the light yield with temperature (Fig. 2.6). It makes possible its use in extreme temperature conditions, for example, in systems of continuous check of steel band, well-logging, space, etc.

Besides spectrometry in the 1–100 keV range, YAP:Ce crystals have very good energy resolution near half of a MeV. An energy resolution of 4.38% FWHM has been measured at 661.6 keV (^{137}Cs), [44], better than the 6.6–6.8% energy resolution gained with reference scintillation NaI(Tl) crystal.

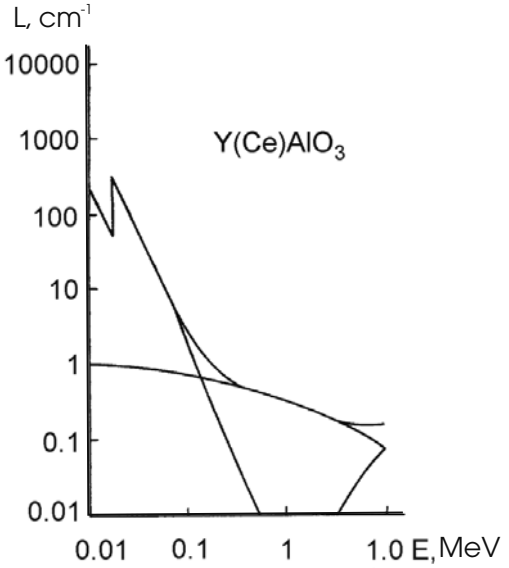

Fig. 2.5. Dependence of the linear attenuation factor L on energy of γ-quanta in $YAlO_3$:Ce single crystal

This apparent paradox for a crystal having a light yield of only 40% of NaI(Tl) is a direct consequence of a much better low-energy linearity of YAP:Ce than NaI(Tl). A similar situation is illustrated by the LuAP:Ce crystal, which has at least the same energy resolution as LSO:Ce in spite of a light yield a factor 2 to 3 smaller.

Another important application of $YAlO_3$:Ce crystals is the detection of α-particles. The mean free path of α-particles in YAP is 8–28 μm in the energy range 4–8 MeV. The light yield ratio γ/α is 3.8. The minimization of the γ-quanta contribution to the noise is achieved by the use of thin crystals. YAP:Ce crystals with a thickness of less than 100 μm are easily produced now. Figure 2.6 shows the ^{226}Ra source amplitude spectrum measured with a $\emptyset$ 25 × 0.1 mm YAP:Ce crystal collimated by a 1.5-mm diameter hole in a 2-mm thick aluminum foil. This is a good setup for low background spectrometry of α-particle emitting isotopes.

The spectrometric performance of other scintillators is also widely described in the literature [45]. Alcali halide scintillators are still the most used for routine measurements in the range up to 10 MeV, mostly because of their well-developed production technology and low cost. However, this situation is changed in favor of oxide materials when the combination, of at least a high light yield, fast response and high stopping power is required. We can easily predict that scintillators based on complex structure oxides will dominate in the next 5–10 years.

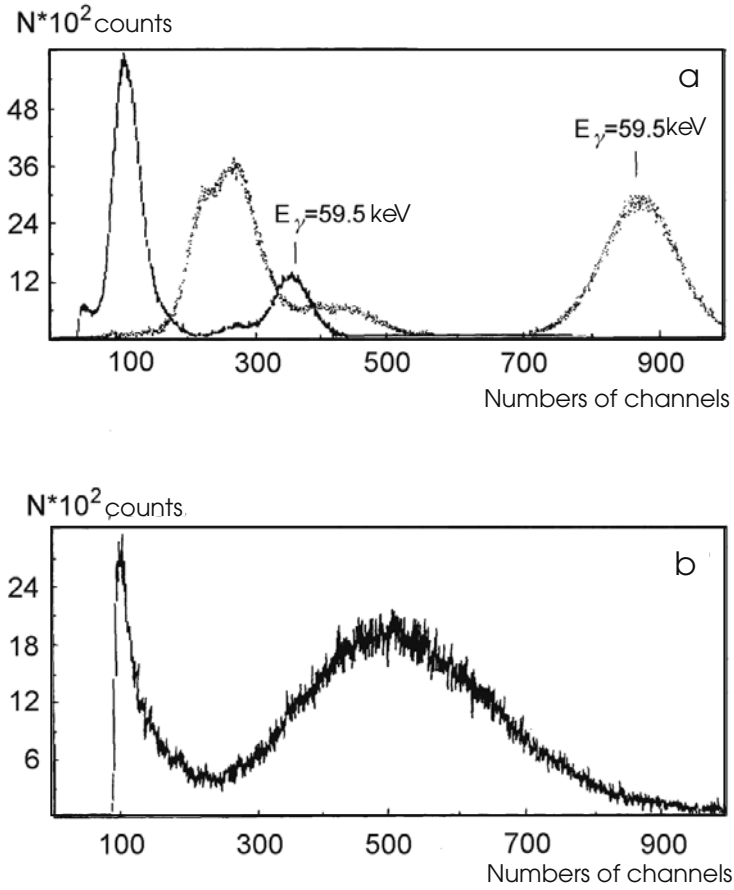

Fig. 2.6. ^{241}Am isotope amplitude spectrum (**a**), NaI(Tl) Ø 25 × 1 mm (dots); $YAlO_3$:Ce Ø 25 × 0.35 mm (continuous line), (**b**) an spectrum of ^{55}Fe measured with the same YAP:Ce, $T = 300\,\mathrm{K}$

2.3 User's Requirements for Medical Imaging

2.3.1 Introduction and Historical Background

At the same time Rutherford was studying α particles on a zinc sulfide scintillating screen, and Wilhelm C. Roentgen, also using a similar device, was able to record the first X-ray picture of his wife's hand. That was probably the first example of technology transfer between particle physics and medical imaging, and the beginning of a long common history.

The interest for thallium-doped sodium iodide, NaI(Tl), introduced in 1948 by Hofstadter [4] was suddenly boosted by the invention in 1958 of the Anger camera concept [46], where a large NaI(Tl) slab is read out by several

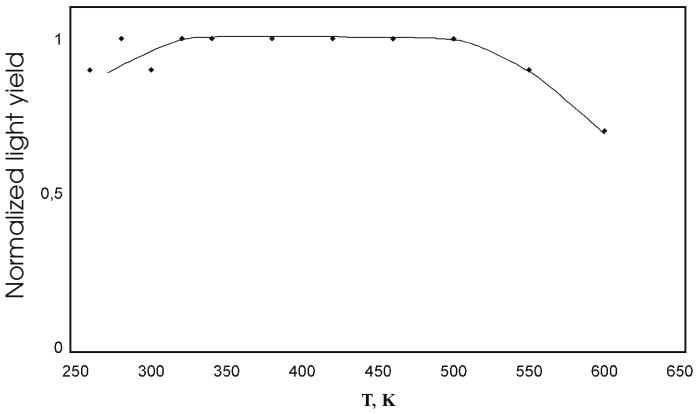

Fig. 2.7. YAlO3:Ce scintillator light yield dependence versus temperature

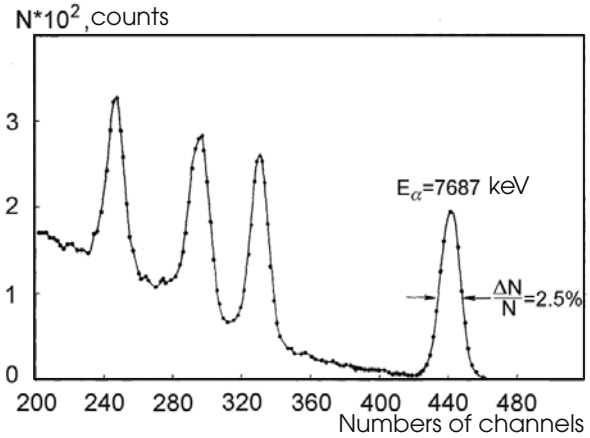

Fig. 2.8. Energy distribution of α-particles emitted by ^{226}Ra source

photomultipliers (PMT), allowing a relatively precise determination of the γ conversion point. This invention offered unprecedented perspectives in the field of nuclear medicine imaging and noninvasive clinical investigations. Several imaging devices have been built with a large number of NaI(Tl) crystals arranged on a sphere (hair drier) or on a circle (hair shrinker) around the head of a patient. But in spite of its very high light output, sodium iodide suffers from a relatively low density (3.67 $\mathrm{g\,cm^{-3}}$), which limits the spatial resolution and the image quality.

This is why, the discovery of attractive scintillation properties in Bismuth Germanate (BGO) by Weber & Monchamp in 1973 was immediately recognized for its potential for γ cameras, because of its very high density

($7.12\ \mathrm{g\,cm^{-3}}$). But systematic use of BGO in medical imaging could be made possible only through the large effort of the L3 collaboration at the CERN LEP collider, to develop with several companies low-cost mass production technology for BGO, in particular with the help of the Shanghai Institute of Ceramics in China. Today BGO still represents a very large fraction of the γ-ray medical imaging market.

The need for high-density but much faster scintillators for the new generation of hadron colliders triggered a large R&D effort worldwide in which the Crystal Clear collaboration at CERN [16] has played a major role since 1989. New crystals have been developed, like lead tungstate (PWO), which will be the basic element of the largest crystal calorimeter ever, built for the CMS experiment at LHC, with nearly 100 tons of crystals. Moreover, systematic study of the physics underlying the fundamental scintillation mechanisms has led to a much better prediction capability in the search for new scintillating materials. New ultra dense, very fast, and efficient scintillators are being studied and are now in the phase of the mass production technology development. Several of them have a high potential for medical imaging devices.

2.3.2 The Different Medical Imaging Modalities

The field of medical imaging is in rapid evolution and is based on five different modalities: X-rays radiology, emission tomography, ultrasonic tomography, magnetic resonance imaging (MRI), and electrophysiology with electro- and magnetoencephalography (EEG and MEG). More recently, direct optical techniques such as bioluminescence and infrared transmission are also emerging as powerful imaging tools for non-too deep organs. Only X-rays radiology and emission tomography are using scintillators and are described here in more details. Total volume of scintillators for medical application exceed few hundred tons [47].

2.3.2.1 X-Rays Radiology

This is the most popular technique, which comprises X-ray radiography, computed tomography (CT), and tomo-densitometry (DXA). The general trend is to progressively replace the film by digital devices, as already used for CT. Besides direct conversion detectors such as amorphous Silicon or CdZnTe, scintillation materials are widely developed for this application. For small scintillation screen thickness (0.1 to 0.2 mm), which is well adapted to the lowest x-ray energies (for instance, about 20 keV for x-ray mammography), ceramics are well adapted. On the other hand, for dental x-ray diagnostics (about 60 keV) and full-body x-ray computed tomography (about 150 keV) the required stopping power would need much thicker screens. This would induce too much light yield loss when classical ceramics screens are used. A large R&D effort is under way by several companies to replace them by

detector arrays made of CsI(Tl) needles or small crystals (for example, calcium tungstate CaWO or YAP) directly coupled to photodiode arrays or segmented photomultipliers.

2.3.2.2 Scintillators for CT Applications

Single Crystalline Materials

One of the most widespread scintillator applications in medical diagnostics is CT imaging (X-ray computed tomography). The principle of CT is based on the detection of X-ray attenuation profiles from different irradiation directions. This technique allows a three-dimensional (3D) reconstruction of attenuation density within the human body. These density profiles can then be viewed from different directions and analyzed in a succession of slices allowing a full 3D reconstruction of the anatomical image.

The X-ray detector is typically built up by using a scintillation material coupled to a photosensitive array of Si-diodes. There are several specific sensor properties requirements (such as high X-ray absorption, spectral correspondence of scintillator emission and photo-receiver efficiency, hard radiation stability, and low afterglow level [48]) that define the limits for the search of new CT scintillation materials [48, 49].

Among them, the material stability under X-radiation, light output temperature stability, and a minimum level of afterglow are certainly the most critical in comparison with any other applications [48, 50]. Modern X-ray CT system is producing about 1,000 projections (subject slices) per second. This imposes severe constrains on both the decay time and afterglow. Afterglow is known to produce ghost images through a "memory effect" which deteriorates the quality of the images. The main parameters of scintillators used for CT systems are listed in Table 2.3.

Historically, the first material for this application was CsI(Tl) with a high light output green emission matching well the maximum sensitivity of Si photodiodes. However, the scanning speed increase resulted in high, rigid demand to suppress the afterglow, and even the best CsI(Tl) samples could not satisfy the requirements for the new scanner generation. The mechanism of afterglow will be described in detail in Chap. 5. This is why, CsI(Tl) has been progressively replaced by $CdWO_4$ (CWO), which is now the basic component of all modern CT devices.

For CWO detectors the conversion factor is about 0.01 electrons/eV [50]. A high detector conversion factor and good crystal uniformity are mandatory for a high-contrast resolution over a wide range of X-ray attenuation. But the main motivation to use a new material was the possibility to reduce the afterglow at a level of 0.005% in 3 m after the irradiation. So far, this result remains unsurpassed.

Another important parameter for such applications is the light yield stability under temperature changes or irradiation.

Table 2.3. Scintillators characteristics for CT [51–53]

	CsI–Tl	BGO	CWO	$(Y,Gd)_2O_3$: Eu	Gd_2O_2S:Pr, Ce,F
Type	Single crystal	Single crystal	Single crystal	Ceramic	Ceramic
Density (g/cm^{-3})	4.52	7.13	7.99	5.9	7.34
Thickness to absorb 99%	6.1(2.2)	2.8(1.2)	2.6(1.1)	5.8(2.2)	2.9(1.1)
Emission band	550	480	495(580),	610	520
Light output(%)	85	9	38	34	51
Conversion factor,	45	450	100	—	—
Decay time (μs)	1	0.3	2, 15	1000	~ 2.4
Afterglow,	0.5–5(6)	0.005(3)	0.005(3)	0.1(100)	0.01(3)
Temp. stability (%/°C) at 25°C	0.02	−0.15	−0.30	$< \|0.04\|$	−0.6
Rad. damage (%)	+13.5(450)	—	−1.8(775)	−1.0(450)	—

Temperature Dependence of Detector Gain

The temperature dependence of the luminescence yield $I(T)$ under excitation at 300°K is explained in terms of the probability of nonradiative transitions by Mott's equation $I(T) \approx (1 + w_0 \exp(-\varepsilon/\mathrm{kT}))^{-1}$ [51] with frequency factor $w_0 = 4.25 \times 10^6$ and thermal activation energy $\varepsilon = 0.49\,\mathrm{eV}$. As was shown in [50], this theoretical curve coincides well with the temperature dependence of the CWO crystal and the CT detector response. This value is not the best among CT scintillators, but satisfies current engineering demands.

Radiation Damage

In medical CT, the maintenance of the system imposes a continuous exposure to radiation and the crystals accumulate a certain level of radiation damage. This could result in variation of sensitivity and deterioration of the accuracy of the system. The typical exposure rate of a CT scanner is about $1\,\mathrm{rad.s^{-1}}$. However, because of a strong absorption in the scintillator entrance face, the dose rate could exceed $\sim$50 $\mathrm{rad.s^{-1}}$ in this part of the crystal that may lead both to detector gain drift and spectral sensitivity loss, and finally to the crystal deterioration. The main part of the scintillation efficiency degradation is recoverable after 1 h of relaxation. It means that the CWO exploitation has to take into account the balance between the accumulation and recovery of radiation damage. There are several channels of radiation-induced scintillation losses such as decrease of crystal transparency [53] and variations of luminescence yield due to modifications of the emitting centers [49]. Radiation damage effects are related to internal crystal defects, deviation from stoichiometry, and traces of impurities. These phenomena and potential CT scintillator improvements will be discussed in Chap. 5.

Ceramics Materials

In spite of their wide use, CWO crystals are not the ideal choice for CT application due to their brittleness and the toxicity of cadmium. This has been an argument for the search of a new generation of CT scintillators. This search was initiated by General Electric and Siemens in the mid of 1980s when they introduced the first polycrystalline ceramic scintillators. The host materials were Y_2O_3 and Gd_2O_3 and their mixtures [54], after doping by Pr and Tb, demonstrated reasonable properties. Nevertheless, their transmission was rather low, ceramics being more translucent than transparent. The Eu^{3+} activator efficiently traps electrons to form a transient Eu^{2+} state, allowing holes to form Pr^{4+} and Tb^{4+} and, therefore, competes with the intrinsic traps responsible for afterglow. This energy trapped on the Pr and Tb sites decays nonradiatively in presence of the Eu ions reducing therefore the level of afterglow [54].

Three mol% of Eu_2O_3 doping to $(Y,Gd)_2O_3$ allows to reach 65% of CsI(Tl) efficiency with emission at 610 nm. The relatively long decay time (∼1 ms) can be accepted because of the low afterglow level.

Gd_2O_2S:Pr,Ce,F ceramics has a shorter decay time, a higher light output, a low afterglow, but the emission peak is at 511 nm, which is less convenient for Si photodiodes.

These two types of ceramics known as UFC and Hilight are widely used in off-the-shelf CT scanners. However, the search for more efficient ceramics continues. $Gd_3Ga_5O_{12}$:Ce,Cr [48] is considered to be a good candidate. During the last years Lu_2O_3:Eu, Tb were investigated also. But, at this stage, the afterglow level is relatively high and will be a major limitation if no solution is found to suppress it.

$SrHfO_3:Ce^{3+}$ and $BaHfO_3:Ce^{3+}$ ceramics are other candidates for both CT and probably PET devices [48]. Both of them are high-density materials and have a short decay time and reasonable light yield (up to 20,000 photon/MeV). Moreover, their afterglow level is small.

These examples show that new materials investigation and research remain highly actual and that the potentialities resulting, for example, and from the impressive progress in nanotechnologies to produce new transparent ceramics will offer new perspectives for CT scanners.

Detector Engineering

The demand for a better spatial resolution for X-ray CT scanners and the progress in photodetectors PSPMT (positive sensitive photo multipliers) and Si-photodiodes matrixes have triggered a strong development effort for pixel-based arrays and matrixes design. The main applications for such devices are X-ray CT and industrial and security systems.

Linear scintillation arrays are widely used in CT systems with two main designs: ladder type scintillators and medical CT linear arrays.

The first type of arrays coupled to Si-photodiodes is based on pixels of 1–2 mm in cross section and up to 2 mm in thickness. The typical number of pixels varies from 8 to 16, 32, or even 64 in such arrays. They are mainly based on $CdWO_4$ and CsI(Tl), although some ceramic scintillators are also available now.

The second type requires thicker pixels. Typical sizes are (1–2)×(20–30)×(2–3) mm^3. It reflects the necessity of multislice image reconstruction for medical analysis.

Two-dimensional arrays for medical applications were designed over 30 years ago. The first prototypes were based on NaI(Tl) crystal that required hygroscopic protection and had a big gap between elements due to MgO powder used as light collector and for optical separation of pixels. Important progress of two-dimensional (2D) matrix design was correlated with the development of advanced photodiode matrixes in the last 10 years. Such "sandwiches" have a better spatial resolution and real-time, visualization potential.

Last years' engineering efforts showed that multilayered assemblies [55] initially developed for astrophysics detectors can be efficiently used for medical applications.

State-of-the-art array design is based on minimization of the two main parameters: pixel size and gap between pixels. These issues are critical to reach the best spatial resolution and to minimize losses inside the gap between pixels.

Pixel Size

The choice of the scintillating material is, of course, the key for a higher segmentation of a new generation of CT scanners. The choice of the material is also important because the pixel size is determined by mechanical properties of the crystal-like hardness, cleavage, machining ability, etc. Thus, the minimal pixel size is now slightly different for various materials, namely, 0.3 mm for CsI(Tl), CWO, and BGO; 0.5 mm for CaF_2:Eu and LSO.

It should be noted that so small pixel size will lead to a considerable increase in the number of channels to an increased complexity of the acquisition system. As a result, important electronics upgrades will be necessary. Last decade trends led to specific technology for matrixes manufacturing. So-called columnar structure screens were developed [56, 57]. Strong efforts to develop a solid-state dynamic X-ray sensor with digital readout have been carried out. The current design is based on large a-Si photodiodes (substrate) coupled to a CsI(Tl) layer. The scintillator layer growth is nucleated on the pattern substrate and transferred to a columnar system separated with grain boundaries as seen in Fig. 2.6. Each CsI(Tl) column is not only a scintillation pixel but also a light guide. This guide prevents or at least strongly suppresses the radial light spread and might be the way to obtain very high spatial resolution. Columnar structure growth technique allows to get 3–5-μm diameter

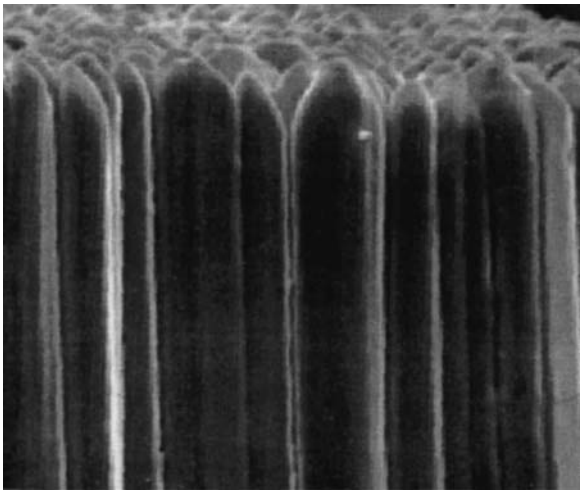

Fig. 2.9. Column structure of vapor deposited CsI(Tl)

columns and the pixel size is defined by the Si pad size as seen from Fig. 2.9. Currently, flat panel detector size of up to $40 \times 40\,\mathrm{cm}^2$ is available to image the human chest.

The example of flat panel development shows that matrix detectors and flat screens could be developed from two different production technologies of the same scintillator. Other materials could follow the same route. A typical example is the ceramic material Gd_2O_3S:Tb for X-ray intensifying screens [58, 59]. The emission at 545 nm is very convenient for coupling to photodiodes with a sensitivity peak in the green–red range of the spectrum. Recently, Agfa introduced a $43 \times 43\,\mathrm{cm}^2$ flat panel on the basis of this material deposited on a matrix a-Si:H photodiodes (pixel size $160 \times 160\ \mu\mathrm{m}^2$). This is practically the same size as was achieved for CsI(Tl) screens.

BaFBr:Eu [60] is the typical inorganic stimulated phosphor for digital radiography. A more detailed review of these materials is available in references [47, 48, 58].

It should be noted that it is possible to use nonpixilated screens for the low-energy X-rays. If X-rays are absorbed in a very thin crystal layer, the angle of the emitted light is small (for the thin film) and the cross talk to the neighbor photo receiver is negligible maintaining therefore a good spatial resolution. The search for materials for such applications is of very high importance now.

Separator Size and Thickness

Separators are put into the gap between crystal pixels to prevent the photon leakage from pixel to pixel. It is obvious that this material should be as

thin as possible and possess good reflectivity and low transparency. Practically used materials are white powder (TiO_2, MgO, more than 1 mm thick, reflectivity 100%), Teflon, Tyvek^{TM} sheets (0.5–0.15 mm thick and 98% reflectivity), and aluminized composites (VM2000 type, about 0.1 mm thick and 95% reflectivity).

Each pixel geometry and matrix design depends, in general, on the array specification. Modern specifications require less than 2–4% cross talk (leakage) between neighbor channels. A powder reflector as well as thin films (like Teflon, Tetratex, BHA films) possesses the best reflectivity, but they are not suitable for the bonding process. They need also to be relatively thick to have good properties. White paints and/or epoxy covering is suitable for relatively large-sized pixel designs. Metals (lead, tungsten, or tantalum) prevent optical leakage between matrix elements, but do not allow reaching a good reflectivity. At the same time, the metal separator can absorb the radiation incident to the separator surface before it strikes the light sensor. These metallized films (such as VM2000) are the most appropriate materials due to the best balance of reasonable reflectivity, thickness, and cross talk.

Total light collection in a matrix element (linear array) depends on separator type and reflectivity as well as on crystal surface conditions. These conditions are important not only for the best light output, but also for the best uniformity and minimal spread of the data from pixel to pixel. The nonuniformity of the best matrixes should not exceed 2–5%. Such rigid specifications require good and very uniform crystal surface treatment. The large quantity of elements in 2D matrix does not allow checking each element. Good surface quality should be obtained from a minimum number of mechanical operations. Crystal damage, subsurface intrinsic stresses, and material recrystallization at the production stage may deteriorate the performance of some pixels. The light output spread for the same CsI(Tl) elements might reach 15% when the surfaces are treated in a slightly different way.

The matrix uniformity is based on high accuracy and low cross dimensions tolerances. For hard materials (BGO, CWO, GSO), these tolerances should not exceed ± 0.01–0.02 mm and could even reach the level of about 50 microns. For the soft scintillators (such as CsI), this value is always higher.

2.3.2.3 Emission Tomography

The working principle of emission tomography is to image γ-rays emitted by radiotracers injected to the patient. Contrary to X-ray CT and nuclear magnetic resonance, which provide very precise images of the anatomy of organs, nuclear imaging modalities give in vivo access to the functioning of these organs.

SPECT Tomography

In single photon emission computed tomography (SPECT), a molecule involved in the metabolism of the patient is labelled by a single photon emitter

(usually $^{99}T_c$ emitting one 140 keV γ-ray). After injection it concentrates in some organs or tumours and allows the imaging of them by the reconstruction of the γ-ray emitting points. The most popular technique is based on the "Anger logic" [46], where γ-rays are directed through a multihole collimator to a large slab of NaI or CsI scintillator (Fig. 2.10).

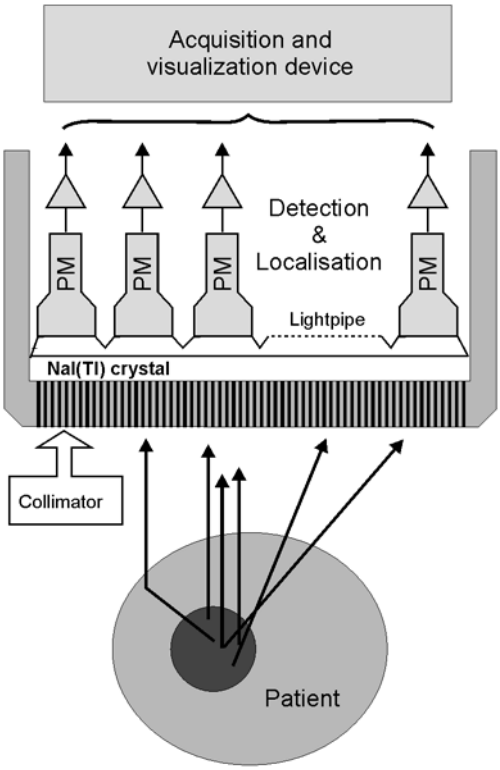

Fig. 2.10. Principle of the Anger camera

The coordinates of the interaction point are then determined by comparing the signals from a set of PMTs coupled to the crystal, by the center of gravity method. This technique is still largely used in many hospitals and medical imaging laboratories, but suffers from a relatively poor space resolution, of the order of a few centimetres. A modern approach uses the direct coordinate determination with Position-Sensitive PMTs (PSPMTs) coupled to scintillation multicrystal array based on CsI or YAP crystals. Several devices have been developed, such as HIRESPECT, a YAP mammography camera in Italy with a resolution of 0.7 mm, as well as peroperative probes.

The Anger logic proved to be quite effective (the same principle was earlier applied for astrophysical telescope design [61]) with a good price–performance

ratio. Indeed a detector for whole-body screening (i.e., with a cross section up to 600×500 mm) may be completed with 35–40 PMT. (The practice shows that the replacement of 3″ PMT by 2″ PMT, the use of hexagonal, and square PMTs does not significantly improve the resolution of the whole system.) The above engineering solution has therefore remained almost unchanged up to now and SPECT diagnostics is still the most largely used method of nuclear medicine. There is today no real alternative to NaI(Tl) crystals. Only scintillators with a significantly better energy resolution (approximately 3–4%) could make a step forward. The recently discovered family of rare earth halide scintillators, with in particular $LaCl_3$:Ce, $LaBr_3$:Ce [62, 63] and LuI_3:Ce [87] open new perspectives with light yields in the range of 50000 to 100,000 photons/MeV and energy resolution as good as 3% with a ^{137}Cs source. However, their application is still limited by the cost of these materials and the difficulty to produce them in large size.

A more realistic alternative is CsI(Na) halide scintillators in large monoblocks and CsI(Tl) pixilated (matrix) detectors, which are used, in portable cameras. Continuous CsI(Na) crystals $50 \times 50 \times 4.6$ mm with white entrance and black edge reflecting was used for a flat-panel-based mini gamma camera for lymph nodes studies [64]. The intrinsic resolution level of this system is better than 1.5 mm. This system is therefore competitive with more complex pixilated designs [65]. Some investigations [66,67] confirmed the ability to reach almost the same system efficiency when using pixilated, partly pixilated, and continuous detectors, and demonstrated the flexibility of the detector design to optimize its performance.

A CsI(Tl) crystal coupled to a photodiode allows to significantly reducing the size of the detector while maintaining a good sensitivity. Such a design includes 4,096 scintillation pixels. The DIGIRAD imager (pixilated detector size of 214×21 cm) has been evaluated during a clinical myocardial study [68]. This detector is smaller in size than a conventional gamma camera detector, and can be used as portable gamma cameras complementing the whole-body systems.

Such functional system designs may compete with direct converters based on semiconductors (CdTe, CdZnTe, etc.). These systems have a better energy resolution, but their use is presently limited by a low production yield and the technical problems to produce high-grade semiconducting crystals with good uniformity.

It must be noted that some attempts a few years ago to use two SPECT cameras in coincidence in order to obtain a pseudo PET system (of rather limited performance) has led to the development of 25-mm thick NaI(Tl) plates able to record with a reasonable sensitivity 511 keV γ-quanta [69–73].

Positron Emission Tomography

Positron emission tomography (PET) makes also use of molecules involved in different metabolic functions of the human body, allowing therefore precise

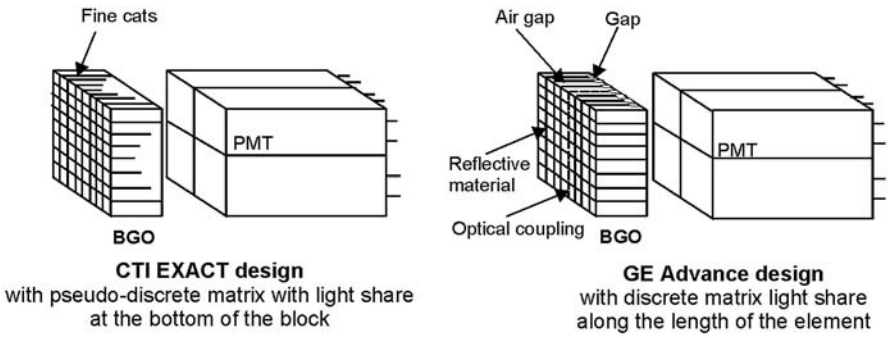

Fig. 2.11. PET detector module design

functional imaging. They are labelled here with β^+ emitter isotopes, which are generally produced in a cyclotron. These PET tracers, injected into a patient, simulate natural sugars, proteins, water, and oxygen presence in human body. The PET measures the uptake of the tracer in different organs or tumors and generates an image of cellular biological activities. These PET images can be used to quantitatively measure many processes, including sugar metabolism, blood flow and perfusion, oxygen consumption, etc. Recently, the need for specialized PET scanners designed for experimental small animal studies (mouse, rat, rabbit) was recognized as a powerful tool for fundamental research of disease models, new therapeutic approaches, and pharmacological developments. The most commonly used isotopes are ^{18}F with a lifetime of 109.8 min, ^{11}C (20.4 min), ^{13}N (10 min), and ^{15}O (2.1 min), which are all among the basic building blocks of organic systems and can therefore easily be chemically introduced in molecules involved in metabolic or pharmaceutical reactions. A typical example is FDG (fluorodeoxyglucose), which allows monitoring the energetic consumption of the cells in different parts of the body. Once fixed in some organs or tumours, the molecule emits positrons decaying in 2 back-to-back γ-rays, which are detected in coincidence in rings of scintillators (Fig. 2.12). Until recently, as a result of compromise between performance and cost, PET scanners were using partially segmented BGO crystals readout by groups of 4 PMTs, allowing a reconstruction precision of the order of 4 to 5 mm (Fig. 2.11). Modern machines are going progressively to higher segmentation of the crystals and of the readout to achieve higher spatial resolution. Resolutions of the order of 1 mm are considered to be within reach. Another important parameter is the sensitivity, which relates the number of useful detected events to reconstruct an image to the dose injected to the patient.

It must be noticed that PET scanners allow localizing radiotracers uptakes in the human body but do not deliver precise anatomical images, such as MRI or X-ray CT, for instance. A new generation of scanners combines the very high sensitivity of PET for metabolic imaging to the high spatial

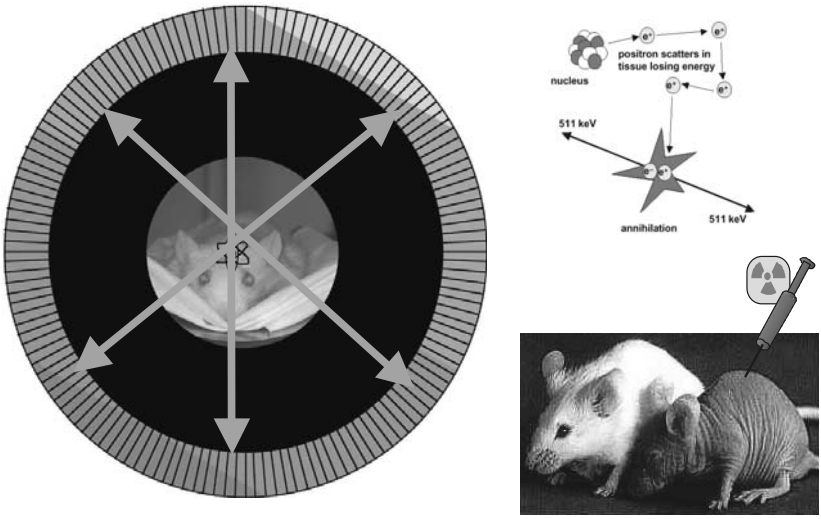

Fig. 2.12. Working principle of a PET scanner

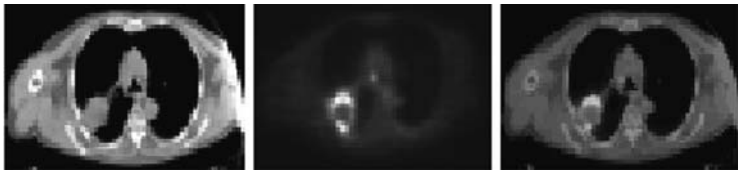

Fig. 2.13. Primary lung cancer imaged with the SMART scanner. A large lung tumor, which appears on CT as a uniformly attenuating hypodense mass, has a rim of FDG activity and a necrotic center revealed by PET. Photo: courtesy of D. Townsend, University of Tennessee

resolution anatomic information delivered by X-ray CT or another anatomical modality. They provide impressive images giving the very precise localization, of active areas of organs and tumors (Fig. 2.13). PET scanners are very powerful tools for basic research in cognitive sciences, clinical oncology, and kinetic pharmaceutical studies.

Requirements for an Optimal Scintillator

The first important requirement for a scintillator to be used in medical imaging devices is the stopping power for the given energy range of X- and γ-rays to be considered, and more precisely the conversion efficiency. Clearly materials with high Z and high density are favored but the position of the K-edge is also important as can be seen on Fig. 2.14. For low-energy X-ray imaging (below 63 keV), the attenuation coefficient of yttrium, cesium, and iodine are quite high and crystals such as YAP and CsI are good candidates. Above the

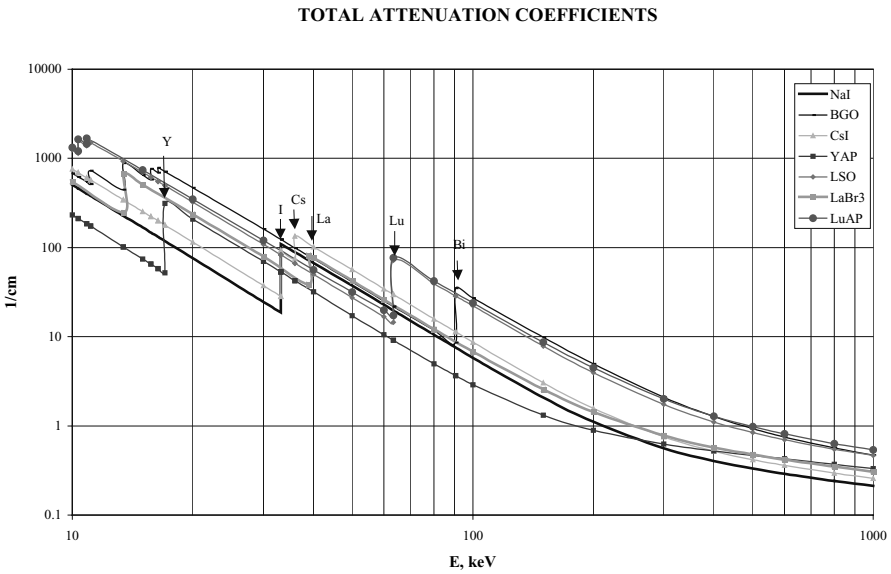

Fig. 2.14. Attenuation coefficient in several high Z materials

K-edge of Lu (63 keV) and Bismuth (90 keV), the situation is quite different and BGO- and Lutetium-based crystals will be clearly favored for ^{99}Tc (90 keV) SPECT and PET scanners (511 keV). Heavy scintillators are also useful to reduce their thickness and the parallax error in ring imagers.

A short absorption length is important not only to increase the number of detected X- or γ-rays for a given detector thickness but also to maintain a good spatial resolution over the whole field of view. A short crystal will reduce the effect of the radial elongation as shown in Fig. 2.15. Another approach is to use a combination of two or more crystals mounted on top of each others (phoswich configuration) with different emission wavelength or decay time so that the depth of interaction (DOI) determination is made possible through the correct identification of the crystal hit.

A high light yield is also mandatory to improve the energy resolution, which is essentially limited by the photo statistics and the electronic noise at these energies. A better energy resolution allows a higher rejection of Compton events and improves therefore the spatial resolution and the sensitivity. The sensitivity is a very critical parameter of nuclear medical imaging as it reflects the number of useful events per unit of injected dose to the patient. A higher sensitivity means a smaller injected dose or a better image contrast.

A short scintillation decay time allows to reduce the dead time and therefore to increase the limiting counting rate. Moreover, by reducing the coincidence gate, the signal-to-background ratio is improved which has a direct impact on the image quality. Here again the sensitivity and image contrast are increased for a given patient dose, or the dose can be reduced. It must

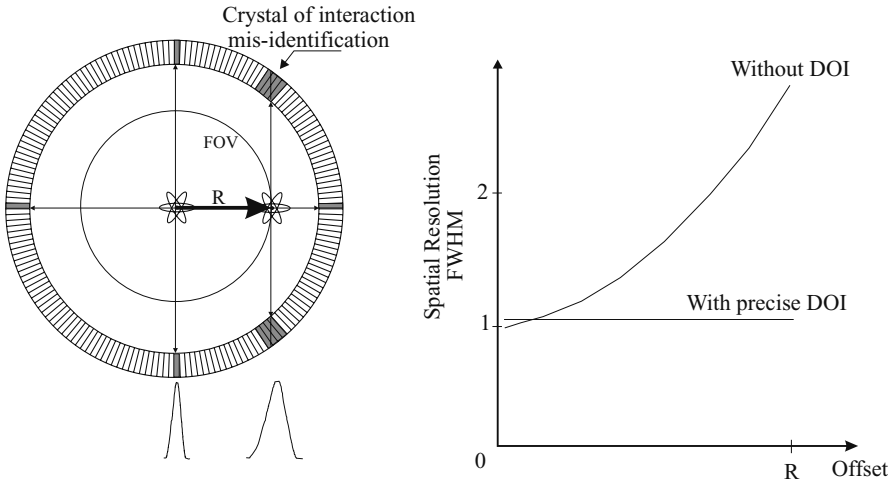

Fig. 2.15. Radial elongation distortion in a PET scanner

be noticed that very fast scintillators can open the way to scanners using the time of flight information, which will help reducing the background by selecting a narrow region of interest along the coincidence line.

Sodium iodide (NaI) and, more recently, caesium iodide (CsI) have been for a long time the most common scintillators used in nuclear medical imaging devices, mostly because of their very high light yield and relatively easy and cheap production methods. But their low density and slow decay time considerably limits the performance of these devices. The large effort made by the L3 collaboration at CERN to develop cheap mass production technology of BGO crystals has introduced this material in the field of medical imaging, mostly because of its very high density and conversion efficiency. Most of the PET scanners produced in the last decade were built with BGO crystals. Unfortunately a much smaller light yield than NaI and a decay time of 300 ns are still limiting factors.

There is a need for a crystal having the light yield of NaI, the density of BGO, but at least 10 times faster than BGO. What matters in fact is the largest possible number of photons emitted in a short gate of typically a few tens of nanoseconds. This crystal has been developed for about 15 years. This is the lutetium orthosilicate LSO:Ce and its variation LYSO:Ce with a few percentage of yttrium substituting to lutetium ions. LSO and LYSO are progressively replacing BGO in modern PET scanners. During the last decade the crystal clear collaboration at CERN has been deeply involved in the development of another attractive crystal in this category, the lutetium aluminum perovskite LuAP:Ce, also with the yttrium heavily doped compound LuYAP:Ce [74], which is described in Chap. 7. This crystal has a much better linearity at low energy than LSO, which results in an even better

energy resolution in spite of a light yield about a factor 2 smaller. Moreover, its properties perfectly match the one of LSO, which makes the combination LSO–LuAP the ideal phoswich for depth of interaction determination.

There are a number of other possible candidates for PET applications that are being studied by different groups. They are listed in Table 2.4.

Table 2.4. Properties of scintillation materials with high photoabsorption coefficient

Material	ρ ($\mathrm{g\,cm^{-3}}$)	Z_{eff}/photo-abs. Coeff.at 511 keV ($\mathrm{cm^{-1}}$)	Y (ph Me $\mathrm{V^{-1}}$)	τ_{sc} (ns)	λ_{sc}, (nm)	S_t (ph $\mathrm{Mev^{-1}\,ns^{-1}}$)	$1/\tau_{\mathrm{scu}}$ (MHz)
$BaLu_2F_8$	6.94	63/0.22	870	1+slow	313	870	1,000
$BaLu_2F_8$:Ce	6.94	63/0.22	400	35+slow		11	30
LuF_3:Ce	8.3	61.1/0.31	8,000	23+slow	310	347	43
Gd_2O_2S: Pr,Ce,F	7.34	61.1/0.31	40,000	2100	580	19	0.4
Lu_2s_3:Ce	6.2	66.7/0.24	28,000	32	592	875	31
$CdWO_4$	7.9	64.2/0.26	19,700	2000	495	9.85	0.5
$ZnWO_4$	7.87	62.5/0.27	21,500	22000	480	0.97	0.05
$CaWO_4$	6.1	63.8/0.22	6,000	600	430	10	107
$PbWO_4$ (PWO)	8.28	75.6/0.48	100	6	420	17	170
$Bi_3Ge_4O_12$ (BGO)	7.13	75.2/0.37	8,200	300	505	27	3.3
$Lu_3AI_5O_{12}$:Sc	6.7	62.9/0.21	22,500	610	270	37	1.6
$LuAIO_3$:Ce (LuAP)	8.34	64.9/0.29	11,400	17+slow	365	670	58
Lu_2SiO_5:Ce (LSO)	7.4	66/0.28	27,000	40	420	675	25
$Lu_2Si_2O_7$:Ce (LPS)	6.23	64.4/0.21	30,000	30	380	1,000	13
$LuBO_3$:Ce	7.4	67.5/0.28	26,000	39	410	660	26

If we restrict this list to crystels having a light yield of more than $10^4\,\mathrm{Ph\,MeV^{-1}}$ and a decay time of less than $\tau_{\mathrm{sc}} = 100\,\mathrm{ns}$, the number of good candidates is restricted to 6 only: LuF_3, Lu_2S_3, $LuAlO_3$, Lu_2SiO_5, $Lu_2Si_2O_7$, $LuBO_3$ from which four are complex oxide compounds.

2.4 Safety Systems

There are three main areas of safety detector equipments making use of scintillators: express control of luggage and passengers, search for explosive materials, and remote detection of fissile materials.

The technical solutions for the first application are very similar to single photon γ-camera and X-ray CT scanners, which are developed for medical

applications. The point is to rapidly identify a suspect luggage in a few cubic meters large container moving across the inspection device. An important requirement for such a scanner is the highest possible throughput. The spatial resolution is related to the need to localize and possibly to identify the suspect object in a large container. Two other applications have attracted more and more attention in the last 10 years.

For the remote detection of explosives, methods of nuclear radiation detection look very promising. These methods are based on the detection of either natural or induced characteristic neutron and γ-rays. Actually, the most useful element-sensitive approaches are based on activation by a neutron source, either fast neutrons from the ^{252}Cf radioisotope or fast-thermal neutrons from a pulsed electronic neutron generator. The neutron-based methods are grouped in three categories: thermal neutron analysis TNA, fast neutron analysis FNA, and pulsed fast neutron analysis PFNA. In these methods, neutron-induced reactions such as elastic scattering, (n, γ), (n, p), (n, n'), and neutron activation are used [75]. Neutrons initiate fast nuclear reactions on some elements, some of them producing characteristic γ-rays. By allowing the fast neutrons to be thermalized between pulses, a large number of elements such as N, Cl, S, Ca, or their ratio in mixtures can be identified through the following (n,γ) reactions:

Element	**Reaction**	**Cross Section (mb)**	**Eγ (MeV)**
C	$(n, n'\gamma)$	200	4.44
O	$(n, n'\gamma)$	750	6.13
N	(n, γ)	75	10.83
Cl	(n, γ)	4,300	6.11
S	(n, γ)	520	5.42

One can see that the majority of nuclei, which are important for explosives identification, emit γ-quanta in the energy range $E_\gamma \geq 4\,\text{MeV}$. Detection methods based on scintillation crystals have significant advantages over other methods in this energy domain where the creation of pairs under ionizing radiation in the scintillation material already dominates.

The requirements for the scintillation material are therefore similar as for low-energy calorimetry. For such applications, the most important scintillation crystal parameters are the following: high stopping power which determines the detector sensitivity; high light yield which determines the detector energy selectivity; fast decay time of scintillation because of the possible use of two important registration regimes: (1) with pulsed fast neutron analysis the registration is gated for better signal-to-noise ratio and (2) with reliable time of flight (TOF) information which is also applied for background rejection and useful identification of the source along the γ-ray path; stability of the scintillator parameters under ionizing and neutron irradiation, as stable and slow recovering defects can appear in the scintillation material modifying

their detecting properties and, as a consequence, decreasing their sensitivity. This negative effect can be cumulative with the dose, inducing a global worsening of the scintillation detector parameters properties. Moreover, an additional low sensitivity to neutrons is required. Currently, multidetector systems based on conventional BGO, $CdWO_4$, CsI (Na), or NaI(Tl) scintillation crystals are used for this application.

Fissile materials undergo spontaneous fission, or α-decay with the production of radionuclides and γ-rays, which provide a good signature of their presence. These radionuclides are (1) nuclei of the main isotope, (2) nuclei from isotopes of the same chemical element, and (3) isotopes related to the technology of the fissile materials production and enrichment.

The method of fissile materials remote detection and warheads inspection based on n-radiation detection was applied in practice in the framework of the Nunn–Lugar program for the control of dissemination of nuclear weapons. In this frame, the γ-channel of detection was not allowed, as it would have given too easy an access to secret characteristics of the nuclear device. Now, the detection through the γ-channel is permitted and opens new possibilities to distinguish the radiation of nuclear explosive devices (NED) based on both enriched uranium and weapon plutonium, from the radiation of separate fissile materials or radioactive substances, which can also be illegally imported or exported. The characteristic integrated yield of γ-radiation from NED in the energy range up to 10 MeV can reach $10^5\gamma$-quanta per second and is comparable with the yield of neutron radiation. The most useful energy range to detect fissile material is $E_\gamma \geq 3$ MeV because of (1) the absence in this range of natural radioactive sources, allowing therefore an acceptable signal-to-background ratio, and (2) the high penetration power of these energetic γ-quanta for the case of deliberate concealment of the self-radiation of NED.

However, convenient registration techniques of γ-quanta with NaI(Tl) or CsI(Na) scintillation crystals allow detecting masked fissile materials in a relatively short acquisition time at a distance not exceeding a few tens of meters. Moreover, the introduction in the detecting system of convenient charge particle shielding does not result in a significant increase of the detection distance. The detecting distance is strongly dependent on γ-quanta registration efficiency. A simple increase of the detector area increases the signal but also the noise level and does not allow a precise detection at larger distances. A high efficiency for the γ-quanta detection is achieved by the use of heavy scintillation materials. Moreover, a phoswich geometry based on two different crystals on top of each other, coupled to PMT, is an attractive solution. The requirements to the scintillators of the phoswich are listed in Table 2.5.

The relatively thin forward scintillator in the phoswich is used to measure the background whereas the relatively long main scintillator will operate in the 3–10 MeV range. Playing with different decay times and scintillation luminescence spectra allows a more precise and fast measurement of the signal and the background allowing an increase of the detecting distance. A good

Table 2.5. Technical requirements for a scintillator-based phoswich detector for fissile materials control

Requirement	Main Scintillator	Forward Scintillator
Density ($g\,cm^{-3}$)	$\geq$7	$\geq$7
Decay time (ns)	$\leq$20 ns	$\leq$1,000 ns
Scintillation spectrum (nm)	350–450	450–550

combination of the two scintillators of the phoswich can be obtained from the scintillators listed in Table 2.4 excluding Lu-based materials, because of the natural radioactivity of the 2.5% abundant ^{176}Lu isotope.

2.5 Astrophysics

Space physics is making use of scintillators in two different locations: the low orbit satellites and space or interplanetary missions. The low-orbit satellites are shielded by the earth magnetic field, relaxing therefore the requirement for radiation hardness of the scintillation material. Most of the scintillation materials can be used depending on the energy range of the detected γ-radiation. However, the payload is limiting the size of such detectors and not two dense materials are sometimes selected to reduce the weight.

In the interplanetary space, the sun wind from charged particles strongly influences the detecting properties of the scintillation materials. For these missions, high radiation hardness to ionizing radiation and low level of induced radioactivity are required. The same applies to detectors, which are transported to the planets. Although the studies in this domain are still not systematic, one can state that relatively light, fast, and bright scintillators are the most prospective ones for space missions in the future and that $LaBr_3$, YAP, and (Lu–Y)AP are likely to become the scintillators of choice.

The list of the main projects performed in gamma astrophysics from the beginning of the 1990 is given in Fig. 2.16. Most of the current data on cosmic γ-sources have been accumulated from different gamma telescope measurements. The main peculiarity of these measurements was based on the design of position-sensitive telescopes, which is not a simple task. Two classes of position-sensitive devices were developed in the last decades. These designs are using continuous scintillation crystal or pixilated detector geometries [76].

Scintillation detectors with continuous crystal are generally based on Anger camera logics as for nuclear medicine gamma cameras (SPECT system, see Sect. 2.3). An example of such gamma camera is the SIGMA mission on GRANT where a 12.5-mm thick NaI(Tl) crystal is viewed by 61 hexagonal PMT through a 12.5-mm thick glass. This glass encapsulates the hygroscopic crystal and plays the role of a light guide for the light sharing between the PMTs. An energy resolution of about 10% FWHM is achieved at 120 keV

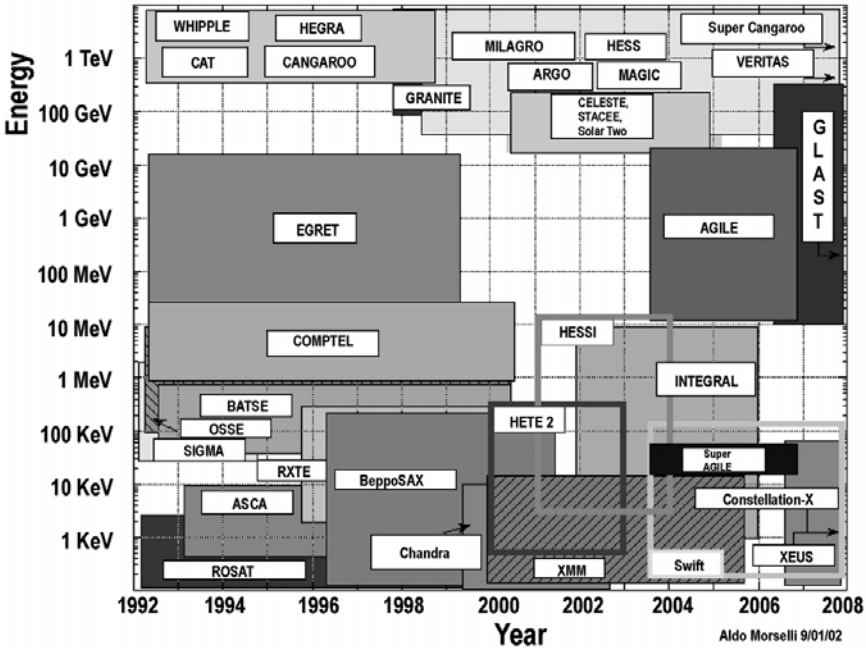

Fig. 2.16. List of the main projects for gamma astrophysics from the beginning of 1990 [84]

with a position resolution of 4 mm at this energy. The detector is surrounded by an active CsI(Tl) veto shield to limit the entrance aperture to about one steradian.

The use of an array of small discrete detectors offers an alternative to continuous crystal detector. This design uses the same reconstruction principle as HEP calorimeters (see Sect. 2.1) or some medical cameras. An example of gamma telescope based on pixilated detector is the imager of the INTEGRAL detector [77, 78]. INTEGRAL is made of 3 layers hexagonal CsI(Tl) scintillation bars. There are three planes with 2,880 scintillation elements each coupled to silicone photodiodes. This arrangement provides good imaging and sensitivity in the 50 keV–10 MeV range. BGO scintillators are used as veto shields as in several other detectors. This includes 38 bars with dimensions $20 \times 90 \times (310-345)$ mm. Because of special light collection conditions, the constraints on light attenuation are very high (more than 3 m at the wavelength of emission of BGO: 480 nm). Moreover, these conditions must be maintained under the harsh radiation conditions in space.

The investigations of the high-energy component of cosmic γ-radiation are of crucial importance to understand the emission mechanisms of galactic sources. This is the goal of several experiments such as the one of the GILDA mission [79].

The high-energy γ-ray astrophysics greatly developed in the beginning of 1990 following the results of the EGRET experiment [80]. The satellite observations have brought more detailed data about the well-known γ-ray sources, but has also led to the discovered new ones, both galactic and extragalactic, especially active galactic nuclei and gamma bursts.

The most serious problem affecting the EGRET telescope is the decrease of detection efficiency at high energies, because of the use of anticoincidence counters placed around the detector.

The objective of the Energetic Gamma Ray Experiment Telescope (EGRET) is to make a major advance in high-energy (20 MeV to about 30 GeV) γ-ray astrophysics, using a γ-ray telescope with more than an order of magnitude greater sensitivity and better angular and energy resolution than previous instruments. The study of the γ-ray sky reveals the sites of the most energetic interactions occurring in astrophysics. Because these interactions are generally associated with dynamic, nonthermal processes in nature, γ-ray astrophysics provides an excellent opportunity to learn about the evolution of the universe. In addition, since high-energy γ-rays have a low-interaction cross section, they have a very high penetration power and can reach the Earth from essentially any part of the Galaxy or universe.

EGRET detected γ-rays in the 20 MeV–30 GeV range. It had a very large field of view, approximately 80° in diameter, although the instrument point-spread function and the effective area degrade significantly beyond 30° off-axis. The effective area on-axis was more than 1,000 cm^2 between 100 MeV and 3 GeV. The angular resolution was strongly energy dependent, with a 67% confinement angle of 5.5° at 100 MeV, falling to 0.5° at 5 GeV on axis; bright γ-ray sources can be localized with approximately 10′ accuracy. The energy resolution of EGRET was 20–25% over most of its range of sensitivity. The arrival times of photons were recorded with approximately 50-μs accuracy. The instrument uses a multilevel thin-plate spark chamber system to detect γ-rays by the electron–positron pair production process. A calorimeter using NaI(Tl) is placed beneath the instrument to provide good-energy resolution over a wide dynamic range. The energy of the γ-ray is determined in large part from measurements made in an eight radiation-length thick, 76 cm × 76 cm square NaI(Tl) scintillator crystal below the lower time-of-flight scintillator plane. The NaI(Tl) detector is covered by a plastic scintillator anticoincidence dome to prevent triggering on events not associated with γ-rays.

The first scintillators for gamma telescopes were relatively simple and did not trigger large developments on scintillators. But this situation was progressively modified by the higher requirements for space physics experiments and investigations for a new generation of scintillators for space started with the GLAST project (Global Large Area Space Telescope) [81, 82].

The GLAST Mission is part of NASA's Office of Space and Science Strategic Plan, with launch foreseen in 2006. GLAST is a new generation high-energy γ-ray observatory designed to study celestial γ-ray sources in the energy band extending from 10 MeV to more than 100 GeV. It is a follow-up of the CGRO-EGERT program, which was operational between 1991 and 1999.

GLAST has more advanced missions and has to cover several important directions in astrophysics:

1. Understand the mechanisms of particle acceleration in pulsars and other space sources.
2. Create a precise map of γ-ray source in the sky: unidentified sources and diffuse emission.
3. Determine the high-energy behavior of γ-ray bursts and transients.
4. Probe dark matter and early universe.

The observation of γ-ray pulsars is an important tool to understand supermassive black holes through jet formation and evolution studies, and to set constraints on the star formation rate through photon–photon absorption over extragalactic distances. There is also a possibility to observe monoenergetic γ-ray "lines" above 30 GeV from supersymmetric dark matter interactions, to detect decays of relics from the very early universe, such as cosmic strings or evaporating primordial black holes; or even to use γ-ray bursts to detect quantum gravity effects.

The GLAST (Global Large Area Telescope) has a field of view about twice as wide (more than 2.5 steradians), and sensitivity about 50 times that of EGRET at 100 MeV and even more at higher energies. Its 2-year limit for source detection in an all-sky survey is 1.6×10^{-9} photons cm^{-2} s^{-1}(at energies greater than 100 MeV). It will be able to localize sources with a position accuracy of 30 arc seconds to 5 arc minutes. Yet, it is a relatively small and inexpensive mission, which will be launched by a simple Delta II rocket.

The calorimeter of GLAST measures the energy of the cosmic γ-rays. CsI(Tl) bars, arranged in 16 flat towers, give both the longitudinal and transverse information about the energy deposition pattern. Once a γ-ray penetrates through the anticoincidence shield, the silicon-strip tracker and the lead converter planes, it is then absorbed in the cesium-iodide calorimeters. This produces scintillation in the cesium-iodide crystal, and the resultant light flash is photoelectrically converted to a voltage pulse. This voltage signal is then digitized, recorded, and relayed to earth by the spacecraft's onboard computer and telemetry antenna. Cesium-iodide blocks are arranged in two perpendicular directions, to provide additional positional information about the shower [82].

The GLAST project was at the first time requiring an engineering study on the scintillation material. It was necessary to develop a position-sensitive detection capability from unique long scintillation crystals.

Long scintillator crystals used in HEP projects require a light output as uniform as possible along the scintillator. The light yield uniformization was used in many experiments using different techniques (painting the BGO crystals for the L3 experiment, depolishing one lateral face for the CMS PWO crystals, etc.). In the case of the 6624 CsI(Tl) scintillators of the electromagnetic calorimeter BELLE (KEK) [83], a light nonuniformity of less than 7% along the 300-mm length of the crystal was achieved. Such an approach was also used for the BaBar CsI(Tl) scintillator treatment to unify the light output to 6% [84].

Contrary to the HEP case, a surface treatment can be applied on long crystals to induce on purpose a nonuniform distribution of the light output [85]. Figure 2.17 describes schematically the principle of position sensitivity of long length scintillator and conditions to be fulfilled to achieve such a property. This approach works particularly well for a large aspect ratio (small cross section as compared to the length).

Such a light output distribution can be easily tested in the same way as it is for systematic quality control of HEP crystals. For 20 mm × 20 mm × 400 mm CsI(Tl) crystals with unpolished side surfaces, Fig. 2.18 shows characteristic pulse height spectrum with a ^{22}Na collimated source placed at different positions along the crystal.

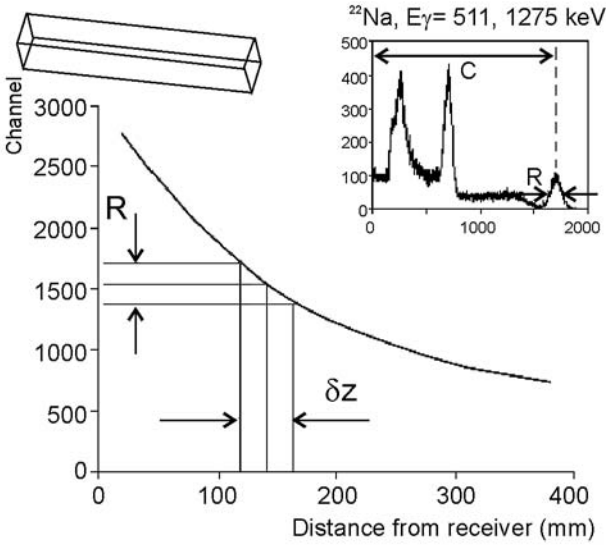

Fig. 2.17. Principle of position determination on a long scintillation crystal. The side surface of the detector is depolished to induce a strong light collection dependence on the emission point position. The accuracy of the position determination δz is defined by light yield c, the pulse height resolution R, and the slope of the curve at the point of interaction

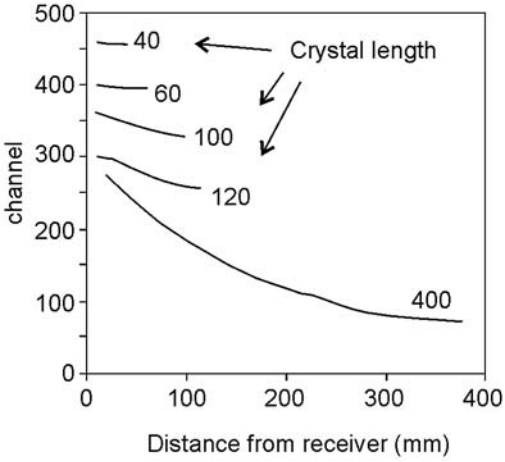

Fig. 2.18. Light yield distribution in scintillators of different lengths. Reflective properties of the detector surface, its coating, and parameters of signal amplification are kept unchanged, so comparison can be made. If detector shortens, average light yield becomes higher, the curve levels [85]

The position resolution values for detectors of different length have been calculated according to (2.3). The position of the collimated source of ionizing particles z can be determined by the measured value of the light yield c. The accuracy δz of the source position determination is defined by the value of the pulse height resolution (PHR) of the detector R and the slope α of function $c(z)$ at the point of measurement:

$$tg\alpha = \lim_{\triangle z \to 0} \frac{\triangle c}{\triangle z} \,, \qquad (2.3)$$
$$\delta_z = c\frac{R}{tg\alpha} \,.$$

To achieve a better position sensitivity, one needs to improve the light yield and energy resolution of the detector and to keep the $c(z)$distribution as steep as possible. These requirements are somewhat contradictory. In practice, a good determination of the position of the γ conversion point in a crystal results from a compromise between these parameters as a function of the state of the art for the light collection procedure.

The dependence of the position resolution on the detector length and position of the collimated source is shown in Fig. 2.19.

It is seen that the position resolution remains more or less constant over the whole volume of the detector when its length varies in the range 200 to 380 mm. Equation (2.3) can be rewritten in a form giving more physical sense to this phenomenon:

$$\delta z = \frac{R}{\ln c_z} \qquad (2.4)$$

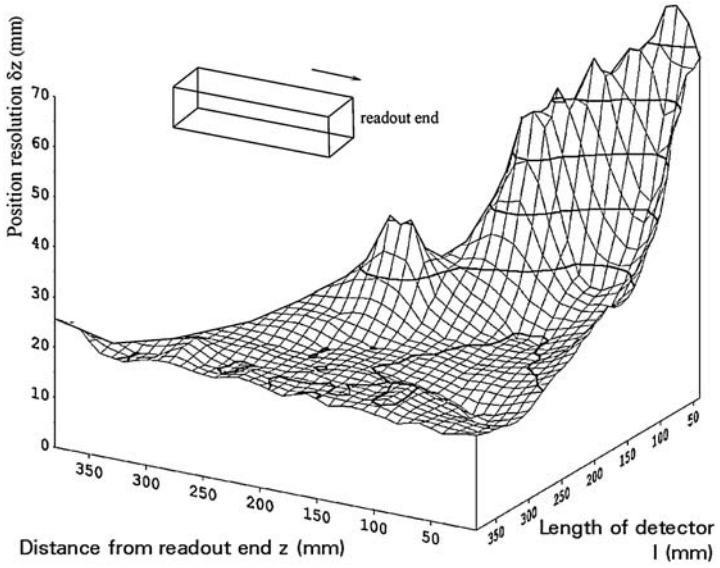

Fig. 2.19. Position resolution of detectors of different lengths from (2.3)

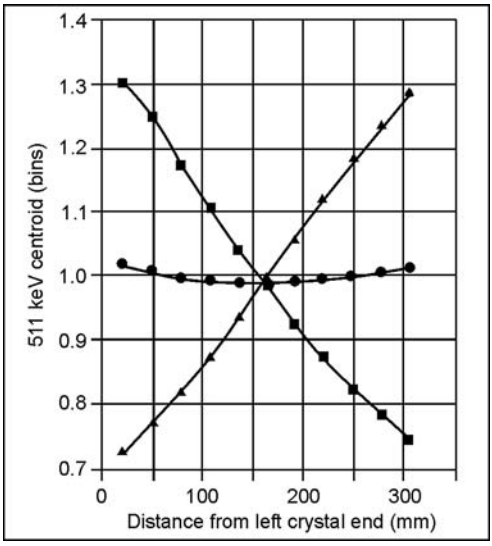

Fig. 2.20. CsI(Tl) crystal light output distribution for the GLAST gamma telescope assembly. Oblique curves show the typical light output distribution along the scintillator as seen from each end. The horizontal curve shows a good uniformity of the mean value within 5%

It was shown [89] that the optimal cross section/length ratio is 1:10 or less. But the total size of the detector is restricted by the attenuation factor K of the light propagating along the crystal. In the example given, $\exp(-l \cdot K) = 0.82$. As the scintillator becomes longer the need for a higher transparency increases.

The position resolution can be improved by combining signals from two photo-detectors coupled to opposite ends of the crystal. Figure 2.20 shows the light output distributions for the GLAST type position-sensitive detector [86].

Two position-dependent curves are obtained from the light distribution measurements from opposite ends of the crystal. The mean value is uniform within 5%.

There are more and more examples of crystal detectors used for astrophysics experiments and this trend should continue with the growing interest in γ-ray astrophysics.

References

1. Derenzo SE, Moses WW, Huesman RH, et al. (1993) Quantification of Brain Function:Tracer Kinetics and Image Analysis in Brain PET. Elsevier Science Publishers, Amsterdam, pp 25
2. L3 Collaboration, Adeva B et al. (1990) The construction of the L3 experiment. Nucl Instr Meth Phys Res A289: 35–102
3. Birks JB (1951) The specific fluorescence of anthracence and other organic materials. Proc Phys Soc (London) Letters to the Editor, pp 365–366. . . . . .
4. Hofstadter R (1948) Alkali halide scintillation counters. Phys Rev 74: 100–101
5. Oreglia et al. (1982) Study of the reaction psi → gamma gamma J / psi. Phys. Rev. D 25: 2295–2277
6. Kubota Y et al. (1991) The CleoII detector. CLNS 91/1122
7. Proton-Antiproton Annihilation and Meson Spectroscopy with the Crystal Barrel, C. Amsler, Rev. Mod. Phys. 70 (1998) 1293
8. Ray RE (1994) The KTeV Pure CsI Calorimeter. In: Proc. Fifth International Conference on Calorimetry in High-Energy Physics, World Scientific, New Jersey, pp 110–114
9. The Belle Collaboration, Technical Design Report, KEK Report 95-1, April 95
10. The BaBar Collaboration, BaBar Technical Design Report, SLAC-R-95-457
11. Novotny R, Riess R, Hingmann R et al. (1987) Detection of hard photons with BaF_2 scintillators. Nucl Instr Meth Phys Res A262: 340–346
12. GEM Letter of Intent, SSCL SR-1184, November 1991
13. CMS Technical Proposal, CERN/LHCC 94-38, December 1994
14. L3P Letter of Intent, CERN/LHCC 92-5 (1992)
15. ALICE Collaboration Technical Proposal, CERN/LHCC/95-71 (1995)
16. R&D Proposal for the study of new fast and radiation hard scintillators for calorimetry at LHC: Crystal Clear Collaboration, CERN / DRDC P27 / 91–15, project RD-18
17. Lecoq P, Li PJ, Rostaing B (1991) BGO radiation damage effects: optical absorption, thermoluminescence and thermoconductivity Nucl Instr Meth Phys Res A300: 240–258

18. Annenkov A, Auffray E, Borisevich A, et al. (1999 Suppression of the radiation damage in lead tungstate scintillation crystal. Nucl Instr Meth Phys Res A426: 486–490
19. Ilmas ER, Liidya GG, Lushchik Ch.B (1965) Photon multiplication in crystals. Optics Spectroscopy 18: 255–263 (In Russian)
20. Birks JB (1951) Scintillation from organic crystals: Specific fluorescence and relative response to different radiations. Proc Phys Soc A64: 874–877
21. Birks JB (1951) The Specific Fluorescence of Antracene and Other Organic Materials. Proc Phys Soc (London), Letters to the Editor, pp 364–365
22. Dorenbos P, de Haas JTM, van Eijk CWE (1995) Nonproportionality in the scintillation response and the energy resolution obtainable with scintillation crystals. IEEE Trans Nucl Sci 42: 2190–2202
23. Rooney BD, Valentine JD (1997) Scintillator light yield nonproportionality: calculating photon response using measured electron response. IEEE Trans Nucl Sci 44: 509–516
24. Pringle RW, Standil S (1950) The gamma-rays from neutron-activated gold. Phys Rev 80: 762–763
25. Aitken DW, Beron BL, Yenicay G, et al. (1967), The fluorescent response of NaI(Tl), CsI(Tl), CsI(Na), and CaF (Eu) to X-rays and low energy gamma rays, (1967) IEEE Trans Nucl Sci vol. NS-14, pp. 468–477
26. Rooney BD, Valentine J (1997) Scintillator light yield nonproportionality: calculating photon response using measured electron response. IEEE Trans Nucl Sci 44: 509–516
27. Uchiyama Y, Kouda M, Tanihata C et al. (2001) Study of energy response of $Gd_2SiO_5 : Ce^{3+}$scintillator for the ASTRO-E hard X-ray detector. IEEE Trans Nucl Sci 46: 379–384
28. Moses WW (2002) Current trends in scintillator detectors and materials . Nucl Instr Meth Phys Res A487: 123–128
29. Menghesha W, Taulbee TD, Rooney BD et al. (1998) Light yield nonproportionality of CsI(Tl), CsI(Na), and YAP. IEEE Trans Nucl Sci 45: 456–641
30. Menghesha W, Valentine JD (2000) A technique for measuring scintillator electron energy resolution using the compton coincidence technique. In: Mikhailin VV (ed) Proc of the Fifth Int Conf on Inorganic Scintillators and Their Applications, SCINT99. Moscow State University, Moscow, pp 173–178
31. Balcerzyk M, Moszynski M, Kapusta M (2000) Energy resolution of contemporary scintillators. Quest for high resolution, proportional detector. In: Mikhailin VV (ed) Proc of the Fifth Int Conf on Inorganic Scintillators and Their Applications, SCINT99. Moscow State University, Moscow, pp 167–172
32. Balcerzyk M, Klamra W, Moszynski M, et al. (2000) Nonproportionality and temporal response of ZnSe:Te scintillator studied by large area avalanche photodiodes and photomultipliers. In: Mikhailin VV (ed) Proc of the Fifth Int Conf on Inorganic Scintillators and Their Applications, SCINT99. Moscow State University, Moscow, pp 571–576
33. Baryshevsky VG, Korzhik MV, Moroz VI et al(1991) $YAlO_3$:Ce—fast-acting scintillators for detection of ionizing radiation. Nucl Instr Meth Phys Res B58: 291–293
34. Korzhik MV, Misevich OV, Fyodorov AA (1999) $YAlO_3$:Ce scintillators: application for X- and soft γ-ray detection. Nucl Instr Meth Phys Res B72: 499–501
35. Baryshevsky VG, Korzhik MV, MorozVI, et al. (1992) YAlO3:Ce scintillator for the detectors of ionizing radiation. IET, 3:86–92 (In Russian)

36. Baryshevski VG, Korzhik MV, Bogatko AV, et al. (1992) Scintillator YAlO3:Ce3+ for the α-particles spectrometry. Izvestia AN BSSR, Physics 2:5 (In Russian)
37. Kachanov VA, Rykalin V, Korzhik M, et al. (1992) Light source for energy stabilization of calorimetric detectors based on photodetectors. Nucl Instr Meth Phys Res A314: 215
38. Drobyshev GYu, Korzhik MV, Missevitch OV, et al. (1993) An application of YAlO3:Ce scintillator to detect soft γ-quanta. IET 3: 176 (In Russian)
39. De Notaristefani F, Pani R, Scopinaro F, et al. (1995) First results from a YAP:Ce gamma camera for small animal studies IEEE Trans. Nucl. Sci. 43, 3264–3271
40. Korzhik M, Missevitch O, Kholmetskii AL, et al. (1994) YAlO3:Ce scintillation detector for transmission Mossbauer spectroscopy. 4-th Seeheim workshop on Mossbauer spectroscopy Abstracts Seeheim, Germany Institute fur Anorganische und Analiytiche Chemie, der Jogannes Gutenberg Universitat, Mainz, p 126
41. Fedorov AA, Kholmetskii AL, Korzhik M, et al. (1994) High-performance transmission Mossbauer spectroscopy with YALO3:Ce scintillation detector. Nucl Instr Meth Phys Res B88: 462–464
42. Kobayashi M, Shinkawa T, Sato T et al. (1994) YALO3:Ce-Am light pulsers as a gain monitor for undoped CsI detectors in a magnetic field. Nucl Instr Meth Phys Res A337:355–361
43. Missevich Increase of the productivity and precision of Mossbauer measurments in transmission and scattering geometry. Ph.D. Thesis. Minsk, 2000, p. 150 (In Russian)
44. Moszynski M (2003) Inorganic scintillation detectors in γ-rays spectrometry. Nucl Instr Meth Phys Res A505: 101–110
45. Globys ME, Grinev BV (2000) Inorganic scintillators. New and traditional materials. Acta, Kharkov (in Russian)
46. Anger HO (1958) Anger camera for Nuclear Medicine. Rev Sci Instr 29:p27–45
47. Moses WW (2000) Scintillator requirements for medical imaging In: Mikhailin VV (ed) Proc of the Fifth Int Conf on Inorganic Scintillators and Their Applications, SCINT99. Moscow State University, Moscow, pp 11–21
48. Blasse G (1994), Scintillator materials, Chem Mater, 6:1465–1475
49. Greshkovich C, Duclos S (1997), Ceramic Scintillators, Annu Rev Mater Sci 27: 69–88
50. Deych D, Dobbs J, Marcovici S, Tuval B (1996) Cadmium tungstate detector for computed temograhy. In: Dorenbos P, van Eijk CWE (eds). Inorganic scintillators and their application. Delft University Press, pp 36–39
51. Kinloch DR, Novak W, Raby P, Toepke I (1994) New developments in cadmium tungstate. IEEE Trans. Nucl. Sci, 41: 752–754
52. Yoshida M, Suzuki A, Uchida Y et al. (1988), Application of Gd_2O_2S ceramic scintillator for X-ray solid state detector in X-ray CT, Jpn J. Appl. Phys, 27:L1572-L1575
53. Rossner W, Grabmaier BC (1991) Phosphors for X-ray detectors in computed tomography. J Luminescence 48–49:29–36
54. Kostler W, Winnacker A, Rossner W, Grabmaier BC (1993), Effect of Prcodoping on the X-ray induced afterglow of $(Y,Gd)_2O_3$:Eu, J Phys Chem Solids 56: 907–913

55. Levin CS, Habte F, Foudray A (2004) Methods to extract more light from minute scintillation crystals used in an ultra-high resolution positron emission tomography detector, Nucl Instr Meth Phys Res A527:35–40
56. Wieczorek H, Frings G, Quadfield P, et al. (1995) CsI:Tl for solid state X-ray detectors, Proc. In Dorenbos P, van Eijk CWE (eds). Inorganic Scintillators and Their Applications, Delft University Press, 547–554
57. Gyueseong Cho, Kyung Soo Lee, Do Kyung Kim, Koan Sik Joo, Annealing effect on optical emission properties of pure and Na doped CsI thin films for X-ray radiographic application, In: Mikhailin VV (ed). Proc of the Fifth Int Conf on Inorganic Scintillators and Their Applications, SCINT99. Moscow State University, Moscow, pp 391–397
58. Van Eijk CWE (2002) Inorganic scintillators medical imaging. Phys Med Biol, 47:R85–R106
59. Blasse G, Grabmaier BC (1994), Luminescent Materails, Springer, Berlin, pp 84–162
60. Sonoda M, Takano M, Miyahara J, Kato H (1983), Computed radiography utilizing scanning laser stimulated luminescence, Radiology 148: 833–838
61. Roques JP, Paul J, Mandrou P, et al. (1990) The sigma mission on the granat satellite, Adv Space Res, 10:223–232
62. Patent PCT W001/60944
63. Patent PCT W001/60945
64. a. Fernandez MM, Benlloch JM, Cerda J, et al. (2004) A flat-panel–based mini gamma camera for lymph nodes studies. Nucl Instr Meth Phys Res, A527: 92–96

    b. Benlloch JM, Escat B, Fernández M, et al. (2003) Performance tests of a medical mini gamma-camera (summary). Nucl Instr Meth Phys Res, A504: 232–233
65. Weisenberger AG, Bradley E, Majewski S, Saha M, (1998) Development of a novel radiation imaging detector system for in vivo gene imaging in small animal studies. IEEE Trans Nucl Sci, NS-145(3):1743–1749
66. Giokaris N, Loudos G, Maintas D, et al. (2004) Crystal and collimator optimization studies of a high-resolution γ-camera based on a position sensitive photomultiplier. Nucl Instr Meth, A527: 134–139
67. Gektin AV, Gavryluk V, Boyarintsev AYu, Gayshan V (2003), Light spread function control for SPECT/PET systems, In: Second ITBS Conference, Milos, 26-30 May 2003 (abstracts), p 39
68. Bull U, Bartenstein P, Kirsch CM, Schicha H (2000) Combination systems for SPECT, coincidence, PET and CT. Technical spectrum, operating assumptions and possible areas of application, Nuklearmedizin, 39(1): 3–6.
69. Delbeke, D, Martin, WH, Patton, JA, Sandler, MP (2001) Value of iterative reconstruction, attenuation correction, and image fusion in the interpretation of FDG PET images with an integrated dual-head coincidence camera and X-ray-based attenuation maps, Radiology, 218(1): 163–71
70. Patent France 2,237,206
71. Patton JA, Delbeke D, Sandler MP (2000) Image fusion using an integrated, dual-head coincidence camera with X-ray tube-based attenuation maps, J Nucl Med, 41(8): 1364–1368
72. McElroy DP, Sung-Cheng Huang, Hoffman EJ (2002) The use of retro-reflective tape for improving spatial resolution of scintillation detectors, IEEE Trans Nucl Sci, 49: 165–171

73. Ricard M (2004) Imaging of gamma emitters using scintillation cameras. Nucl Instr Meth Phys Res, A527: 124–129
74. Trower WP, Korzhik MV, Fyodorov AA, et al. (1996) Cerium-doped lutetium-based single crystal scintillators. In: Dorenbos P, van Eijk CWE (eds). Inorganic scintillators and their application. Delft University Press, pp 355–358
75. Womble PC, Schultz FJ, Vourvopoulos G (1995) Nondestructive characterization using pulsed fast-thermal neutrons. Nucl Instr Meth Phys Res, B99: 757–760
76. Dean AJ (1992) Imaging is high-energy astronomy. In: DeNotaristefani F, Lecoq P, Schneegans M (eds). Heavy scintillators for scientific and industrial applications. Frontieres, France, pp 53–64
77. INTEGRAL Assessment Study Report. (1991) ESA Publication ESA SCI 91, pp 1–31
78. Ubertini P, Cocco GD, Lebrun F (1997), The IBIS Telescope on Board INTEGRAL, Proc. of the Second INTEGRAL Workshop, ESA SP-382, pp 599
79. a. Barbiellini G, Boezio M, Casolino M, et al. (1991) The GILDA mission: a new techniques for gamma-ray telescope in the energy range 20 MeV – 100 GeV. http://ifctr.mi.cnr.it/agile
b. Mergeletti S, Barbiellini G, Budini, et al. (1999) GeV-TeV gamma-ray Astrophysics. Workshop "Towards a Major Atmospheric Cerenkov Detector VI." Snowbird, Utah, pp 11–23
80. http://cossc.gsfc.nasa.gov/
81. Johnson WN, Grove JE, Phlips BF, et al. (2001) The construction and performance of the CsI hodoscopic calorimeter for the GLAST beam test engineering module. IEEE Trans Nucl Sci, 48: 1182–1189
82. Atwood WB, Ritz S, Anthony P et al. (2000) Beam test of gamma-ray large area space telescope components, Nucl. Instr. Meth. A446: 444–460
83. Shwarz B (2000) Electromagnetic calorimeter of the BELLE detector. In: Mikhailin VV (ed) Proc of the Fifth Int Conf on Inorganic Scintillators and Their Applications, SCINT99. Moscow State University, Moscow, pp 186–190
84. BaBar Collaboration. BaBar Technical Design Report, SLAC-R-95-457
85. Gektin AV, Gavrylyk V, Zosim D (2000), Long length scintillators for the Position-Sensitive Radiation Detectors, IEEE NSS/MIC. Abstracts, p. 263
86. Gektin AV, Zosim D., Boyarintsev AY, et al. (2004), Long position sensitive CsI(Tl) detectors for the GLAST project, IEEE Nuclear Science Symposium and Medical Imaging Conference, Abstracts, N16-7, p 45
87. Dorenbos P, Contribution to the SCINT05 conference on scintillators and their industrial applications, Alushta, Ukraine, Sept. 2005

3 Scintillation Mechanisms in Inorganic Scintillators

Abstract. Details of energy transfer phenomena and scintillation mechanisms in luminescent media excited by ionizing radiation are discussed in this chapter. The sequence of relaxation of electronic excitations is described: creation of electron-hole pairs, energy transfer to emitting centers of interest and quantum efficiency of these luminescent centers. The theoretical limit of the light yield is usually much higher than the experimental one. The limiting factors at each step of relaxation are considered in self-activated, doped and cross-luminescent scintillation materials. The final stage of luminescent center excitation mechanism in scintillators has a strong influence on the scintillation parameters. It is discussed in detail here. Finally, different examples are given of charge transfer and non-radiative relaxation processes of the scintillating centers through their coupling with the crystal lattice.

3.1 Introduction: How to Answer High Light Yield, Short Decay Time, and Good Energy Resolution

The demand for new and better scintillating materials is very strong for many kinds of applications. Of course, there is no unique best scintillator. Depending on the particular requirements of the application considered, different scintillators would be preferred.

Among the desirable properties of a good scintillator, high efficiency, fast scintillation, and good energy resolution are of most importance in a number of cases.

As it will be demonstrated in the next paragraphs, the light yield depends on many parameters that play a role in the three stages of relaxation of electronic excitations: creation of electron–hole pairs, energy transfer to emitting centers of interest, and quantum efficiency of these centers. The theoretical limit of the light yield is usually much higher than the experimental one. The optimization of scintillators in terms of light efficiency will consist to play with these parameters, which strongly influence the scintillation process.

The scintillation kinetics depends essentially on the energy transfer and the nature of the luminescence centers. In doped materials, the choice for the dopant ion determines the range of time response of the scintillator. For nanosecond time scale response, only few ions are of interest, those exhibiting parity-allowed emission transitions like $5d$–$4f$ transitions of rare-earth ions. Intrinsic fluorescence centers can also exhibit fast fluorescence.

The energy resolution R is the ability for a scintillator to distinguish radiations of slightly different energies. It is usually described as a function of different contributions:

$$R^2 = R_{\mathrm{np}}^2 + R_{\mathrm{inh}}^2 + R_{\mathrm{tr}}^2 + R_{\mathrm{lim}}^2$$

R_{np} is a factor of nonproportionality, which accounts to the fact that in some scintillators, the number of emitted photons is not proportional to the incident energy. Then, secondary electronic excitations of various energies lead to a distribution of light yields, which increases the energy resolution. R_{inh} is related to the inhomogeneity of the crystal, inducing local variations of the light efficiency. R_{tr} is related to the efficiency of the light collection by the detector (usually a photomultiplier PM). R_{lim} is the intrinsic resolution of the detector, described by the well-known Poisson law.

$$R_{\mathrm{lim}} = 2.35\sqrt{\frac{1 + v\,(\mathrm{PM})}{N_{\mathrm{phe}}}}\ ,$$

where $v(PM)$ is the variance of the photomultiplier gain and N_{phe} is the number of photoelectrons emitted by the *PM*.

For an ideal scintillator, the first three contributions are negligible and R_{lim} gives the energy resolution. The light yield being proportional to N_{phe}, a good energy resolution, requires a high light yield.

In many cases, the energy resolution R is actually larger than the theoretical limit R_{lim}. The inhomogeneity of the crystal can be reduced and often cancelled by improving the crystal growth conditions and the light collection can be improved as well. On the other hand, the nonproportionality is a puzzling problem, much more difficult to solve because its origin is not well understood yet. For example, while known scintillators such as cerium-doped orthoaluminates or lanthanum halides compounds exhibit a weak nonproportionality, cerium-doped silicates are strongly "nonproportional." It seems that the structure more than the composition of the crystal may influence the nonproportional behavior.

3.2 Relaxation of Electronic Excitations

Relaxation of electronic excitations involves complex mechanisms. A description of multiplication and thermalization processes has been proposed by different authors using various models (see recent reviews [1–3] and references therein). The purpose here is not to go into the details of phenomenological models, nor to discuss their merit but rather to use simple schemes of relaxation of electronic excitations deduced from simulations and which account qualitatively for the energy distribution and space correlation of excitations. These schemes, first proposed by Vasil'ev, use the band structure of the material. They provide a pedagogical description of the various steps of relaxation

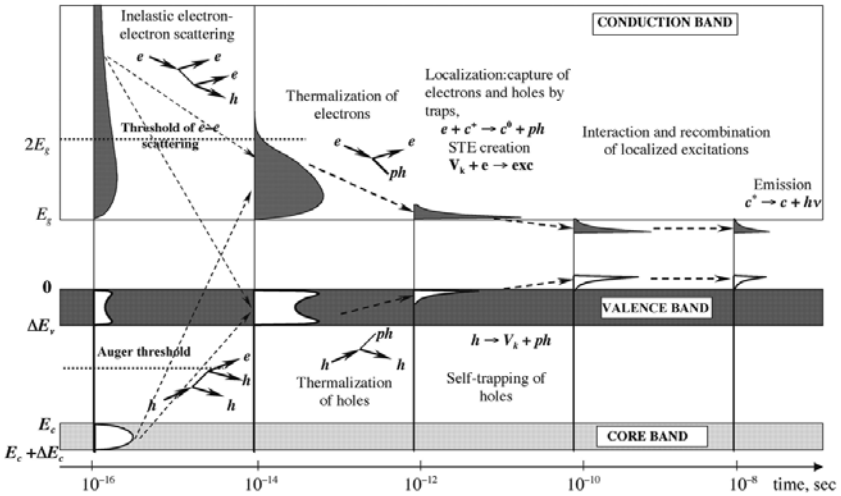

Fig. 3.1. General scheme of relaxation of electronic excitations in an insulator with two channels of relaxation. e for electrons, h for holes, ph for phonons, hν for photons, V_{k} for self-trapped holes, c_i^n for ionic centers with charge n

from the primary high-energy excitation to final process of light emission by luminescent centers.

A general scheme is represented in Fig. 3.1. For simplicity, only one core band is represented with top energy E_{c} and bandwidth ΔE_{c}. The valence band (top energy $E_{\mathrm{v}} = 0$ and bandwidth ΔE_{v}) and the conduction band (bottom energy E_{g}) are separated by the forbidden band of the insulator (band gap width E_{g}). Five main stages can be considered.

The first one starts with the production of primary excitations by interaction of ionizing particles with the material. For very high incident particle energy, the excitations are essentially deep holes h created in inner-core bands and hot electrons e in the conduction band. Then, in a very short time scale ($10^{-16} - 10^{-14}$s), a large number of secondary electronic excitations are produced through inelastic electron–electron scattering and Auger processes with creation of electrons in the conduction band and holes in core and valence bands. At the end of this stage, the multiplication of excitations is stopped. All electrons in the conduction band have an energy smaller than $2E_{\mathrm{g}}$ (e–e scattering threshold) and all holes occupy the valence band if there is no core band lying above the Auger process threshold (general case).

The second stage is thermalization of electronic excitations with production of phonons, leading to low kinetic energy electrons in the bottom of the conduction band and of holes in the top of the valence band.

The next stage is characterized by the localization of the excitations through their interaction with stable defects and impurities of the material. For example, electrons and holes can be captured by different traps or

self-trapped in the crystal lattice. Excitons, self-trapped excitons, and self-trapped holes (V_K centers) can be formed with emission of phonons. Localization of excitations can be sometimes accompanied by displacements of atoms (defect creation, photostimulated desorption).

The two last steps are related with migration of relaxed excitations and radiative and/or nonradiative recombination. It is important to consider the interaction between excitations themselves, which can result in the decrease of the number of excitations. This point, which will be discussed later in the next paragraph, is responsible for density effects, nonproportionality of energy response of scintillator, and nonexponential decay kinetics. The very last stage describes the luminescence of emitting centers excited by the final electronic excitations (correlated electron–hole pairs, excitons, separated electrons, holes, etc.) through sequential capture of charge carriers or various energy transfers.

The general scheme of Fig. 3.1 describes the scintillation mechanisms in the case of ionic crystals with simple energy structure. However, important groups of scintillators exhibit a more complicated band structure.

It is, in particular, the case of crystals containing rare earth. For example, in cerium-based or cerium-doped compounds, cerium $4f$ and $5d$ levels fall within the forbidden energy band gap. They must be involved in the scheme of relaxation of electronic excitations because they may play an important role in the scintillation processes (Fig. 3.2). Indeed, rare-earth ions (RE) can be directly excited through impact excitation provided that their concentration is large (it is particularly true for fully concentrated rare-earth compounds). But this excitation is efficient only by electrons with kinetic energies above

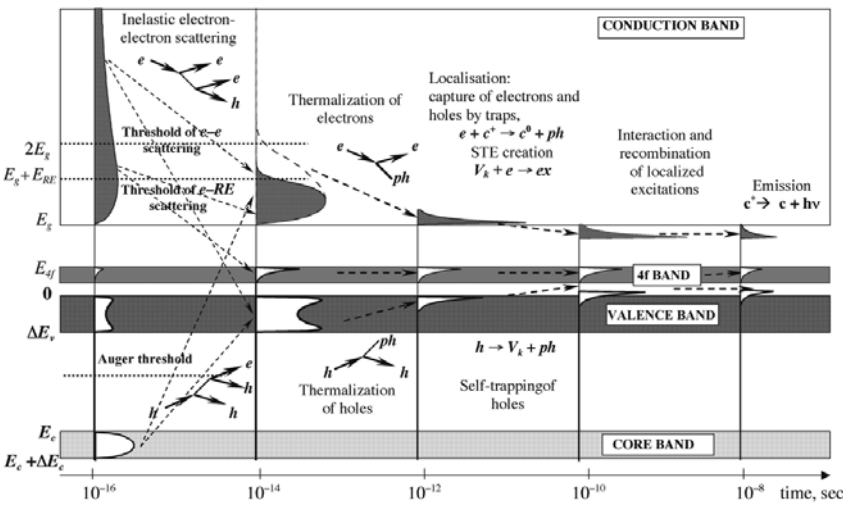

Fig. 3.2. Scheme of relaxation of electronic excitations in rare earth containing crystals

the threshold of e–RE scattering and below the threshold of e–e scattering. In this case, the production of electron–hole pairs with holes in the valence band is not possible. When this process occurs, it is strongly dominant since the density of states in the valence band is much higher than that in rare-earth bands.

This additional pathway of excitation for rare-earth luminescent ions is not detrimental to the creation of electron–hole pairs since it involves electrons with kinetic energy lower than the threshold of e–e scattering and which cannot produce more electronic excitations. Therefore, it would be expected a high light yield for rare-earth crystal scintillators.

Actually, it is not so simple because other factors must be taken into account which can limit the scintillation efficiency and which will be analyzed later.

Cross-luminescent materials belong to another class of scintillators. The mechanisms will be described in more details in the next paragraph. In the scheme of the relaxation of electronic excitations of cross-luminescent systems for which core-valence transition is responsible for a fast subnanosecond luminescence (archetype: BaF_2 with 5pBa as outermost core band), the outermost core band, lying less than $2E_g$ below the bottom of the conduction band, must be taken into account in the representation of the electronic structure (Fig. 3.3). In the first stage is represented the threshold of e–e scattering with production of outermost core band holes ch, at higher energy than that of e–e scattering with production of valence band holes h and anion excitons. At the end of this stage coexist two types of holes since ch cannot relax into the valence band through Auger effect, which is energetically forbidden. After thermalization, localization and eventually interaction of excitations, ch

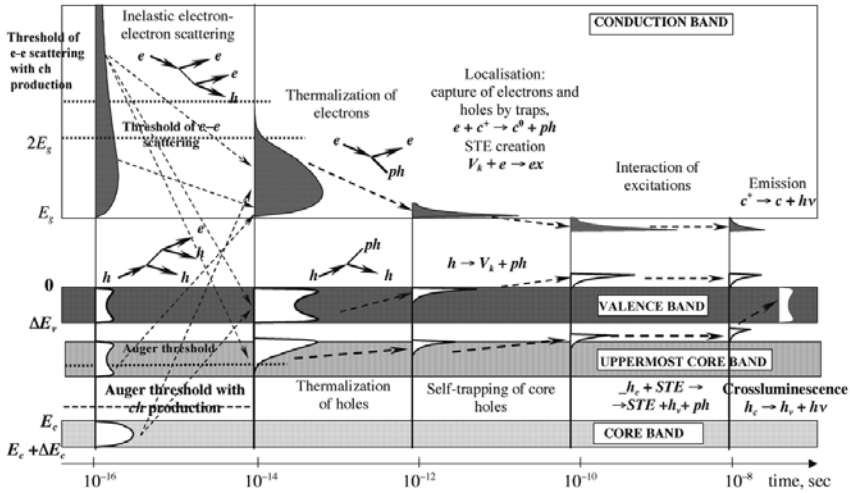

Fig. 3.3. Scheme of relaxation of electronic excitations in cross-luminescent crystals

and h, and self-trapped anion exciton STE can coexist during a relatively long period. In the last stage, only core band holes ch are responsible for cross-luminescence.

3.3 Limiting Factors at Each Step of the Energy Relaxation

The formula for light yield Y mentioned in Chap. 2 also may be expressed as the product of three factors [1, 4]:

$$Y = N_{\mathrm{eh}} S Q \tag{3.1}$$

N_{eh} is the conversion efficiency expressed as a number of electron–hole pairs or excitons, S is the probability of transfer to emitting centers, and Q is the luminescence quantum yield.

These three processes can be considered as successive events, which can be related to the different stages of relaxation of electronic excitations previously described in Sect. 3.2. Let us consider the factors, which limit the scintillator light, yield at each of these three processes.

3.3.1 Creation of Electronic Excitations

Electronic excitations, which are potentially available in the scintillator as donors in the transfer process to luminescence centers, are produced during the first two stages described in Figs. 3.1–3.3: multiplication and thermalization stages.

$\mathrm{N_{eh}}$ is usually expressed via the average energy $\mathrm{E_{eh}}$ required for the creation of a thermalized e–h pair. Considering $\mathrm{E_{inc}}$ as the energy deposited by an ionizing particle, we have

$$N_{\mathrm{eh}} = \frac{E_{\mathrm{inc}}}{E_{\mathrm{eh}}} \tag{3.2}$$

The first estimations of E_{eh} around (2–3)E_{g}, E_{g} being the forbidden energy band gap, were made quite some time ago [5,6]. It is therefore obvious that the parameter, which limits the production of electron–hole pairs and excitons, is E_{g}; the larger it is, the lower is N_{eh}.

It should be noted that N_{eh} is a relevant factor only in the case of a simple insulator such as that described in Fig. 3.1. But in crystals with more complicated electronic structure, additional types of excitations can be created, or/and all the electron–hole pairs and excitons are not useful excitations leading to scintillation. For these systems, the light yield η predicted by formula (3.1) deduced from empirical models is usually much larger than the experimentally observed scintillation yield.

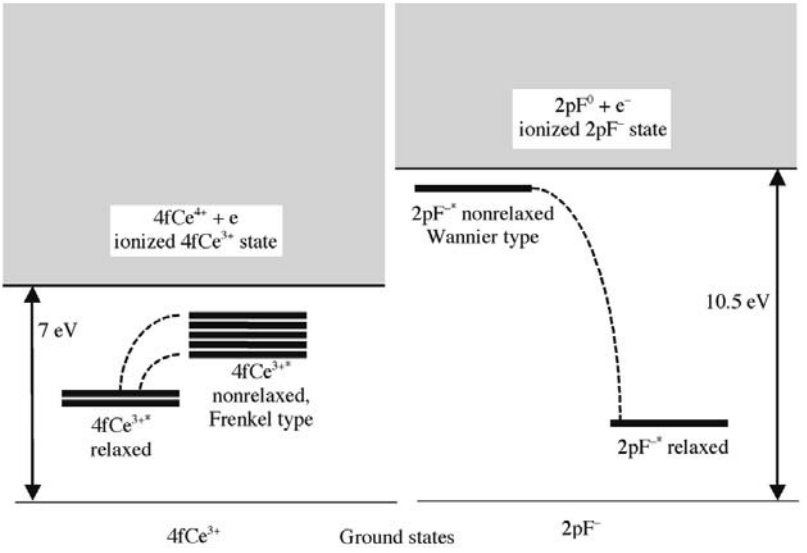

Fig. 3.4. Simplified scheme of coexistence of two types of excitons in cerium fluoride

3.3.1.1 Case of Cerium Compounds

CeF_3 is a model system for analyzing the scintillation mechanisms in ionic crystals and many studies have been devoted to this scintillator (see, for example, [3, 7–22]).

In cerium compounds, cerium $4f$ levels fall within the forbidden band-gap. As a result, two types of excitons can be formed: Ce Frenkel excitons and anion Wannier exciton. A simplified scheme (Fig. 3.4) shows that rare-earth ion excitation is not efficient through energy transfer from anion exciton as well as through sequential capture of holes and electrons by Ce^{3+} ions as demonstrated later in Subsect. 3.3.2.1.

"Useful" excitations can be produced only through impact excitation and only by electrons with kinetic energies in a narrow band between the two thresholds of e–e scattering and of e-RE scattering (Fig. 3.2). For such system, it is clear that the number of scintillation-active excitations cannot be estimated by expression (3.1). In fact, the number of useful excitations is reduced by a factor of around 5 in CeF_3. This fact partially explains the relatively low yield of CeF_3.

3.3.1.2 Case of Scintillators with Core-Valence Transitions

Systems with high-lying outermost core bands can give rise to so-called cross-luminescence involving core-valence transitions [23]. For example, in the case of BaF_2, a Ba^{2+} 5p core hole can decay only radiatively and not via an Auger process. Cross-luminescence is very sensitive to track effects [24–27].

Therefore, the scintillation efficiency can be calculated using expression (3.1) only if the conversion efficiency is expressed as the number of Ba^{2+} 2p core holes rather than as the total number of excitations [22].

3.3.2 Transfer to Luminescence Centers

This process involves the third and fourth stages of relaxation of electronic excitations described previously in Figs. 3.1–3.3. It is a very critical part of the scintillation mechanism since electron–hole pairs or excitons can be affected by many events during their migration and before they interact with luminescence centers, and can result in nonradiative recombination. This can limit the number of effective donors in the energy transfer processes to the acceptors and substantially change as well as the time dependence of the scintillation.

3.3.2.1 Limitation in Charge Carriers Capture Probability

When donors are electron–hole pairs, the usual channel of excitation for acceptors is a charge transfer process with a sequential capture of charge carriers. For scintillators with high light yield, the capture efficiency must be high. It is, for example, the case of Na- and Tl-doped CsI crystals for which the scintillation emission originates from perturbed or impurity-trapped exciton centers, which are efficiently excited because of the enhanced cross section for electron, capture at Tl^+ and Na^+ impurities [28, 29]. In Ce^{3+}-doped or based-crystals, the hole is first captured and its capture probability strongly depends on the position of the Ce $4f$ level in the forbidden band gap. In cerium-doped oxides and halides, Ce $4f$ level is usually lying very low in the gap close to the top of the valence band [16], and these systems can lead to very efficient scintillation (LSO, LuAP, $LaCl_3$, etc.). On the other hand, Ce^{3+}-doped fluoride crystals cannot exhibit very high light yield because Ce 4f is lying around 3–4 eV above the valence band [16] and the hole capture probability is low. It should be noted that in CeF_3, the Auger cascade over Ce core levels is terminated by the transfer of the hole to the fluoride valence band because the probability of the forbidden Auger transition Ce 4p–Ce $4f$ is very low [3]. It was shown before that the main channel of Ce excitation is through impact by electrons. Excitons can transfer their energy to luminescence centers as well. The dominant process is then nonradiative energy transfer.

3.3.2.2 Specific Killer Ions

The presence of specific ions with active luminescent centers is sometimes undesirable and incompatible with the emission of intense scintillation. These ions can exist as impurities or be constituent of the material. In the case of

impurities, their nature and concentration depend on the purity of starting materials and/or the techniques used for the crystal elaboration. They can compete with active ions for the capture of charge carriers and/or interact with them, and induce severe limitations in scintillation efficiency.

For example, in cerium-doped or cerium-based crystals, in general, the presence of ions with two or more stable valences is harmful. It is due to the fact that cerium itself has two stable valence states Ce^{3+} and Ce^{4+} and can exchange electrons through a metal–metal charge resulting to mutual quenching transfer process. Ce-doped tungstates and vanadates do not exhibit cerium scintillation because of Ce-W and Ce-V interaction of this type [30].

It is known that simultaneous presence of Yb and Ce leads to their mutual fluorescence quenching [31, 32]. Ce^{3+} is a good hole trap and Yb^{3+} a good electron trap. It is a consequence of a particular stability of empty Ce^{4+} $4f$ shell and of totally filled Yb^{2+} 4f shell. In the presence of electron–hole pairs, the initial state (Ce^{3+} Yb^{3+}), after capture of holes by Ce^{3+} and electrons by Yb^{3+} pass by an intermediate (Ce^{4+} Yb^{2+}) excited state and after relaxation and tunnel electron exchange, returns nonradiatively to the initial state.

Quenching of the same type can occur for other couples such as Ce^{3+} + Eu $^{3+}$, Ce^{3+} + nitrate, and Ce^{3+} + carboxylate ([33] and references therein).

Recently, a new very promising scintillator was discovered: cerium-doped lutetium pyrosilicate crystal (LPS) $Lu_2Si_2O_7$:Ce [34]. This material exhibits a very high light yield when it is grown by the melting zone technique, while its scintillation is absent or very weak when it is elaborated by the Czochralski method. From EPR measurement, it was shown that the quenching of Ce fluorescence is due to the presence of Ir^{4+} impurity ions introduced by the crucible [35]. The mechanisms of quenching have not been elucidated yet, but it could be related to a charge transfer process between Ce^{3+} and Ir^{4+} ions.

In cerium-doped systems, Ce^{3+} and Ce^{4+} centers can coexist. Ce^{4+} has no electron in the $4f$ shell, but can be excited through a charge transfer process after capture of an electron from the valence band. The charge transfer state ($Ce^{3+} + h_v$) relaxes nonradiatively to the ground state. The presence of Ce^{4+} nonradiative recombination centers must be avoided in Ce-doped scintillators. In the case of fluorides, crystal growth under vacuum in reducing atmosphere is a solution to eliminate Ce^{4+} ions. In oxides, when it is possible, annealing in reducing atmosphere can be used. Co-doping with 4+ ions can give good results as well.

3.3.2.3 Self-Trapping, Trapping, Creation of Defects

Self-trapping is a very frequent process in insulating materials. For example, self-trapping holes, so-called V_K centers, can be formed, leading to a decorrelation of electrons and holes. Recombination of electrons with mobile V_K centers [$V_K + e^-$] close to luminescent centers can excite them. Self-trapped excitons (STE) can be formed as well directly from electron–hole

pairs or by trapping electrons in the V_K centers. STE can exhibit luminescence and transfer its energy to luminescent centers. Self-trapping is an intrinsic property of materials. It can strongly influence the efficiency and the time dependence of the scintillation. To interpret the scintillation properties of cerium-doped $LaCl_3$, $LuBr_3$, and $LuCl_3$, O. Guillot-Noël et al. [36] proposed a model involving three different mechanisms which correspond to three different energy transfer processes and which appear at different time ranges: very fast energy transfer by direct correlated electron–hole capture on Ce^{3+}, fast energy transfer by binary electron–hole recombination ($[V_K + e^-]$ on Ce^{3+}) and slower energy transfer by diffusion of STE. They were able to evaluate the relative contribution of the mechanisms through the analysis of the scintillation decay profiles and of the X-ray–induced emission spectra. Their model works well in the case of Ce-doped LaF_3. For the other systems, the temperature dependence of the total yield cannot be explained at low temperature where it is observed a strong quenching. This quenching is probably due to trapping effect, which was not taken into account in their model.

Indeed, some of the electrons and holes can be trapped at more or less deep trapping levels and cannot excite directly luminescent centers through sequential capture but eventually indirectly after releasing from the traps. As a result, a strong luminescent quenching and very long components in the fluorescence decays can be observed in the temperature region of glow peaks. It has been demonstrated that this quenching phenomenon occurs for the X-ray–excited charge transfer luminescence of ytterbium containing aluminum garnets [37, 38].

3.3.2.4 Interaction of Excitations

It was shown through the study of a number of crystals excited by photons of high energy (VUV and X-excitations) using synchrotron radiation that the relaxation of primary electron and hole in a crystal leads in general to the formation of nanometric scale regions containing several electronic excitations separated by short distances. The interaction between closely spaced electronic excitations may lead to luminescence quenching so-called local density–induced quenching [12, 24, 39, 40].

Examples of interactions between closely spaced electronic excitations in an insulator are illustrated in Fig. 3.5. They all produce emission of phonons. An exciton may disappear after interaction with a close low-energy electron e or hole h (processes 1 and 2), a core hole c may interact with a low-energy electron through dipole–dipole or Fano process and low-energy electron and hole are formed (mechanisms 3 and 4), interaction of a core hole with a valence band hole may lead to two valence band holes (mechanism 5). If two excitons interact, one may disappear and the other one may gain energy and reach a higher excited state or disintegrate into an electron–hole pair. Finally, the electron–hole pair can be bound into an exciton again or the components

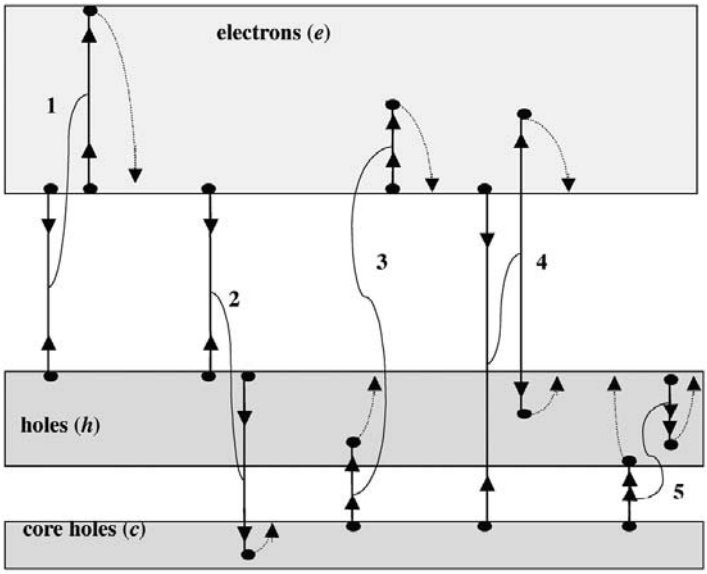

Fig. 3.5. Possible interactions between closely spaced electronic excitations in an insulator. Arrows pointing toward each other show recombination processes, in opposite direction: creation of electronic excitations, in the same direction: increase in the electronic excitation energy. Thin curves denote the interaction, and dotted arrows: electronic excitation thermalization

can decay independently. It should be noted that interaction can be not only of dipole–dipole type, but of other types such as exchange, tunneling, Fano, etc., which strongly depend on the excitations distance and are controlled by the overlap of wave functions of the interacting particles. For dipole–dipole interaction, the interaction radius is 1 to 5 nm; for other types of interaction, it is less than 1 nm.

For electronic excitations created in different events of photon absorption, the probability to be created at such short distances is very low for nonlaser densities of excitation. On the contrary, secondary electronic excitations created by inelastic scattering of photoelectrons or Auger decay of core holes can be quite closely spaced. The process is illustrated in Fig. 3.6. The hot electron relaxes through inelastic electron–electron scattering with creation of secondary excitations. The spatial distribution of such excitations is governed by the diffusion length, which depends on the hot electron energy according to a nonmonotonous function. It is therefore possible to obtain a nonuniform spatial distribution of electronic excitations. The core holes relax according to the Auger mechanism, but in this case, the excited regions are much smaller because the mobility of holes is much smaller in insulating materials. Figure 3.6 shows regions of different sizes (typically 1–5 nm) containing several (4–7) electronic excitations. In these clusters of high local

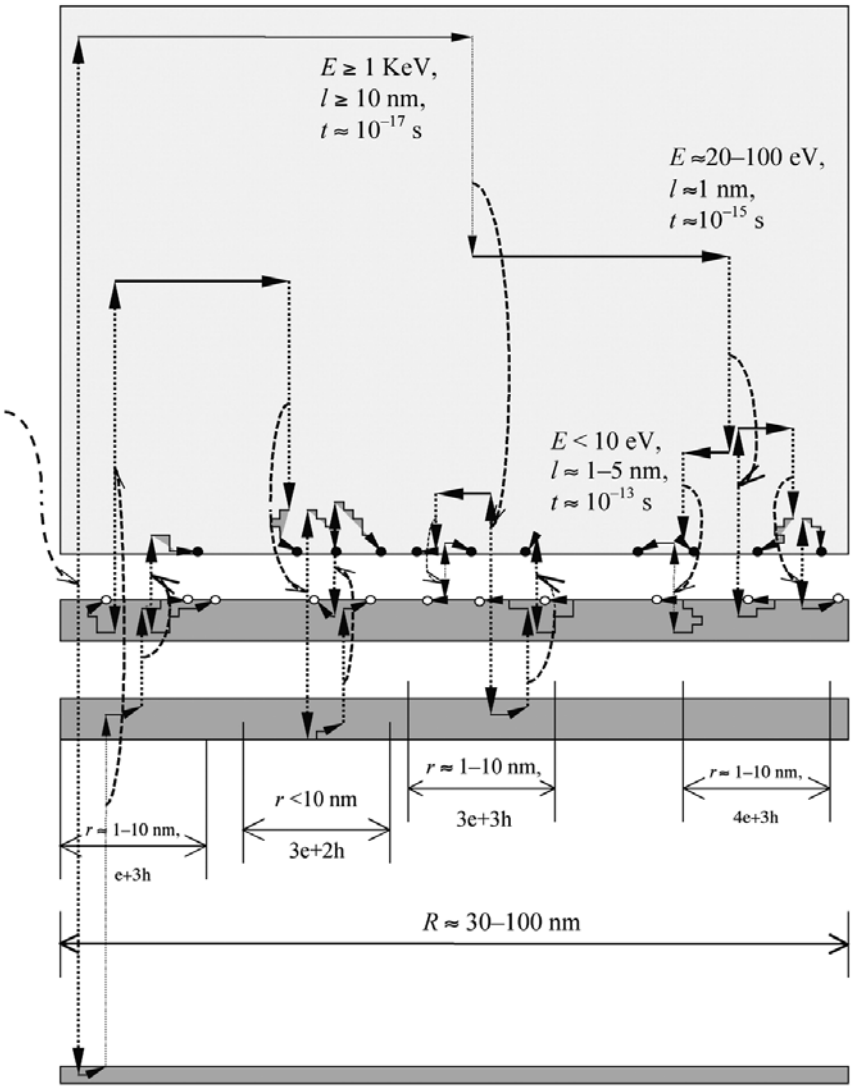

Fig. 3.6. Spatial distribution of electronic excitations created by the absorption of a high-energy photon. The notations are similar to the ones used in Fig. 3.5. Solid circles are electrons; open circles are holes after thermalization. Energy, temporal, and spatial scale characteristics for the process are presented, as well as the composition and dimension of clusters of excitations

e and h density, the interaction between excitations can modify their localization and can even create defects in crystals. In addition, these clusters can excite close luminescent centers, and their interaction is responsible for the acceleration of the fluorescence kinetics and total or partial luminescence quenching. The first evidence of such effect was observed in CeF_3 [41].

Peculiar fast intrinsic luminescence observed in alkali halides, and in particular in CsI, was shown to be the result of interaction of several electron–hole pairs at the initial stage of relaxation [42, 43]. The probability of the effects of correlated relaxation of electronic excitations with the creation of an emission center depends on the crystal and can be quite high. It is clear that the estimation of the light output of scintillators such as CeF_3 or CsI must take into account the role played by regions of high densities of excitation. For example, in the case of CeF_3, interaction of excitations is estimated to reduce the light output by a factor of 2 to 5.

3.3.3 Emission of Luminescent Centers

This process occurs after excitation of the emitting centers. It is the very last stage of relaxation of electronic excitations. The emission mechanisms depend on the electronic structure of both luminescent ions and crystal lattice in which they are imbedded, and on their mutual interaction.

At this stage, there are many processes, which may limit the luminescence efficiency. Some are related with nonradiative transitions, others with energy transfer. Most of them are well known and it is of interest here to list the main ones, which will be analyzed in more detail in next paragraphs.

3.3.3.1 Electron–Phonon Coupling

Ions in a host lattice interact with the vibrations of the lattice, inducing nonradiative transitions. Whatever the strength of the coupling, there is always a competition between radiative and nonradiative transitions. The quantum efficiency, defined as the ratio of the number of emitted quanta to the number of absorbed quanta, is 1 in the absence of competing radiation less transitions. It is usually the case for luminescent ions in efficient scintillators. In case of intermediate and strong coupling strength, the Stokes shift can induce thermal quenching. In case of weak coupling strength, for which the Stokes shift is absent, nonradiative process can occur through multiphonon emission. In any case, the presence of intermediate excited states between the emitting level and the ground state is harmful because it is a source of nonradiative relaxation. As a matter of fact, Tl^+, Bi^{3+}, or Ce^{3+} ions, which exhibit large free gap below their $6p$ or $5d$ emitting levels, are much more efficient luminescence centers than, for example, $5d \rightarrow 4f$ luminescence Pr^{3+} ions where many $4f$ levels are lying between $5d$ and the ground state.

3.3.3.2 Photoionization and Charge Transfer Quenching

When the emitting level of the luminescent centers is degenerated in the conduction band, autoionization or photoionization usually occurs, resulting to a delocalization of the electron.

It may be free in the conduction band and recombine radiatively or nonradiatively through different processes and/or can be trapped in lattice defects. This process decreases the quantum efficiency of the luminescent ions and modifies the fluorescence kinetics giving rise, for example, to afterglow.

But the electron after ionization can be still bounded to the luminescent center, forming an exciton where the hole is located at the center. This exciton, known as impurity-bound exciton, can recombine radiatively and give rise to another kind of luminescence. This process can completely quench the luminescence of interest.

Some luminescent ions, namely rare-earth ions, when embedded in some crystals, may exhibit charge transfer transitions in the same energy range as transitions between localized states. After capture of an electron of the valence band, a charge transfer state can be formed which can partly or totally quench the luminescence, depending on its energy related to the one of the emitting level (see the case of Eu^{3+}-doped oxysulfides in Subchap. 3.6).

3.3.3.3 Concentration Quenching

Interaction between luminescent centers increases with their concentration in materials. Energy migration through nonradiative energy transfer can take place if the concentration is high enough. The excitation energy can travel over a long distance in the solid and reach a quenching site where it is lost nonradiatively. This phenomenon is called concentration quenching, and becomes effective for concentrations of few atomic percent of dopant ions. A very good example is given by CeF_3, which has a modest light yield in spite of a very high concentration of Ce^{3+} ions.

However, fully concentrated crystals can exhibit efficient luminescence. It is the case of very pure samples, which contain a very low concentration of killer centers. It is also the case of systems in which the luminescent ions show an emission with a large Stokes shift. As a result, the relaxed excited state is out of resonance with the neighboring ions and the energy migration cannot occur. Concentrated systems, which exhibit efficient scintillation, are, for example, $Bi_4Ge_3O_{12}$ (BGO) and CeF_3.

3.3.3.4 Reabsorption

The light emitted by luminescent centers comes out from the solid after a more or less long path over many lattice constants. It depends on the size and on the shape of the solid-state scintillator and on the configuration in which it is placed in the device using integrated techniques.

The luminescence traveling through the scintillator can be reabsorbed either by an identical or by different luminescent centers.

In the first case, the reabsorption is also called radiative energy transfer. This phenomenon leads to a lengthening of the fluorescence decay, but, in principle, does not affect the emission efficiency.

In the second case, the luminescence can be strongly quenched and the light yield of the scintillator substantially reduced. In large-size scintillators, reabsorption can be really an important limiting factor, and much care must be taken to grow transparent crystals in the wavelength region of luminescence. Many kinds of absorption centers can be present in crystals such as lattice distortions, point defects, color centers, etc. Using very pure starting materials, improvement of crystal growth, special annealing, etc., can reduce their number. It is often a big challenge to maintain a high light yield for large crystals of several tens of centimeters in length.

3.4 Creation and Quenching of Radiating Centers

In this paragraph, we will address a problem which has not received as much attention as the relaxation of the hot carriers and their thermalization but which has a strong impact on the parameters of scintillation; we discuss here the final stage of luminescent center excitation mechanism in scintillators under ionizing radiation. The final stages of the different scintillation mechanisms in inorganic compounds have been discussed briefly in Sect. 2.2. Here we focus our attention on oxide crystals doped with Ce^{3+} because the Ce^{3+} ion interconfiguration luminescence presumes the simultaneous presence of different excitation mechanisms [44]. The charge transfer excitation mechanism of the doping ion luminescence naturally appears from the fact that heterovalent Ce ions have a high cross section for capturing holes. Valbis [45] proposed this mechanism of scintillation for $YAlO_3$:Ce^{3+}. Another mechanism of scintillation, which we defined as energy transfer excitation mechanism, arises in oxide crystals where intrinsic luminescence centers exist. The bright scintillation through sensitizing of the Ce^{3+} luminescence occurs in complex structure oxide crystals, (1) which, when undoped, have an intrinsic excitonic luminescence from relaxed excited states; and (2) which, when Ce^{3+} doped, have a reasonable overlapping of the intrinsic matrix luminescence band and the activator absorption interconfiguration bands [46]. This mechanism had been recognized in Gd-based crystals [47, 48] and then in many other oxide compounds. A good evidence of the contribution of this mechanism in the scintillation of Ce^{3+}-doped Y and Lu-based crystals came up from experimental data. Table 3.1 shows the maxima of the intrinsic luminescence in several complex structure oxide crystalline compounds. Some of them, especially Y and Lu-based crystals, the technology of which is being extensively developed, have two characteristic intrinsic luminescence bands. These bands with maxima near 40,000 and 32,000 cm^{-1} (5 eV and 4 eV) are the common features of Al, Si, B, Be complex structure crystalline compounds. The short wavelength self-trapped exciton (STE) intrinsic luminescence band appears

Table 3.1. Peak maximum of intrinsic luminescence bands in some complex structure oxide crystals

Crystal	High-Energy Band Maximum (cm^{-1})	Low-Energy Band Maximum (cm^{-1})	Reference
$Y_3Al_5O_{12}$	39,200	33,600	13, 14
$YAlO_3$	44,800	33,600	7
Y_2SiO_5		33,200	15
$Lu_2Al_5O_{12}$		33,300	16
Lu_2SiO_5	39,060	31,750	9
$LuAlO_3$		31,350	1
Sc_2SiO_5		31,250	17
$Y_3Ga_5O_{12}$		32,800	18
Na_2ZrSiO_5		34,480–31,250	19
K_2ZrSiO_5		33,300	19
$K_2ZrSi_2O_7$		33,300	19
$Cs_2ZrSi_2O_7$		33,300–31,250	19
$Al_2Be_3Si_6O_{18}$	33,600	28,000	20
Al_2BeO_4	34,000	28,400	20
Be_2SiO_4	33,600	27,600	20
LiB_3O_5		32,800	21
$Li_2B_4O_7$		31,000	22

because of an interband transition $a_{1g}(\sigma) \rightarrow t_{1u}(\pi)$ and the long wavelength one is caused by radiative recombination of self-trapped holes STH [49]. The STE and STH luminescence intensity variations with temperature are opposite [50], so the thermodissociation of STE is an additional source of STH. A detailed examination of complex oxide compounds structure as well as results of EPR measurements [51] show that hole and excitons self-trapping occurs in oxygen sites of regular and slightly distorted oxygen polyhedra. The stabilization of O^--type centers and excitons near a vacancy in the heaviest cation site in complex compounds is considered as an alternative interpretation. However, it is inconsistent with the crystal growth peculiarities in the Y_2O_3–Al_2O_3 system. A strong aluminum oxide leakage from the melt is observed for perovskite crystal growth inducing Al vacancies in the crystal. The situation is even more dramatic in the case of $LuAlO_3$ where even a very small deficiency of Lu in the melt favors the growth of the garnet phase instead of the perovskite.

The combined luminescence of STE and STH gives a high light yield potential at room temperature in many complex structure crystals especially in oxides. For instance, both undoped $YAlO_3$ and $LuAlO_3$ show a wide luminescence band with maxima near 320 nm at room temperature, which is a superposition of the STE and STH luminescence. The total light yield of the scintillation exceeds 11,000 ph/MeV, while when the crystals is doped with cerium with concentration $\sim 10^{17} cm^{-3}$ or more, the STE and STH luminescence is

completely quenched in perovskites. It is a relatively rare situation when both intrinsic bands are quenched. In Ce-doped $Lu_2Al_5O_{12}$ and $Y_2Al_5O_{12}$ garnets, the quenching of STE luminescence arises only when the STH recombination and the Ce^{3+} interconfiguration emission have been observed simultaneously under ionizing radiation. Figure 3.7 shows excitation spectra of the Ce^{3+} luminescence in lutetium perovskite indicating sensitization of the Ce^{3+} luminescence by STE and STH. Besides Ce^{3+}interconfiguration $f \rightarrow d$ transitions in the range 200–320 nm, two peaks near 154 and 162 nm have been observed in luminescence excitation spectra. These bands are assigned, respectively, to the direct excitation of STE and STH in the crystal.

Besides STE and STH luminescence quenching, the Ce^{3+} impurity ion changes the conditions of holes self-trapping in the crystal. It is observed through excitation spectra in Ce-doped lutetium perovskite that the 162- nm (STH) excitation band is detected at near liquid helium temperature in integral excitation spectra, measured as a weak shoulder of the 154- nm band in low-temperature instantaneous spectra and disappears at room temperature. It is obvious that hole self-trapping in Ce-doped crystals is strongly suppressed because of the capture of the holes by the trivalent cerium ions.

Moreover, lutetium perovskite shows 75–84 nm excitation bands, which are due to transition from filled $4f^{14}$ shell of Lu^{3+} ion to the conduction band [53]. They are observed in instantaneous and integral measurement regimes, indicating that Ce^{3+} ions capture not only trapped but also "hot" holes from conduction band. Thus, the capture of the holes by Ce^{3+} plays a more significant role in the scintillation creation in lutetium than in yttrium-based crystals. This difference is also seen from the scintillation kinetics.

The scintillation kinetics is a single exponential in YAP:Ce and the decay constant of scintillation kinetics τ_{sc} is about the double of the radiation time of the luminescence kinetics under intracenter excitation τ_r. This is due to the slow STE and STH diffusion in a majority of complex structure oxide crystals based on light elements similar to Y [44]. On the contrary, Lu perovskite has a nonexponential scintillation kinetics that is rather well approximated with three exponents as seen in Fig. 3.8. The longest component is due to specific trap center in Lu perovskite. The shortest one is close to τ_r. The difference between τ_r and τ_{sc} of the initial part of the scintillation kinetics is a reasonable parameter to suggest this excitation mechanism of the radiating centers. A progressive change of the dominating excitation mechanism is observed in the $YAlO_3$–$LuAlO_3$ solid solution system when the Lu fraction is increased in the crystal. Figure 3.9 shows this variation of the fast scintillation component as a function of the substitution of Y by Lu in the crystal.

When the energy transfer excitation mechanism dominates [44], the light yield dependence on activator concentration is maximum. The maximum is determined by the STE diffusion rate and shifted to the higher concentration region for a slower diffusion. Such dependence is well recognized for

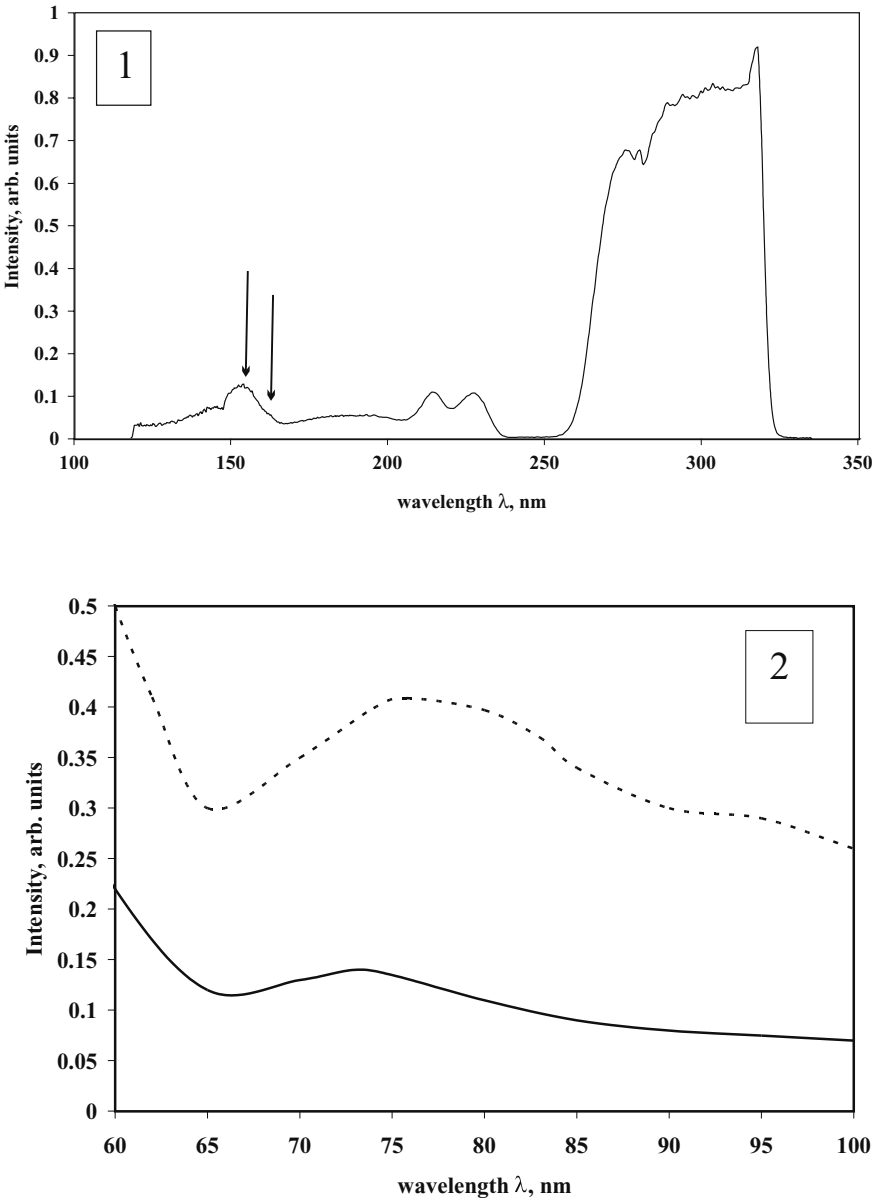

Fig. 3.7. Luminescence excitation spectra of Ce^{3+} luminescence ($\lambda_{lum} = 350$ nm) in $LuAlO_3$:Ce in the ranges 325–100 (1) and 100–60 (2) nm at 9°K. *Solid lines* represent spectra measured in integral regime and *dashed lines* are for spectra measured within 16 ns after excitation

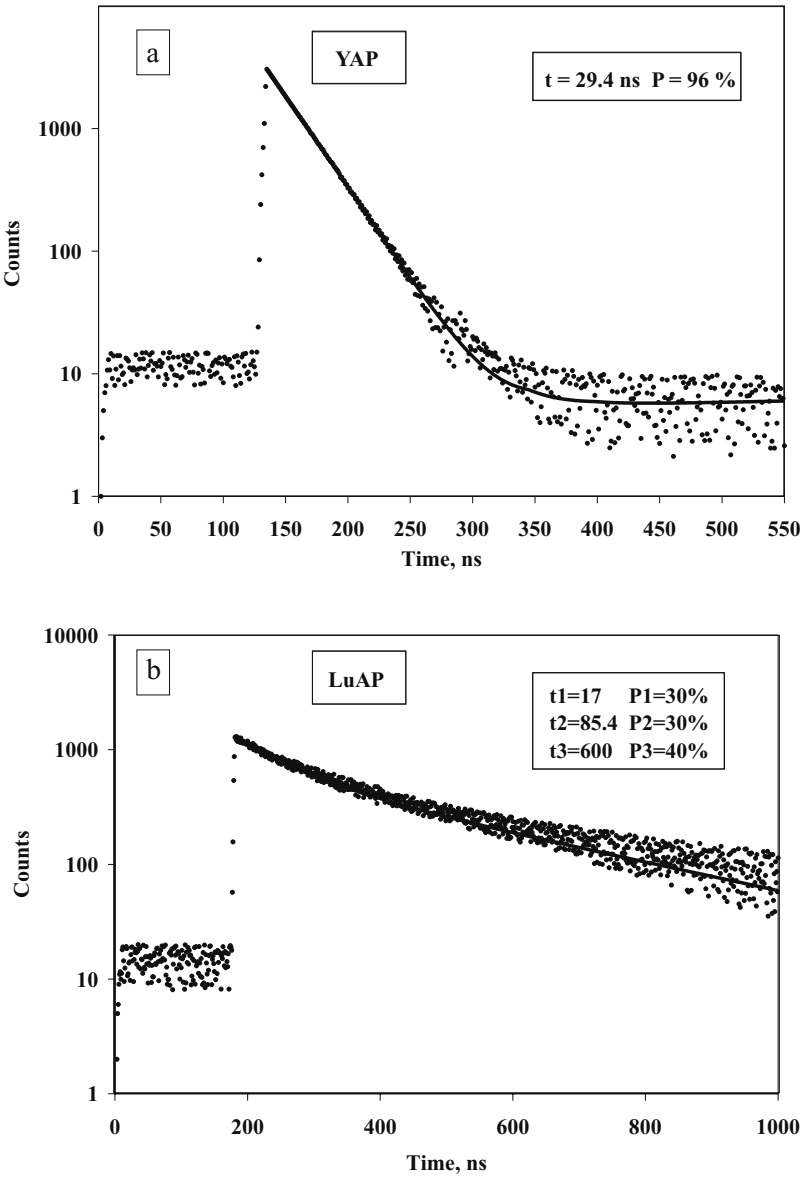

Fig. 3.8. Initial part of the scintillation kinetics of $YAlO_3$:Ce (**a**) and $LuAlO_3$:Ce (**b**) at room temperature (Pog scale)

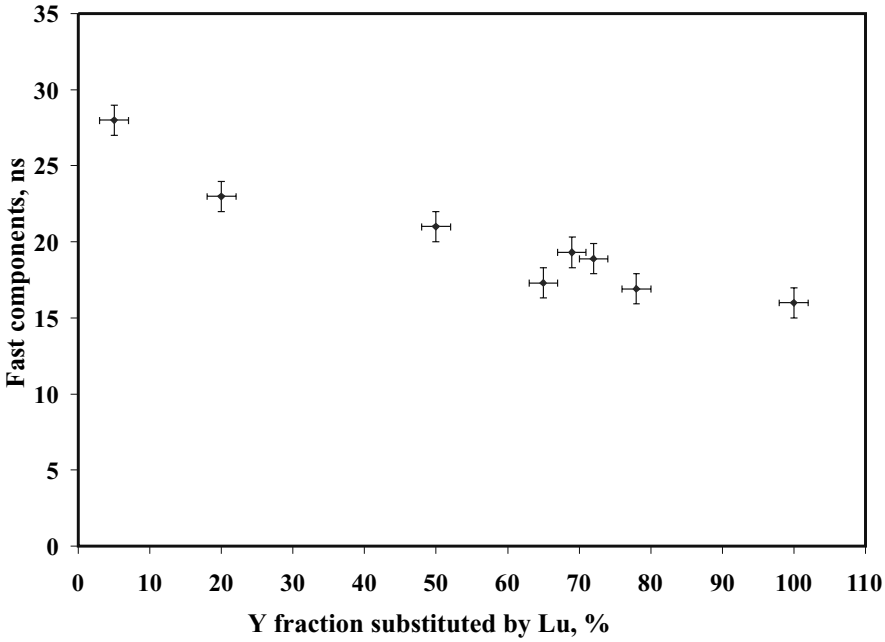

Fig. 3.9. Fast component of scintillation versus Y substitution by Lu in $(Y_{1-x}$–$Lu_x)AlO_3$:Ce, $T = 300\,K$

$YAlO_3$ and Gd_2SiO_5 doped with Ce^{3+}. Figure 3.10 shows the variation of the $YALO_3$:Ce light yield with the activator concentration.

In case of charge transfer excitation mechanism, the light yield dependence versus concentration has no maximum and reaches the saturation at relatively high activator concentration. It indicates that the scintillation light yield, where excitation charge transfer mechanism is prevailing, can be increased by an increase in the activator concentration. Figure 3.11 shows the variation of the $(Lu_{0.5}$–$Y_{0.5})AlO_3$:Ce light yield with the absorption coefficient of the maximum of the first allowed Ce^{3+} interconfiguration absorption band, which is proportional to the activator concentration. A similar dependence was seen in (Y–Lu)AlO_3 and $LuAlO_3$ crystals [54].

Both mechanisms of excitation show light yield temperature dependence strongly related to the presence of additional electron traps in the crystal. Figure 3.12 shows simulation results [44] of light yield temperature dependence for a perfect $YAlO_3$:Ce crystal (the temperature change of diffusion coefficient is taken into account) and for a crystal which has a shallow trap with a thermoactivation energy $E_{TA} = 0.2\,eV$ and a frequency factor $s \sim 1 \cdot 10^{12}\ s^{-1}$. In fact, shallow traps, at the relaxation stage, are additional sources of STE. Similar light yield temperature dependence is measured in different perovskite scintillation crystals [44, 55] (Fig. 3.13). A shift of the curve slope to the high-temperature region occurs because of an increase of

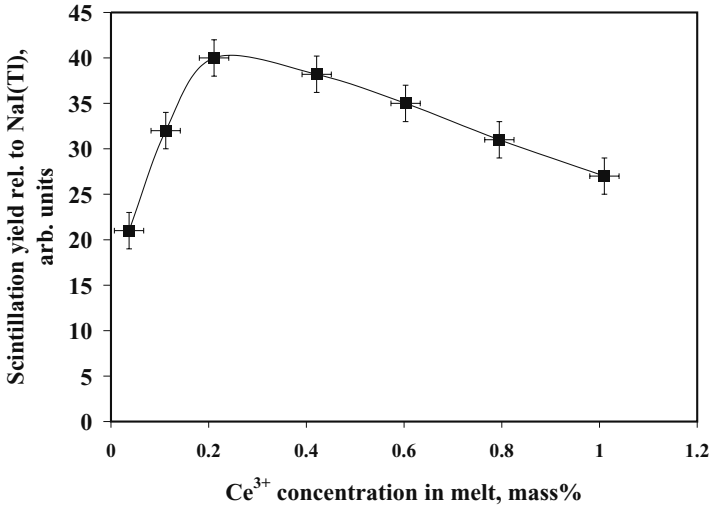

Fig. 3.10. Room temperature $YALO_3$:Ce light yield versus activator concentration

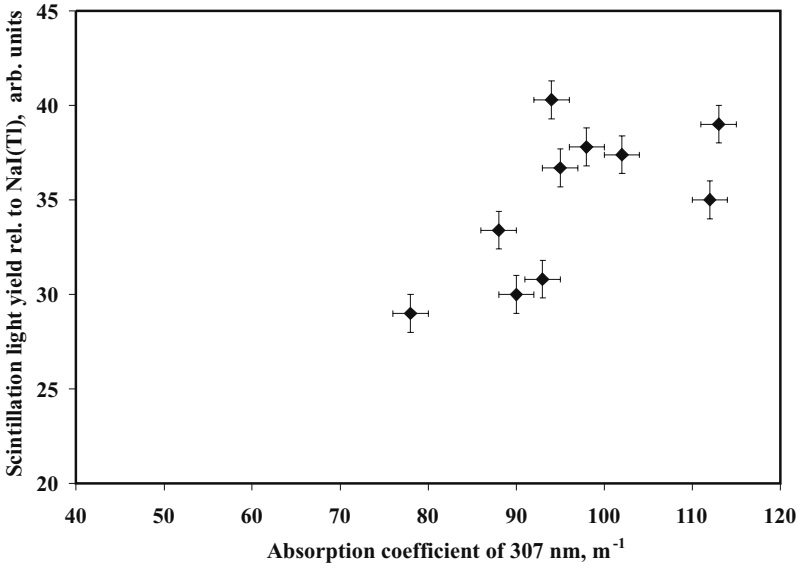

Fig. 3.11. Room temperature $(Lu_{0.5}–Y_{0.5})AlO_3$:Ce light yield versus absorption coefficient at 307 nm

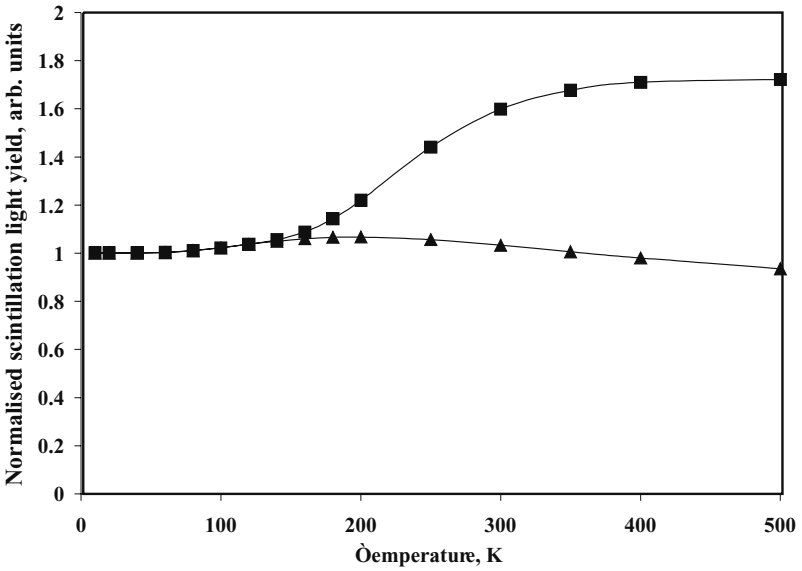

Fig. 3.12. Temperature dependence of the normalized scintillation light yield of $YAlO_3$:Ce in the case of no defect (triangle) in the crystal and crystal with one type of electron trap (square) for a middle slow diffusion of STE and activator concentration $\sim 10^{18}$ cm^{-3}

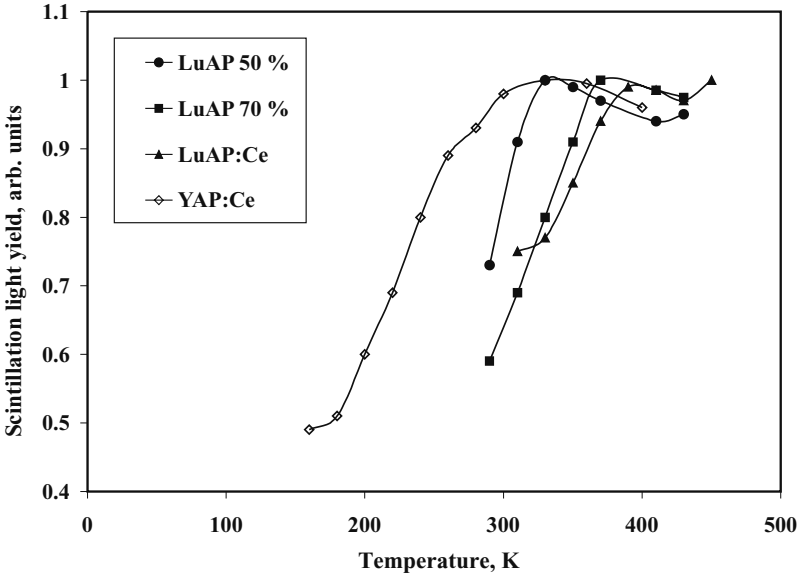

Fig. 3.13. Light yield temperature dependence in $YAlO_3$, $(Y_{0.5}–Lu_{0.5})AlO_3$, $(Y_{0.3}–Lu_{0.7})AlO_3$, $LuAlO_3$ crystals doped with Ce

the thermoactivation energy of the characteristic electronic center with an increase of the Lu fraction in the crystal. One can conclude that the variation of the electron trap centers concentration in YAP–LuAP crystals is an efficient way to control the crystal LY temperature dependence.

The determination of the radiating centers excitation mechanism is relatively obvious in crystals when the luminescence quantum yield is close to 1. However, in reality, synthetic crystals have specific defects and uncontrolled impurities, which very frequently introduce an additional quenching of the luminescence, and distort or even suppress the effective mechanisms of the radiating centers excitation. These quenching processes have to be minimized to achieve a high scintillation light yield. Not only the quenching of the intracenter Ce^{3+} luminescence has to be avoided but also the quenching of the STE by impurities and nonradiative STH relaxation has also to be suppressed.

3.5 Thermal Quenching

The luminescence thermal quenching phenomenon observed in luminescent centers embedded in a solid is always related to electron–phonon interaction and radiationless processes [3, 56].

To represent the electronic energy-level diagrams of the active ion by taking into account its interaction with the vibrating host lattice, the simplest model is the single-configurational coordinate (SCC) model.

This model considers only one vibration mode, a symmetrical stretching mode so-called breathing mode, described in the harmonic oscillator approximation. The configuration coordinate Q describes the vibration and represents the distance between the luminescent ion and the ligands. For more details, the reader can refer to the early work of Struck and Fonger [57] or to a review paper by Blasse [30].

This model is very convenient to describe thermostimulated processes leading to nonradiative recombination and thermal quenching of the luminescence.

3.5.1 Nonradiative Relaxation to the Ground State

A typical SCC diagram is represented in Fig. 3.14.

The energy E is plotted versus the coordinate Q. Potential curves of the ground state g and of one excited state e are represented by parabolas. The horizontal lines represent the vibration levels. The vertical lines indicate the optical transitions for which the probability is maximum (Franck Condon approximation). The equilibrium distance Q_g between the luminescent ion and the ligands, when the system is in its ground state, does not change during the absorption transition (Born-Oppenheimer approximation), but

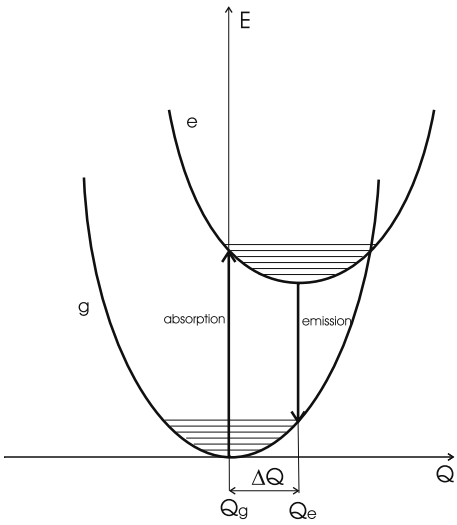

Fig. 3.14. The configurational coordinate diagram. The energy E is plotted versus the coordinate Q. The ground state g and one excited state e only are represented by potential curves with offset ΔQ. Absorption and emission transitions are indicated

changes into Q_e after relaxation of the excited state. The ion–ligand distance is, in general, larger in the excited state inducing parabolas offset. As a result, the emission transition from the relaxed excited state is shifted toward lower energy than the absorption transition (Stokes shift).

The Stokes shift is a measure of the interaction between the emitting center and the vibrating lattice. The larger is the Stokes shift the stronger is the electron–phonon coupling.

For weak coupling, the parabolas are not significantly shifted and the emission spectra show narrow lines (case of f–f transitions of rare-earth ions). In the case of intermediate coupling for which the parabolas are weakly shifted, vibronic spectra of broad emission lines are observed reflecting the progression in stretching vibration of the luminescent ion (case of uranyl pseudomolecules in oxides, such as UO_2^{2+}). Strong coupling leads to broad emission bands (case of mercury-like ions Tl^+, Pb^{2+}, Bi^{3+}, $5d \rightarrow 4f$ transitions of rare-earth ions, self-trapped excitons, molecular groups such as $(WO_4)^{2-}$, charge transfer transitions, etc.).

In the case of intermediate or strong coupling (Fig. 3.15a), the relaxed excited state may emit luminescence through radiative transition to the ground state. It may relax nonradiatively to the ground state if the temperature is high enough to allow the excitation to reach the crossing of the two parabolas.

This model accounts, therefore, for the thermal quenching of luminescence, and even for the total absence of luminescence at a given temperature when the Stokes shift is strong enough.

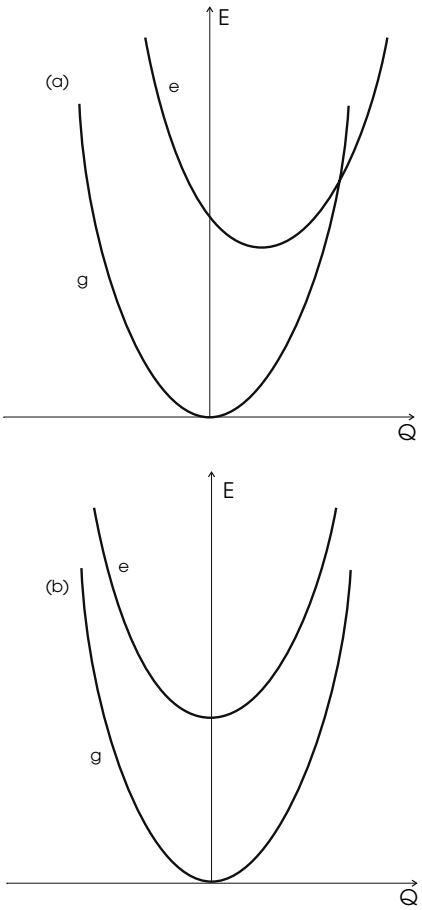

Fig. 3.15. Configurational coordinate diagrams illustrating (**a**) the case of intermediate/strong electron–phonon couplings and (**b**) the case of weak electron–phonon coupling

Many applications require use of scintillators at room temperature, and efficient scintillators must obviously contain luminescent centers with a quantum yield as close to 1 as possible without thermal quenching. It is, for example, the case of most Tl^+ or Ce^{3+}-doped scintillation crystals.

However, a particular case is the well-known BGO ($Bi_4Ge_3O_{12}$) scintillator for which the relatively low light output is essentially due to a room temperature quantum efficiency of only 0.13 because of thermal quenching [4].

There are cases where the thermal quenching may not have a harmful consequence. For example, $PbWO_4$ is a fast scintillator because of thermal quenching. Of course, its light yield is very weak as well, but it is nevertheless a good fast scintillator for some applications in high-energy physics for which

its interest is more related to the rapidity of the scintillation than to its efficiency.

Another interesting case is the Ce^{4+} center. Ce^{4+} is a full shell ion. No $4f$–$4f$ electronic transitions can occur because of empty $4f$ level. Nevertheless, charge transfer absorption transitions can be observed in the UV region but usually no radiative emission transitions due to a very large Franck Condon offset and a consequent crossover. Ce^{4+} is not a luminescent center. It often coexists with Ce^{3+} luminescent centers in cerium containing scintillating materials, and is a very harmful nonradiative recombination center.

Applications may require scintillators with high light output at temperature greater than room temperature. It is the case of oil well logging in which scintillation detectors are used to measure the natural or induced radioactivity of rocks. One of the most important requirements for borehole γ-ray detectors is the temperature response because of variable and relatively high borehole temperatures. Good candidates for such application are cerium-doped lutetium ortho-aluminates such as $LuAlO_3$ (LuAP) or $Lu_{1-X}Y_xAlO_3$ (LuYAP), and a new inorganic scintillator: cerium-doped lutetium pyro-silicate Ce^{3+}:$Lu_2Si_2O_7$ (LPS) [58] which all display a high light yield above room temperature.

In the case of very weak coupling ($4f$ levels of rare-earth ions), the parabolas are not significantly shifted (Fig. 3.15b). That does not mean that nonradiative relaxation to the ground state is impossible. It can occur through a so-called multiphonon nonradiative emission process. This process was first studied by Weber [59–61] and then by many other authors in a number of different rare-earth doped crystalline materials. It was demonstrated that spontaneous multiphonon emission rates strongly depend on the energy gap to the next-lower level (exponential energy gap dependence) and therefore on the number of phonons required to conserve energy (host dependence via phonon frequency spectrum). Nonradiative contribution to relaxation is significant even for large transitions corresponding to the simultaneous emission of 5–6 phonons.

In Fig. 3.16 is shown a schematic energy-level scheme of few rare-earth ions, where are indicated the emitting levels and which reflects the nonradiative relaxation rules previously described.

Blocks indicate higher energy configuration such as $4f^{n-1}$ $5d$ and charge transfer (CT). The energy of these levels strongly depends on the host lattice contrary to $4f$ levels. As a result, the emission from some $4f$ levels depends on the energy of lowest $5d$ or CT levels. For example, in the case of Pr^{3+}, the high-energy $4f$ ^1S_O level can emit fluorescence only when the $5d$ levels are located at higher energy. Reversely, $5d$ emission can be obtained only if the lowest $5d$ level is below ^1S_O. Indeed, Pr^{3+}-doped crystals may exhibit fast scintillation when Pr^{3+} ions are in the presence of a strong crystal field, which lowers the lowest $5d$ level. A large energy gap exists between the ground state and the $5d$ and CT lowest excited states of Ce^{3+} and Yb^{3+}, respectively. In

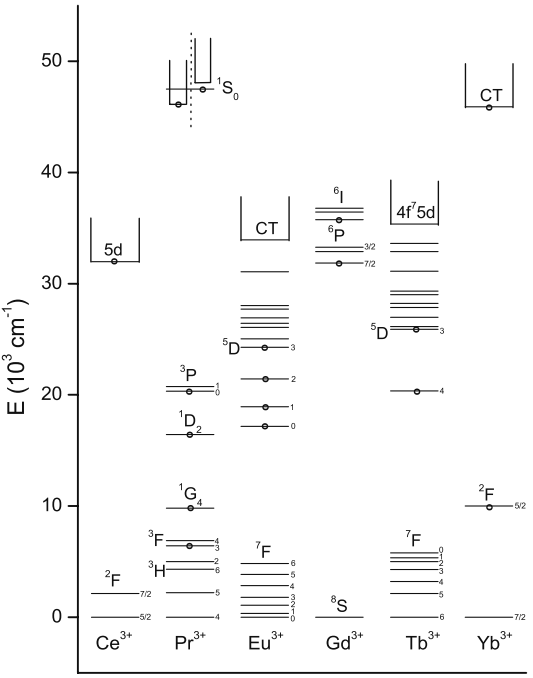

Fig. 3.16. Energy-level diagrams of some rare-earth trivalent ions. Circles indicate emitting levels. Blocks indicate levels of $4f^{n-1}5d$ and charge transfer (CT) higher energy configurations

principle, an efficient luminescence is expected if the Stokes shift is not too large.

3.5.2 Thermostimulated Photoionization and Trapping Effects

Photoionization of dopant ions in crystals can occur at relatively low energy when their localized ground and excited states are close or degenerated to/in the conduction band. This phenomenon may be of importance in luminescent and scintillating insulators because it may be the source of significant change in light efficiency and excited states dynamics. However, their importance was often underestimated in the past. It will be described in the next subchapter.

We will give here a few examples of thermostimulated photoionization.

Ce-doped Lu_2SiO_5 (LSO) is a well-known efficient scintillator at room temperature. Photoconductivity spectra obtained through direct photoconductivity measurements [62] and using the resonant microwave cavity technique [63–65] allow to estimate the energy difference between the bottom of the conduction band and the localized Ce^{3+} $5d$ emitting level. It is around a few tenths of eV, which still enable to observe significant photoconductivity

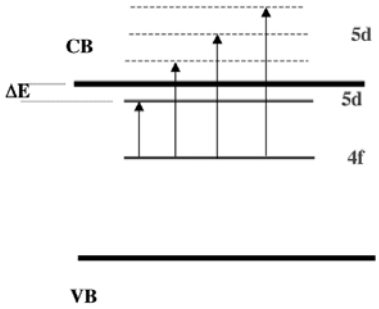

Fig. 3.17. Energy-level scheme of Ce^{3+} $4f$ and $5d$ levels in an ionic crystal. VB: valence band; CB: conduction band. The lowest $5d$ emitting level is lying in the forbidden gap close to the bottom of the conduction band, allowing thermostimulated photoionization

signal at room temperature through thermal activation. Figure 3.17 shows a simple energy-level scheme describing the process.

Similar results were obtained in the case of $Y_3Al_5O_{12}$:Ce. For using such scintillators at room temperature, it is therefore important to carefully control the temperature, because the light yield and the fluorescence decays are strongly temperature dependent. The efficiency drops down quickly and afterglow appears for temperatures slightly above room temperature.

The thermal quenching of scintillation of LaI_3:Ce crystal is explained by thermostimulated photoionization as well [66]. In this case, the lowest $5d$ state of Ce^{3+} is still closer (0.1 eV) to the bottom of the conduction band. As a result, this compound is a poor scintillator at room temperature but presents good scintillation properties for temperatures below 100°K.

Strong thermal quenching of scintillation may be the result of efficient trapping. This kind of quenching is observed only under excitation of the host lattice by ionizing radiations, and not under direct excitation of luminescent centers. It is due to the fact that high-energy excitation produces charge carriers, which may be trapped and cannot therefore excite luminescent centers, or only after a delay depending on the escape probability of trapped electrons which itself depends on temperature. In the temperature range where glow peaks are detected, revealing the presence of traps, a quenching of the scintillation is therefore expected and, as a consequence, a modification of the scintillation decay profiles.

Such trapping effects have been clearly identified in a number of scintillators. For example, ytterbium-containing YAG crystals exhibit X-ray–excited charge transfer luminescence. Its intensity drops drastically and its decay shows a very strong slow component at temperature below 120 K where thermoluminescence peaks are detected (Fig. 3.18) [37, 38]. The strong thermal quenching of X-ray induced emission of $LuBr_3$:Ce and $LuCl_3$:Ce observed

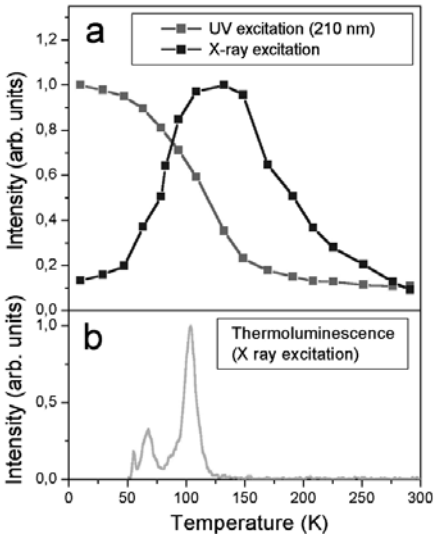

Fig. 3.18. Temperature dependence of the 333- nm integrated charge transfer emission band intensity (**a**), and thermoluminescence of YAG:Yb(50%) (**b**)

below 250 K is not understood by authors of [36] in the frame of their energy transfer model. It could be, however, interpreted by trapping effects as well.

3.6 Charge Exchange Processes Photoionization and Charge Transfer

To fully understand the electronic properties of a luminescent ion-crystal system, it is of importance to pay attention not only to localized transitions of the dopant ion, but also to charge exchange processes between the ion and the host crystal. In semiconductors, these exchange processes are the major phenomena while they are, in principle, of less importance in wide band-gap ionic crystals. However, their importance was underestimated too long, and it was demonstrated that they often occur in many transition metal and rare-earth ions activated compositions. When it is the case, these phenomena may lead to luminescence quenching of the dopant ion and may give rise to charge transfer luminescence. It is, therefore, of most interest to analyze them in doped scintillator crystals.

Photoionization and charge transfer of impurity ions in crystals are both dealing with electron transfer. They are, respectively, electron donor and electron acceptor transitions of the impurity. These processes were described using very simple phenomenological models. Jorgensen's formulation [67–69] later improved by Nakazava [70] was able to elucidate the systematic variation of the energies of CT transitions through the $4f^n$–series of rare-earth

ions. McClure and C. Pedrini used a simple electrostatic model to interpret the variation of the photoionization threshold of rare-earth impurity ions in crystals [71–73]. More recently, Thiel et al. [74] used photoemission spectroscopy for locating the energy of localized rare-earth impurity levels relative to host band structure in optical materials, and proposed an empirical model to describe the systematic trends of $4f$ binding energies.

3.6.1 Charge Transfer

Charge transfer can play a role in the luminescence process when the charge transfer states (CTS) are lying at relatively low energies close to the emitting levels of dopant ions (UV–visible region).

Energies of lowest charge transfer absorption transitions can be estimated by the empirical Jorgensen model:

$$\sigma = [\chi(X) - \chi(M)] \times 30,000 \text{ cm}^{-1} , \tag{3.3}$$

where $\chi(X)$ is the optical electron-negativity of the ligand anion and $\chi(M)$ is the optical electron-negativity of the central dopant ion. For ligands, $\chi(F) = 3.9$ [69], $\chi(O) = 3.2$ [75], $\chi(S) = 2.8$ [69].

Absorption bands are therefore expected at much higher energy in fluorides than in oxides, oxysulfides, and sulfides where CT transitions are usually observed in the UV–visible region.

Considering the case of rare-earth dopant ions in oxides, for example, in YPO_4 [70], Fig. 3.19 shows that Eu^{3+} (χ(Eu) = 1.75 [67]) and Yb^{3+} (χ = 1.6 [67]) are the ions for which the luminescence has the biggest chance to be perturbed by charge transfer states.

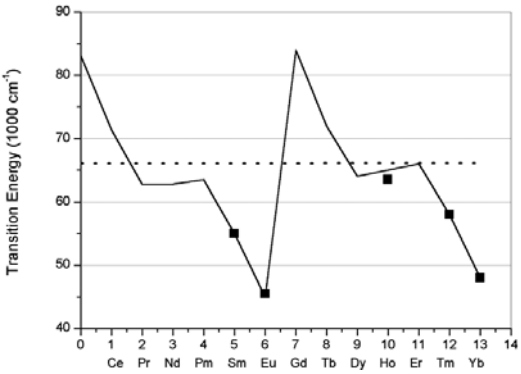

Fig. 3.19. Energy of the lowest charge transfer absorptions of rare-earth doped YPO_4 crystals. *Black squares*: experimental data; *solid line*: calculation; *broken line*: host lattice absorption edge

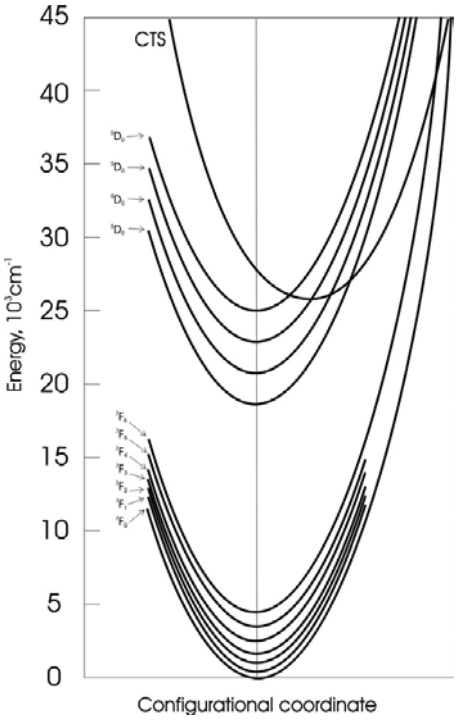

Fig. 3.20. Configuration coordinate diagram for the $4f$ and the lowest charge transfer state (CTS)of Eu^{3+}-doped Y_2O_2S, illustrating sequential quenching of ^5D emmissions

In Eu^{3+}-doped oxysulfides (La_2O_2S,Y_2O_2S), the minimum of the CTS is at rather low energy, leading to a strong sequential temperature-dependent quenching of ^5D_J emissions, as shown in Fig. 3.20 [76, 77].

This quenching depends, of course, on the host material. For example, the ^5D emissions quench sequentially in the order $^5D_3$, $^5D_2$, $^5D_1$, $^5D_0$ with increasing temperature, and corresponding quenching occurs at lower temperatures in the La compound. For Y_2O_3:Eu^{3+}, for which CTS bands are lying at much higher energies (about 10,000 cm^{-1} higher than in the oxysulfides), no thermally promoted $^5D \rightarrow$CTS transitions occur and no sequential quenching of the ^5D emissions are observed at temperature below 700°K.

In this case, it is possible to make use of CTS to efficiently absorb UV radiation and obtain strong red $^5D \rightarrow ^7F$ luminescence after nonradiative decay to the lower $4f$ levels. This red phosphor is used in fluorescent tubes.

It should be noted that in Eu^{3+}-doped materials, CTS emission is not observed because of radiationless relaxation through lower $4f$ excited states.

CT luminescence of Yb^{3+} is often observed in oxides and oxysulfides [78–80]. The electronic structure of Yb^{3+} is very favorable since the only

$4f^2F_{5/2}$ excited state is located around 10,000 cm^{-1} (1.25 eV) above the ground state $^2F_{7/2}$. Because of the large gap between the CTS and $^2F_{5/2}$ state, CT luminescence can be observed.

Recently, the observation of UV scintillation in yttrium/ytterbium aluminum garnets [81] opened the field of investigation to a new class of scintillating crystals with interesting fast luminescence properties, very attractive for radiation detection in general, and for neutrino physics, in particular [82], because of the high neutrino capture cross section by ytterbium. For this purpose, a detailed study of luminescence properties of ytterbium containing garnets and perovskites has been undertaken [36–38, 83, 84].

Localized levels of Yb^{3+} in the gap of the host and lowest CTS are presented in a single configuration coordinate diagram (Fig. 3.21).

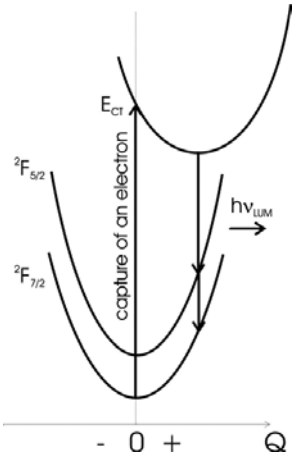

Fig. 3.21. Absorption and emission charge transfer transitions of Yb^{3+}-doped crystals using a simple configuration coordinate diagram

After capture of an electron from the ligands, a CTS is formed which can be described as an Yb^{2+} ion with a hole nearby in the valence band. Its potential curve has his minimum shifted toward larger Q corresponding to a larger Yb^{2+}-ligand ion equilibrium distance (Yb^{2+} radius > Yb^{3+} radius). If the shift is not too large, radiative relaxation is possible and then two broad emission bands separated by roughly 10,000 cm^{-1} (the energy difference between $^2F_{5/2}$ and $^2F_{7/2}$ states = 1.25 eV) are expected to be observed. For example, in the case of Yb^{3+}:YAG, the emission bands are peaking around 330 (the most intense) and 500 nm, and CT absorption occurs in the range 200–240 nm as predicted by the Jorgensen's model [37, 38].

CT luminescence of Yb^{3+}, because of its short radiative lifetimes (a few to a few tens of nanoseconds depending on the host lattice and the temperature) due to allowed transitions, is attractive for development of fast

scintillators capable to discriminate very short events. The fluorescence intensity can be high, but often thermal quenching processes occur below room temperature either due to cross-over from the CT-excited state to the ground state, or due to thermally activated photoionization involving the escape of a hole from the CTS to the valence band [81].

3.6.2 Photoionization

Photoionization of rare-earth ions in crystals has been observed and studied for $4f^n \rightarrow 4f^{n-1}\ 5d$ transitions. Indeed, the $4f^{n-1}\ 5d$ states can be close to the bottom of the conduction band and even degenerated within the continuum. In this case, the $5d$ electron can be delocalized in the conduction band resulting in a partly or complete quenching of the $4f^{n-1}\ 5d \rightarrow 4f$ luminescence.

It is why the first evidence of photoionization of rare-earth ions has been observed with divalent rare-earth ions and trivalent cerium ion, which usually exhibit $5d \rightarrow 4f$ luminescence [72–75, 85, 86]. Photoionization studies of impurity-doped crystals were motivated by the fact that their photo-physical properties were strongly dependent on photoionization process. It is the case for some potential solid-state laser materials such as CaF_2:Eu^{2+}, YAG:Ce^{3+}, crystals exhibiting persistent spectral hole burning like CaF_2:Sm^{2+}, and scintillator crystals of special interest here.

Photoionization processes particularly concern cerium-doped crystals, which are an important class of fast and efficient scintillators.

Let us consider the single configuration coordinate diagrams representing the localized levels of Ce in the gap of the host (Fig. 3.22).

Photoionization and CT energy thresholds can be calculated from thermodynamic cycles. In the case of Ce^{4+}, as previously mentioned, CT absorption and radiationless emission occur. In Ce^{3+}, $4f \leftrightarrow 5d$ transitions are usually observed in UV and visible range. Strong and fast luminescence may occur from the lowest $5d$-excited state providing this state is lying below the bottom of the conduction band, which is the case of the state ($Ce^{4+} + e_c$) in the diagram. This state is obtained after photoionization, e_c stands for an electron in the conduction band. Contrary to $Ce^{3+}5d$ excited states, the potential curve of ($Ce^{4+} + e_c$) is shifted toward negative Q since the Ce^{4+} ion radius is smaller than Ce^{3+} radius. The potential curve configuration represented in Fig. 3.22 corresponds to the case where the emitting level is lying well below the conduction band, and photoionization does not play any role in the luminescence process at room temperature (case of efficient cerium-doped scintillator crystals such as many Ce^{3+}-doped halides and oxides).

The opposite situation is when the lowest $5d$-excited state is degenerated in the conduction band. Then, the luminescence may be fully quenched even at low temperature due to autoionization. This is the case of cerium-doped sesquioxides (Ln_2O_3,Ln = La,Y,Lu) or some oxysulfides (La_2O_2S) [63].

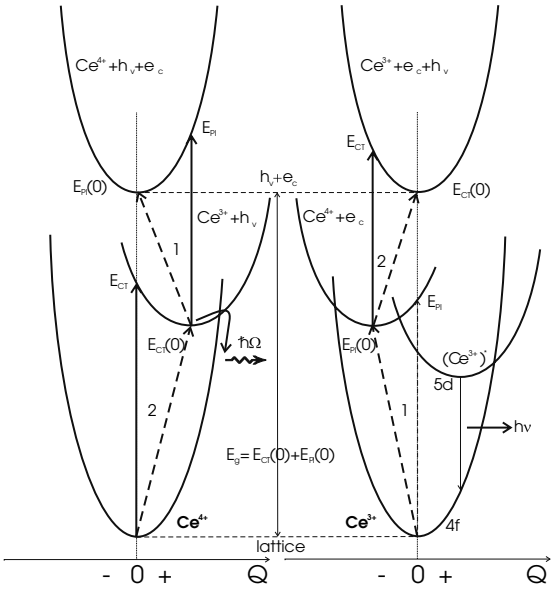

Fig. 3.22. Photoionization (1) and charge transfer (2) mechanisms of Ce^{3+} and Ce^{4+} ions embedded in crystal lattice, illustrated through single configuration coordinate diagrams

The intermediate case is when the emitting level is located closely below the bottom of the conduction band. Then, thermally assisted photo–ionization may occur leading to luminescence quenching at temperature below or above room temperature. The most efficient cerium-doped oxide scintillator at room temperature is Lu_2SiO_5:Ce (LSO), but its light yield rapidly decreases above room temperature. It was shown that the localized $5d$ level is located around only some tenths of eV below the conduction band, allowing photoionization even at room temperature through thermal activation [63]. $LaCl_3$:Ce^{3+} [36, 87–89] and $LaBr_3$:Ce^{3+} [90, 91] are scintillators with very high light yield, but LaI_3:Ce^{3+} exhibits efficient scintillation only at room temperature. The proximity of the Ce^{3+} lowest $5d$-excited state to the host conduction band leads to efficient autoionization process of Ce^{3+} above 150°K and therefore prevents any scintillation at room temperature [67].

The three cases are summarized in Fig. 3.23.

3.6.3 Impurity-Trapped Exciton

Electron-transfer transitions, in which an electron on the metal-impurity ion moves to lattice states, are not often observed. However, such transitions have been identified [73, 92, 93]. For example, in divalent rare-earth (Yb^{2+}, Eu^{2+}), doped, highly ionic crystals (such as alkaline earth fluorides), the so-called "anomalous" emission bands [94–99] were assigned to radiation from an

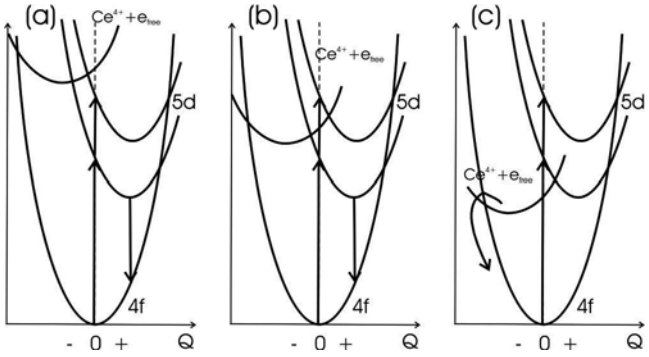

Fig. 3.23. Three scenarios for the fluorescence mechanisms of Ce^{3+} ions in crystals taking into account the state of the *bottom* of the conduction band (Ce^{4+} + e_{free}). (**a**) Intense fluorescence of Ce^{3+}. (**b**) Partly quenched fluorescence of cerium. (**c**) Total quenching of the Ce^{3+} fluorescence

impurity-centered exciton, which is the lowest excited state of the impurity-crystal system. Excitation of any of the localized levels of the impurity ion leads either to photoionization or to radiationless relaxation into lower levels. Normally, the lowest excited state localized level would be the emitting level, but when this level lies above the exciton energy it may relax into it, and the delocalized exciton may then emit instead.

For example, in the case of SrF_2:Yb^{2+} compound, the trapped exciton geometry is probably that expected for a trivalent impurity ion, Yb^{3+}, at a divalent site with an electron delocalized over the 12 next-neighbor metal–ion sites about 0.41 nm away. The collapse of the F^- cube around the Yb^{3+} could displace the F^- ions by about 0.02 nm, and would account for the large Stokes shift (Fig. 3.24).

It was demonstrated, through a detailed analysis of the fluorescence and the photoconductivity properties of Yb^{2+} in CaF_2, SrF_2 and BaF_2 [32], that all the 5*d* excited states of Yb^{2+} are degenerated in the conduction band, and that strong red shifted luminescence of ytterbium-trapped exciton is observed in CaF_2 and SrF_2. The negative shift of the exciton curve increases from CaF_2 to SrF_2 and even more for BaF_2. In the latter case, the shift is so large that the exciton relaxes nonradiatively to the ground state and no fluorescence at all is detected.

Impurity-trapped exciton luminescence has been observed in other systems such as titanium in sapphire [100] and BaF_2:Eu^{2+} [93].

This latter case is very interesting since Eu^{2+} ion in CaF_2 and SrF_2 exhibits typical and intense blue emission due to $5d \rightarrow 4f$ transitions while in BaF_2, a broad yellow emission band is detected because of europium-trapped exciton (Fig. 3.25).

The impurity-bound exciton model might be used to describe the fluorescence mechanisms in the well-known efficient CsI:Tl scintillator. A large

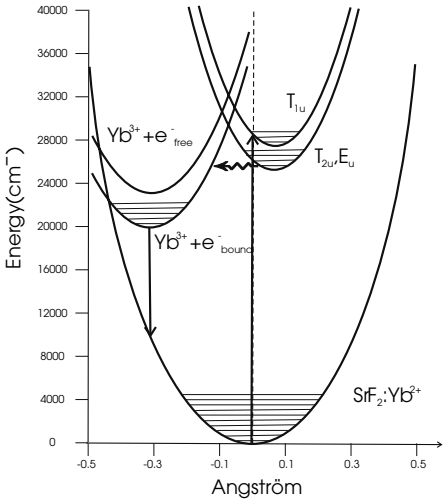

Fig. 3.24. Fluorescence mechanisms of ytterbium-bound exciton in Yb^{2+} doped SrF_2

number of publications deal with the origin of its yellow broad emission band and of its high light output. It comes out from the more recent studies that the centers emitting this fluorescence are of exciton type and related with thallium ions as well [101, 102]. These centers could be a host–exciton (the hole is in the valence band) with a thallium ion nearby, or a thallium-bound exciton (Tl^{2+} + e_{bound}) in which the hole is trapped in the thallium ion and the bound electron is delocalized in the neighboring Cs^+ ions, as it is sometimes the case in alkaline earth fluorides doped with divalent rare-earth ions.

It should be noted that the formation of impurity-bound exciton is strongly promoted when the impurity ion has two stable valence states such as Eu, Yb, Ti. It should be the case of Ce as well. However, no cerium-bound exciton fluorescence has been identified yet. It does not mean that such exciton state does not exist, because it can relax through a radiationless process to the ground state.

Because the exciton state lies below the bottom of the conduction band, its presence may induce a thermal quenching of the dopant ion fluorescence at lower temperature or a total quenching without photoionization depending on the relative positions of the localized states of the impurity ion, of the impurity-trapped exciton state, and of the bottom of the conduction band. But it may emit intense red shifted fluorescence with different properties, which can be of interest for scintillation.

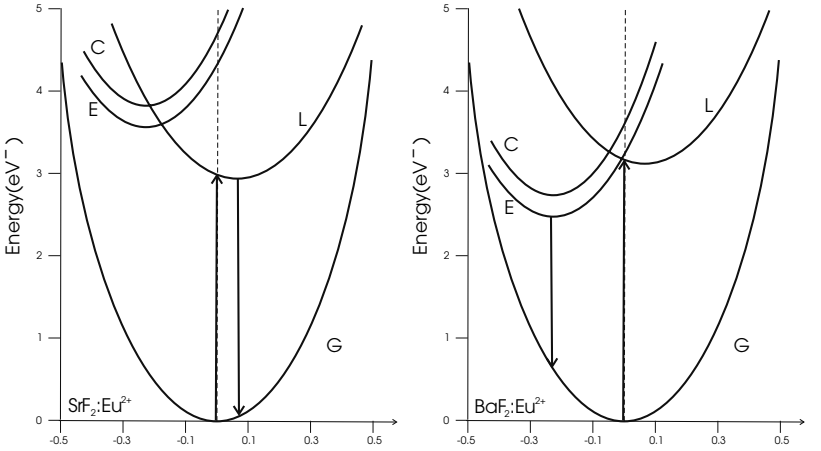

Fig. 3.25. Configuration coordinate diagram to explain the luminescence and photoconductivity spectra of SrF_2:Eu^{2+} and BaF_2:Eu^{2+}. The parabolas for the different states are the ground state G, a localized state L, the impurity-trapped exciton state E, the conduction band state C (Eu^{3+} + free electron). L is displaced outward by 0.1 Å. A and C are displaced inward by 0.2 Å. For G and L, $W = 0.04\,\text{eV}$ and for C and E, $W = 0.05\,\text{eV}$. The energy minima are placed according to spectroscopic data

References

1. Rodnyi PA, Dorenbos P, van Eijk CWE (1995) Energy loss in inorganic scintillators. Phys Stat Sol (b) 187:15–29
2. Bertram RH, Lempicki A (1996) Efficiency of electron–hole pair production in scintillators. J Luminescence 68:225–240
3. Vasil'ev AN (1996) Polarization approximation for electron cascade in insulators after high-energy excitation. Nucl Instr Meth Phys Res B 107:165–171
4. Lempicki A, Wojtowicz AJ, Berman E (1993) Fundamental limits of scintillator performance. Nucl Instr Meth Phys Res A333:304–311
5. Shockley W (1961) Problems related to p–n junctions in silicon. Solid State Electron 2:35–60
6. Klein CA (1968) Bandgap dependence and related features of radiation ionization energies in semiconductors. J Appl Phys 39:2029–2038
7. Pédrini C, Moine B, Gâcon JC, Jacquier B (1992) One- and two-photon spectroscopy of Ce^{3+} ions in LaF_3–CeF_3 mixed crystals. J Phys Condens Matter 4:5461–5470
8. Wojtowicz AJ, Berman E, Lempicki A (1992) Stoichiometric cerium compounds as scintillators, II. CeP_5O_{14}. IEEE Trans Nucl Sci 39:1542–1548
9. Nikl M, Mares JA, Mihokova E, Beitlerova A, et al. (1993) Energy transfer processes in CeF_3 single crystals. Solid State Com 87:185–188
10. Wojtowicz AJ, Balcerzyk M, Berman E, Lempicki A (1994) Optical spectroscopy and scintillation mechanisms of $Ce_xLa_{1-x}F_3$. Phys Rev B49:14880–14895

11. Williams RT, Thoma ED, Bunton PH (1994) Energy localization and decay in highly ionic crystals. Mater Res Soc Symp 348:331–342
12. Pédrini C, Belsky AN, Vasil'ev AN, et al. (1994) Fluorescence properties of CeF_3 and of some other cerium doped crystals and glasses under VUV and X-ray synchrotron excitation. Mater Res Soc Symp 348: 225–234
13. Wojtowicz AJ et al. (1994) Scintillation mechanism and radiation damage in $Ce_xLa_{1-x}F_3$ crystals. Mater Res Soc Symp 348: 455–461
14. Moses WN, Derenzo SE, Weber MJ, et al. (1994) Scintillation mechanisms in cerium fluoride. J Luminescence 59:89–100
15. Wojtowicz AJ et al. (1994) Scintillation light trapping and radiation damage in CeF_3. IEEE Trans Nucl Sci 41:713–718
16. Bouttet D, Dujardin C, Pédrini C, et al. (1996) X-ray photoelectron spectroscopy of some scintillating materials. In: Dorenbos P, van Eijk CWE (Eds) Proc Int Conf on Inorganic Scintillators and Their Applications, SCINT'95. Delft University Press, The Netherlands, pp 111–113
17. Pédrini C, Bouttet D, Dujardin C, et al. (1996) Energy transfer and quenching processes in cerium-doped scintillators. In: Dorenbos P, van Eijk CWE (Eds) Proc Int Conf on Inorganic Scintillators and Their Applications, SCINT'95. Delft University Press, The Netherlands, pp 103–110
18. Belsky AN, Glukhov RA, Martin P, et al. (1997) VUV excitation of intrinsic luminescence of ionic crystals with complicated band structure. Simulation. J Luminescence 72–74:96–97
19. Glukhov RA, Pedrini C, Vasil'ev AN (1997) Modelling of energy conversion and transfer in scintillators. In: Yin Zhiwen, Feng Xiqi, Li Peijun, Xue Zhilin (Eds) Proc Int Conf on Inorganic Scintillators and Their Applications, SCINT'97. CAS, Shanghai Branch Press, Shanghai, pp 111–114
20. Glukhov RA, Belsky AN, Pedrini C, Vasil'ev AN (1998) Simulation of energy conversion and transfer in CeF_3 after VUV photon absorption. J Alloys Compounds 275–277:488–492
21. Belsky AN, Kamenskikh IA, Mikhailin VV, et al. (1999) Energy transfer in inorganic scintillators. Rad Eff Defect S 150:1–10
22. Vasil'ev AN (2000) Relaxation of hot electronic excitations in scintillators: account for scattering, track effects, complicated electronic structure. In: Mikhailin VV (Ed) Proc of the Fifth Int Conf on Inorganic Scintillators and Their Applications, SCINT99. Moscow State University, Moscow, pp 43–52
23. Rodnyi PA (1992) Core-valence transitions in wide-gap ionic crystals. Soviet Phys Solid State 34:1053–1066
24. Belsky AN, Glukhov RA, Kamenskikh IA, et al. (1996) Luminescence quenching as a probe for the local density of electronic excitations in insulators. J Electron Spectrosc Relat Phenom 79:147–150
25. Terekhin MA, Vasil'ev AN, Kamada M, et al. (1995) Effect of quenching processes on the decay of fast luminescence from barium fluoride excited by VUV synchrotron radiation. Phys Rev B 52:3117–3121
26. Glukhov RA, Kamada M, Kubota S, et al. (1996) Effect of quenching processes on decay of fast luminescence from BaF_2. In: Dorenbos P, van Eijk CWE (Eds) Proc Int Conf on Inorganic Scintillators and Their Applications, SCINT'95. Delft University Press, The Netherlands, pp 204–205
27. Glukhov RA, Pedrini C, Vasil'ev AN, et al. (2000) Track effects in crossluminescence. In: Mikhailin VV (Ed) Proc of the Fifth Int Conf on Inorganic Scin-

tillators and Their Applications, SCINT99. Moscow State University, Moscow, pp 448–452
28. Chernov SA, Deych RG (1996) Luminescence mechanisms in CsI-based scintallators. In: Dorenbos P, van Eijk CWE (Eds) Proc Int Conf on Inorganic Scintillators and Their Applications, SCINT'95. Delft University Press, The Netherlands, pp 419–422
29. Chernov SA (1997) Relaxation of electron–hole pairs and scintillation mechanism in alkali halide crystals. J Luminescence 72–74:751–752
30. Blasse G (1988) Luminescence in inorganic solids: from isolated centers to concenterd systems. Prog Solid State Chem. 18:79–171
31. Wojtowicz AJ, Wisniewski J, Lempicki A, et al. (1995) Scintillation mechanisms in rare earth orthophosphates. Rad Eff Defect S. 135:305–310
32. Korzhik MV, Drobyskev GYu, Kondratiev DM, et al. (1996) Scintillation quenching in cerium-doped ytterbium-based crystals. Phys Stat Sol (b) 197:495
33. Blasse G, Schipper W, Hamelink JJ (1991) On the quenching of the luminescence of the trivalent cerium ion. Inorganica Chimica Acta 189:77–80
34. Pidol L, Kahn-Harari A, Viana B, et al. (2003) Scintillation properties of $Lu_2Si_2O_7$:Ce^{3+}, a fast and efficient scintillator crystal. J Phys Condens Matter 15:2091–2102
35. Pidol L, Guillot-Noël O, Jourdier M, et al. (2003) Scintillation quenching by Ir^{3+} impurity in cerium doped lutetium pyrosilicate crystals. J Phys Condens Matter 15:7815–7821
36. Guillot-Noël O, de Haas JTM, Dorenbos P, et al. (1999) Optical and scintillation properties of cerium-doped $LaCl_3$, $LuBr_3$ and $LuCl_3$. J Luminescence 85:21–35
37. Guerassimova N, Garnier N, Dujardin C, et al. (2001) X–ray–excited charge transfer luminescence in YAG:Yb and YbAG. J Luminescence 94–95:11–14
38. Guerassimova N, Garnier N, Dujardin C, et al. (2001) X-ray excited charge transfer luminescence of ytterbium-containing aluminium garnet. Chem Phys Lett 339:197–202
39. Glukhov RA, Vasil'ev AN (1995) Monte-Carlo simulation of the creation of excited region in insulators by a photon. Rad Eff Defect S 135:813–817
40. Glukhov RA, Vasil'ev AN (1994) Monte-Carlo study of energy losses in hot stage of electronic excitation relaxation in scintillators. Mater Res Soc Symp 348, pp 387–392
41. Pédrini C, Moine B, Bouttet D, et al. (1993) Time-resolved luminescence of CeF_3 crystals excited by X-ray synchrotron radiation. Chem Phys Lett 206:470–474
42. Belsky AN, Vasil'ev AN, Mikhailin VV, et al. (1994) Experimental study of the excitation threshold of fast intrinsic luminescence of CsI. Phys Rev B 49:13197–13200
43. Belsky AN, Cortes R, Gektin AV, et al. (1997) Excitation mechanisms of CsI fast intrinsic luminescence. J Luminescence 72–74: 93–95
44. Korzhik MV (2003) Physics of Scintillators on a Base of Oxide Compounds. Belarusian University, Minsk, p 263 (in Russian)
45. Averkiev VV, Valbis JA (1985) Luminescence Crystals and Convertors of Ionizing Radiation. Nauka, Novosibirsk, 1985, pp 30–35 (in Russian)
46. Korzhik MV, Trower WP (1995) Origin of scintillation in cerium doped oxide crystals. Appl Phys Lett 66: 2327–2328

47. Baryshevski VG, Kondratiev DM, Korzhik MV, et al. (1994) Mechanism of scintillation in Ce-doped gadolinium orthosilicate Gd_2SiO_5:Ce crystals. J Luminescence 60–61:956–959
48. Suzuki H, Tombrello TA, Melcher CL, et al. (1994) The role of the gadolinium in the scintillation processes of cerium- doped gadolinium oxyorthosilicate Nucl Instr Meth Phys Res A 346:510–521
49. Murk V, Kuznetsov A, Namozov B, Ismailov K (1994) Relaxation of electronic excitations in YAG and YAP crystals. Nucl Instr Meth Phys Res 91(1994):327–330 and references in the paper
50. Kuznetsov AI et al. (1982) Vacuum ultraviolet photo-luminescence of $YAlO_3$. Trudy Instituta Fiziki AN Estonskoi SSR 53:83–96 (in Russian)
51. Schirmer OF, Blazey KW, Berlinger W, Diehl R (1975) ESR and optical absorption of bound-small polarons in $YAlO_3$. Phys Rev B11:4201–4211
52. Cooke DW, Bennett BL, Muenchousen RE, et al. (2004) Intrinsic ultraviolet luminescence from Lu_2O_3, Lu_2SiO_5 and Lu_2SiO_5:Ce. J Luminescence 106:125–134
53. Dujardin C, Pedrini C, Gacon JC, et al. (1997) Luminescence properties and scintillation mechanisms of cerium- and praseodymium-doped lutetioum orthoaluminate. J Phys Condens Matter 9:5229–5243
54. Pedrini C, Dujardin C, Garnier N (2000) Proceedings of III Ural Workshop on Advantaged Scintillation and Storage Optical Materials, Ekaterinburg, Russia, pp. 3–29
55. Glodo J, Wojtowicz AJ (2000) Thermoluminescence and scintillation properties of LuAP and YAP. J Alloys Compounds 300–301: 289–294
56. DiBartolo B (1980) Radiationless Processes. Plenum Press, New York
57. Struck CW, Fonger WH (1975) Unified model of the temperature quenching of narrow-line and broad-band emissions. J Luminescence 10:1–10
58. Pidol L, Viana B, Kahn-Harari A, et al. (2005) Scintillation and thermoluminescence properties of $Lu_2Si_2O_7$: Ce^{3+} crystals. Nucl Instr Meth Phys Res A. 537:22–26
59. Weber MJ (1966) Relaxation processes for excited states of Eu^{3+} in LaF_3. In: Crosswhite HM, Moos HW (Eds) Optical Properties of Ions in Crystals. Interscience, New York, pp 467–484
60. Weber MJ (1967) Selective excitation and decay of Er^{3+} fluorescence in LaF_3. Phys Rev 156:231–241
61. Weber MJ (1967) Probabilities for radiative and nonradiative decay of Er^{3+} in LaF_3. Phys Rev 157:262–272
62. Yen WM, Raukas M, Basun SA, et al. (1996) Optical and photoconductive properties of cerium-doped crystalline solids. J Luminescence 69:287–294
63. Joubert MF, Kazanskii SA, Guyot Y, et al. (2003) A new microwave resonant technique for studying rare-earth photoionization thresholds in dielectric crystals under laser irradiation. Opt Mater 24:137–141
64. Guyot Y, Loudyi H, Kazanskii S, et al. (2004) rare-earth photoionization study by the resonant microwave cavity technique. Radiat Meas 38: 753–757
65. Joubert MF, Kazanskii SA, Guyot Y, et al. (2004) Microwave study of photoconductivity induced by laser pulses in rare-earth–doped dielectric crystals. Phys Rev B 69:165217
66. Bessière A, Dorenbos P, van Eijk CWE (2005). Luminescence and scintillation properties of the small band gap compound LaI_3:Ce^{3+}. Nucl Instr Meth Phys Res A 537:22–26

67. Jorgensen CK (1962) Electron transfer spectra of lanthanide complexes. Mol Phys 5:271–277
68. Jorgensen CK (1964) M.O. description of diatomic molecules containing a transition group atom. Mol Phys 7:417–424
69. Jorgensen CK (1971) Modern Aspects of Ligand Field Theory. North-Holland, Amsterdam
70. Nakazawa E (2002) The lowest $4f$-to-$5d$ and charge-transfer transitions of rare-earth ions in YPO_4 hosts. J Luminescence 100:89–96
71. Pédrini C, Mc Clure DS, Anderson CH (1979) Photoionization thresholds of divalent rare-earth ions in alkaline earth fluorides. J Chem Phys 70:4959–4962
72. Mc Clure DS, Pédrini C (1985) Excitons trapped at impurity centers in highly ionic crystals. Phys Rev B32: 8465–8468
73. Pédrini C, Rogemond F, Mc Clure DS (1986) Photoionization thresholds of rare-earth impurity ions. Eu^{2+}:CaF_2, Ce^{3+}:YAG, and Sm^{2+}:CaF_2. J Appl Phys 59:1196–1201
74. Thiel CW, Crugnel H, Wu H (2001) Systematics of $4f$ electron energies relative to host bands by resonant photoemission of rare-earth ions in aluminum garnets. Phys Rev B64:085107
75. Vugt N, Wigmans T, Blasse G, et al. (1973) Electron transfer spectra of some tetravalent lanthanide ions in ZrO_2. J Inorg Nucl Chem 35:2601–2602
76. Struck CW, Fonger WH (1970) Role of the charge-transfer states in feeding and thermally emptying the ^5D states of Eu^{+3} in yttrium and lanthanum oxysulfides. J Luminescence 1–2:456–469
77. Struck CW, Fonger WH (1971) Dissociation of Eu^{+3} charge-transfer state in Y_2O_2S and La_2O_2S into Eu^{+2} and a free hole. Phys Rev B4:22–34
78. Nakazawa E (1978) Charge-transfer type luminescence of Yb^{3+} ions in $LuPO_4$ and YPO_4. Chem Phys Lett 56:161–163
79. Nakazawa E (1979) Charge transfer type luminescence of Yb^{3+} ions in RPO_4 and R_2O_2S (R=Y, La, and Lu). J Luminescence 18–19: 272–276
80. Van Pieterson L, Heeroma M, de Heer E, et al. (2000) Charge transfer luminescence of Yb^{3+}. J Luminescence 91:177–193
81. Bressi G, Carugno G, Conti E (2001) New prospects in scintillating crystals. Nucl Instr Meth Phys Res A 461:361–364
82. Chipaux R, Cribier M, Dujardin C, et al. (2002) Ytterbium-based scintillators, a new class of inorganic scintillators for solar neutrino spectroscopy. Nucl Instr Meth Phys Res A 486:228–233
83. Kamenskikh IA, Guerassimova N, Dujardin C, et al. (2003) Charge transfer fluorescence and f-f luminescence in yttrium compounds. Opt Mater 24:267–274
84. LUMDETR 5th European Conference on Luminescent Detectors and Transformers of Ionizing Radiation, Sept. 1–5 (2003), Pargue, Czech Republik, abstract book p. 17
85. Pédrini C, Pagost PO, Madej C, et al. (1981) Photoconductivité due à l'autoionisation de Ce^{2+} dans CaF_2, SrF_2 et BaF_2. J de Phys 42: 323–330
86. Pédrini C, Gaume-Mahn F, Mc Clure DS (1982) Photoconductivity due to autoionization of divalent rare-earth impurities in crystals having the fluorite structure. In: Mc Carthy GJ, Siber HB, Rhyne JJ (Eds) The Rare Earths in Modern Science and Technology, vol 3, pp 165–169
87. Blasse G, Schipper W, Hamelink JJ (1991) On the quenching of the luminescence of the trivalent cerium ion. Inorg Chim Acta 189:77–80

88. Van Loef EVD, Dorenbos P, van Eijk CWE, et al. (2000) High-energy–resolution scintillator: Ce^{3+}activated $LaCl_3$. Appl Phys Lett 77:1467–1468
89. Van Loef EVD, Dorenbos P, van Eijk CWE, et al. (2001) Scintillation properties of $LaCl_3$:Ce^{3+} crystals: fast, efficient, and high-energy resolution scintillators. IEEE Trans Nucl Sci 48:341–345
90. Van Loef EVD, Dorenbos P, van Eijk CWE, et al. (2001) High-energy–resolution scintillator: Ce^{3+} activated $LaBr_3$. Appl Phys Lett 79:1573–1575
91. Van Loef EVD, Dorenbos P, van Eijk CWE, et al. (2002) Scintillation properties of $LaBr_3$:Ce^{3+} crystals: fast, efficient and high-energy–resolution scintillators. Nucl Instr Meth Phys Res A 486:254–258
92. Moine B, Courtois B, Pédrini C (1989) Luminescence and photoionization processes of Yb^{2+} in CaF_2, SrF_2 and BaF_2. J Phys France 50:2105–2119
93. Moine B, Pédrini C, Courtois B (1991) Photoionization and luminescences in BaF_2:Eu^{2+}. J Luminescence 50:31–38
94. Kaplyanskii AA, Smolyanskii PL (1973) Polarized luminescence of CaF_2–Yb^{2+} crystals. Opt Spectrosc 34 :361–362
95. Rent EG (1976) Luminescence of divalent Eu and Yb ions in fluorite-type crystals. Opt Spectrosc 40:55–57
96. Kaplyanskii AA, Medvedev VN, Smolyanskii PL (1976) Spectra, kinetics, and polarization of the luminescence of CaF_2–Yb^{2+} crystals. Opt Spectrosc 41:615–619
97. Zapasski VS, Feofilov PP (1976) Magneto-optical studies of the radiative state of divalent ytterbium in fluorite crystals. Opt Spectrosc 41:620-622
98. Kaplyanskii AA, Medvedev VN, Smolyanskii PL (1977) Stress polarization of luminescence and the structure of emitting states of CaF_2–Yb^{2+} crystals. Opt Spectrosc 42:74–78
99. Rent EG (1978) Characteristics of the broadband luminescence of Eu and Yb ions in crystals with the flurite structure. Opt Spectrosc 45:291–294
100. Wong WC, Mc Clure DS, Basun SA, et al. (1995) Charge-exchange processes in titanium-doped sapphire crystals. II. Charge-transfer transition states, carrier trapping, and detrapping. Phys Rev B51:5682–5698
101. Spaeth JM, Meise W, Song KS (1994) The nature of the X-ray–induced luminescence and the hole centers in CsI:Tl studied by optically detected electron paramagnetic resonance. J Phys Condens Matter 6:3999–4008
102. Nikl M (2000) Wide band gap scintillation materials: Progress in the technology and material understanding. Phys Stat Sol (a) 178:595–620

4 Influence of the Crystal Structure Defects on Scintillation Properties

Abstract. This chapter discusses the influence of different crystal structure defects on the scintillation crystal conversion efficiency, energy transfer, luminescence yield and light collection, as well as on their radiation hardness. During the synthesis of crystalline media defects are inevitably produced and are classified according to their size and shape: point, linear and three-dimensional defects. Another type of defects are produced in the scintillators under ionizing radiation. Charged particles as light as electrons create charge defects in crystals. Heavier charged particles like protons, α-particles, hadrons and nuclear fragments loose much more energy when colliding with the lattice ions, resulting in relatively large damaged area of several crystallographic cells. The impact of these radiation induced defects on the radiation damage is presented, in particular on the scintillation efficiency and on crystal transparency. The dynamic of these effects is discussed in detail, for the damage building as well as for its recovery. The chapter concludes with practical considerations on how to improve scintillator radiation hardness.

The crystal scintillation properties are strongly related to their crystallographic structure. In spite of fact that the majority of scintillation crystals are isotropic for the propagation of light the scintillation efficiency depends on the other hand on the quality of the crystallographic structure and on the presence of defects. In fact all the components of the scintillation yield (conversion efficiency, transport, luminescence yield and light collection) are to some extent dependent on the structural quality of the lattice.

The conversion efficiency can vary as a function of the crystal alloying by replacement of a fraction of lattice ions by isovalent ions. It is also dependent on modifications of solid solutions which is one of the modern trends in research and development of new scintillators, for example LYSO and LuYAP.

The energy transfer is influenced by a wide range of structure-sensitive phenomena, for example, carrier capture in deep and shallow traps, color centers and other radiation-induced defect formation, chemical transformations of the activator with parasitic centers, relaxation of electronic excitations at point defects, etc.

The yield of luminescence depends also on the quality of the crystal. The selection of the optimum activator concentration and its homogeneous distribution in the crystal lattice are necessary to optimize this parameter.

Harmful impurities cause perturbations in the scintillation mechanism and are often related to the appearance of afterglow phenomena.

The light collection is extremely sensitive to the material transparency. The presence of absorbing and scattering centers in a host crystal, inhomogeneity of refractive index due to internal stresses, etc. are common sources of light losses.

The different causes of scintillation loss are schematically shown in Fig. 4.1. It is clear that all of them are directly or indirectly connected with imperfections of the crystal structure.

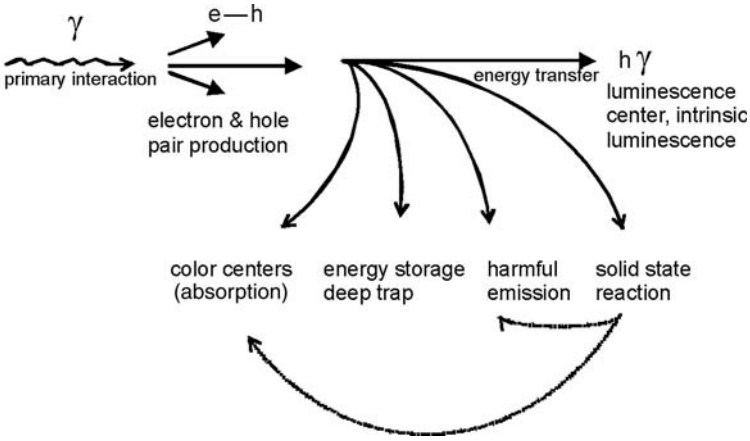

Fig. 4.1. A channel of scintillation loss

In most of the cases scintillators are based on single crystals which provide the best and most homogeneous conditions for the scintillation process: (i) minimization of parasitic defects, excitation and trap carriers, (ii) maximum purity of the material, (iii) optimum distribution of the activator, etc. More detailed information about single crystal growth, purity, and quality is given in Chap. 6.

4.1 Scintillation Media

In addition to single crystalline scintillators other solid inorganic materials are known and widely used. The role of the defects in such media is different from the single crystalline form.

- *Scintillation glasses.* These were the first choice for high energy physics in the mid 1960s. Li-based glasses are the cheapest commercially available solution for neutron detection [1]. A glass scintillator composed of Tb-doped gadolinium silicate glass is used in large area and fiber optic plate detectors

for industrial X-ray inspection systems [2]. Glasses are attractive media because of their relatively simple technology. On the other hand, the irregular lattice structure does not allow us to create efficient carrier transfer conditions and as a result all known glass scintillators have a relatively low light yield.

- *Polycrystalline scintillators.* Single crystal press forging is the way to increase the mechanical strength of materials. "Single-polycrystal" transformation is a typical procedure for material hardening. The easy to cleave crystals (such as alkali halides) can be forged or extruded at elevated temperatures for some applications, for example well logging that requires rugged scintillators [3]. Some time ago forging technique was efficiently developed for the large area scintillator design used for Anger (SPECT) camera [4]. It was found that the specific plastic deformation and the introduction of internal stresses did not suppress significantly the luminescence yield [5].
- *Scintillation powder.* This scintillation medium is typical for the screen development and applications. The low transfer of light between powder grains allows us to obtain a high spatial resolution in such screens. X-ray phosphor powders are extensively used in medical digital radiography. There are two main options for these materials: conventional intensifying screens and photo stimulated storage screens. Examples are LaOBr:Tm and Gd_2O_2:SiTb for X-ray intensifiers and BaFBr:Eu [6] based screens for storage applications. However, the problem of producing X-ray screens with a high scintillation efficiency is not really solved yet. Scintillation powder in itself is not a very convenient material for practical use. Therefore in the beginning of the 1980s a new technology was developed for the production of scintillators in the form of fine-dispersive particles distributed in an organic polymerized material matrix [7–10]. In particular, BaFCl:Eu and BaFBr:Eu powders in polyvinylnaphthalenetoluene matrix, alkali halides doped by Tl ions mixed with organic compounds of the benzene series [8], or organic siloxanes [11], etc. were proposed as the media for low energy X-ray detection. The organic material must have a refraction index as close as possible to the one of the powder. The advantage of such a method is the possibility of making detectors of any area, shape, and thickness. It may be used as a coating on practically all substrates. Such scintillators ensure a maximum light collection and a good matching to the light receiver.
- *Scintillation ceramics.* These types of scintillators have been developed and used for medical and industrial CT applications [12, 13]. Several compositions of such ceramics are shown in Table 4.1 with a relatively high yield, reasonable radiation hardness, and low afterglow in spite of the high concentration of structure defects. Typical ceramics have an average grain size of 30 μm and reach after isostatic pressing a relative density of more than 99.9% of the corresponding single crystal. These scintillators are usually slightly transparent or even translucent but the recent trend is to produce

more and more transparent ceramics by the introduction of nanotechnologies to produce very fine grain raw materials.

- *Scintillation films.* Epitaxial growth is the currently used method to obtain thin scintillation films. This is an efficient way for X-ray screen production. Practically all known bulk scintillation materials are also available in thin films.

Table 4.1. Comparison of some properties of single crystalline and ceramics scintillators

Material	X-ray attenuation coefficient (cm^{-1})		Emission λ (nm)	Relative light output (%)	Primary decay time (s)	After-glow (%)	Radiation damage (%)
	70 keV	500 keV					
CsI:Tl	34	0.49	550	100	1×10^{-6}	0.3	+13.5
$CdWO_4$	56	0.91	530	30	5×10^{-6}	0.02	−2.9
$Y_{1.34}Gd_{0.6}Eu_{0.06}O_3^f$	26	0.71	610	70	1×10^{-3}	<0.01	< -1.0
Gd_2O_2S:Pr,Ce,F	52	0.8	510	80	3×10^{-6}	<0.01	−3.0
$Gd_3Ga_5O_{12}$:Cr,Ce	32	0.7	730	40	14×10^{-5}	0.01	−0.3
$BaHfO_3$:Ce	64	0.95	400	15	25×10^{-9}	NA	NA

These examples illustrate the different criteria and influence of defects on the properties of scintillators. Nevertheless some basic principles have been progressively defined by experience in developing and optimizing scintillator production for large scale applications.

4.2 Defects in a Crystal

Traditionally the classification of crystal lattice defects is based on their size. Usually three kinds of defects—point, linear, and three-dimensional—are identified.

Point defects are ion vacancies and interstitials, impurity atoms or ions and their primary aggregates, radiation-induced defects like color centers. Such defects are characterized by quick internal stress relaxation with the distance from the point defect, and weak interaction with other defects.

Linear defects are dislocations with all possible configurations such as dislocation loops and/or dipoles and different dislocation substructures [14]. These defects, particularly when they appear in clusters, are the source of internal stresses.

Moving dislocations can discharge some isolated or aggregated point defects. Dislocations can also help charge transfer and color centers bleaching.

There are different kinds of three-dimensional defects which appear as macroscopic inclusions into the crystal lattice, for instance, foreign phases, voids, pores, and so on.

4.2.1 Internal Point Defects

There is always a certain concentration of internal point defects (anion and cation vacancies, some clusters of them) in a crystal in thermodynamic equilibrium. The equilibrium concentration of such defects is generally not high, about 10^{12} cm^{-3}, but their actual content may be much higher at room temperature. Plastic deformation of the material, internal stress relaxation, mechanical cutting, and sample treatment may introduce up to 10^{18} cm^{-3} vacancies. In specific cases crystal annealing at high temperatures can also increase the concentration of vacancies for example through the dissociation of electric dipoles [15, 16].

An increase of the concentration of vacancies leads to the formation of clusters of two, three, or even more vacancies [16]. Such defects do not influence the crystal transparency, although they can initiate the capture of carriers and energy storage mechanisms in the crystal.

In some crystals internal defects can induce absorption bands (especially in the UV range) which are likely to decrease the crystal transparency at the light emission wavelength. As an example we note that an increase of the absorption coefficient from $0.01\,cm^{-1}$ up to $0.02\,cm^{-1}$ in the scintillation light spectrum results in a decrease of the light output of the standard NaI(Tl) detector up to 30–40% and in a significant deterioration of the energy resolution.

4.2.2 Impurities

Impurities in crystals are far more diverse in comparison with internal point defects. It is related not only to the chemical elements diversity but also to the differences in electron shell structure types and valency and to the ability to create different kinds of dipoles and primary aggregates. Impurity ions with parameters close to some of the lattice ions can form solid solutions, i.e. states where they replace the matrix ions in some crystal lattice sites. This is particularly true for isovalent impurities with an ionic radius close to the one of some lattice ions. Heterovalent impurities can also be introduced in the crystal lattice but their excess (or deficit) charge must be compensated by other point defects. As a rule, heterovalent impurities form impurity-vacancy dipoles, and the electric neutrality of the lattice (charge compensation) is conditioned by their close association with the corresponding vacancy. In the recent years it has been stipulated that in some fluorides and complex

three- and four-component dielectrics the compensation may also occur by association with interstitials ions.

In general one can distinguish activating impurities (i.e. impurity influencing the scintillation process itself) and parasitic impurities that decrease scintillation efficiency.

4.2.3 Linear Defects

As a rule, only point defects are considered to influence the scintillator performance and their radiation hardness. Linear defects such as dislocations are assumed to have a small contribution to these effects. This approach is strictly speaking not correct. In the early 1980s the "deformation luminescence" phenomenon was discovered and described [17]. This effect embraces a range of phenomena during crystal deformation giving rise to the excitation of luminescence under the displacement of dislocations. In practice the internal stresses are not large enough to produce the displacement of dislocations. However, in the processes of crystal growth and during the mechanical treatment, deformation-induced effects may become quite large. There are other processes where the deformations influence the scintillator performances. A typical example is the press forging technique for the crystal hardening and density increase [4]. Crystal extrusion allows us to manufacture long length scintillators with practically the same scintillation performance as for single crystals grown by traditional methods. The first large samples of SPECT detectors were based on NaI(Tl) crystals deformed at high temperatures. Another example is the transformation of a single crystalline medium to a polycrystalline state. The progress of the forging technology allow us to obtain high material transparency, good scintillation performance (energy resolution), and good homogeneity of the polycrystalline bulk. As a matter of fact this technique of crystal preparation does not limit the crystal size. Figure 4.2 illustrates an example of a press forged NaI(Tl) crystal.

Different phenomena are observed in deformed crystals.

Moving dislocations cause the formation of numerous vacancies and vacancy complexes in crystals [15, 20]. The concentration of such defects may reach the level ($10^{18}\,\mathrm{cm}^{-3}$) which is comparable or even exceeds the concentration of impurities. Obviously, "deformation-induced" vacancies are in no way different from "normal" vacancies resulting from the thermodynamic equilibrium, but their concentration is by 5–6 orders of magnitude larger.

Post-deformation-induced luminescence is now a well-known phenomenon and it was described in [18] for the first time. Later, the same effect was studied for pure CsI in respect to fast UV scintillation optimization. It is possible to demonstrate the correlation between the luminescence yield and the excess of vacancies produced by plastic deformation. The vacancy concentration in this case grows with the increase of deformation (ε) as $\varepsilon^{2/3}$ [19]. In the luminescence spectra of such samples new bands at 460–480 nm appear as seen in Fig. 4.3. This new emission has a decay time of about 1–6 μm and is parasitic

Fig. 4.2. A NaI(Tl) large size slab after press forging

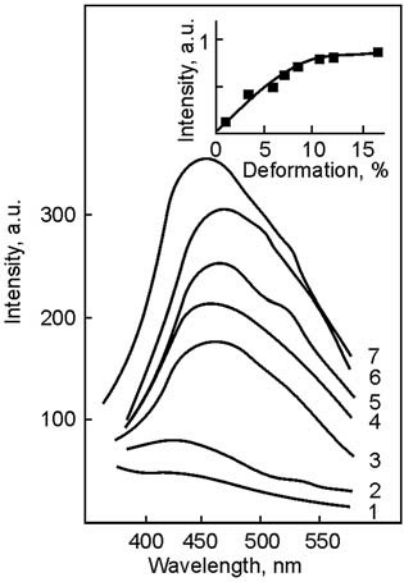

Fig. 4.3. Luminescence spectra of deformed CsI crystals: (*1*) no deformation, (*2*) 1%, (*4*) 3%, (*5*) 7%, (*6*) 8.5%, (*7*) 17%, (*3*) the same as (*7*) after 40 days of aging [20]

to the fast UV scintillation. With time the vacancy excess concentration is gradually relaxed through their diffusion and sink into dislocations and grain boundaries. However, the crystal does not reach the equilibrium concentration level (and, correspondingly, the fast/total ratio) even after dozens of days.

The deformation conditions (deformation rate and degree, the deformation temperature, crystallographic orientation of the sample, and so on) are

extremely important from the point of view of the introduction of vacancies, their stability, and evolution. In [15], for example, it was shown that point defects in alkali-halide crystals do not practically accumulate at temperatures higher than approximately 250 °C. They are actually being formed, but due to their high mobility, they sink to the dislocations.

The deformation sensitization of activated scintillators is an effect which is connected with dislocations in the crystal. Moving dislocations interact not only with each other but also with impurity defects (activator ions), which can be initially localized in the crystal lattice in a nonrandom way, especially for highly doped crystals where the distance between activator ions is not very big and they can easily interact with each other and form complex centers decreasing the luminescence efficiency. Moving dislocations can contribute to the activator homogenization. In [21] it was shown that in CsI(Tl) (7×10^{-2}% Tl) and CsI(Na) (8×10^{-3}% Na) the deformation did not change the luminescence spectra. But while increasing the CsI(Tl) deformation (0%, 2.8%, 6.6%), the ratio of the activator luminescence intensity was increasing as 1:2:2.3. A similar result was observed for CsI(Na) too for which the light output increased by a factor 1.5 after 3% deformation. This phenomenon was named "deformation sensitization" and can be applied not only to dielectrics but to semiconductor crystals also [22]. It illustrates the deformation engineering potential regarding the features of scintillation materials.

In spite of a long story of scintillators there are only a few scintillation materials where crystal defects were investigated in detail. Some of them are complex structure compounds. Oxides have in general a lower plasticity, higher hardness, and brittleness than halides. This is the reason for more precise studies of the influence of point defects on the scintillator performance. Lead tungstate (PWO) is a good example where characteristic defects have been studied by means of electron paramagnetic resonance (EPR) and thermo-stimulated luminescence (TSL).

PWO is very sensitive to the conditions of its synthesis. During the PWO crystal growth by the Czochralski method from stoichiometric raw material a dominant leakage of lead from the melt takes place, leading to the creation of cation vacancies V_c on the lead site in the host [23]. This is also confirmed for the crystals obtained by the modified Brigeman method [24].

Independently of the crystal growth technology, after an X-ray irradiation and the consequent filling of the traps created by point structure defects, only three characteristic electron centers can be observed in lead tungstate by EPR.

The shallowest of them occurs in all crystals since it is an intrinsic defect: an additional electron autolocalized at an anionic WO_4^{2-} complex via a Jan-Teller distortion creating a WO_4^{3-} polaronic center [25–27]. This trap is emptied near 50 K with an activation energy of 50 meV. The electrons released recombine radiatively or are caught by deeper traps.

The second one is a Pb^{1+}-V_0 center which is stable in the crystal up to 175 K [28, 29]. It is not excluded that instead of a Pb^{2+} ion another one (impurity related) may create such a center near an anion vacancy, but what is important is that an electron is trapped by a heterovalent cation in the vicinity of an oxygen vacancy. This center is clearly detected by a relatively large deviation of the g factor of all such magnetically nonequivalent species from g_e. This center is photoionized by IR light with a threshold of 0.9 eV.

The third one is a WO_4^{3-} electron center which is created on the basis of a regular tungstate anionic complex disturbed by a nearby rare-earth (RE) trivalent impurity ion such as La, Lu, or Y [26]. It decays near 97 K. Careful partial annealing experiments showed that the rate of decrease of the EPR intensity of WO_4^{3-}-La coincides with the TSL emission in this temperature region [28,29]. In addition, the doping of the crystal with stable trivalent RE ions such as La, Lu, Gd, and Y with concentrations of some tens of ppm redistributes electron trapping centers, reducing the number of deep ones [30,31]. Such ions localized at Pb sites introduce in the crystal an extra positive uncompensated charge and will thus compete with the creation of V_0 vacancies. In addition the doping ions introduced in a non perfectly stoichiometric crystal (due to PbO evaporation) occupy empty lead sites in the lattice and so suppress the superstructure fraction with its distorted tetrahedra in the crystal. Another way to compensate the cation vacancies is the creation of the 2RE-V_c centers during the doping. However, the small concentration of cation vacancies and compensating centers (typically less than 100 ppm) and their casual distributions in the melt and in the resulting crystal make the probability of creating such associations rather small.

Other intrinsic defects based on cation or anion vacancies with paramagnetic ground state, which are typical of other tungstate crystals, have never been detected in PWO crystals. This indicates that centers such as isolated F^+ (anion vacancy V_0+ e) and O^- have either no energy levels in the forbidden band or are delocalized in the conduction and valence bands. Therefore the only candidates for metastable color centers in PWO crystals under irradiation are cation vacancies capturing two holes of the type $O^-V_cO^-$ and oxygen vacancies simple or complex centers capturing even amounts of electrons.

In crystals with RE doping a second trap center is detected through TSL only with an activation energy of 130 meV. This center is not paramagnetic and is probably a RE-$(WO_4)^{4-}$ center. This is in agreement with the fact that RE-doped PWO crystals show a larger TSL intensity around 100 K as compared to undoped ones. An electron release from the 130 meV traps causes the simultaneous production of lower electron centers by retrapping, as well as through the creation of RE-$(WO_4)^{3-}$ giving an increase of TSL intensity in that resgion.

The deepest electron trap center is a Frenkel-type defect which occurs in the crystal as a result of the displacement of an oxygen ion into an intersite

position. The V_0 vacancy created by the Frenkel defect can also trap electrons giving a center such as $(WO_3)^{2-}$. Such a center appears at irradiation, is stable at room temperature, and shows absorption spectra close to the WO_3 center near the Frenkel defect. Frenkel defect produces an optical absorption band at 360 nm which is converted under ionizing radiation in an absorption band with a maximum near 410 nm. The defects associates and their trapping properties have been discussed in [23, 32].

Each type of defects can potentially influence the scintillation performance. Due to the disposition of electronic centers near the bottom of the conduction band it seems possible to distinguish the influence of each category of defects on the crystal scintillation properties. In spite of a fast exchange of electrons between shallow polaronic and RE distorted regular centers with the conduction band which contribute therefore to the scintillation, there is also a flow of electrons to the deep traps. At high WO_4^{2-}-RE centers, concentration in the crystal this outflow becomes so important that it produces a visible decrease of the crystal light yield. It appears therefore that the strong radiation hardness requirement for the PWO crystals imposes the doping with trivalent rare-earth ions which reduce the light yield of the crystal. The only possibility of meeting both radiation hardness and higher light yield would be to reach a much better structural quality of the crystal than is presently technically possible.

4.3 Change of the Optical and Luminescence Properties by Crystal Defects

4.3.1 Scintillation Light Absorption by Crystal Defects

Absorption bands as well as internal nonuniformities, for example scattered inclusions, gas bubbles, and voids, influence the light collection and contribute to light losses by scattering and absorption. This is particularly important for long scintillators as well as for IAD applications. This is why the study of the optical absorption spectrum in the scintillation emission range is a very important tool to probe the intrinsic quality of the crystal.

The most essential contribution to optical absorption is related to internal point defects, impurities, and radiation-induced point defects.

BaF_2 scintillator is one of the most illustrative examples to demonstrate the influence of impurities on optical and luminescent properties of a crystal. The major drawback of BaF_2 resulting from the emission in the deep UV range is to a great extent compensated by its ultrafast decay time. This behavior corresponds to a very specific mode of scintillation, the so-called cross-luminescence which was then discovered in several other materials (see Chap. 2).

For such materials it is necessary to achieve a very high transparency of the material in the UV range. The main problem is that alkali earth fluorides

are easily contaminated by oxygen and hydroxyl ions which are at the origin of strong absorption bands in the UV range. A theoretical study of the charge state stability and electronic structure of O^0, O^-, and O^{2-} centers in BaF_2 [33] allowed us to identify a large number of transitions from 2p to 3s and 5s states. In [34] Hartree–Fock–Slatter local density discrete variation cluster calculations were made to obtain the energy levels of H_s^-, O_s^-, and O_s^{2-} ions in BaF_2 crystals. Table 4.2 summarizes the possible optical absorption bands in the VUV and UV ranges.

Table 4.2. Calculated optical absorption band of H_s^-, O_s^--, and O_s^{2-}-doped BaF_2 [34]

Impurities	$\lambda_{abs.}$ (nm)	[eV]	Cross transitions
H_S^-	209	[5.9]	$H^-(1s) \rightarrow H^-$ (2s)
O_S^-	230	[5.4]	F^- (2p) $\rightarrow O^-$(2p,3p)
	175	[7.2]	F^- (2p) $\rightarrow$ O−(3p)
	170≈175	[7.0≈7.2]	O^- (2p) $\rightarrow Ba^2$+(5d)
O_S^{2-}	292	[4.2]	F^- (2p) $\rightarrow O^{2-}$ (3p)
	200	[6.2]	O^{2-}−(2p) $\rightarrow Ba^2$+(6s)
	130	[9.5]	O^{2-} (2p) $\rightarrow Ba^2$+(5d)

As far as O^- and O^{2-} ions are concerned, the absorption bands are mainly the result of cross transitions between oxygen ions and Ba^{2+} or F^- ions which significantly contribute to absorption around 200–240 nm.

The UV absorption spectrum of BaF_2 samples shows a strong absorption peak in hydrolyzed crystals as seen in Fig. 4.4 [34] which overlaps the fast emission band.

These problems are essentially caused by the presence of oxygen and hydroxyl ions in the material, but in an indirect way [35]. A good example is given by NaI(TI) crystals grown from melt with different hydrolysis levels or in an atmosphere reach in I_2.

The following reaction takes place at high temperatures [36]:

$$2NaI + H_2O + 1/2O_2 \rightarrow 2NaOH + I_2$$

It releases I_2 and NaOH accumulates in the melt. On the other hand, in iodide reach melt of alkali metals the metathesis decomposition reactions with oxygen predominate over hydrolytic reactions:

$$4NaI + O_2 \rightarrow 2Na_2O + 2I_2$$
$$2NaI + O_2 \rightarrow Na_2O_2 + I_2$$
$$NaI + O_2 \rightarrow NaO_2 + 1/2I_2$$
$$4NaI + 1/4O_2 + 1/2CO_2 \rightarrow 1/2Na_2CO_3 + 1/2I_2$$

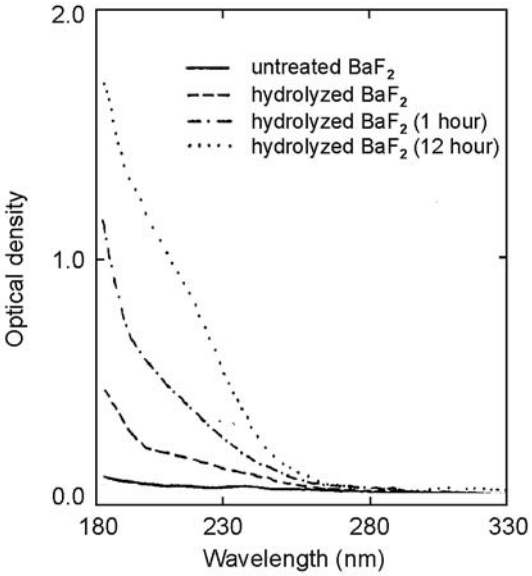

Fig. 4.4. Absorption spectrums for different hydrolyzed BaF_2 [34]

In the case of an excess of I_2 in the atmosphere there is also an increasing probability of generating poly-alkali I_3^- synthesis in NaI crystals [36, 37]. As a result of the accumulation of iodine in the crystal absorption bands appear which overlap with the activator's luminescent spectrum as seen in Fig. 4.5. These specific bands at 340–360, 380, 420, 470, and 520 nm are created by optical transitions between molecular states of I_2^0 molecules and more generally I_n ($n \geq 2$) of different structures and orientations. They are observed in several iodine-loaded solutions and matrixes [38] as well as in irradiated alkali-iodide crystals [39].

The negative influence of the intrinsic absorption in the range of scintillation is clearly seen in the deterioration of the NaI(Tl) crystal performances as shown in Fig. 4.6.

The presence of various impurities having absorption bands in the UV range also affects the transparency of a material in the range of scintillation emission. A typical example is Pb ions in BaF_2. The Pb^{2+} absorption peak efficiently absorbs the fast scintillation and is a critical issue for BaF_2 scintillator development. The data on the role of oxygen containing impurities and polyvalent anions on the detector scintillation efficiency are given in [40].

The negative influence of too high oxidization level in oxide crystals on their transmission spectrum is a well-known phenomenon. This is the reason for yellowish color of not well-optimized tungstate and molibdate crystals. In fact, two wide absorption bands with maxima near 370 and 420 nm cause the crystal's yellowish coloration [41, 42]. The origin of the long wavelength band

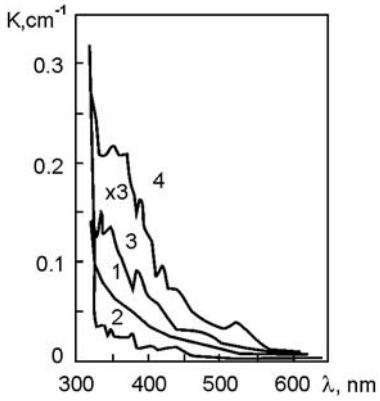

Fig. 4.5. Absorption spectra of NaI(TI) crystals, grown in melt hydrolysis conditions; (*1*) before annealing; (*2*) after annealing at 550°C; (*3*) spectrum 2 subtracted from spectrum 1, note the factor ×3 in scale; (*4*) NaI-I_2 crystal

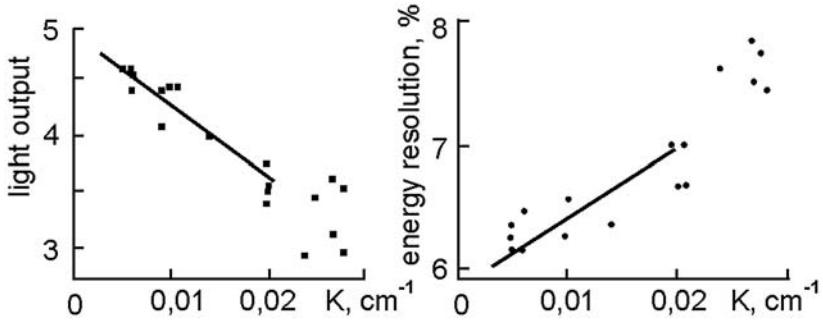

Fig. 4.6. Dependence of light output C (**a**) and energy resolution R (**b**) for NaI(TI) standard detectors

has been understood from the analysis of the electron density distribution in Bi-doped crystals [23, 43]. This band is related to a charge transfer transition in a localized gap state about 1 eV below the bottom of the conducting band. The same localized gap state is created by trivalent lead ions. Crystals grown in air usually show the 420-nm absorption band; however, this band is strongly suppressed in crystals grown in a neutral gas atmosphere or doped with trivalent RE. Moreover, the 420-nm band intensity increases when annealing in air at temperatures close to the crystal's melting point but it disappears under a long vacuum annealing followed by a fast temperature decrease, especially in Bi-doped crystals. However, the yellow color of Bi-doped crystals may be easily recovered just by short, about 5 h, annealing at 950 K in air. The diffusion of oxygen during the annealing is unlikely to explain such changes. One can state that both trivalent lead and bismuth impurity ions provoke the yellowish coloring of the crystal, although the former

seems to be dominant. The same absorption band is observed in lead molybdate as noted in [42] which can be easily predicted from the similarity of the electronic band structures of lead tungstate and molybdate.

4.3.2 Harmful Luminescence and Afterglow

Any luminescence with a decay time much longer than the main scintillation decay time can be defined as afterglow. As was discussed in Chap. 3, this phenomenon is important for different applications and in particular very critical for medical CT devices.

In practice, present technologies for the synthesis and single crystal growth do not allow us to reach an ideal purity and the level of residual parasitic impurities remains the essential limitation of the scintillation efficiency. The efficiency losses are connected with either carrier capture by various traps or energy storing sites. Consider the example of a pure CsI scintillator for which several models have been developed. This material is a unique example of intrinsic luminescence in the alkali-halide scintillators family [46] which found several applications because of its fast scintillation [44, 45]. Figure 4.7 shows its scintillation kinetics and time-resolved scintillation luminescence spectra.

Besides the fast 10-ns scintillation component related to the luminescence peak at 300 nm other emission bands are also observed. They are connected to other slowly decaying centers. In particular, the emission caused by the presence of oxygen ions in the crystal has been identified. These emissions in the green range have a decay time of several microseconds which is typical for ions such as O_2^-. Moreover under irradiation and/or temperature treatment reactions easily occur from O^{2-} ions to O_2^-. All these centers introduce additional harmful luminescence, quench the fast emission and cause afterglow to scintillation. The methods for preventing harmful luminescence and afterglow are generally related to the crystal growth technology. They are (i) preliminary purification of raw material, (ii) additional melt purification, and (iii) attempts to reach the best structure performance.

In activated scintillators one of the mechanisms at the origin of high afterglow level is related to the formation of complex activator luminescence centers. In CsI(Tl), for example, the radiation-induced spectrum shows contributions from Tl_2^0 and Tl^{2+} activator centers. Such centers are formed under UV irradiation. Their combination with F-centers is responsible for afterglow. To prevent the formation of such centers and decrease the amount of afterglow such crystals need to be stored in the dark.

The stability of such centers is not high and dissociation temperatures for Tl_2^0 and Tl^{2+} reach 70°C and 140 °C, respectively. Consequently, low-temperature (130–140°C) annealing of the crystals is also a way to lower the afterglow level and to increase the radioluminescence output by 40–50%.

However, there are examples of the positive role of some doping ions for the scintillation yield of the fast component related to cross-luminescent

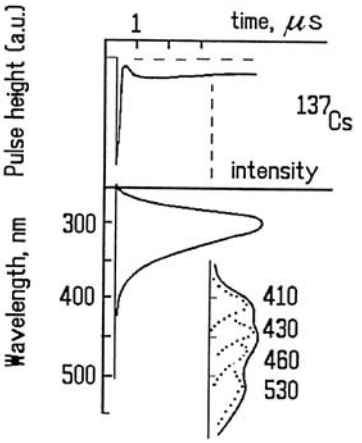

Fig. 4.7. Scintillation kinetics and time-resolved scintillation luminescence spectra of pure CsI scintillator [47]

scintillators, such as BaF_2. The ultrafast core valence luminescence (about 1 ns) in the crystals is accompanied by slow exciton luminescence (600 ns). Improvement of such kinds of scintillators requires quenching this excitonic luminescence. It was shown that different dopings of BaF_2 such as La, Y, Cd allow us to efficiently suppress the exciton luminescence [48].

The precipitation techniques used to synthesize transparent ceramic scintillators is a good approach for obtaining a homogeneous distribution of doping of ions used to reduce the afterglow. Afterglow in $(Y,Gb)_2O_3$:Eu scintillators can be significantly reduced by the addition of heterovalent Pr^{3+} or Tb^{3+} ions to the lattice [49]. The Pr^{3+} and Tb^{3+} additives readily trap holes to form Pr^{4+} and Tb^{4+} which compete with the intrinsic traps responsible for afterglow. This energy trapped on the Pr or Tb sites decays nonradiatively in the presence of Eu ion [50], so the afterglow emission is reduced. These techniques have been used to reduce afterglow in rare-earth oxides [51], oxysulfides [51, 52], and $Gd_3Ga_5O_{12}$:Cr,Ce [53] ceramic scintillators.

4.3.3 Low Background Problem

The influence of parasitic impurities on the background counting rate of scintillators is also an important aspect of the registration efficiency of scintillation materials for several applications. Some isotopes present in the host material are radioactive. There are lots of such intrinsic or extrinsic "radiative" elements, such as K, Cs, and Rb isotopes in halide scintillators or ^{176}Lu in all lutetium-based scintillators. This phenomenon can introduce nonnegligible counting rates for some applications. This is for example one major drawback of LSO for low-energy single photon emission computed tomography (SPECT) imaging as well as for low background applications. Lutetium

has a naturally occurring stable ^{176}Lu isotope that has a very long half-life, 10^{10} years. The abundance of this isotope is approximately 2.76% and it produces a beta decay resulting in several gammas in the range of approximately 100 keV to 700 keV. In a 20% energy window centered at 140 keV the count rate in a 4 mm by 4 mm by 10 mm pixel is approximately 2 counts s^{-1}. This is definitely an unacceptable background for a gamma camera application. It is much less a problem for a PET because of its working mode in coincidence.

4.4 Radiation Damage of Scintillators and Radiation Hardness Improvement

Scintillators as ionizing radiation sensors are naturally subject to radiation influence. Therefore the stability of their parameters under ionizing radiation is mandatory.

From a pragmatic point of view the question of scintillator radiation hardness is reduced to the estimation of the detector scintillation efficiency change when exposed to different kinds of radiation. The practical criterion of the scintillator resistance to radiation is the value of the scintillator efficiency losses under radiation, i.e. the reduction of its light yield. This criterion does not have an unambiguous interpretation as the level of radiation damage depends not only on the type of radiation but also on the dose, dose rate, and recovery (aging) conditions (such as optical bleaching, storage temperature, and exploitation). These aspects appear to be important in the definition of the criteria because they correspond to the working conditions of the detector in general. This is why the study of radiation damage in different scintillators is at the origin of a large multidisciplinary R&D effort carried out in many scientific laboratories worldwide.

From the physical point of view the problem is to study the deterioration mechanisms of the material optical transparency and of the luminescence yield.

The crystal transparency usually drops as a result of the formation of color centers under irradiation. This process obviously affects the light transport efficiency from the point of emission to the photodetector.

The luminescence yield can also be modified if the luminescence centers are subject to transformations under irradiation. Fortunately, the scintillation mechanism is very stable in many crystals, for example, in self-activated scintillation crystals such as $Bi_3Ge_4O_{12}$ and $PbWO_4$, where the oxy-anion complexes from the matrix are the luminescent centers. For these crystals the radiation damage is only related to the optical transmission damage through the formation of color centers. In activated scintillators (NaI(Tl), CsI(Tl), LSO:Ce, GSO:Ce, $LaBr_3$:Ce, and others) both the scintillation efficiency and the crystal transparency can be potentially damaged under irradiation.

The possible impact of the radiation damage is very dependent on the application. If we consider for example the criteria and measurements of the

radiation damage for application of medical imaging (CT) and HEP detectors, they are clearly different. If, in the first case, instability is defined as a change of the functional parameters by a few percents only, in the second case, where the radiation dose is by 5–6 orders of magnitude greater, the light yield deterioration can reach several tens of percents. Depending on whether we consider low or high doses and dose rates the damage mechanisms can be different.

One of the most demanding applications in terms of radiation hardness is high energy physics (HEP). This problem has encouraged large scale R&D efforts on scintillator radiation damage studies.

Since the last decade the development of HEP projects has been based on the development of BaF_2 scintillators for the Superconducting Super Collider (SSC) project [54] in the United States, as well as CeF_3 and PWO crystals for the Large Hadron Cllider (LHC) at CERN in Europe [55]. One of the most critical requirements for these scintillators was to reach a low level of radiation damage [56]. The other example of recent years' developments concerns radiation hard CsI(Tl) scintillator for medium energy physics projects such as BELLE [57] and BaBar [58]. The same basic problems and physical mechanisms have been seen in both classes of materials. The effect of radiation damage results from a combination of two components. The first is connected with structure defects preexisting in the crystal, and the second is conditioned by the defects being produced in the crystal by the interaction with the radiation.

4.4.1 Radiation Defects in Dielectrics

Charged particles even as light as electrons create defects in crystals. About 1 MeV electrons are able to transmit a kinetic energy of the order of 50 eV to an ion. Heavier charged particles such as protons, α-particles, hadrons, and nuclear fragments lose much more energy when collide with the lattice ions. For such interactions with heavy particles, even with a modest energy of about 1 MeV, a relatively large area of several crystallographic cells can be damaged.

Neutron bombardment, either slow or fast, causes the greatest damage to the crystal structure. Slow neutrons have in general a large capture cross section by the different atoms of the crystal cell. When this happens a considerable energy is released, which creates important defects in the crystal. A neutron with an energy of 1 MeV colliding with an oxygen atom transfers an energy of $\sim$40 keV. Consequently a strong neutron bombardment causes deep changes in the crystalline structure of inorganic compounds.

The results of all these interactions are radiation-induced modifications of the crystalline dielectric structure. They are of the same type for various crystalline compounds and different types of ionizing radiation with the only difference that the doses and the dose rates necessary to produce the same effect are substantially different from material to material. Such structure

modifications observed under irradiation can be divided into several groups [59].

The first group consists of microscopic structure changes for which the main structure parameters and particularly the spatial symmetry group do not change. This is by far the most frequent case where the most important parameter is the concentration of initial defects in the crystal inducing the capture of free carriers by vacancies and their recombinations, defects aggregations, sink into dislocations, grain boundary, and crystal surface effects. This concerns the majority of cases where the irradiation rate level is not too high (this is even true up to the dose rates expected in the LHC). There is a rapid relaxation of the lattice and the damage is limited to some electronic structure reconfigurations in the vicinity of preexisting defects in the crystal.

Radiation defects are specific for every kind of ionizing radiation and are determined by the structural configuration of the lattice.

The macroscopic observed effects in the crystals, such as optical transmission, conductivity, and thermo-luminescence properties, result from the integration on a large volume of microscopic structure modifications.

The second group of structure changes consists of modifications of the configuration of the nearest surrounding atom. In a way, this corresponds to the formation of a kind of superstructure associated with the preexisting defects. This situation appears when the defect concentration becomes comparable to the content of some of matrix ions or atoms, i.e. concentrations of the order of 10^{18}–10^{20} cm^{-3}.

Deeper structural changes are generally related to extrinsic element inclusions and substantial deviations from stoichiometry. This corresponds to the radiolysis stage. Such changes are typical, for example, for neutron irradiation with integral fluence of $\sim 10^{20}$ neutrons or more. Such changes have been observed in many compounds under neutrons, electrons, and γ-irradiation [60, 61]. At this level of irradiation the scintillation mechanisms are strongly degraded. At a relatively low dose rate ionizing radiation induces charge transfer to some matrix ions and vacancies preexisting in the crystal before irradiation.

In ionic crystals, containing anions and cations, five possible simple point defects of the crystalline structure have been observed: anion vacancy V_a, cation vacancy V_c, cation replacement by impurity ions, extrinsic atoms in intersite positions, and Frenkel-type defects (anions and cations in interstitial sites).

In halide crystals the electron captured by anion vacancy forms F-center ($V_a + e^-$). In oxide compounds the oxygen vacancies, depending upon the energy level of the corresponding electron traps in the forbidden band, capture one or two electrons, which are in excess in the conduction band after irradiation, with the formation of $F^+(V_a + e^-)$ and $F(V_a+2e^-)$ electron centers. Cation vacancies, in contrast, capture excess holes from the valence band, forming one- and two-hole centers. Heterovalent matrix and impurity

ions undergo modification of their electronic configuration under the influence of ionizing radiation. Frenkel defects, as a result of the displacement of an anion or cation, behave as electron or hole centers, respectively.

In oxide crystals interstitial oxygen causes a distortion of the nearest oxygen polyhedra, creating additional shallow electron traps. Once they have trapped electrons or holes (it is said that they are recharged defects) the defects are in a stable or metastable state. In many cases electron and hole centers (especially Frenkel-type defects) are metastable at room temperature and their relaxation is characterized by a complex decay time curve. To a certain extent, all the color centers are metastable because there is always a temperature at which the annihilation of electron and hole centers takes place, which leads to the recovery of the lattice to its original state.

The main peculiarity of many recharged defects is their ability to absorb light, i.e. to create absorption bands in the transparency window of the scintillator. For this reason these defects are called color centers [62]. The intensity of the absorption depends on the concentration of the color centers as well as on their type, through the cross section of photons to create electronic transitions. Naturally, the effect of induced absorption for metastable centers is temporary. Such centers generally exhibit a natural recovery of the transparency of the crystal with a temperature-dependent kinetics.

The formation and accumulation of color centers in ionic crystals is a multistep process [63, 64]. The first stage of accumulation is connected with the carrier capture by preexisting defects. In this case the energy of formation of color centers is usually small. It is obvious that the kinetics of the accumulation of color centers at this stage depends on the quality of the initial structure and on the purity of the single crystal.

With irradiation doses of the order of 0.1–1.0 Mrad the second stage of crystal coloring takes place, where the accumulation of color centers is caused by their formation and stabilization at regular sites of the lattice [64]. This stage of the accumulation of color centers also depends on the quality of the crystal structure. For most of the HEP modern experiments the requirement for a good stability of scintillator performances is for doses in the 1–10 Mrad range.

At the third stage an active aggregation of color centers and the formation of inclusions from crystal components start to take place [65]. The aggregation of such kind of defects can lead to the formation of colloid metal particles in a crystal. The sizes of the particles are such that their absorption bands can also be within the visible range of wavelengths and absorb scintillation photons [66].

4.4.2 Radiation Stimulated Losses of Scintillator Transparency

As a result of the previous consideration it appears clearly that for the majority of practical situations the damage is essentiality the result of an increased

absorption in the crystal. This mechanism is extremely important and therefore let us consider it in more details.

4.4.2.1 Color Centers and Transparency Losses

As a typical example let us consider CsI(Tl) crystals. CsI(Tl) radiation damage has been discussed by many authors [67–71]. Test results for long CsI(Tl) scintillators were described in [70, 72] but the physical nature of scintillation efficiency decrease has not been considered.

Figure 4.8 shows an optical absorption spectrum for CsI crystals containing various color centers. F-centers formed by electrolytic electron coloration create an absorption band with a maximum at 780-nm. The 780-nm band absorbs only a small portion of the light from the 550-nm emission band. Three experiments were performed to study the absorption of hole color centers. Induced absorption spectra were measured for an aqueous solution of Csl + I_2 (curve 1), CsI crystals additively colored in iodine vapors (curve 2), and the same crystals subject to electrolytic hole coloration (curve 3). In all cases absorption bands with 280 and 340 nm maxima, corresponding to

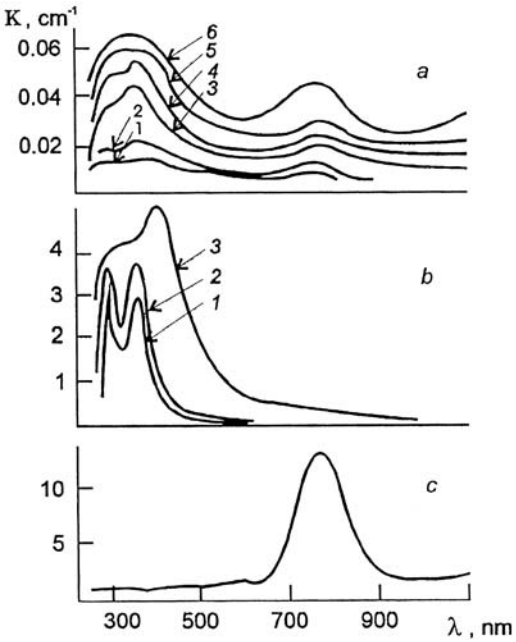

Fig. 4.8. Induced absorption spectra relative to an uncolored CsI sample. **a** γ-irradiation (^{60}Co, 0.2 MRh^{-1}) with doses (MR): 0.01 (*1*); 0.06 (*2*); 0.12 (*3*); 0.69 (*4*); 2.2 (*5*)); 7.2 (*6*). **b** Hole coloration: I_2 dissolved in CsI aqueous solution (*1*); additively colored crystal (*2*); electrolytically (holes) colored crystal (*3*). **c** Elecrolytically (electrons) colored crystal

the so-called V_2 and V_3 color centers [73–75], were observed. In γ-irradiated samples, color centers of both electron and hole types are formed (Fig. 4.8a).

The absorption of hole centers is situated in the wavelength range of excitation of Tl ions. As a matter of fact the absorption of hole centers reduces the energy transfer to the luminescence centers. A wide band of electron color centers overlaps a part of the CsI(Tl) luminescence band so that part of the scintillation light is reabsorbed inducing a reduction of the light collection efficiency (see Chap. 6) and of the scintillator overall light yield.

In the case of formation of stable color centers in a crystal the absorption of scintillation photons is proportional to the reduction of crystal transparency convoluted to the emission spectrum. In this case the efficiency losses are easily calculated by the classic methods of light collection estimation [76, 77].

In the general case, however, radiation-induced variations of the light yield are to be attributed not only to the degradation of the crystal transmission but also to possible variations in the conversion efficiency. The calculated curves of the light yield change along the scintillator length for different induced absorption and conversion efficiency are shown in Fig. 4.9 [72].

While increasing the absorption coefficient at the emission wavelength, the light output decreases. In this case it is not the number of scintillation photons in the crystal which decreases but the share of these photons yielding out of the crystal. It is also important to notice that the number of photons collected at the end of a long crystal becomes sensitive to the position where the scintillation took place, and as it moves from the detector exit window, the value of the light yield constantly decreases.

When simulating the efficiency losses due to the transparency degradation in an irradiated crystal, one should take into account that the distribution

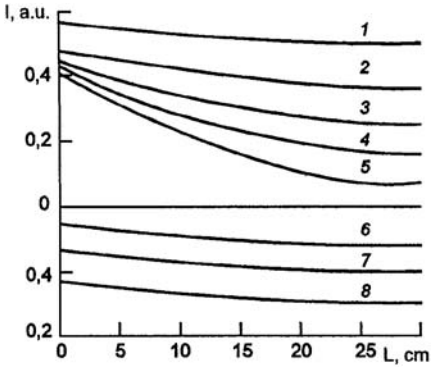

Fig. 4.9. Light output versus longitudinal coordinate for various values of light absorption coefficient k (cm^{-1}) and conversion efficiency η (arbitrary units): (*1*) $k = 0.01$; (*2*) $k = 0.02$; (*3*) $k = 0.03$; (*4*) $k = 0.04$; (*5*) $k = 0.06$; (*6*) $k = 0.01$, $\eta = 1$; (*7*) $k = 0.01$, $\eta = 0.85$; (*8*) $k = 0.01$, $\eta = 0.68$

of color centers with the crystal is simply related to both the distribution of defects in the crystal structure and the distribution of the absorbed energy (Buger's formula) which is in general not homogeneous. For medium energy particles (several MeV) the radiation dose close to the entrance surface is by the orders of magnitude higher than on the opposite face of the detector. At higher energies (GeV) the peak of the energy release is at several radiation lengths (5 to 7) from the entrance window. Correspondingly the crystal coloring (i.e. distribution of color centers) is not homogeneous. This effect must be taken into account both while testing samples and simulating the light collection in a scintillator. This is especially important for high-energy physics. In long-length crystals, usually used in electromagnetic calorimeters, radiation losses due to reabsorption of scintillations by color centers are the dominant effect because of the long path length of light rays related to the length of the crystal and to the large number of light reflections on side surfaces of the scintillator block.

4.4.2.2 Metastable Color Centers

It must be realized that the phenomenological behavior of a scintillator exposed to radiation depends not only on the situation of stable defects but is also very much influenced by metastable color centers, particularly in a range of dose rate corresponding to the kinetics of these defects. Moreover, there are also short lifetime color centers created simultaneously with the excitation of the emission centers. Such centers are connected with very shallow traps and can absorb the scintillations light, i.e. cause short lifetime (also called transient) induced absorption bands.

Let us consider a simple model where ionizing radiation produces at the same time excited luminescence centers and color centers with concentrations $n^i(t)$, $n^c(t)$ decaying with time constants τ^i and τ^c, respectively. Assuming these concentrations of emission centers and color centers to be small enough to neglect correlation effects between them, we can consider that color centers disappear as a result of the recombination of electron and hole centers, as well as of their photoionization under the absorption of scintillation photons with cross section σ. Moreover, the length 1 of the scintillator is such that $1/c \ll \tau^d$, τ^c, where c is the speed of light. Let's define f as the total number of photons detected by the photodetector with a response time $\tau^d \ll \tau^c$ and a detection efficiency equal to 1. For simplicity the light collection problems and spectral distribution of the light are not considered here. Thus the system evolution is described by the kinetic equations [78]:

$$\begin{aligned} \frac{\mathrm{d}n^i}{\mathrm{d}t} &= -\frac{1}{\tau^i} n^i \,, \\ \frac{\mathrm{d}n^c}{\mathrm{d}t} &= -\frac{1}{\tau^c} n^c - c\sigma n^c f \,, \\ \frac{\mathrm{d}f^i}{\mathrm{d}t} &= \frac{1}{\tau^i} n^i - c\sigma n^c f - \frac{1}{\tau^d} f \,. \end{aligned} \tag{4.1}$$

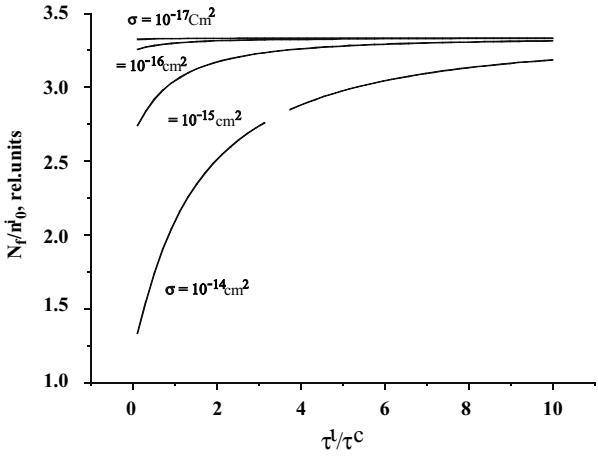

Fig. 4.10. N_f dependence upon the relation τ^i/τ^c for different cross sections of scintillation light absorption by short lifetime color centers

The scintillator response, which is proportional to the number of photons, to be detected by the photodetector, is $N_f = \int_0^\infty f\mathrm{d}t \cdot N_f$, normalized to n_0^i at the beginning of the process, depends on the ratio τ^i/τ^d, where n_0^i is the initial concentration of the excited radiating centers. Figure 4.10 shows the set of curves for different photon absorption cross sections by the color centers. Here $n_0^i = n_0^c = 1 \times 10^{18}$ cm^{-3} and σ has been chosen in the range of the typical spin and parity allowed transitions 10^{-14}–10^{-18} cm^2.

For small absorption cross section there is no change in the number of photons detected by the photodetector. However, the photon losses rapidly increase with increasing absorption cross section in the range of 10^{-16} to 10^{-14} cm^2. It is obvious that this effect is maximal when τ^i and τ^c are of the same order of magnitude. The absorption of photons by color centers is proportional to both the absorption cross section and the color center concentration. In real conditions where there are in general different types of color centers, we will observe the superposition of their contributions according to formulas (4.1).

Thus, even in the absence of metastable color centers but at high concentration of shallow traps, short lifetime centers can lead to a decrease of the scintillation output under the conditions of relatively high-energy release by ionizing radiation in a crystal.

The influence of short-lifetime absorption on the scintillation yield for the detection of γ-quanta and electrons at a small dose rate is negligible. However, the effect becomes substantial for a high excitation rate, for example, in the case of an intense pulse of high-energy γ-quanta.

As an example let us consider the influence of transient absorption on the light yield of a lead tungstate crystal. Recently, besides slowly recovering

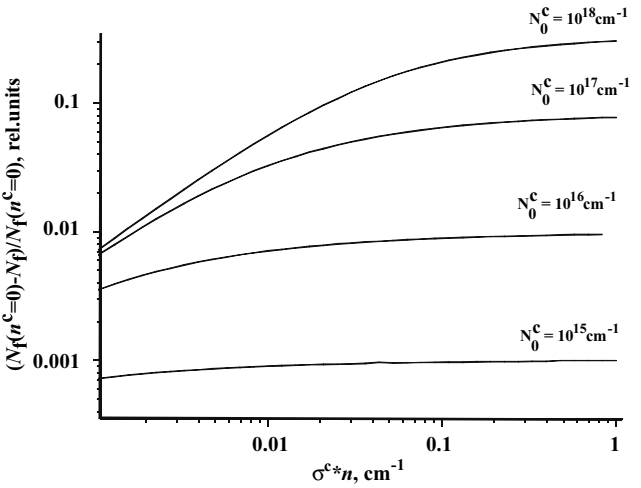

Fig. 4.11. Variation of the value $(N_f\ (n^c = 0) - N_f\ )\ /\ N_f(\ n^c = 0)$ as a function of $\sigma * n^c$ for concentrations of different color centers

color centers, a very fast decaying color center has been detected. This is a shallow electron type center, which forms a wide, short-wavelength, transient absorption band in the crystal with a maximum near 3.5 eV [79, 80] through the $^1A_1 \rightarrow {}^3T_1, {}^3T_2$ transitions in the unstable $WO_3{}^{2-}$ irregular tungstate center. Figure 4.11 shows the change as a function of $\sigma * n^c$ of the value $(N_f(n^c = 0) - N_f)/N_f(n^c = 0)$ where $N_f(\mathrm{n}^c = 0)$ is the number of photons to be detected in the case of the absence of color centers, for different color centers concentrations. This value is directly related to the deviation of the detector response from linearity. The decay time of scintillation τ^{I} is chosen to be 12 ns, a value of 60 ns is chosen for τ^c, and the value of the transient absorption $\sigma * n^c$ is estimated as $0.008\,\mathrm{cm}^{-1}$ from experimental data [79–81]. The typical concentration of oxygen vacancies, which produce these short-living color centers in lead tungstate, is about $10^{18}\,\mathrm{cm}^{-3}$.

Thus, the concentration of the color centers will be about 10^{17}–$10^{18}\,\mathrm{cm}^{-3}$ if we assume that 10–100% of point structure defects can trap charge carriers under ionizing radiation. One can see that the possible decrease of the light yield through transient absorption can be as large as 2–4%. On the one hand, this value may not seem very high. However, it can be critical for the practical use of scintillator (see, for instance, CT applications in Chap. 3).

Under very high irradiation doses the concentration of the color centers becomes high enough so that they start to actively interact with each other forming complex (new types) defects. Even radiation-hard crystal (such as for instance PWO) can become practically opaque to visible light. It is noteworthy that metastable defects after aggregation are transformed into very stable ones and that scintillation properties do not recover after several months

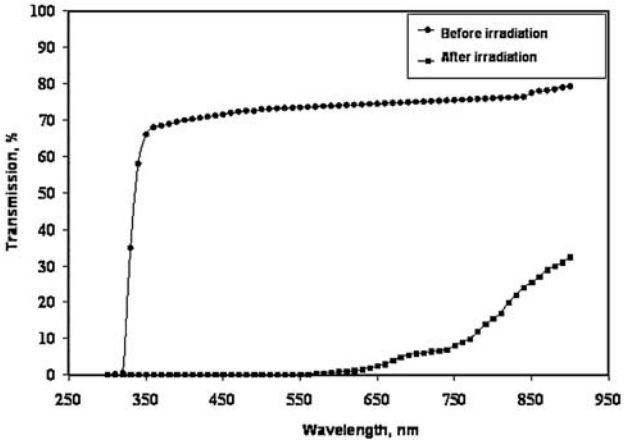

Fig. 4.12. Optical transmission spectra of the lead tungstate crystal with 0.2 mm width before and after irradiation by fast neutrons with 1.6×10^{20} neutrons cm^{-2} integral fluence. The measurement of the samples exposed to radiation was made a year and a half after irradiation

or even years of relaxation. Such situations arise when the concentration of radiation-induced damage reaches the same order of magnitude as regular ions of the lattice. Figure 4.12 shows the optical transmission spectrum of a 0.2-mm-thick lead tungstate plate before and after irradiation by fast neutrons with a fluence of 1.6×10^{20} neutrons cm^{-2}. An almost complete blackening of the material is observed. No scintillation can be seen anymore because the scintillation photons are immediately reabsorbed after their emission in the bulk of the material. A similar result was observed for BaF_2 scintillators but for much less heavy irradiation conditions [82]. After irradiation by a ^{60}Co source up to a dose of 1 Mrad crystals did not recover their transparency even after 260 days.

4.4.2.3 Impurity and Radiation Induced Color Centers

Considering the conditions of color centers formation and accumulation on the preexisting defects it is possible to divide them into two groups, namely, defects containing matrix base ions or vacancies and impurity-related defects. As the vacancy concentration corresponding to the crystal thermodynamic equilibrium at room temperature does not exceed $10^{-13}\,\mathrm{cm}^{-3}$ the concentration of color centers will be negligible for a visible change in crystal transparency even if all vacancy-type defects capture electrons or holes and create stable color centers. But real scintillators always contain different impurities potentially influencing the crystal transparency. Even the purest scintillation crystals contain impurities at the level of at least a few ppm. From the viewpoint of radiation coloring heterovalent impurities are the most harmful. In

such cases, the electrostatic balance in the crystal is restored by the formation of impurity-vacancy dipoles in which the vacancy compensates for the excess charge of the anionic or cationic impurity. A priori both types of impurities are harmful. The stabilization of an electron or a hole causes the stabilization of the center with opposite charge and, as a consequence, the creation of a stable color center.

The basic mechanisms of impurity-stimulated crystal coloring are described in [83–85]. Several studies were carried out in connection with the development of BaF_2 scintillator for the SSC project. In [54,55] many investigations are reviewed. To summarize it was shown that some cation impurities favor the accumulation of color centers, while some others slightly increase the radiation resistance of crystals.

From the alkaline-earth fluorides studies (CaF_2, SrF_2, BaF_2) the attention must be focused on two possible scenarios. The first one involves substitution impurity ions such as transition metal ions (partly filled 3d shell) and rare-earth ions (partly filled 4f shell). These types of impurities can easily change their valence state under irradiation and they have optical absorption bands in the visible and near ultraviolet spectrum. Even traces of such impurities can produce a significant radiation damage. The second scenario involves oxygen and hydrogen. These impurities can be introduced from the raw material and atmosphere during the growth process. The most likely mode of incorporation is OH^- ions substituting to fluorine. A low vacuum allows more moisture to enter into the crystal growth furnace. The scenario of radiation damage involves two process: the creation of F^- and $H^-$and the dissociation of OH^- radicals into O^- and interstitial $H_0{}^{\mathrm{i}}$ centers.

The optical absorption of an irradiated crystal before and after annealing is shown in Fig. 4.13. These data demonstrate the necessity to define special conditions to minimize the introduction of oxygen and hydrogen into the crystal. At some radiation dose the conversion of OH^- to UV active absorption centers is optimal. But annealing of UV absorption centers above a threshold temperature is possible as well as optical bleaching of these absorption bands.

According to [86] several metal impurities can also create additional complex color centers. They are produced according to the following chemical reactions:

$$\mathrm{M}^n + \mathrm{O}^{2-} + \mathrm{V}_\mathrm{a}^+ \rightarrow \mathrm{M}^{(n+1)+} + \mathrm{O}^{2-} + \mathrm{F} \ ,$$
$$\mathrm{M}^n + \mathrm{O}^{2-} + \mathrm{V}_\mathrm{a}^+ \rightarrow \mathrm{M}^{(n+1)+} + \mathrm{O}^{-} + \mathrm{F}^- \ ,$$

where M^{n+} is a metal ion, O is an oxygen ion, V_a is a vacancy of a fluorine ion and F is one "F" type color center.

O^{2-} is the most harmful ion for the radiation resistance of BaF_2. It is one of the three components of the complex color centers formation. OH^- is harmful through the production of oxygen and hydrogen centers.

It should be emphasized that the M^{n+} ion in the formula of complex color center must be a variable valence ion which can offer one or more free

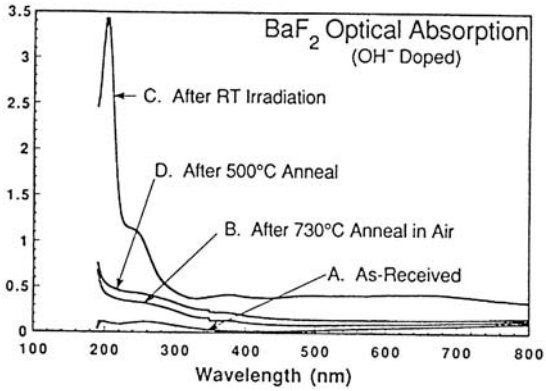

Fig. 4.13. Optical absorption as a function of (**B**) heat treatment, (**C**) irradiation (X-rays, 15 min), and (**D**) thermal annealing in argon [86]

electrons to form a complex color center during the irradiation. At the same time its valence state can affect the energy levels of simple color centers such as F and F^- centers and stabilize them at room temperature.

Similar effects are also typical for alkali-halide crystals where air components, oxygen above all, are the dominant impurities. The sources of such impurities are related to the insufficient purity of the raw material, the absorption of air components on the surface of raw material powder grains and the atmosphere of the single crystal growth furnace (see Chap. 6).

4.4.3 Radiation-stimulated Losses Scintillation Efficiency

Radiation damage studies in different scintillators showed that if scintillation losses are in most of the cases caused by the creation of color centers, they can in some cases be associated with a decrease of the luminescence yield. We will consider here some specific channels of the luminescence yield losses.

4.4.3.1 Excitation Reabsorption

The comparison of radiation-induced absorption with experimental data for Tl^+ excitation and emission bands [20, 72] reveals an overlapping of the hole-type center absorption maximum in Csl with that of the Tl ions excitation spectrum. The presence of stable hole centers causes a certain fraction of excitations to be trapped rather than transferred to TI^+ thereby causing nonradiative losses. As a result, the efficiency of energy transfer to luminescence centers drops, causing a decrease in the scintillation efficiency. The irradiation dose increases the concentration of hole centers and lowers the scintillation efficiency.

Thus, the radiation-induced color centers cause not only a loss in the light output of Csl(TI) crystals due to the transmission decrease (electron-type color centers), but they also influence the scintillation mechanism as a result of reabsorption of the TI^+ ion excitation (hole-type color centers).

At relatively small radiation doses the reabsorbing defects are related to the primary radiation point defects and color centers [72]. Sometimes such losses are not necessarily accompanied by the formation of visible color centers. In such cases the process is revealed by TSL measurement as it is related to the efficiency of energy storage in deep traps. In the crystal materials for which this efficiency is high can be used for information storage or dosimeters. A typical example in the sequence of alkali-halide crystals is given by CsI which is a scintillation matrix and by LiF for which the storage energy is so much larger that it has become the most widely used dosimeter material. Recent studies [87] of a multicomponent matrix of ABX_3 type (A—alkali metal, B—alkali-earth metal, X—halide ion) showed that special alloying makes it possible to suppress or, in contrast, increase the energy storage efficiency in a crystal (Table 4.3) Thus, the possibilities of radiation damage accumulation as a result of a modification of the structure cause the complete degradation of its scintillation features.

Table 4.3. Efficiency of luminescence and energy storage in $LiBaF_3$

Material	Core Valence	Self Trapped Exciton	Ce^{3+}	O^{2-}	Storage
$LiBaF_3$ pure	+++	+++	–	–	+
$LiBaF_3$(Ce)	++	++	+++	–	+
$LiBaF_3$(O)	++	++	–	++	++
$LiBaF_3$(Mg)	+–	–	–	–	+++
$LiBaF_3$(Mg,O)	+	+	–	++	+++
$LiBaF_3$(Ce,O)	++	++	++	+	+

At very high radiation dose absorption centers can be produced by rather complex radiation-induced defects. But in most of the cases the damage is caused by preexisting point defects and color centers.

4.4.3.2 Activator Ion Recharge

Another channel of luminescence efficiency losses is the reduction of activator ions concentration as a result of charge transfer process or solid state chemical reactions.

Since most of scintillators are activated crystals it is of importance to introduce activator ions in the correct valence state to guarantee the scintillation. This is often a difficult aspect of the crystal growth process (see Chap. 6).

Cerium-doped scintillation crystals suffer both optical absorption induced by ionizing radiation and scintillation mechanism damage. Depending on the conditions of synthesis the cerium ion is introduced in the crystals with a 2^+, 3^+, or 4^+ valence states, although the 3 valence state only gives rise to scintillation. The change in the balance between the different valence states under the action of irradiation (especially the recharge of Ce^{3+} ions to the Ce^{4+} state) reduces the concentration of luminescence centers and therefore the scintillation yield.

Let us consider the recharge of such impurity ions by irradiation. The "3+" cerium ion in oxide crystals and glasses are able to suppress slow recombination processes because of their large hole capture cross section. Furthermore, in some cases Ce^{3+} ions also favor the suppression of deep electron centers, thus causing a quick relaxation of some of the radiation-induced optical absorption. For this reason cerium is introduced in the fabrication of glasses when they have to be radiation hard. However, under irradiation of cerium-doped crystals, besides the well-known radiation-induced optical absorption bands, the effects of cerium ions recharge may be observed too. The radiation-induced variation in the concentration of three valence cerium ions means that the scintillation mechanism is modified. The irradiation of cerium-doped crystals may therefore reveal both changes in the optical properties of the crystals, i.e. formation of color centers, and variation in the luminescence efficiency through the modification of the initial valence state of the activator.

The radiation-induced spectra in undoped and Ce^{3+}-doped $YAlO_3$ crystals, as well as in $YAlO_3$:Ce_3^+ and $(Lu_{0.7}$-$Y_{0.3})AlO_3$:Ce_3^+ crystals, illustrate this situation.

In a nonactivated crystal the induced absorption extends over the whole visible range, its peak value reaching $400\,m^{-1}$ at maximum as seen in Fig. 4.14. For comparison even noncompensated lead tungstate crystals grown from cleaned raw material have an induced absorption coefficient two orders of magnitude smaller. The reason for such a big difference resides in a considerable shift from the optimal stoichiometry. The deficit of one of the cations causes a large increase of the anion (oxygen) vacancies contents in the crystal associated with a larger concentration of formation of color centers and to a worsening of the radiation hardness.

However, the induced absorption spectrum is deeply modified by cerium doping. The long-wavelength absorption bands are strongly suppressed. An intense peak near 270 nm is detected in the spectrum of activated crystals made by different methods. Figure 4.15 shows the induced absorption spectrum measured in $(Lu_{0.7}$–$Y_{0.3})AlO_3$:Ce^{3+} crystal grown by the Czochralski

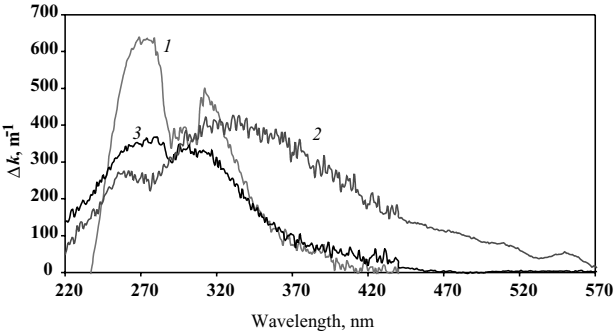

Fig. 4.14. Induced absorption spectra in $YAlO_3$ crystals grown by horizontal freeze method in vacuum: 1—Ce doped, 2—undoped crystal, 3—$YAlO_3$:Ce grown by the Czochralski method in Ar atmosphere. The conditions of irradiation are ^{60}Co (1.2 MeV), dose rate 7 kGy h^{-1}, accumulated dose 103 Gy, $T = 300$ K

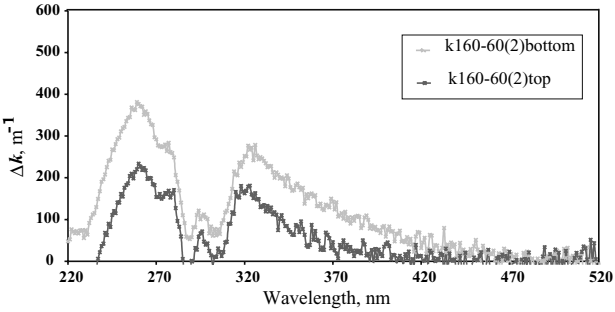

Fig. 4.15. Induced absorption spectra in $(Lu_{0.7}–Y_{0.3})AlO_3:Ce^{3+}$ crystals samples grown by the Czochralski method in inert gas atmosphere and cut out from the upper and lower part of a 180-mm long boule. Irradiation: ^{60}Co (1.2 MeV), dose rate 7 kGy h^{-1}, accumulated dose 103 Gy, $T = 300$ K

method in inert gas atmosphere. The measurements were carried out for the samples cut out from the upper and lower parts of a 180-mm long ingot. The induced absorption spectra are quite similar in shape and intensity for both yttrium mono-aluminate and solid solution of Lu–Y aluminate. It is quite evident that the defect formation process in both crystals is similar when using the same growth method, and, consequently, the approach for radiation hardness improvement for these crystals has to be the same.

In the induced absorption spectra of YAP and $(Lu_{0.7}–Y_{0.3})AlO_3$ crystals doped with Ce^{3+} ions there is a clear window near 300 nm. It is caused by the change in the Ce^{3+} ions excitation band intensity related to the change of the valence state of some of the activator ions. In other words, the radiation induces a charge transfer process and the transformation of the Ce^{3+} to Ce^{2+} valence state. Simple comparison between the initial and induced absorption

spectrum in this window indicates that at least 5% of Ce^{3+} ions are being recharged. Crystal annealing in oxygen atmosphere restores the initial spectra of activator absorption by a re-oxidation of the Ce^{2+} ions.

4.4.3.3 Radiation-Induced Chemical Reactions

While considering the effects induced by ionizing radiation it is necessary to distinguish one more aspect of it. It concerns radiation-induced chemical transformations, namely, the modifications in the impurity defects structure. The above-mentioned example of BaF_2 scintillators transparency loss is also typical here.

The absorption spectra from VUV to UV of BaF_2 before and after γ-irradiation are shown in Figs. 4.13 and 4.16.

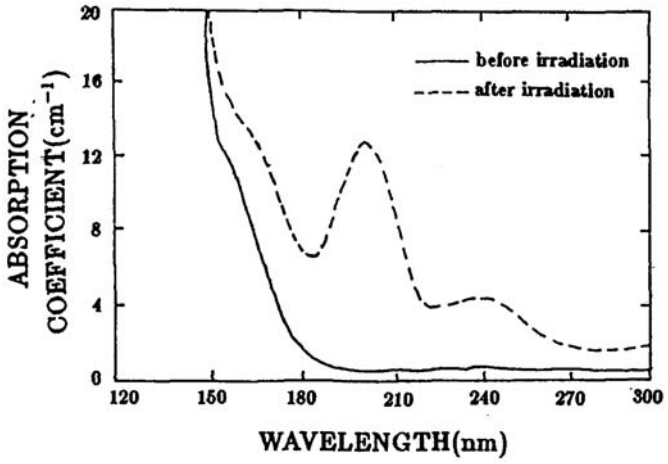

Fig. 4.16. Absorption spectra of hydrolyzed BaF_2, before and after irradiation [34]

A large radiation damage occurs in a treated sample, although no obvious absorption at 192 nm was found before irradiation. This result indicates that only a small amount of hydroxyl or oxygen impurities can lead to a serious radiation damage in BaF_2. Furthermore after irradiation a new peak of absorption at about 200 nm in the IR spectrum emerged, which is related to the H_S^- center.

The radiation-induced change was also observed in the EPR spectrum of hydrolyzed BaF_2 [34]. The spectrum was taken at room temperature with the magnetic field along the $\langle 100 \rangle$ crystal axis. Before irradiation no EPR signal was observed which means that the thermal treatment itself did not produce any modification of the EPR spectrum in BaF_2. After irradiation two groups of lines appeared separated by about 54 mT and symmetrically

placed around $g = 2$. It was concluded that this EPR signal is due to an interstitial atomic hydrogen $H_i{}^0$ in the center of an empty cube of fluoride. Moreover, the complex signal was observed in the central part ($g \sim 2$) of the same EPR spectrum. According to [86] one can state that the edge is probably due to the absorption of $O_S{}^{2-} - F^+$ related to the transition from the 2p level in oxygen to the 1s level of the F center. The EPR spectrum suggests that $H_i{}^0$ exists in treated BaF_2 after irradiation. H_i^0 centers come from the dissociation of OH^- through the radiolysis process,

$$OH^- \rightarrow O_S{}^- + H_i^0$$

The complex signal in the central part ($g \sim 2$) of the spectrum is partially due to $O_S{}^-$.

After irradiation two new absorption bands are observed in the UV range (Fig. 4.16). The H_S^- absorption peaks were also found in the UV and in the IR region. These results suggest that the absorption at 204 nm and ∼240 nm corresponds to H_S^- and O_S^- centers, respectively. The H_S^- center is probably produced by the process

$$H_i^0 + F \rightarrow H_S^-$$

where the center F is created independently under irradiation.

These examples cover only a small part of radiochemical reactions. In alkali-halide scintillators with activator-based luminescence there are also solid-state reactions involving thallium ions. The formation of complex color centers (such as for BaF_2) leads to both transparency loss and decrease in the activator luminescence efficiency. Due to some chemical reactions some centers are created which capture the electron excitations. On the other hand, these new centers can also produce additional luminescence.

Radiation damage of pure CsI scintillators is another interesting example which shows not only a drop of the scintillation yield under ionizing radiation but a complete redistribution of the scintillation kinetics. For this scintillator both the light output value of the fast UV scintillation (the emission peaks at about 300 nm) and the Fast/Total ratio (i.e. the ratio of the fast scintillation intensity to the total light output, i.e. the total amount of fast and slow components) are important parameters. An increase of the radiation-induced slow luminescence characterizes this material. Figure 4.17 shows that for increasing radiation dose the Fast/Total ratio decreases [20].

4.4.4 Approaches to Radiation Hardness Improvement

There are plenty of publications describing the radiation damage effects in many scintillators. However, there are a few descriptions of the methods of improving the radiation hardness of materials and there are no practical recommendations on the production technology of radiation hard scintillators. Primarily, they include (i) preventing radiation coloring in order to maintain the transparency of the scintillator at the emission wavelength; (ii) providing

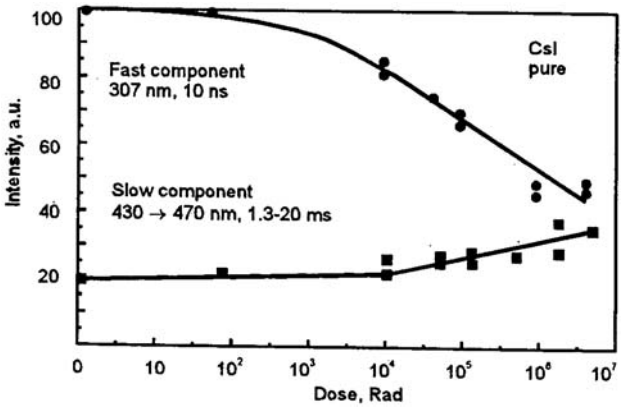

Fig. 4.17. Dose dependence of fast and slow emission components for nominally pure CsI scintillators

a good stability of the activator's state; (iii) suppressing parasitic luminescence; (iiii) minimizing losses at the energy transfer stage, etc.

This is generally considered as being part of the "know-how" of the crystal producers. However, it is very instructive to consider some general engineering approaches to produce radiation hard scintillators. These approaches are based on crystal annealing for the suppression of radiation defects; optical bleaching, i.e. the process of optically stimulated color centers annihilation; specific doping; etc.

Among the different methods of simultaneously suppressing the two radiation damage mechanisms (production of absorbing color centers and decrease of the scintillation efficiency) the use of specific doping is the most effective and widely applied. Certainly the first step is to try to produce crystals with the best intrinsic quality by the use of the highest purity raw materials and by reducing as much as possible the concentration of initial defects. But there is a technological and economic limit to this approach above which compensation of preexisting defects by specific impurities can be successfully used [88].

At the crystal growth of complex oxide compounds for instance, there is a progressive deviation from stoichiometry in the melt and in the grown crystal due to the different vapor pressures of the components of the melt. This leads to the creation of cation vacancies V_c and, as a consequence, to the production of charge-compensating anionic oxygen vacancies V_0 and associated defects of the same type. There is therefore a need to compensate the loss of cations and to simultaneously suppress the increase in the concentration of oxygen vacancies. This can be achieved by additional doping with an impurity ion of $(n+1)$ stable valence state, where n is the valence of the evaporating cation, and with an ionic radius as close as possible as the one of this cation in order to be easily localized in the same oxygen polyhedron. Besides, its segregation coefficient in the crystal growth process should be as close as possible to

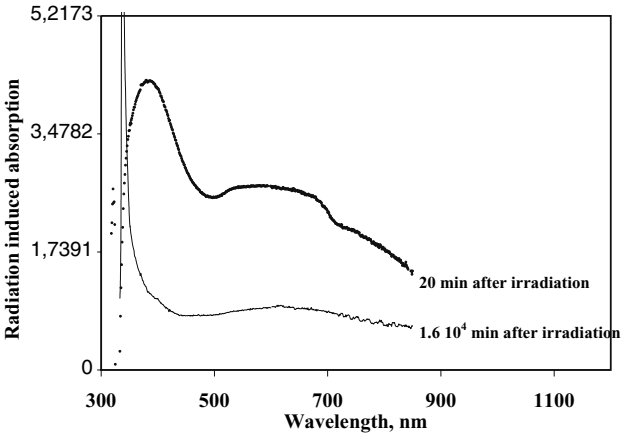

Fig. 4.18. Induced absorption spectra in a nonactivated lead tungstate crystal, measured 20 and 1.6×10^4 min after irradiation, radiation source is ^{60}Co, the dose rate is 10^4 rad h^{-1}, the irradiation time is 20 min, $T = 300$ K

one to allow for a homogeneous distribution. Such ions decrease the total amount of cationic vacancies in the crystal and bring an additional positive uncompensated charge which prevents the emergence of the V_0 vacancies.

Considering the PWO scintillator there is a dominating lead leakage from the melt during the growth leading to the formation of cationic vacancies V_c in the localization of the lead ion in the crystal lattice. A trivalent yttrium ion localized in the lead ion position meets all the above-mentioned requirements. As a result the concentration of cationic vacancies is strongly reduced and, consequently, the creation of anionic vacancies is also suppressed which significantly increases the radiation hardness of the crystal.

As is shown in Fig. 4.18 an undoped PWO crystal shows a dramatic deterioration of its optical transmission in the visible region under ionizing radiation. Crystal doping with yttrium with a concentration of approximately 100 ppm leads to a reduction of the absorption over the whole spectral range by an order of magnitude at least. A more detailed description of induced absorption spectrum and compensation mechanisms is presented in [23]. The same positive effect can be observed in the $PbWO_4$ crystals doped with trivalent La, Gd, and Lu ions. On the other hand, doping with heterovalent rare-earth ions such as Yb and Eu increases the induced absorption up to 200 m^{-1} [90].

Figure 4.19 shows the change of induced absorption at $\lambda = 420$ nm in the $PbWO_4$ crystals doped with different impurities depending on the accumulated dose of ^{60}Co γ-rays (1.23 MeV). For the accumulated doses of 10^4, 10^5, 10^6, 10^7, 10^8 rad, the dose rates were 10^4, 10^5, 3.3×10^5, 4.55×10^5, 10^6 rad h^{-1}, respectively. Crystals with a small number of vacancies because of La (Y-type ion) ion doping are characterized by an independence of the induced absorption with the dose rate up to 10^5 rad h^{-1}. It means that in

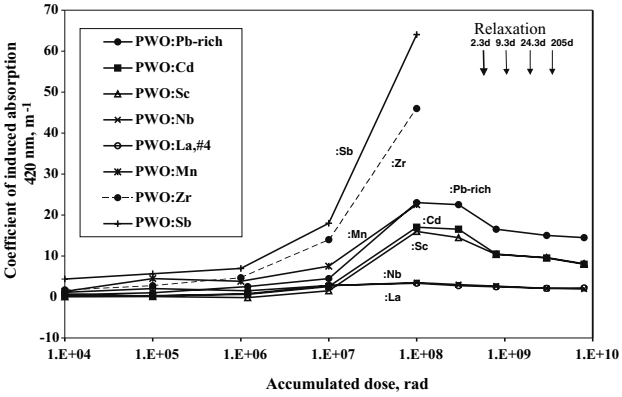

Fig. 4.19. Changes of induced absorption at $\lambda = 420\,\text{nm}$ in PWO crystals, activated with different impurities depending on the accumulated dose when irradiated by ^{60}Co (1.2 MeV), $T = 300\,\text{K}$ [95]

crystals with a small number of rechargeable centers, relatively small dose rates can cause the saturation of formation of electron and hole centers. On the other hand, for crystals doped with Sb and Zr ions a continuous increase of the induced absorption is observed that is obviously the consequence of a considerable rechargeable damage concentration with slow relaxation.

As the dose rate increases above 10^5 rad h^{-1} an additional increase of the induced absorption at $\lambda = 420\,\text{nm}$ takes place which grows with the dose rates. It is due to the fact that the first cause of the lead tungstate crystal matrix damage is the formation of a Frenkel pair. The signature of the Frenkel-type defect in lead tungstate is an absorption band near 350 nm. Under irradiation two electrons are captured by the Frenkel defect and form a deep electronic center [23,98]. This capture produces an annealing of the 350 nm band with a transfer to another band at 410 nm.

Depending on the concentration of the doping the induced absorption spectrum can be significantly modified because of the relative action of different color centers suppression mechanisms. For a concentration of 20–30 ppm La in the crystal, i.e. in the case when only a fraction of the vacancies is compensated by the trivalent impurities there is a strong suppression of the 620 nm band. But new bands at 520 and 470 nm as well as at 720 nm appear which have been masked in the absence of doping by the wide 620 nm band in the induced absorption spectrum. Figure 4.20 shows the spectrum of induced absorption for a $PbWO_4$:La crystal with a relatively small La concentration. At higher trivalent activator concentration there is a further decrease of all the color centers absorption bands. It is clearly shown in Fig. 4.21 for a crystal doped by 100 ppm Y^{3+} ions for measurements 1,674, 27,010, 86,185, and 165,883 s after irradiation. For optimal doping conditions the induced absorption spectrum envelop remains practically the same due to the simultaneous

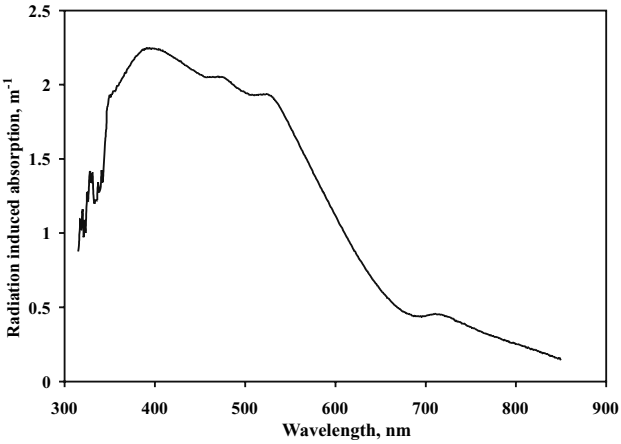

Fig. 4.20. Induced absorption spectrum of a $PbWO_4$:La crystal, the length is 23 cm, the La concentration is 20–30 ppm, the radiation source is ^{60}Co, the dose rate is 10^4 rad per hour, T = 300 K

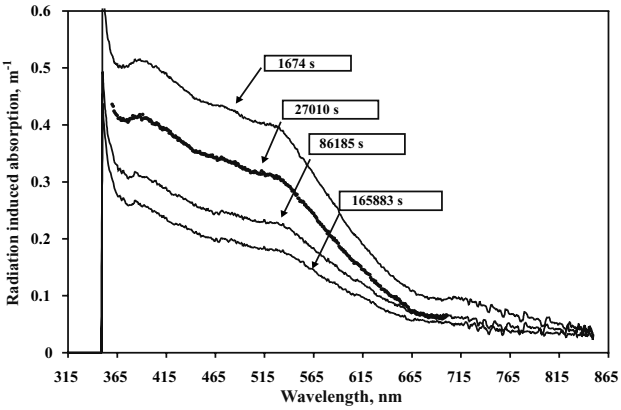

Fig. 4.21. Induced absorption spectra in the lead tungstate crystal, activated by yttrium ions with 80–100 ppm concentration, measured 1,674, 27,010, 86,185, and 165,883 s after irradiation, the source of radiation is ^{60}Co, the dose rate is 104 rad h^{-1}, the radiation time is 20 min, T = 300 K

suppression of all the bands and does not affect the light yield nonuniformity especially for long-size crystals. Such crystals with a low induced absorption are presently used for the production of the CMS calorimeter in CERN. Comparison of the spectra in Figs. 4.18, 4.20, and 4.21 shows that induced absorption spectra are different depending on the concentration of compensating impurity in the crystal. It means that damage and recovery kinetics of such crystals will also be different. It may have a negative impact on the energy resolution of calorimetric systems working in irradiation environment

with a complex time profile. That is why for precise electromagnetic calorimetry not only the value of the induced absorption at a given wavelength but also the reproducibility of the induced absorption spectrum from crystal to crystal in the scintillation spectral range has also to be specified.

The approach which works well for oxides is not as efficient for cross- luminescent fluoride crystals. An additional problem there is related to the possible UV absorption by optical transitions of the doping ion. Many rare- earth ions show in this region interconfiguration and charge transfer transitions. The method of radiation hardness improvement by doping with isovalent or aliovalent impurities has been investigated for the BaF_2 scintillator. The influence of alkali, alkali-earth, and rare-earth doping on the BaF_2 radiation damage has been systematically investigated. Doping ions have been divided into three groups: harmless elements, harmful elements, and useful elements. For example, La^{3+}, Lu^{3+}, and Y^{3+} are harmless for the radiation hardness of BaF_2 if the doping level is only of a few ppm. A strong absorption band was found at 1 ppm of Ce^{3+} or Pr^{3+} doping. The crystals doped with Eu^{3+}, Yb^{3+}, and Dy^{3+} show completely different results. These elements can eliminate color centers in the visible range and increase radiation hardness up to 1 Mrad irradiation while undoped crystals become brown at the same dose.

These studies were unfortunately stopped when the SSC project was closed down. The complete implementation of these ideas and methods for improving the radiation hardness in nonoxide crystals has been fulfilled for the CsI(Tl) and CsI(pure) scintillators.

The previous examples refer to the increase of the radiation hardness of undoped (self-activated) scintillators. However, as was already mentioned, most scintillators are activated crystals. The YAP:Ce scintillator is a characteristic example. The initial and gamma-radiation induced absorption spectra for different $YAlO_3$ crystals are shown in Fig. 4.22. The initial absorption center of the Ce^{3+}-doped crystal in the near UV range results from interconfiguration transitions from the ground state $4f^15d^0$ of the Ce^{3+} ion to a triplet level with the $5d^1$ configuration split by the crystal electrostatic field. Under irradiation the crystal shows an induced absorption at the level of several hundreds of inverse meters in the 220–500 nm spectral region. Doping the crystal with zirconium at the level of 100 ppm considerably improves these results.

The radiation-induced absorption in the emission range has been nearly completely suppressed in crystals doped with zirconium or annealed in hydrogen. Moreover, the recharging effect of Ce^{3+} also decreases and does not exceed 2%. In the $YAlO_3$ crystal growth process there is a dominant aluminum leakage from the melt [89]. The aluminum ion vacancies are compensated by zirconium ions localized in an oxygen octahedron. Zirconium ions also reduce the V_0 concentration in the crystal suppressing electron centers based on oxygen vacancies.

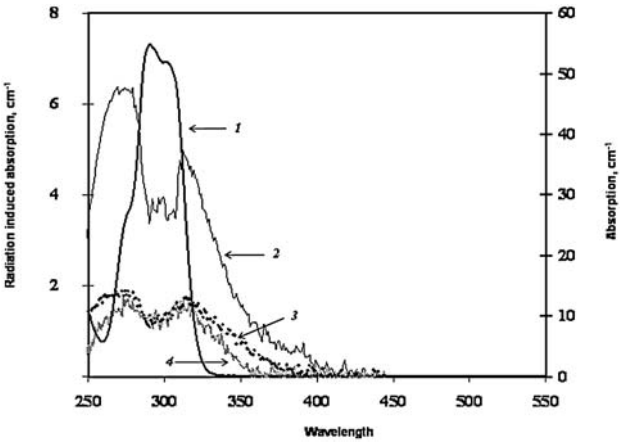

Fig. 4.22. Room temperature absorption spectra of the $YAlO_3$:Ce crystal: initial (*1*) after irradiation (*2*); induced absorption of a grown $YAlO_3$:Ce,Zr crystal (*3*) and the crystal grown and annealed in hydrogen (*4*); irradiation conditions: ^{60}Co (1.2 MeV), dose rate 7 kGy h^{-1}, accumulated dose 90 Gy

This approach is less suitable for complex oxides where one cation is localized in sites with several coordinations, for example, in crystals of $Y_3A_{15}O_{12}$, $Lu_3A_{15}O_{12}$ of the garnet structure, where aluminum ions are localized in octahedral and tetrahedral coordinations. The Zr ion is not really effective as it will go preferentially in octahedral coordination sites and leave uncompensated cation vacancies in tetrahedral sites. In this case co-doping by two impurity ions is required, one for each coordination site.

In conclusion it must be noticed that in spite of a longstanding research and development for radiation hard scintillators, no universal approach to suppress radiation damage has been found, if it exists at all.

Different approaches have been used for different materials. Figure 4.23 shows the level of radiation hardness for CsI(Tl) at the beginning (before intensive R&D effort) and at the end of the 1990s [91]. The possibility of radiation hardness improvement has allowed this crystal to be used not only for barrels but also for the end caps calorimeters where the radiation levels are generally one order of magnitude higher. The example demonstrates that the potential for radiation hardness improvement has not been exhausted even for thoroughly studied materials.

However, all the above-mentioned examples illustrate the basic mechanisms of radiation damage and the different methods which are applied to improve radiation hardness of scintillators. One may confidently say that the potential to produce more radiation hard scintillators is far from being exhausted.

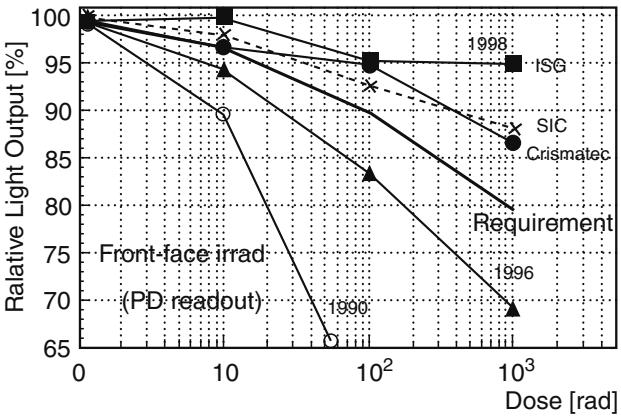

Fig. 4.23. CsI(Tl) scintillator. Radiation damage improvement during the last decade

4.5 Recovery of the Radiation-Induced Absorption

In many cases the radiation damage process is balanced by a spontaneous recovery of the crystal optical and luminescence parameters. This recovery occurs during irradiation and continues after irradiation is stopped. Such a phenomenon is typical both for halide and for oxide scintillators. The majority of radiation induced centers are not stable in time and their relaxation during the aging is the reason for the scintillation performance recovery. Moreover, point structure defects such as vacancies are generally not stable in the crystal at room temperature as they tend to sink to the dislocations or to the free surfaces. Therefore the recovery of the crystal structure also leads to the radiation damage recovery however in a longer time scale.

The recovery rate can also be accelerated by ionization of color centers by optical photons or by heating up the crystal up to a temperature where thermo-ionization of the deep electron and hole centers becomes possible. A well-known example of enforced recovery is the so-called optical bleaching of damaged materials: in a short time the initial spectral properties of the crystal are recovered by light illumination at a proper wavelength of the bulk material.

Most of the scintillation crystals are installed in complex experiments for a long operational time, and in a strong radiation environment, which makes enforced recovery difficult for technical reasons. Heating the detector is very often practically impossible. In real situations an acceptable radiation hardness behavior can be reached by tuning some of the crystal parameters in order to match the radiation exposure time profile to the damage and recovery kinetics of the crystal. For instance, a year cycle of the LHC accelerator will consist of three 60 days operation periods with high radiation levels, interleaved with 14 days stop intervals, where no radiation will be applied to

the experiments. After these three cycles there is a longer stop of the accelerator for about 150 days. During each of the 60 days periods the radiation level will follow the cycle of the accelerator beam intensity profile, with a continuous decrease of the collision rate during the runs, followed by machine refills. In spite of a precise monitoring system to correct for the crystal optical parameters changes, it is important to tune the crystal damage building and recovery kinetics to damp as much as possible the radiation exposure variations.

In the radiation environment of modern particle physics experiments the creation of new defects due to inelastic scattering of damaging particles is negligible. The radiation damage in the crystals in a relatively short time scale is therefore only the result of a charge-state change of preexisting point structure defects, which produce color centers. As a consequence the recovery process is driven by the relaxation of electronic states of these defects. As an example the model of the transmission radiation damage and recovery in lead tungstate crystals was proposed in [92]. It has been used for the optimization of the crystal technology development for the particular radiation environment of the CMS experiment at LHC. It is shown that the PWO transmission damage reaches a saturation level, which is dose-rate-dependent up to the point where the rate of trapping of the charge carriers induced by radiation is exactly balanced with the rate of spontaneous relaxation at this working temperature. In the case of a random distribution of the defects of type i in the crystal and in the absence of interaction between them the radiation damage will reach a saturation level after a certain time which is determined by the concentration of preexisting defects. The amount of damaged centers of type i is described by the following differential equation:

$$\frac{\mathrm{d}N_i}{\mathrm{d}t} = -\omega_i N_i + \frac{S}{d_i}(N_i^* - N_i) \,, \tag{4.2}$$

where N_i is the number of damaged centers of type i at time t, ω_i is the recovery rate of damaged centers of type i, S is the dose rate, N_i^* is the number of preexisting defects of type i, and d_i is the damage constant of the mentioned centers, which depends on the capture cross section of free carriers by the centers of type i. The induced absorption coefficient k produced by irradiation is proportional to the concentration of absorbing centers N through $k = \sigma N$, where σ is the cross section of the absorbing center. The solution of (4.2) can been given in terms of induced absorption:

$$k = k_\mathrm{sat} \frac{S}{S + \omega d} \left\{ 1 - \exp\left[-\left(\omega + \frac{S}{d} \right) t \right] \right\} \,, \tag{4.3}$$

where $k_\mathrm{sat} = N^* \sigma$ is the saturated induced absorption coefficient when all centers are damaged. The recovery of the transmission after the end of the irradiation at time t_0 is described by the following equation:

$$k = k_\mathrm{sat} \frac{S}{S + \omega d} \left\{ 1 - \exp\left[-\left(\omega + \frac{S}{d} \right) t_0 \right] \right\} \exp(-\omega(t - t_0)) \,. \tag{4.4}$$

Further investigations of short-term transient absorption, as well as the detection of photoionization processes involving electron centers, allowed us to develop a more adequate model of the radiation-induced absorption and of its recovery in lead tungstate crystals. A detailed description of electron and hole centers is given in Sect. 4.2 and [23, 98]. The defect energy level diagram in the forbidden band of a PWO crystal is shown in Fig. 4.24. In practice the electron centers created by irradiation in doped and undoped lead tungstate crystals can be divided into three groups. The first group consists of polaronic WO_4^{3-} centers, distorted regular centers WO_4^{2-}, and WO_4^{3-}-RE (where RE is a rare-earth cation). These centers are rather shallow, decay through the conduction band, and contribute to the scintillation mechanism. They can create a transient absorption band near the transmission band edge but it is not easy to distinguish their contribution from the background of fundamental absorption.

The second group is formed by different irregular WO_3^{2-} centers and more complex defects related to them. They have an average lifetime in the crystal

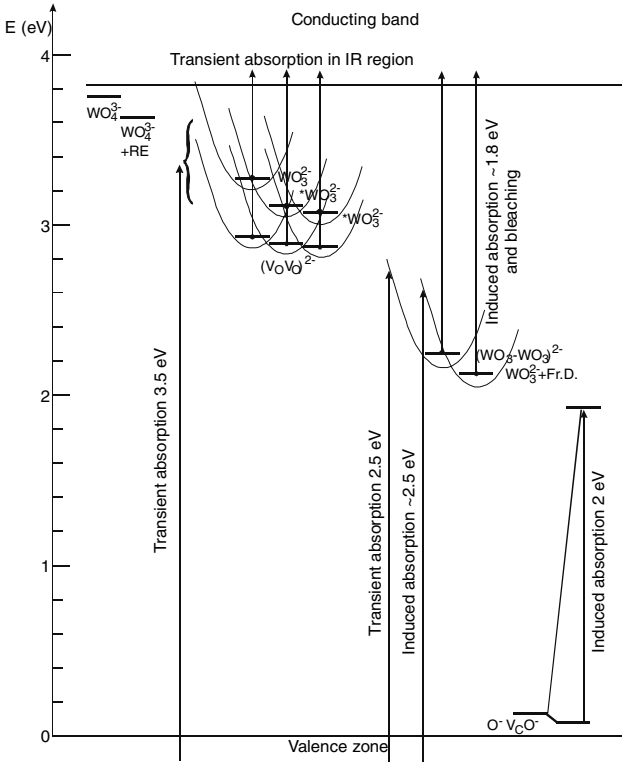

Fig. 4.24. The energy level diagram of electron- and hole-type centers in the forbidden band of PWO crystals

of about 10^{-6} s or even less and are quickly annihilated through thermoactivation at room temperature. In contrast to the centers of the first group, these irregular electron centers are either activated through a neighbor luminescence center WO_3, or their released electrons are captured by deeper traps such as MoO_4^{2-}. The ionization of these centers seems to be responsible for the transient absorption in the IR region [98]. The Pb^{1+}-V_0 center (where V_0 is an oxygen vacancy) contributes also to the IR transient absorption in the spectral region below 1,000 nm. Moreover, this group of defects is likely to form a wide, short-wavelength, transient absorption band in the crystal with a maximum near 3.5 eV.

The last group consists of associates of a dimer of $(WO_3–WO_3)^{2-}$ centers having captured two electrons and the Frenkel defect associated with $(WO_3)^{2-}$, which can also capture two electrons. The ionization of these deeper electron centers can also be observed through the bleaching by long-wavelength light [93] in the region of 1.8 eV ($\lambda \geq 700$ nm). The calculated annihilation rate of the deep associative center is in good agreement with experimental data [93–95] where a fast optical transmission recovery component has been detected. In contrast, the decay time of the electron center based on the Frenkel defect is much slower than the recovery time reported in [96]. In fact, slowly decaying induced absorption bands appear in lead tungstate crystals due to charge intracenter transitions of the Frenkel defect and di-hole centers. When crystals are doped with Latype trivalent ions the centers of the second and third groups are strongly suppressed. Figures 4.18, 4.20, and 4.21 show how the induced absorption spectra are modified from undoped to doped crystals. Depending on the crystal growth conditions and doping concentration at least five bands can be seen, peaked near 350–400, 470, 520, 620, and 720 nm. Following the description of the defects the transition between the ground and first excited state of the $O^-V_cO^-$ center is responsible for the 620 nm absorption band. The 720 nm band is due to the $(WO_3–WO_3)^{2-}$ center and the short-wavelength (350–400 nm) radiation-induced absorption band is caused by the recharge of the $(WO_3)^{2-}$-Frenkel defect center as mentioned above. The origin of the 470 and 520 nm bands is still debated [23]. Following a simple model of the thermo-activation and thermo-luminescence (TSL) data of electronic centers [97], one can estimate the spontaneous recovery time constants at room temperature of the $(WO_3–WO_3)^{2-}$ center and $(WO_3)^{2-}$-Frenkel defects to be 480 s and 10^4 s, respectively. Both absorption recovery constants can be observed in undoped crystals but their contribution in La(Y)-doped crystals is negligible. Figures 4.25a and 4.25b show the induced absorption recovery kinetics of undoped crystals at 400 nm (decay of electronic centers) and 600 nm (decay of hole centers). The kinetics curves are fitted with an exponential assuming that all centers decay through thermo-activation. The recovery kinetics is well described by two exponentials with 1,760 s (0.5 h) and 272,000 s (75 h) decay times. If the fast component is likely to be due to the decay of the $(WO_3–WO_3)^{2-}$ center, the longest one

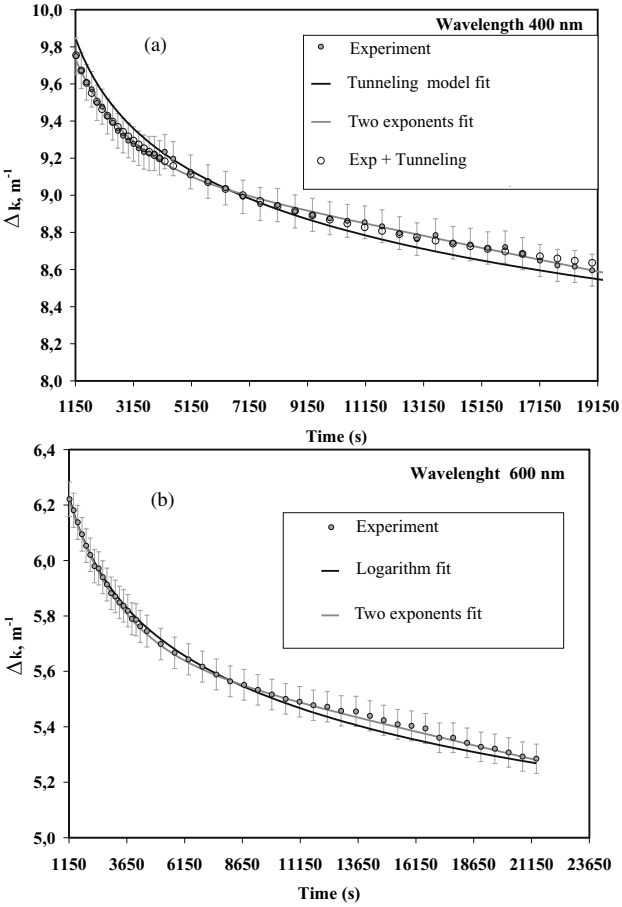

Fig. 4.25. Room temperature induced absorption recovery kinetics at 400 (**a**) and 600 (**b**) nm in an undoped lead tungstate crystal and their fits with (4.4) and (4.6)

cannot be attributed to the thermal decay. It seems that the only possibility of the electron/hole deep defects recombination is through the tunneling of the electron. Deep electron and hole centers do not have a correlated spatial distribution in the crystal and the tunneling rate approximation for a casual center distribution describes well the process of recovery in doped and undoped crystals.

PWO crystals present a unique situation where only two types of slowly decaying defects, the electronic Frenkel-type defect and the $O^-V_cO^-$-type centers, have a tunneling relaxation channel. Thus, the kinetics of defect concentration $n_t(t)$ decrease through tunneling of both electron$^-$ and hole-type centers is described by the same equation [97]:

$$n_t(t)/n_t(0) = 1/\left[1 + n_t(0)(\pi a^3/6)\ln^3 \nu t\right], \tag{4.5}$$

where $a = h/2\pi[2m(U_{\max} - E)]^{1/2}$, $n(0)$ is the initial concentration of electron defects, m is the mass of the electron, $U_{\max} - E$ is the difference between the potential barrier and the center energy, and ν is the hit frequency of the electron in the vibronic potential which is well approximated by the average frequency of the crystal phonon spectrum (500 cm^{-1}). In fact, the concentration of the defects at $t = 0$ is not defined. However, for numerical estimations, the concentration of the defects at very short time after irradiation (1 s for instance) can be chosen as the initial point.

The value $U_{\max} - E$ for a Frenkel defect associated with $(WO_3)^{2-}$ can be estimated taking into account the following argument. It is not less than 0.7 eV which is the thermo-activation energy of the center; however, it cannot be more than the ionization energy 1.8 eV of the center. In our approximation we used a value of 0.7 eV. As far as $U_{\max} - E$ and ν are defined, and $n(t)/n(0) = \Delta k(t)/\Delta k(0)$, where Δk is the induced absorption coefficient at the specified wavelength, the fit can give an estimation of the concentration of the defects in the crystal.

Thus the recovery which accounts for thermo-activation and tunneling effects is expressed by the equation

$$n(t)/n(0) = \left(\sum_i k_{i,\exp}(t) + k_{\mathrm{tun}}(t)\right)/k(0) \tag{4.6}$$

$$= \sum_i n_i(0)/n(0) \exp\left(-\frac{t}{\tau_i}\right) + n_t(0)/n(0)[1 + n_t(0)(\pi a^3/6)\ln^3 \nu t] \ ,$$

where $\Delta k_{i,exp}(0)$ is the induced absorption contribution of the exponential component of number i at $t = 0$, and $\Delta k_{\mathrm{tun}}(0)$ is the induced absorption contribution of centers recombining through tunneling at $t = 0$. Fit results are shown in Figs. 4.25 and 4.26 where recovery curves have been obtained from several standard CMS ECAL crystals after low-dose-rate (0.15 $\mathrm{Gy\,h}^{-1}$) irradiation. Data of the fit for different crystals are summarized in Table 4.4, where δt is the time between the end of irradiation and the beginning of measurements, λ is the wavelength of the measurement, and τ_{i} is the recovery constant of the exponential component number i. In these calculations we considered only one exponential component. The sum $\Delta k_{\exp}(0) + \Delta k_{\mathrm{tun}}(0) = \Delta k^{\mathrm{experimental}}$ is the value of the induced absorption measured immediately after the end of irradiation.

Undoped crystals show a fast recovery even 1,100 s after irradiation in the region of 400 nm (2.5 eV) where the $(WO_3{-}WO_3)^{2-}$ centers contribute. The decay time constant correlates well with the annihilation time of these traps determined through TSL measurements. The same fast component is observed at 600 nm. However, as seen from the fit, the majority of the electron and hole centers annihilate through tunneling. The best fit for 395 and 600 nm is found for $n(0) = 2.8 \times 10^{18}$ and 4.9×10^{18} cm^{-3}. The concentration of Pb^{2+} ions in the crystal is about $11 \times 10^{22}\,\mathrm{cm}^{-3}$, so the partial concentration

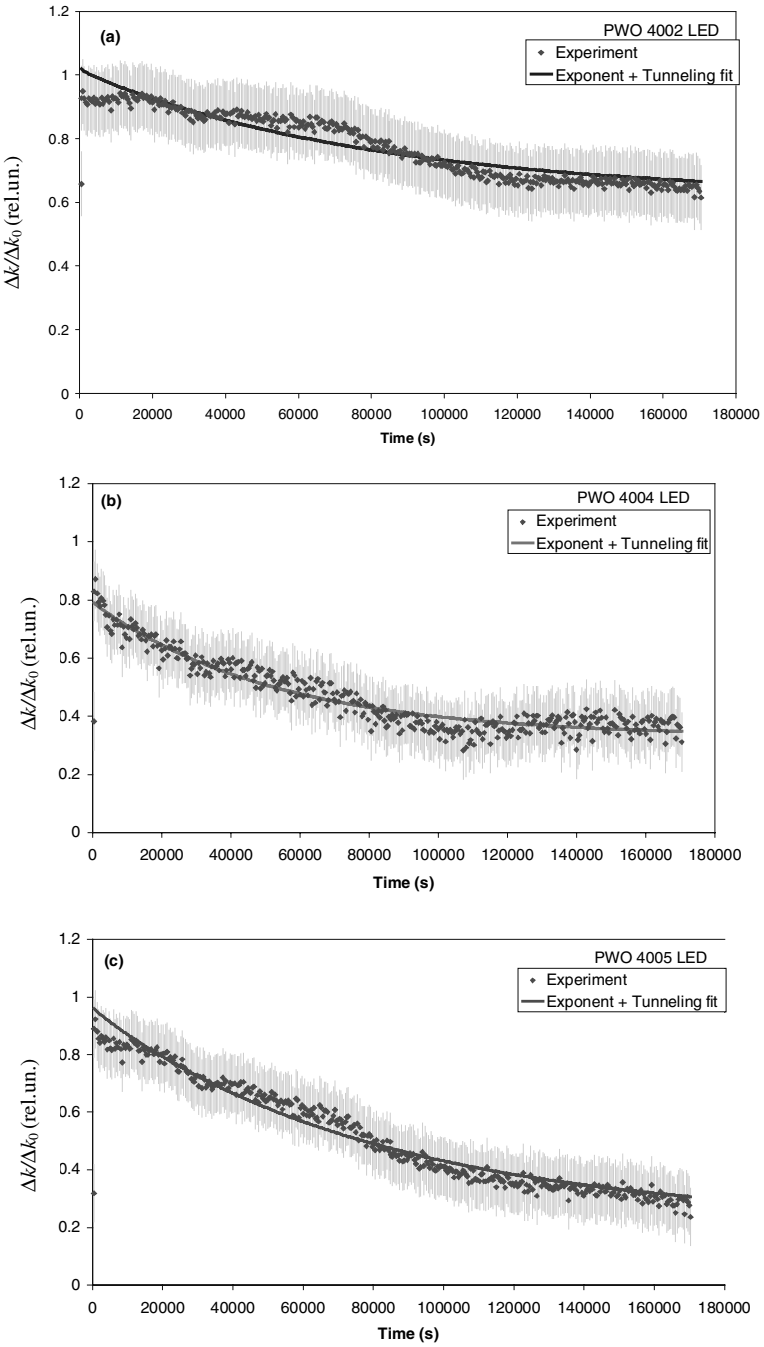

Fig. 4.26. Kinetics of the recovery at 470 nm of CMS ECAL crystals measured after 30 h irradiation with dose rate 0.15 Gy h^{-1} at room temperature. Small oscillations are due to residual temperature effects. Fit made by (4.6)

Table 4.4. Induced absorption recovery fit results of different PWO crystals

Sample	δt (s)	λ (nm)	τ_i (s)	$\Delta k_{exp}(0)$ (cm^{-1})	$n(0)$ (cm^{-3})	$\Delta k_{tun}(0)$ (cm^{-1})
PWO	1,100	395	448	1.1	2.8×10^{18}	20.4
		600	1,430	0.2	4.9×10^{18}	18.7
PWO:Y	1,100	400	77,000	0.75	4.1×10^{17}	0.48
		470	75,000	0.7	3.3×10^{17}	0.34
		600	69,000	0.36	2.7×10^{17}	0.16
		700	590	0.4		
#4002	100	470	81,500	0.068	1.7×10^{17}	0.120
#4004	100	470	53,170	0.051	6.7×10^{17}	0.053
#4005	100	470	80,000	0.103	5.6×10^{17}	0.038

of both types of defects is found to be of the order of tens of ppm. The value of the defect concentration is therefore in good agreement with the concentration value of the doping needed to suppress these defects in the crystal. When the crystal is doped with Y, there is a strong suppression of the $(WO_3–WO_3)^{2-}$ centers. No sign of a fast component with a recovery time less than 1,000 s is seen in doped crystals in the spectral region 400–600 nm. However, when the 620 nm induced absorption band is suppressed in the crystal, the detailed study of the recovery near 700 nm becomes possible. A recovery constant of 590 s is fitted in this spectral region strongly supporting the idea that this induced absorption band is also caused by the $(WO_3–WO_3)^{2-}$ centers as described above. Through the calculation of $\Delta k_{tun}(0)$ in Y(La) doped crystals, one can see that the amount of hole$^-$ and electronic-type centers is dramatically decreased. Moreover, the increase of $\Delta k_{tun}(0)$ corresponds to an increase of $n(0)$.

Nevertheless, an exponential component with a time constant in the range of 60,000–80,000 s is observed in the spectral region 400–600 nm in the recovery of all doped crystals. One could speculate that this slowly recovering center is created by the doping ion; however, as mentioned above, the Y(La) impurity ions do not create deep electron centers in the crystal. On the other hand, with the suppression of the 620 nm induced absorption band, the 470, 520 nm bands in the induced absorption become visible. It is therefore likely that the recovery of these absorption bands is characterized by this long time constant of 60,000–80,000 s. The data obtained and the modeling have shown that the suppression of the deep electronic and hole centers in the scintillation crystal is a good way to tune the recovery processes and to improve the calibration of the calorimeter on a long time scale.

References

1. Van Eijk CWC (2000) Inorganic scintillators for the next generation of neutron beam facilities. In: Mikhailin VV (Ed). Proc. of the Fifth Int. Conf. on Inorganic Scintillators and Their Applications, SCINT99. Moscow State University, Moscow, pp 22–32
2. Bisonnette JP, Munro P (1996) Evaluation of a high density scintillating glass for portal imaging, Med. Phys. 23: 401–406
3. Grynev BV, Seminozhenko VP (1993) Scintillation detectors for ruggedized applications. Osnova, Kharkov (in Russian)
4. Koepke BG, Anderson RH, Stokos RI (1976) Deformation in ceramics materials. In: Bradt RC (ed). Pergamon, New York–London, pp 497–513
5. Blasse G, Grabmaier BC (1994) Luminescence Materials. Springer, Berlin, pp 84–162
6. Koch A, Raven C (1997) Scintallators for high resolution x-ray imaging. In: Yin Zhiwen, Feng Xiqi, Li Peijun, Xue Zhilin (Eds). Proc. Int. Conf. on Inorganic Scintillators and Their Applications, SCINT'97. CAS, Shanghai Branch Press, Shanghai, pp 28–31
7. US Patents 4362946
8. US Patent 3960756
9. US Patent 4374749
10. US Patent 4375423
11. Gektin AV, Shiran NV, Pogorelova NV et al. (2002) Inorganic–organic rubbery scintillators. Nucl. Instrum. Methods Phys. Res. A 486: 191–195
12. Greskovich C, Duclos S (1997) Ceramic scintillators. Annu. Rev. Mater. Sci. 27: 69–88
13. US Patent 4747937.
14. Hirth JP, Lote J (1972) Theory of Dislocation. McGraw-Hill, New York, St. Louis, San Francisco, Toronto
15. Gektin AV, Krasovitskaya IM, Shiran NV (1984) Vacancy formation during plastic deformation of KCl crystals. Solid State Phys. 26: 2515–2517
16. Gektin AV, Serebryanny VYa, Shiran NV (1992) Point defect interaction and vacancy cluster formation in alkali halide crystals. Phys. Status Solidi a 134: 351–358
17. Ossipyan YA, Shmurak SZ (1981) Deformation luminescence and motion of charged dislocations in crystals. Defects in Insulation Crystals. Springer, Riga, Berlin, Heidelberg, pp 135–162
18. Bates CW Jr, Schneider I, Salau A et al. (1976) Strain-induced room temperature photoluminescence in CsI and CsI(Na). Solid State Commun 18: 101–103
19. Tyapunina NA, Tselebrovsky AN (1973) Vacancy concentration on plastically deformed NaCl type crystals. Crystallography 18: 649–650
20. Gektin AV, Shiran NV (1997) Scintillation losses in irradiated CsI-based scintallators. In: Yin Zhiwen, Feng Xiqi, Li Peijun, Xue Zhilin (Eds). Proc. Int. Conf. on Inorganic Scintillators and Their Applications, SCINT'97. CAS, Shanghai Branch Press, Shanghai, pp 115–120
21. Gavrilov VV, Gektin AV (1998) Deformation sensibilization of CsI based crystals. Solid State Phys. 30: 3163–3165
22. Bredikhin SI, Glushuk OA, Shmurak SZ (1982) Deformation sesibilisation of color centers in zinc selenide crystals. Solid State Phys. 24: 2249–2254 (in Russian: Fisika Tverdogo Tela)

23. Annenkov A, Korzhik M, Lecoq P (2002) Lead tungstate scintillation material. Nucl. Instrum. Methods Phys. Res. A 490: 30–50
24. Han Baoguo, Feng Xiqi, Hu Guangin et al. (1999) Annealing effects and radiation damage mechanisms of $PbWO_4$ single crystals. J. Appl. Phys. 86: 3571–3575
25. Böhm M, Henecker F, Hofstaetter A et al. (1998) Shallow electron traps in the scintillator material $PbWO_4$ to thermally stimulated luminescence In: Baccaro S, Borgia B, Dafinei I, Longo E (Eds). Tungstate Crystals. Proc. Int. Workshop on Tungstate Crystals, Rome, pp 139–146
26. Böhm M, Henecker F, Hofstaetter A et al. (1999) Electron traps in the scintillator material $PbWO_4$ and their correlation to the thermally stimulated luminescence. Radiat. Eff. Defects Solids 150: 413–417
27. Laguta VV, Rosa J, Zaritski MI et al. (1998) Polaronic WO_4^{3-} centers in $PbWO_4$ single crystals. J. Phys.: Condens. Matter 10: 7293–7302
28. Hofstaetter A, Alves H, Bohm M et al. (2000) Spectroscopic characterisation of defects in tungstate scintillators. In: Mikhailin VV (Ed). Proc. of the Fifth Int. Conf. on Inorganic Scintillators and Their Applications, SCINT99. Moscow State University, Moscow, pp 128–136
29. Hofstaetter A, Korzhik MV, Laguta VV et al. (2001) The role of the defect states in the creation of the intrinsic WO_3- centers in $PbWO_4$ by sub-band excitation. Radiat. Meas. 33: 533–536
30. Nikl M, Bonacek P, Nitsch K et al. (1997) Decay kinetics and thermoluminescence of $PbWO_4$: La^{3+}. Appl. Phys. Lett. 71: 3755–3757
31. Baccaro S, Bohacek P, Borgia B et al. (1997) Influence of La^{3+}-doping on radiation hardness and thermoluminescence characteristics of $PbWO_4$. Phys. Status Solidi a 160: R5–R6
32. Annenkov AN, Auffray E, Korzhik MV et al. (1998) On the origin of the transmission damage in lead tungstate crystals under irradiation. Phys. Status Solidi a 170: 47–62
33. Wang LM. Chen Y, Wu X (1994) Charge-state stability and optical transitions of oxygen impurities in barium fluoride crystal. Scintillator and Phospor Materials MRS Proc. 348: 399–406
34. Chen Lingyan, Du Jie, Wang Liming, Xiang Kaihua (1994) An investigation of radiation damage induced by hydroxyl and oxygen impurities in BaF_2 crystal. Scintillator and Phospor Materials MRS Proc. 348: 447–454
35. Pena JI (1988) Radiation effects in hydrolised CaF_2, SrF_2 and BaF_2. J. Phys. Chem. Solids 49: 273–278
36. Shamovsky LM, Glushkova AS (1963) Scintillators and scintillation materials. Kharkov 2: 5–2 (in Russian)
37. Nekrasov VN, Ivanovskt LE (1987) Melts 1: 82–85 (in Russian)
38. (a) Okada TJ (1981) Optical behavior of V centers in KI crystals at low temperatures. J. Phys. Soc. 50(2): 582–591
(b) Andrews L (1976) Optical spectra of the dibromide and diodide ions in the matrix-isolated $M^+Br_2^-$ and $M^+I_2^-$ species. Am. Chem. Soc. 98(7): 2152–2156
39. Rzepka E, Bernard M, Lefrant S (1998) V centers in irradiated alkali halide crystals. Nucl. Instrum. Methods Phys. Res. B 32: 235–237
40. Weber M., Lecoq P., Ruchti R., Woody C., Yen W., Zhu Ren-yuan, (Eds)(1994) Scintillator and Phospor Materials (MRS Proceeding, 348) 565pp

41. Korzhik MV, Pavlenko VB, Timoshenko TN et al. (1996) Spectroscopy and origin of radiation centers and scintillation in $PbWO_4$ single crystals. Phys Status Solidi a 154: 779–792
42. Annenkov AA, Fedorov AA, Galez Ph et al. (1996) The influence of additional doping on the spectroscopic and scintillation parameters of $PbWO_4$ crystals. Phys Status Solidi a 156: 493–503
43. Zang Y, Holzwarth NAW, Williams RT (1998) Electronic band structures of sheelite materials $CaMoO_4$, $CaWO_4$, $PbMoO_4$ and $PbWO_4$. Phys. Rev. 57: 12738–12750
44. Kubota S, Sakuragi S, Hashimoto S et al. (1988) A new scintillation material: Pure CsI with 10 ns decay time. Nucl. Instrum. Methods Phys. Res. A 268: 275–277
45. Gektin AV, Gorelov AI, Rykalin VI et al. (1990) CsI-based scintillators in γ-detection systems. Nucl. Instrum. Methods Phys. Res. A 294: 591–594
46. Nishimura H, Sakata S, Tsujimoto T, Nakayama M (1995) Origin of the 4.1 eV luminescence in pure CsI scintillator. Phys. Rev. B 51: 2167–2172
47. Gektin AV, Shiran NV, Charkina TA et al. (1992) radiation stability and afterglow problem for fast CsI-type Scintillators. Heavy Scintillators for Scientific and Industrial Applications. Frontieres, France, pp 493–498
48. Radzhbov A, Istomin A, Nepomnyashikh et al. (2005) Exciton interaction with impurity in barium fluoride crystal. Nucl. Instrum. Methods Phys. Res. A 537: 71–75
49. US Patent 5521387
50. Kostler W, Winnacker A, Grabmaier W (1993) Effect of Pr-codoping on the X-ray induced afterglow of $(Y,Gd)_2O_3$:Eu. J. Phys. Chem. Solids 56: 907–913
51. US Patent 5518658
52. Yoshida M, Nakagawa M, Fuji H et al. (1998) Application of Gd_2O_2S ceramic scintillator for X-ray solid state detector in X-ray CT. Japan. J. Appl. Phys. 27: L 1572–L1575
53. US Patent 5318722
54. Ren-ynan Zhu, Da-an Ma, Newman H (1994) Barium fluoride crystals for future hadron colliders. Scintillator and Phospor Materials. MRS Proc. 348: 91–98
55. Lecoq P (1994) Progress on scintillator research by the Crystal Clear Collaboration. Scintillator and Phospor Materials. MRS Proc. 348: 51–64
56. Baccaro S, Borgia B, Dafinei I, Longo E. (1998) Tungstate Crystals (Proc Int Workshop on Tungstate Crystals. Rome, Italy, 12–14 Oct. 1998), 393pp
57. BELLE Collaboration (1995),Technical Design Report, KEK Report 95-1.
58. BaBar Collaboration(1995), Technical Design Report, SLAC-R-95-457.
59. Kolontsova EV (1977) Radiation induced transformations in solids. In: Trefilov VI (Ed) Radiation Effects in Solids. Kiev, pp 107–112 (in Russian)
60. Kolontsova EV, Kulago EE (1972) Radiation effects in irradiated with neutrons single crystals of $LiNbO_3$, K_2SO_4, $NaNO_3$. Crystallography 17: 1197–1201 (in Russian)
61. Kolontsova EV, Kulago EE, Tomilin NA (1973) Radiation induced phase tension in a quartz. Crystallography 18: 1198–1201 (in Russian)
62. Mott NE, Gurney RW (1948) Electronic Process in Ionic Crystals. Oxford, p 304
63. Gektin AV, Serebrynny VYa, Shiran NV (1988) Color centers accumulation model for ionic crystals, Ukr. J. Phys. (in Russian) 33: 590–592

64. Aqullo-Lopez F, Jaque F (1973) Unified model for all stages of F-coloring of NaC. J. Phys. Chem. Solids 34: 1949–1960
65. (a) Hughes AE, Jain SC (1979) Metal colloids in ionic crystals. Adv. Phys. 28: 717–828
(b) Hughes AE (1983) Colloid formation in irradiated insulators. Radiat. Eff. 74: 57–76
66. Gektin AV, Charkina NA, Shiran NV et al. (1989) Optical absorption of colloidal particles in doped CsI crystals. Opt. Spectrosc. (Russian) 67(5)1989: 1075–1077
67. Kobayashi M, Sakuragi S (1987) Radiation damage of CsI(Tl) above 10^3 rad Nucl. Instrum. Methods 254a: 275–280
68. Renker D (1989) Technical report CERN N89-10 ECFA Study. Week Instrum. Technol. High-Luminosity Hadron Colliders 2: 601–610
69. Schotanus P, Kamermans R, Dorenbos P (1990) Scintillation characteristics of pure and Tl-doped CsI crystals. IEEE Trans. Nucl. Sci. 37: 177–182
70. Hitlin DD, Eigen G (1992) Radiation hardness study of CsI crystals. In: Heavy Scintillators for scientific and industrial applications. Frontieres, France, pp 467–478
71. Kobayshi M, Sakuragi S (1987) Radiation damage of CsI(Tl) crystals above 10^3 rad. Nucl. Instrum. Methods Phys. Res. A 254: 275–280
72. Gektin AV, Globus ME, Shepelev OA et al. (1997) Scintillation losses due to radiation damage in long CsI(Tl) crystals. Funct. Mater. 4: 544–547
73. Schulman J, Compton WD (1963) Color Centers in Solids. Pergamon, Oxford–London–New York–Paris, p 359
74. Hobbs LW, Hughes AE, Pooley D (1973) A study of interstitial clusters in irradiated alkali halides using direct electron microscopy. Proc. Roy. Soc. London A 332: 167–185
75. Jacobs G, Fiermans L, van de Wiele F (1961) Optical absorption of cesium halides with excess halogen. Physica 27: 144–148
76. Globus ME (1993) Spectrometric characteristics of ionizing radiation detectors based on BGO and CWO. Int. J. Radiat. Applic. Instrum. D 21: 131–133
77. Globus M, Grinyov B (1995) Calculations of scintillators for radiation detector systems: dependence of spectrometric characteristics on shape, size and reflector type. IEEE Trans. Nucl. Sci. 42: 357–360
78. Korjik M, Khrutchinsky A, Missevitch O et al. (2002) On the response linearity of scintillation detectors in irradiation environment. CMS IN 2002/056, p 9
79. Williams RT, Yochum HM, Ucer KB et al. (2000) Picosecond and nanosecond time-resolved study of luminescence and absorption of $CdWO_4$ and $PbWO_4$. In: Mikhailin VV (Ed). Proc. of the Fifth Int. Conf. on Inorganic Scintillators and Their Applications, SCINT99. Moscow State University, Moscow, pp 336–341
80. Millers D, Chernov S, Grigorieva L et al. (2000) Luminescence and transient absorption of doped PWO_4 scintillator crystals. In: Mikhailin VV (Ed). Proc. of the Fifth Int. Conf. on Inorganic Scintillators and Their Applications, SCINT99. Moscow State University, Moscow, pp 613–618
81. Grigorieva L. Private communication
82. Yin ZW (1994) Research and development works on BaF_2 crystals in Shanghai Institute of Ceramics. Proc. "Scintillator and Phospor Materials". MRS Proc. 348: 65–76

83. Ramos BS, Hernandes AJ, Muerietta SA et al. (1985) Model for F-center production in alkali halides doped with divalent cation impurities that change their valence state by irradiation Phys. Rev. B 31: 8164–8170
84. Annenkov AN, Auffray E, Borisevich A et al. (1999) Suppression of the radiation damage in lead tungstate scintillation crystal. Nucl. Instrum. Methods Phys. Res. A 426: 486–490
85. Haliburton LE, Edwards GJ (1994) Radiation damage mechanisms in scintillator materials: application to BaF_2 and CeF_3. Scintillator and Phosphor Materials. MRS Proc. 348: 423–434
86. Ren Saooxia, Chen Gang, Zhang Fengyin, Zheng Yanning (1994) The effect of impurities on the radiation damage of barium fluoride crystal. Scintillator and Phospor Materials. MRS Proc. 348: 435–440
87. Shiran N, Gektin AV, Ivanov N et al. (1999) The role of oxygen in energy transfer processes in $LiBaF_3$ scintillator. Mikhailin V., (Ed). Inorganic Scintillators and their Applications. Moscow pp. 230–235
88. Korzhik MV (2003) A general approach to increasing the radiation hardness of complex strucutre oxide scintillation crystals. Nucl. Instrum. Methods Phys. Res. A 500:116–120
89. Smirnova SA, Korzhik MV (1996) Growth of crystals of yttrium-aluminum perovskities with rare earth elements. In: Dorenbos P, van Eijk CWE (Eds). Proc. Int. Conf. on Inorganic Scintillators and Their Applications, SCINT'95. Delft University Press, The Netherlands, pp 495–497
90. Annennkov AN, Auffray E, Chipaux R et al. (1998) Systematic study of the short-term instability of $PbWO_4$ scintillator parameters under irradiation. Radiat. Meas. 29: 27–38
91. Gektin AV, (1999) Halide scintillators. Present status and prospects. In: Mikhailin VV (Ed). Proc. of the Fifth Int. Conf. on Inorganic Scintillators and Their Applications, SCINT99. Moscow State University, Moscow, pp 79–88
92. Annenkov AN, Auffray E, Fedorov A et al. (1997) Radiation damage kinetics in PWO crystals. CMS Note 1997/008, 9 pp.
93. Zhu RY, Ma DA, Newman HB et al. (1996) A study on the properties of lead tungstate crystals. Nucl. Instrum. Methods Phys. Res. A 376: 319–334
94. Nikl M, Bonacek P, Nitsch K et al. (1997) Decay kinetics and thermoluminescence of $PbWO_4$: La^{3+}. Appl. Phys. Lett. 71: 3755–3757
95. Kobayashi M, Usuki Y, Ishii M et al. (1998) Improvement in radiation hardness of $PbWO_4$ scintillating crystals by La-doping. Nucl. Instrum. Methods Phys. Res. A 404: 149–156
96. Nikl M, Nitsch K, Baccaro S et al. (1997) Radiation induced formation of color centers in $PbWO_4$ single crystals. J. Appl. Phys. 82: 5758–5762
97. Annenkov AN, Auffray E, Borisevich AE et al. (2002) On the mechanism of radiation damage in lead tungstate crystal optical transmission. Phys. Status Solidi A 191: 277–290
98. Korzhik MV (2003) Physics of scintillators on a base of oxide single crystals. Belarussian State University, Minsk

5 Crystal Engineering

Abstract. In this chapter definitions and methods are given to analyse phase diagrams of different complex compounds from the material science viewpoint with several examples of well known scintillation materials. It is followed by a description of different technologies and equipments for the growth of single crystals. A special attention is paid to the control of parameters, which are particularly important to satisfy some of the user's requirements, like dimensions and homogeneity of optical properties, purity of the initial material and activator uniformity distribution, stoichiometric composition and minimum concentration of point and linear defects. Different techniques to grow single crystalline scintillation materials such as Bridgeman, Stockbarger, Stoeber, Kyropolos, Czochralski as well as state of the art and modern trends in the industrial production are reviewed. Different ways to design the scintillation detector block in such a way to as to maximize the collection efficiency of the scintillation photons are also discussed.

5.1 Phase Diagrams

A large variety of inorganic compounds have the potential to be a scintillator. Crystal chemistry shows a lot of opportunities when systems with two, three, four, and more components are stable because of the strict laws of chemical and crystallography structure formations. In spite of the fact that the development of new crystalline scintillating materials is to a large extent driven by luminescence research another very important part of the study which requires even more efforts is related to the synthesis of a predetermined material if it is at all possible. An initial step is the study of a phase diagram to define the conditions in which a given composition occurs.

The theory of phase diagrams is described elsewhere [1]. This chapter will consider the phase diagrams from the material science point of view and gives examples for some scintillation materials.

The theory of phase balance is based on thermodynamics and establishes relationships between composition, temperature, and pressure in equilibrium systems.

To predict the phase composition of a compound it is necessary to know the number of phases and the number of independent chemical components, from which these phases are formed. The homogeneous part of a

heterogeneous system is called a phase, and the substances forming phases of the chemical system are called chemical components.

For heterogeneous systems the direction of the reactions is determined by the phase rule. According to this rule, the number of degrees of freedom C in an heterogeneous system in equilibrium is equal to the number of independent components $K + 2$, minus the number of phases F: $C = K + 2 - F$. To predict the behavior of the system with the help of the phase rule it is therefore necessary to know the number of phases and the number of independent chemical components. The number of degrees of freedom is defined by thermodynamic parameters (temperature, pressure, composition), which can be modified without changing the number of coexisting phases. If this number is equal to 0, it is impossible to change either the pressure or the composition and temperature without removing one of the phases. The equilibrium at $C = 0$ is called an invariable one. Equilibrium at $C = 1$ is called a mono-variable one for which a given temperature corresponds to a precise value of the vapor pressure. At such a balance it is enough to set up one parameter only, for example a given temperature is sufficient to set the equilibrium pressure and the composition of phases. Equilibrium at $C = 2$ is called bi-variant and it means that an undefined equilibrium pressure corresponds to the given temperature. So, the composition of phases depends both on temperature and on pressure. Constant temperature does not provide, in this case, a constant composition. This conclusion is of great importance in manufacturing crystals, including scintillation materials.

In the case of the phase equilibrium it is convenient to use phase diagrams. For an unicomponent two-phase system the relationship between temperature T and pressure P can be represented on a 2D diagram. In a two-component system the A–B composition is represented by a three-dimensional diagram. For multicomponent systems the representation is multidimensional and it is graphically possible to present only special cases (cross-sections) of multivariable diagrams.

We will analyze here the most common diagrams: "composition – temperature" for binary systems. Such diagrams are most frequently investigated and represent the greatest practical interest for crystal growth from melt.

5.1.1 Phase Diagram of Continuous Solid Solutions

If the chemical components A and B have similar electronic shells structure, ionic radius, or energies of the chemical bonds, they are likely to form a solid solution (see Fig. 5.1). In this case the liquid phase of the composition lies above a liquidus line (L). The solid solution area lies below the solidus line (S). The area of crystallization lies between the solidus and the liquidus curve.

While cooling the melt with composition X (see Fig. 5.1), crystallization will begin at the temperature corresponding to point L_1 on the liquidus curve. The composition of the crystallized solid phase at this time corresponds to

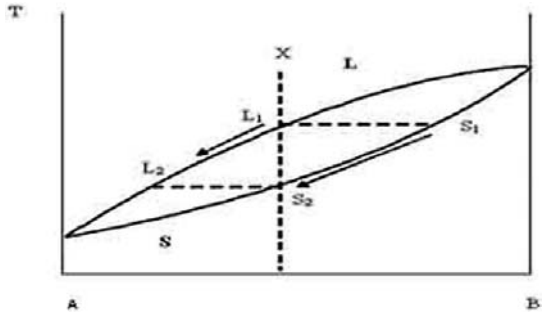

Fig. 5.1. The phase diagram of a binary system with creation of continuous solid solutions

point S_1 on the solidus curve. During further cooling the composition of the crystallized mass will vary along the line S_1–S_2, and the composition of the melt will follow the line L_1–L_2. Thus, the ratio between crystal and melt composition is determined by the line lengths L_2–S_2 and L_1–S_1. If the cooling is very slow the crystal composition will follow the line S^1–S^2. If on the other hand the cooling is fast, a mechanical mixture of crystals having different compositions is formed. This fact is of a very big practical importance for crystallization procedure development.

5.1.2 Eutectic and Distectic Phase Diagram Without Solid Solutions

The diagram for a two-component system A–B is represented schematically in Fig. 5.2. This diagram has two maxima corresponding components' A and B, and a minimum corresponding the eutectic point E.

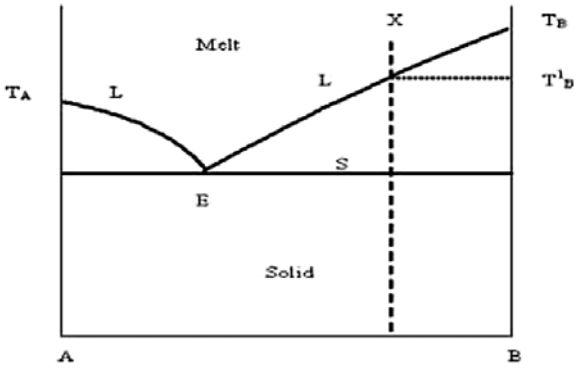

Fig. 5.2. The eutectic phase diagram of a binary system without creation of a compound

This diagram has three domains: the melt area at high temperature, limited by the liquidus curve (L); the area of solid phases at low temperature limited by the solidus horizontal line; and the region of mixed liquid and solid in between.

The crystallization begins when the melt is cooled down to the temperature T_B^1. Further temperature decrease displaces the composition toward the eutectic point E where the solidus and liquidus lines meet. At the eutectic temperature the melt is completely crystallized forming a mechanical mixture of the A and B phases. The eutectic diagram shows that components, A and B coexist but do not react chemically, and that the melting temperature of the pure components decreases to the eutectic point. This apparent contradiction is explained by the fact that there is no chemical interaction in a solid solution. The eutectic diagram shape depends on the difference of the A and B components' melting temperatures. If this difference is small, the eutectic point lies approximately in the middle of the diagram. If the difference is large enough the eutectic point is displaced to a composition with lower melting temperature.

This situation is however rather rare in a binary system A–B. The appropriate phase diagram, for example for the compound A_2B, is shown in Fig. 5.3. The so-called distectic point D, which corresponds to the compound, appears in the phase diagram and divides it into two eutectic phase diagrams between A–A_2B and A_2B–B, respectively.

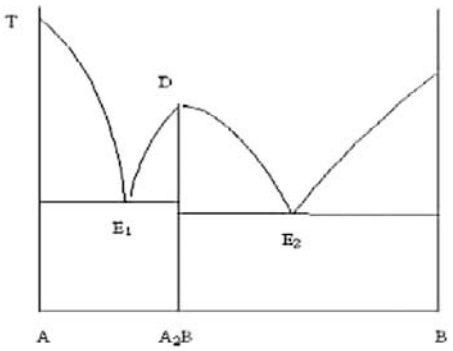

Fig. 5.3. The distectic phase diagram of a binary system with creation of the compound A_2B

5.1.3 Eutectic Phase Diagram with Areas of Solid Solutions

Quite often a stable compound does not form in a two-component system A–B. However, there is generally a high reciprocal solubility of the components in the liquid and to a lesser extent in the solid. In this case the eutectic

diagram with areas of solid solutions α and β (Fig. 5.4) can be drawn. The α and β domains correspond to the solid solution enriched with the A and B components. The areas between L, S, α, and β are L+α and L+β. When cooling the melt with a composition X, down to the temperature of the liquidus, the liquid is enriched with the B component. And then, when the liquid is displaced to the eutectic point, the crystallization of a mechanical mixture of α and β begins. The composition of each solid solution α and β corresponds to the intersection of α and S and β and S curves, respectively.

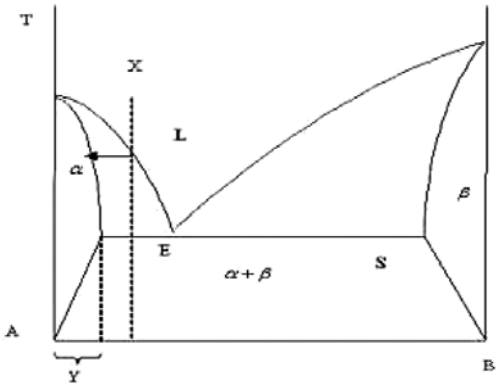

Fig. 5.4. The eutectic phase diagram of a binary system with solid solutions

5.1.4 Impurity Solubility During the Growth

There is a redistribution of impurities between the crystal and the melt during crystallization as shown in the diagrams of Fig. 5.5. Thermodynamically the impurity either decreases melting point (a), or increases it (b).

If the segregation coefficient of the impurity is smaller than 1, the melting temperature of the basic component A decreases. As seen in diagram (a) the crystallization at the temperature corresponding to the point L1 on the liquidus line results in the crystallization of a phase with a smaller impurity content than the melt. A further reduction of the crystallization temperature results in an enrichment of the impurity in both the crystal and the melt. On the other hand, for $k > 1$ the crystal is initially more rich in impurity than the melt, but the impurity concentration in both decreases when lowering the temperature (k is the segregation coefficient, i.e. the ratio of the dopant concentration in the solid state to the dopant concentration in the melt).

5.1.5 Scintillation Crystal Phase Diagrams

Several typical examples of scintillation crystal phase diagrams are discussed below. The synthesis conditions of the widely used alkali-halide scintillators,

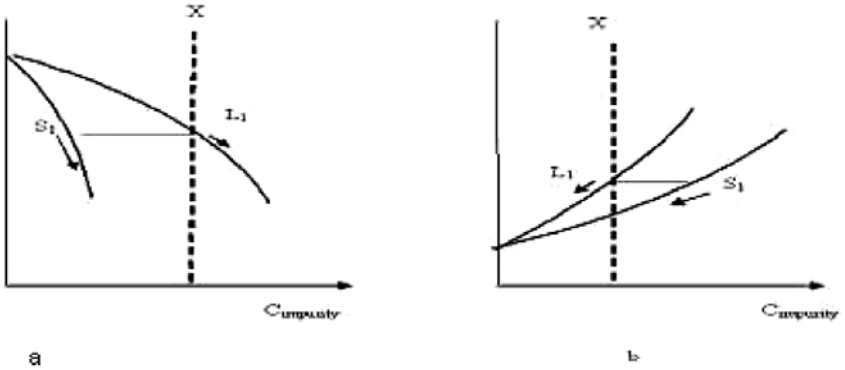

Fig. 5.5. "Crystal–melt" equilibrium in the presence of impurities

NaI and CsI, were studied in the middle of the 1970s [2]. It was shown that these crystals when doped with sodium and thallium ions form an eutectic diagram. The phase diagram of the CsI–NaI system (Fig. 5.6) results from differential thermal analysis data [3, 4] as well as from mathematical simulations [1]. Na ions solubility in the CsI lattice is limited. This limit defines the optimal level of Na doping (about 0.02%).

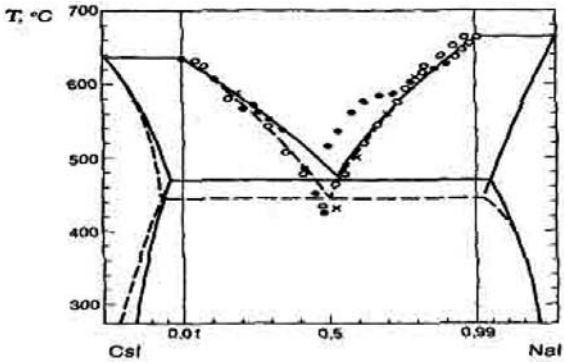

Fig. 5.6. The eutectic phase diagram for the CsI–NaI system [2–4]

The phase diagram of the PbO–WO_3 system was investigated in detail [5] and in particular on the side of a small WO_3 concentration. The study of the area enriched in tungstate anhydride is rather complicated because of the high WO_3 melting temperature and the interaction of WO_3 with the crucible material at temperatures higher than 1,100°C. Nevertheless, it is established that there is an eutectic E_1 (Fig. 5.7) between $PbWO_4$ and WO_3 with 66.5% WO_3, fusing at 930°C. There are two stable phases $PbWO_4$ and Pb_2WO_5 in this system. The other two eutectics E_2 and E_3 have melting temperatures

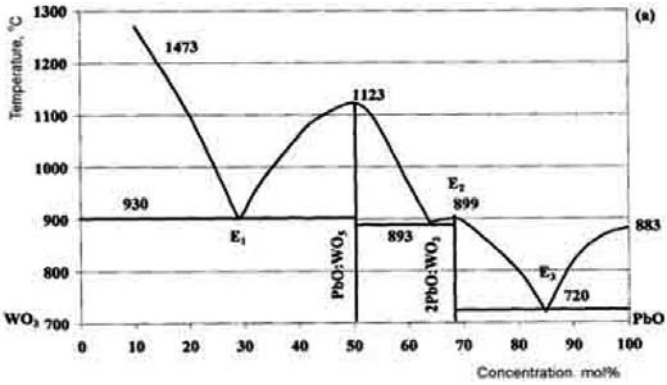

Fig. 5.7. The phase diagram of the PbO–WO_3 system

893°C and 720°C, respectively. The $PbWO_4$ melts congruently, i.e. without decomposition of the compound, at 1,123°C. The analysis of this phase diagram helps us define some practical parameters for the $PbWO_4$ crystals grown by the Czochralski method. First of all, the melting temperature restricts the choice of the crucibles to metals with higher melting points such as platinum, iridium, and their various alloys. It is also important that such crucibles do not interact with melts of similar oxides such as $PbMoO_4$, $CaMoO_4$, and $ZnWO_4$, which are impurities likely to be present in the raw material. Secondly, the possibility of using not only the stoichiometric composition of the raw material but also some excess of either WO_3 or PbO is of great importance, if it is necessary for a better tuning of the scintillation properties of the crystal. This is especially important when the properties of the grown crystals depend critically on the melt stoichiometry or when a strong differential evaporation of the different components of the melt occurs during the growth process. An initial deviation from the perfect stoichiometry can therefore be applied for the compensation of nonstoichiometry defects. The phase diagram does not provide any restriction to the relationship between the weight of the grown crystal and the weight of the initial melt in the crucible. The size of the pulled crystal is only determined by some technological constraints of the equipment such as the size of the crucible and the optimal growth technology. Some restrictions can appear because of the segregation process of additional doping ions which have segregation coefficients >1, La for instance. This doping will be pumped from the melt to the initial part of the crystal if the diameter of the pulled crystal is close to the diameter of the crucible. There is no necessity to create fast heat flow through the growing crystal or supercooling at the crystallization interface which essentially reduces the stability of the process and increases inner stresses in the crystal. A large industrial production of $PbWO_4$ by the Czochralski method [6] has been set up for the needs of the CMS experiment at CERN (see Chap. 7).

Another example of a complex phase diagram is the lutetium aluminate perovskite crystal. There are two stable phases $Lu_3Al_5O_{12}$ and $Lu_4Al_2O_9$ and a metastable phase of $LuAlO_3$ in the system. $Lu_4Al_2O_9$ is formed from oxides at temperature higher than 1,650°C and melts incongruently at 2,000°C; the most stable phase $Lu_3Al_5O_{12}$ is formed below 1,500°C and melts congruently at 2,060°C. In the $LuAlO_3$ phase diagram there is also a metastable phase in a narrow temperature range of 40°C with an incongruent melt. The low system stability is explained by the aspiration of lutetium (the lanthanide with the smallest ionic radius) into the garnet structure. From the phase diagram study one can infer that very small variations of the melt composition or temperature at the crystallization point can introduce a transition from the perovskite to the garnet phase. Therefore the size of the perovskite crystal will be severely limited if the composition of the melt and the temperature gradient are not perfectly under control at the crystallization point.

Another approach to grow this crystal is to set up the growth conditions at a high temperature gradient and a fast cooling of the crystal. The gradient provides the supercooling of the melt and maintains the composition in a metastable molten situation. This method prevents the decomposition of the solidified phase. It is experimentally confirmed that the perovskite phase $LuAlO_3$ can be obtained only by quick crystallization of the stoichiometric melt. It allows us to assume that there is a metastable variant of the phase diagram of the system in which this phase melts congruently at 1,910°C as shown in the inset of Fig. 5.8. The practical implementation of this approach to the growth of a LuAP crystal is a rather complex but manageable process.

Growing LuAP on a seeding crystal (having the same composition as the ingot) is practically impossible, as it decomposes at the contact with the melt and even a strong cooling of the seed does not give a positive result. Growing on an iridium wire is a possibility but the spontaneous crystallization is a very complex technological problem difficult to control for a consistent production. A high temperature gradient also generates important maintenance problems. The garnet phase formation at the seeding stage and during crystal growth is therefore a difficult problem for the optimization of the crystallization process. It should be noted that the first $LuAlO_3$ samples had a lot of garnet inclusions which strongly affected the scintillation performance [7].

One way to increase the domain of stability of the phase diagram is to introduce some quantity of yttrium in the lattice. The modified crystal of $Lu_{1-x}Y_xAlO_3$:Ce in which the Lu ions are replaced with Y ions have practically the same or even better scintillation performance [8, 9] as $LuAlO_3$ but with a smaller density below $8.34\,g\,cm^{-3}$ and therefore a lower photofraction. On the other hand, this composition is much more stable than the pure lutetium perovskite and its melting temperature is slightly lower. Moreover for the crystal growth of such composition it is possible to use a more stable seeding procedure with $YAlO_3$ crystals [10].

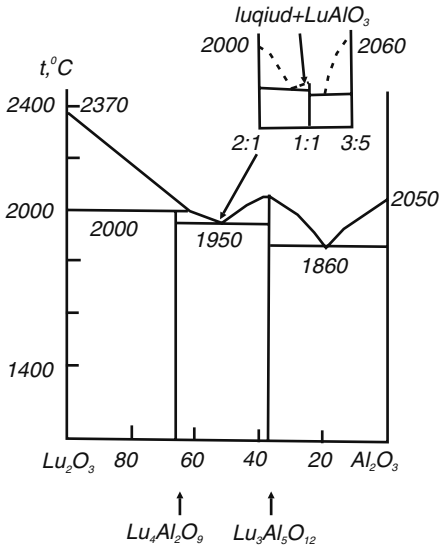

Fig. 5.8. The phase diagram of the Lu_2O_3–Al_2O_3 system. The inset shows the details in the region of the 1:1 ($LuAlO_3$) compound

5.2 Single Crystal Growth

Although most of the applications require their use in a single-crystalline form, inorganic scintillators are used in a large variety of types and shapes. This fact requires a special attention to methods, technologies, and equipment for the single crystal growth. It is worth mentioning that the physics and technology of crystal growth do not depend on their subsequent application. But the specific character of the applications imposes quite often some requirements on the growth process, namely, for dimensions and homogeneity of optical properties, purity of the initial material and activator uniformity distribution, composition stoichiometric, and minimum concentration of point and linear defects.

5.2.1 General Considerations on the Crystallization Process

In general, crystallization is viewed as the formation of a new solid phase in melts, solutions, solid substances, and gases. The formation of a new solid phase can occur both inside the initial phase and on the phase surface. The causes of the new phase formation are critical supersaturating, critical overcooling, or nucleation. A stable nucleus is characterized by a critical size and it takes a definite form defined by the minimum surface energy that can be reached for a given volume. From the theory [11] one can calculate the critical nucleus size and its formation energy, define the relation between the critical supersaturation and the heat of the melt, and consider the effects of diffusion

and heat transfer processes, i.e. describe the kinetics of phases interaction. This allows us to optimize the crystallization process and to grow good quality crystals even at rather high rate of mass production. For the growth of single crystals there must be a unique nucleus; otherwise a multiple nucleation will produce a polycrystal. Various techniques and methods are used to allow the growth of one nucleus only or to select a single nucleus from several ones during the crystallization process. The simplest method is the crystal growth from a previously prepared seed. The seed crystal is usually cut from the same crystal, but it is sometimes possible to use a single crystal of different composition.

Several papers and books describe the basic theoretical principles of single crystal nucleation, growth and growth principles and procedures [2, 11–13]. That is why we shall consider here only a few important aspects of the scintillation single crystal growth.

5.2.2 Basic Methods for Scintillation Crystal Growth

The core of almost all crystal growth methods is the principle of oriented crystallization. Its basic feature is the balance of two different processes: heat transfer and crystal interface transfer.

The methods of crystal growth are usually classified according to the following conditions:

- phase status and composition of the initial phase;
- type of the process driving force (temperature gradient or concentration, or pressure).
- Starting from the first point it is possible to grow single crystals:
- from melts;
- from solutions;
- from gas phase;
- by phase transformations in solid phase.

The classification of the methods within these groups is carried out according to the second point. The temperature gradient is mainly used as the driving force of crystallization. Several methods are used which differ in the way the heat transfer and the hydrodynamic conditions are applied. They are

- creation of temperature gradient between the crystal and the melt by heat transfer from the seed;
- creation of temperature gradient between the crystal and the melt by heat transfer from the seed and pulling up the grown crystal from the melt (Czochralski and Kyropoulos's methods);
- floating temperature gradient through the melt (Bridgeman and Stockbarger's methods), etc.

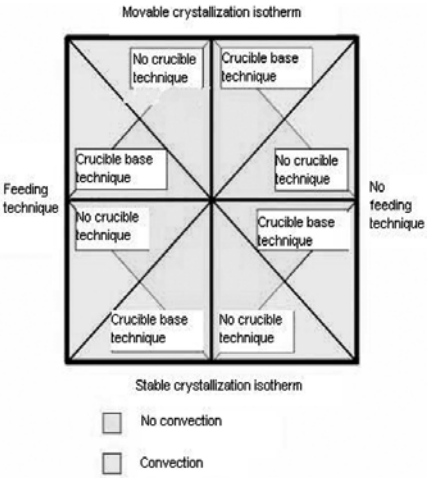

Fig. 5.9. A classification of crystal growth methods

The methods of crystallization are often classified according to such criterion as the presence or absence of a melting pot (crucible). Figure 5.9 illustrates a typical combined classification. Various technical solutions are available to grow single crystals. The implementation of a growing method is characterized by technological features, equipment design, and phase diagram peculiarities.

Finally, one more pragmatic selection criterion of the single crystal growth method concerns the single crystal nucleation and the shaping of the ingot. Through the combination of all these criteria all the methods can be divided into two groups:

- single crystal growth in ampoules such as Bridgeman, Stockbarger, Stoeber [14, 15] and
- single crystal pulling from melt such as Kyropolos, Czochralski, etc. [16, 17].

Below we describe the basic principles of these methods.

5.2.3 Bridgeman and Stockbarger Methods

The external form of the crystals grown in ampoules is strictly set by the geometry of the ampoule (as a rule, it is cylindrical, although, sometimes rectangular ampoules are also used). The growth of complex shape crystals is limited by the necessity of crystal extraction from the ampoule which can be complicated by the adhesion of the crystal material to the ampoule material. (It should be noted that, for this reason, the crystals are subject to deformation during the cooling which induces intrinsic stress in them.)

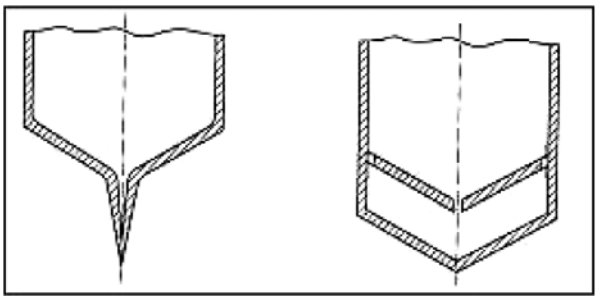

Fig. 5.10. Ampoulous shape for single nucleus selection and single crystal growth [2]

One of the most complex problems of this group of methods is the spontaneous crystallization on the ampoule surface. As a result, the orientation of the crystal is difficult to control. For example, scintillation single crystals of NaI(Tl) have the spontaneous orientation (110) [2], when grown by the Stockbarger method in quartz ampoules, regardless of the speed of growth and of the ampoules shape. Figure 5.10 illustrates the typical shapes of ampoules for the oriented single crystals growth. The single crystal growth is achieved by setting the conditions for the preferred growth orientation or by the use of a well-oriented seed.

A good control of the heat transfer process is a fundamental aspect of single crystal growth technology. The temperature gradient or the homogeneity of the thermal field (radial or axial in relation to the growth of a single crystal) is the driving force of the crystal growth process. Consequently, all the crystal growing furnace elements (heaters, screens, gaseous medium, etc.) act as the main control elements of the crystallization process. Figure 5.11 b shows

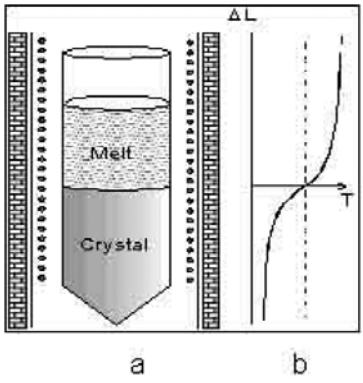

Fig. 5.11. Stockbarger method scheme (**a**) and temperature distribution along the furnace (**b**)

the diagram of the temperature field axial distribution for the Stockbarger method. Figure 5.11a illustrates the corresponding layout for this growing method.

Initially, the raw material is placed in the higher temperatures area (where it melts). The crucible (ampoule) is moved through the thermal gradient zone, where the temperature is lowered below the melting point. This is the area where the crystallization takes place. The volume of the melt will therefore decrease continuously and the growing crystal starts substituting for the melt. It follows that the temperature field parameters change during the crystal growth. The amplitude of these changes is determined by both the configuration of the initial thermal field and the changes in the crystallization process. The system has a nonconservative character because there are losses at the melt–gaseous medium interface besides mass transfer at the melt–crystal interface. As a general rule, when developing a single crystal growth technology it is good to bear in mind that the system is open and is nonconservative in the sense that the losses of separate components are irreversible. The basic principles of crystallization processes in totally open systems are explained in [2]. As the thermal field in the growing crystal system is continuously changing the main problem for all the crystal growth technologies is to find a method to adapt the conditions of heat and mass transfer, which is usually done empirically by a trial and error approach.

A long practice and experience has been accumulated over the years and halide scintillators, for example, NaI (Tl), CsI (Tl), CsI (Na), are successfully grown by the Stockbarger method. This method is also widely used for growing oxide scintillation crystals [18]. The simplicity and relatively low production cost of this method make it very practical for search and synthesis of new scintillation crystals. The principle and basic components of the crystal growing furnace remained almost unchanged since the invention of this method. It comprises two chambers with self-contained top and bottom heaters. The sharp thermal gradient is produced by a diaphragm. The influence of the water-chilled support of the ampoule on the temperature gradient is negligible. The temperature gradient in the furnace exceeds $10^{\circ}\mathrm{C\ cm^{-1}}$. As a rule, the rate of the ampoule transfer does not exceed 1 mm $\mathrm{h^{-1}}$.

If the simplicity and reliability of the Bridgeman and Stockbarger designs make them particularly attractive for many applications these methods are however rather inconvenient for a good homogeneity especially for doped single crystals. A high gradient of the doping impurities is observed in these crystals. The consequence is to reduce the production yield as only a fraction of the ingot can be generally used.

5.2.4 Czochralski and Kyropolos Growth Techniques

When pulling a seeded single crystal from the melt the crucible shape and size do not have a direct influence on those of the crystal. The crystal shape instead is determined only by the parameters of the growth process (mass and

heat transfer, above all). A seed crystal is a prerequisite of these methods. Its crystallographic orientation is transferred to the crystal and is a determining factor for the whole ingot size and quality.

There are two fundamental methods to grow crystals from the melt.

In the classical Kyropolos method [16] the entire crystallization process starts with the seeding and propagates through the melt as a result of a continuous temperature decrease applied during the process. There is no relative movement of the seed and the crucible.

In the Czochralski method [17] the crystal is pulled from the melt. This method is the most widely used for growing oxide scintillators (since virtually all known oxides are produced by this method) as well as for many other scintillators.

The Czochralski growth method is an example of heterogeneous crystallization which takes place at the crystal–melt interface. The crystallization practically starts from the seed crystal. Contrary to the Kiropoulos method the crystal is continuously pulled from the melt and rotates during the growth which helps maintain a good mixing of the melt (Fig. 5.12). The driving force of the process is the temperature gradient at the phase boundary. The temperature gradient determines all the main characteristics of the growth process: crystallization rate, crystal size, and crystallization interface shape. For a constant temperature gradient the pulling rate and crystallization rate should coincide. If the pulling rate is less than the growth rate the crystal increases in diameter and vice versa. This provides the technological means to control the shape of the crystal.

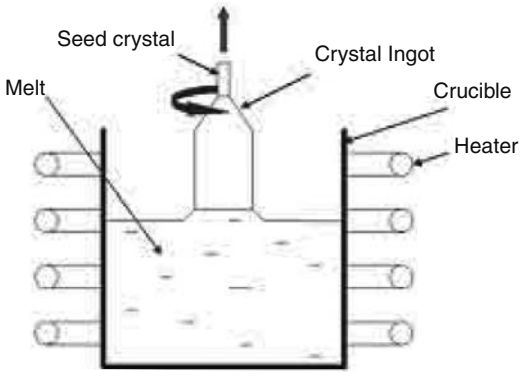

Fig. 5.12. The Czochralski growth method

Crystal pulling and gradient control should be carried out rather smoothly in order to maintain the stability of the process. A sharp increase of the pulling rate can result in the separation of the crystal from the melt and in the discontinuation of the crystallization process. In contrast, a sharp decrease

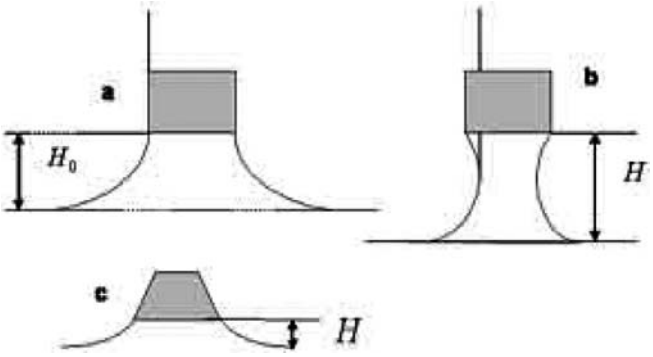

Fig. 5.13. The form of the melt meniscus in the Czochralski method

of the pulling rate will result in the increase of the crystal diameter with an increased risk of polycrystal growth. To provide a stable crystal growth process it is necessary to fix the crystallization interface and the shape of the meniscus of the melt (Fig. 5.13). The meniscus shape is defined by the balance between the surface tension and the weight of the column of the melt lifted to the altitude H:

$$\sigma \left(\frac{1}{R_1} + \frac{1}{R_2} \right) = \rho_{\mathrm{l}} g H \ , \tag{5.1}$$

where σ is the surface tension coefficient; R_1 is the radius of the meniscus curvature in one direction, R_2 is the radius of the meniscus curvature in the perpendicular direction; ρ_{l} is the melt density, and g is the gravity coefficient.

For crystals of diameters much bigger than the height of the meniscus the altitude of the column H_0 at which the growth with a constant diameter can occur is given by

$$H_0 = \sqrt{\frac{2}{\rho_{\mathrm{l}} g}} \ . \tag{5.2}$$

If the crystallization interface is higher than the point H_0 the crystal diameter will be smaller (Fig. 5.13b) and vice versa if it is lower than H_0 (Fig. 5.13c). In practice, however, the operator does not adjust the critical position of the crystallization interface as a function of the meniscus shape. It is in fact easier to adjust and control the temperature and the temperature gradients of the system. It is easy to understand this approach by the analysis of the thermal balance equation at the crystallization interface. First of all there is a heat transfer between the hot liquid and the crystal which is cooler but also the emission of the latent crystallization heat through the crystallization interface. In the first approximation (regardless of the crystal thermal conductivity anisotropy, thermal field asymmetry, and so on) the equation of thermal balance is given by

$$\rho_{\mathrm{s}} V Q = \lambda_{\mathrm{s}} \left(\frac{\mathrm{d}T}{\mathrm{d}X} \right)_{\mathrm{s}} - \lambda_{\mathrm{l}} \left(\frac{\mathrm{d}T}{\mathrm{d}X} \right)_{\mathrm{l}} , \tag{5.3}$$

where ρ_{s} is the density of a crystal, V is the crystallization rate, Q is the latent crystallization heat, λ_{s} and λ_{l} are the thermal conductivities of solid and liquid phases, respectively, and $(\mathrm{d}T/\mathrm{d}X)_{\mathrm{s}}$ and $(\mathrm{d}T/\mathrm{d}X)_{\mathrm{l}}$ are the temperature gradients in solid and liquid phases at the phase boundary, respectively.

From the equation it appears that the maximum crystallization rate is obtained for a minimal gradient in the melt (for example, due to good mixing) and a maximum gradient in the crystal. It is obvious that substances of high thermal conductivity can grow faster than substances of low thermal conductivity. So metals are grown at higher speeds than ionic (dielectric) crystals. More detailed studies of the thermal balance at the phase boundary requires the consideration of many parameters [2, 19, 20]. This may include the heat transfer due to IR emission. It is particularly important for crystals of high melting point because radiative loss is proportional to the fourth degree of the temperature. The form of crystallization interface (flat, convex in melt or concave in the crystal) also influences the result of the analytical solution of the thermal balance equation [2].

5.2.5 Modern Trends in Scintillation Crystal Manufacturing

The last decade has seen new developments of great interest in the understanding of scintillation physics and in the engineering of scintillators. This has been triggered in particular by the increasing demand for HEP and nuclear medicine. The scale of scintillation single crystal production is nearly two orders of magnitude smaller than the scale of semiconductors (such as silicon) manufacturing, but the requirements for crystal dimensions for gamma-ray detection is extremely high [21]. For instance, a full-size crystal for SPECT system reaches $600 \times 500\,\mathrm{mm}^2$ (see Fig. 5.14). Not even mentioning the issue of homogeneity of the scintillation parameters on such a large surface, it is clear that crystals of this size cannot be produced by the above-mentioned methods. All of them are limited regarding the crystal dimensions both geometrically (for example, ampoules in the Stockbarger and Bridgeman methods) and technologically (due to the difficulties in creating the thermal field to ensure a sustainable crystal growth).

5.2.5.1 Large-Size Alkali-Halide Scintillation Crystal Growth

Since the middle of the 1980s a large R&D effort has been spent for large-size crystal pulling methods. The progress in this field has open new possibilities for nuclear medicine cameras.

A major attention has been paid to methods of continuous growth to produce large-size scintillation crystals. It should be mentioned that at the same time a number of projects have emerged for developing continuous pulling

Fig. 5.14. Scintillator for the conventional SPECT system

methods for semiconductors (silicon; for instance see [22, 23]). The case of scintillators, however, has proven to be more complicated. The main reason is the need to provide a regular distribution of the activator impurity along the whole crystal length.

In the practice of homogenous scintillation growth this effort has led to the implementation of the modified Czochralski–Kyropoulos techniques. The essence of the concept is based on a continuous feeding of the melt to compensate its reduction during the single crystal pulling process. The balance between the crystal and the melt is maintained by feeding new raw material in powder or already prepared in the liquid phase.

Figure 5.15 shows the scheme of an installation for continuous large-size alkali-halide single crystal growth with powder feeding [24]. The crucible has a special shape for allowing a continuous and gradual powder feeding. Once molten the additional raw material is transferred to a quite large crucible and rapidly homogenizes due to melt convection.

This technique is not too difficult to operate. In the simplest case the task is simply to maintain a steady crystallization rate (that is to maintain a uniform cross-section and axial growth rate).

$$\begin{aligned} \frac{\mathrm{d}\nu_{\mathrm{S}}}{\mathrm{d}t} &= 0 \,, \\ \frac{\mathrm{d}S_{\mathrm{S}}}{\mathrm{d}t} &= 0 \,, \end{aligned} \tag{5.4}$$

where V_{S} is the axial growth rate and S_{S} is the crystal cross-section.

In the case for which mass transfer is conducted through the crystal melt interface, it means that

$$\frac{\mathrm{d}m_{\mathrm{l}}}{\mathrm{d}t} = \frac{\mathrm{d}m_{\mathrm{s}}}{\mathrm{d}t} \,, \tag{5.5}$$

where $m_{\mathrm{S}}, m_{\mathrm{l}}$ are the masses of the crystal and melt, respectively.

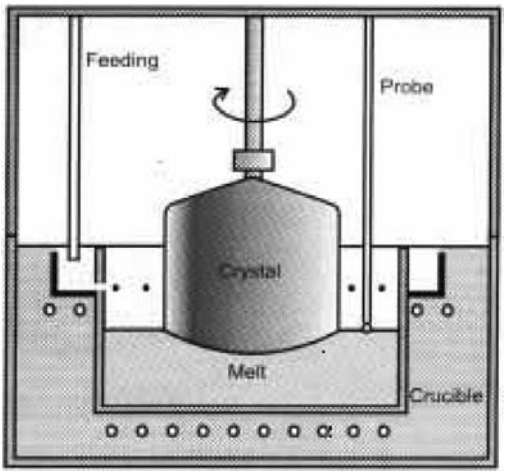

Fig. 5.15. Scheme of a continuous growth technique with the powder feeding system

From (5.4)–(5.5),

$$\frac{\mathrm{d}^2 m_\mathrm{s}}{\mathrm{d}t^2} = \rho_\mathrm{s}\left(\mathrm{s}\frac{\mathrm{d}V}{\mathrm{d}t} + V\frac{\mathrm{d}s}{\mathrm{d}t}\right) = \frac{\mathrm{d}^2 m_\mathrm{l}}{\mathrm{d}t^2}\ , \tag{5.6}$$

where ρ_s is the crystal density.

To pull a crystal at V_s, S_s = const it is necessary to monitor several parameters with the following equipment:

(i) V_s = const: crystal length gauge, melt level control,
(ii) S_s = const: crystal diameter control,
(iii) $\frac{\mathrm{d}m_\mathrm{l}}{\mathrm{d}t}$ = const: the melt weight control, the melt level control,
(iv) $\frac{\mathrm{d}m_\mathrm{s}}{\mathrm{d}t}$ = const: crystal weight control.

Figure 5.16 shows the regulation of the continuous crystal pulling process based on melt level monitoring. For this purpose the oven is equipped with an electric contact sensor responding to the interruption of a circuit when the melt level decreases in the crucible. The accuracy of such a sensor is limited by the meniscus height generated at the sensor's edge. The sensor signal is coupled to the feeding block, which restores the melt level by adding new raw material into the crucible.

One of the most important aspects of the raw material feeding method is to provide a continuous control of the growth process. Any crystallization speed jump (regardless of the initial causes, including temperature jump, melt level jump, etc.) leads to an instantaneous crystallization speed change. Depending on the amplitude of the perturbation this will lead to the creation of intrinsic crystal structure defects as well as activator distribution

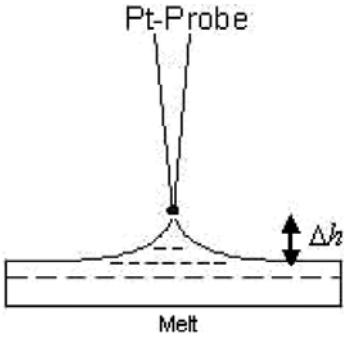

Fig. 5.16. Melt level control scheme with electric contact Pt probe

nonuniformity in the crystal, inclusion of impurities, and capture of the gases dissolved in the melt. It is therefore essential to keep the feeding process as continuous as possible. This procedure is described in detail in [13].

As a first approximation (steady-state process) the crystal diameter is given by the expression

$$d = 2\left(\frac{m}{\pi\rho_{\mathrm{s}}V_{\mathrm{p}}}\right)^{\frac{1}{2}} \tag{5.7}$$

where ρ_{s} is the crystal density, m is the feeding rate, and V_{p} is the pulling rate.

As a second approximation [2], additional factors should be taken into account, for example, single crystal creation and evolution under the melt surface, and material loss due to evaporation from the free surface area of the melt. In general, every such detail makes the control algorithm more complex, but does not affect the system control stability.

The method of automated crystal growth with a melt feeding system is also well known [2, 13, 24, 25]. This method is based on crystal and raw material weight balance equations, but possesses a number of specific features. The essence of this method is the process of pulling the crystal from a small conical crucible (which reduces the evaporation of the initial substance and the activator). Molten raw material is continuously fed from a special toroidal crucible. Figure 5.17 illustrates the main features of this technique.

The concept of the method is presented in Fig. 5.18. The initial stage of radial growth starts in the lowest part of a conical crucible where the melt surface diameter is comparable to the seed crystal diameter. At the radial growth stage a crystal is being pulled at the speed V_{p}. Simultaneously, the melt level is elevated at a rate V_{l} by feeding the raw material at the $\mathrm{d}m/\mathrm{d}t$ mass rate, so that $V_{\mathrm{p}} > V_{\mathrm{l}}$. This is the phase of the continuous diameter increase of the ingot to produce a nice conical shape from the seed to the required diameter ingot (stages b–d, in Fig. 5.18). The melt temperature is adjusted so that the linear speed of the radial growth is essentially equal to that of the melt surface diameter increase. Thus the radial growth from the

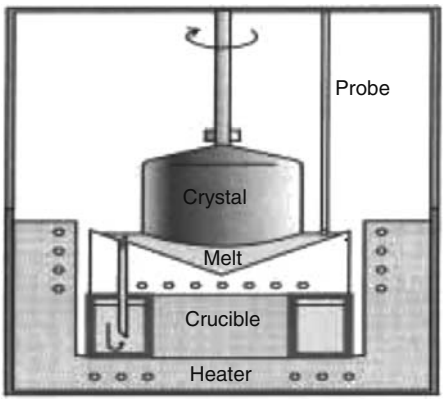

Fig. 5.17. Continuous growth technique with the melt feeding system and RAP (reactive atmosphere processing) capability [25]

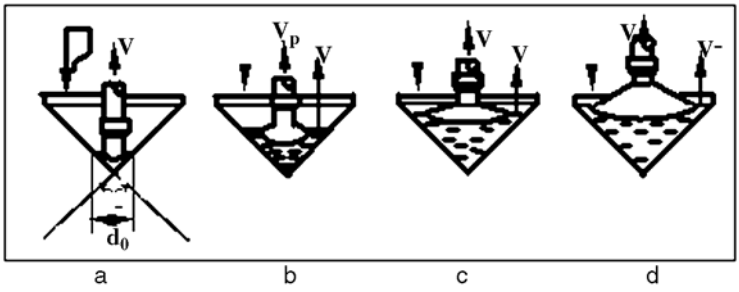

Fig. 5.18. Crystal growth from the conical crucible with the melt level control

seed diameter to the final value of the single crystal ingot is performed by minimizing the free melt surface. It is very important to prevent evaporation of the activator (Tl ions for NaI or CsI crystals) and to maintain a permanent Tl concentration in the melt.

These techniques allow us to combine a lot of specific features which are important for the optimization of scintillation single crystal growth:

1. continuous growth of large-size single crystals;
2. fixed "crystal–melt" interface, i.e. constant growth conditions on the solidifying interface;
3. possibility of raw material and activator feeding;
4. bulky crucibles that allow us to provide a good melt convection (and homogenization);
5. simple control method based on electro-contact probe;
6. possibility of rotating both the crystal and the crucible loaded with melt, allowing a good melt homogenization and maintaining a perfect symmetry of the thermal fields in the growing crystal;

7. extra raw material purification (such as RAP (reactive atmosphere processing) atmosphere treatment);
8. melt feeding, i.e. doping with activated melt.

A number of algorithms of large-size crystal production and technically modified systems for this production are presented in [2]. A typical single crystal ingot is shown in Fig. 5.19. Equipment and alkali-halide single crystal growth techniques are described in detail in [2]. At present these methods are commercially applied for producing NaI(Tl), CsI(Na), CsI(Tl), CsI(pure) single crystal up to 600 mm in diameter and up to 750 mm in height. The total weight of such ingots reaches 400–500 kg.

Fig. 5.19. Large-size halide scintillation single crystal ingot (Courtesy of Amcrys-H, Ltd)

5.2.5.2 Oxide Scintillator Single Crystal Growth

Oxide crystals have in general a tendency toward faceting the interface surface due to the different growth kinetics in various crystallography orientations [26]. As a result the interface can be either round or faceted depending on the growth conditions. Two opposite approaches are used to grow crystals such as $Bi_4Ge_3O_{12}$ (BGO), $CdWO_4$ (CWO), and so on. The conventional Czochralski method (CZ) [29] is based on high temperature gradients to suppress the facets formation. The final ingot is round in shape. An alternative way is the low temperature gradient CZ growth technology [27]. In this case the interface shape is fully faceted [28]. The essential features of this technique are shown in

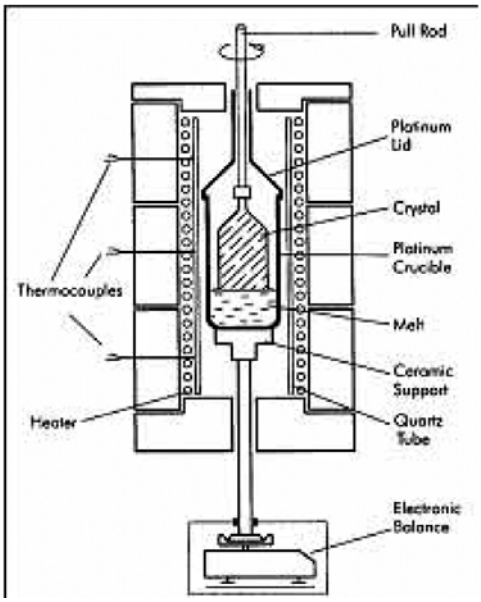

Fig. 5.20. Low gradient Czochralski technique [27]

Fig. 5.20. A special platinum crucible inside the multizone heater allows us to sustain and control axial and radial gradients to about 0.05–1.0°C cm^{-1}. The technique includes the weight control system and is fully automated growth procedure as the visual control is impossible [27]. The quality of the crystal depends on the orientation of the growth direction ({211} plates family or [100]/[111] directions for BGO, for example [27, 28]). As a result, large-size oxide scintillators of diameter up to 180 mm and length up to 350 mm have been grown with this technique.

The reliability and stability of the crystal growth process are essential to maintain a good homogeneity of the scintillator parameters. This aspect has been the focus of all the development efforts on the growth technology of $PbWO_4$ (PWO) for the Large Hadron Collider (LHC) at CERN. In this particular case the technology of conventional large gradient CZ growth has been chosen. Since this is one of the most vivid examples of a large world-wide technological effort on a scintillator we will use PWO to illustrate some aspects of the choice and tuning of the technology to satisfy the end user's requirements. The main challenge in this case was not so much to grow crystals of the right dimensions, but to guarantee a good radial and longitudinal homogeneity within the boules and to ensure a high reproducibility from ingot to ingot.

The result of this unprecedented R&D effort in the field of scintillators is that several tens of thousands single PWO crystals have been grown with a length of 290–310 mm (including the growing cone) and a cross-section of

36–40 mm. Moreover excellent quality ingots up to a diameter of 100 mm can be grown. It is supposed that crystals are annealed in air during industrial production. The detailed description of the crystal growth process is given in [6].

The most important requirements for the PWO crystal growth are as follows:

- The use of a stoichiometric mixture of tungsten oxide WO_3 and Pb_3O_4. The main reason for this choice is to create an excess of oxygen in the melt while growing the crystals in an atmosphere depleted in oxygen.
- Growing in gas atmosphere depleted in oxygen in order to prevent the oxidization of some of the lead ions in the trivalent state. It is now well established that PWO single crystals grown in air in composition contain trivalent lead ions which cause yellow coloration of the crystal.
- Orientation of the seed along the crystallographic axis "a." This allows us to reduce the radial stress in the ingot which results in a better mechanical stability and considerably simplifies the process of mechanical machining.

To increase the efficiency of raw material conversion into the crystalline mass, it is necessary to proceed to several sequential crystallizations from one crucible by means of raw material refilling after each growth process. The possibility of reprocessing rejected crystals as well as waste from mechanical processing is also an important aspect of the economy of the production. Such an approach allows us to bring the coefficient of raw material effective use up to 85%. However, the increasing number of crystallizations in crystals results in a progressive increase of defect concentration. It has been demonstrated that up to 15 successive crystallizations can be made with crystals of 40 mm diameter with a good reproducibility of their parameters if a proper tuning of the stoichiometric composition is made at each refill.

Raw Material Purity

The purity and preparation of the raw material plays a considerable role too, particularly if one wants to have radiation hard crystals. The amount of some impurities such as Li, Be, B, F, Mg, Cl, Mn, Ni, Co, As, Zr, Sr, Rb, Ge, Ga must not exceed 0.05 ppm, the amount of Na, Al, S, Zn should be less than 0.5 ppm, and the amount of P, Ti, V, Cr, Cu should be less than 0.1 ppm.

Crucible Filling

The filling of a crucible with raw materials presents a number of difficulties. The density of the powder being much smaller than the density of the melt, one has to proceed in several steps which results in lengthening the crystal growth cycle and in increasing the danger of raw material contamination with impurities. There are several methods of raw material densification. The easiest and the most commonly used one is tabletting. The raw material is mixed with filling agents (for example, alcohol) and pressed in the form of

tablets matching the size of the crucible. The tablets are then calcinated at a temperature ensuring a maximal mechanical strength and elimination of residues or even traces of the binder. In many cases the density of the tablets may reach up to 70% of the crystal density.

Another approach is the granulation technique. The liquified raw material is exposed to a cold air stream. This method makes it possible to bring the raw material density up to 85–90% of the crystal density.

There is also a possibility of filling the crucible by means of special loading devices. This technique may be realized on separate installations or use specific devices built into the growth installations. An example of such an approach is illustrated in Fig. 5.21. The raw material is spilled into the platinum crucible, and then heated until melting, after which the melt is poured out into a platinum mold. In the process of melt crystallization one can obtain tablets with a density up to 8, close to the PWO single crystal density (8.28), and a diameter 5–6 mm smaller than the inner diameter of the growth crucible.

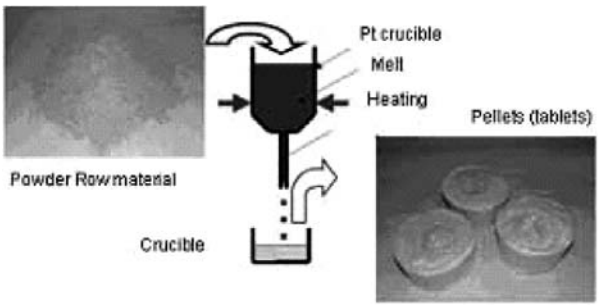

Fig. 5.21. Raw material preparation scheme

The Choice of the Crucible Material

It is an extremely important task to select the optimal crucible for crystal growth because the use of semiprecious metals such as platinum or iridium has a strong impact on the crystal price. The crucible cost reaches 20–50% of the crystal cost and can be even higher for crystals with a higher melting temperature.

The main requirements for the choice of the crucible material are

- metal resistance to the interaction with melt;
- metal cost and availability;
- thermal stability of crucibles and resistance to deformation under thermocycling;
- immunity to atmosphere conditions;

- lifetime and reprocessing capability.

Various kinds of crucibles are used for the Czochralski single crystal growth process. As a general rule, for crystals with melting point below 1,500–1600°C platinum crucibles are used while iridium crucibles are applied for crystals of higher melting points.

In the case of the PWO industrial crystal production optimization, the tuning of the crucible design has allowed an increase of its lifetime up to 8,000 h, i.e. about 1.5 years. Besides, there is a need for an optimization of the form, dimensions, and constructions methods of the crucibles to answer the technical and economic mass production challenges. Two ways have been explored to solve these problems. The first one was to make as thin as possible the side wall of a conventional welded crucible. The second one was to develop a combined platinum–ceramic crucible. A platinum crucible (the inside of which is in contact with the melt) has no joints. It is produced from a 0.6 mm platinum sheet by deep drawing method. The outside of a combined crucible is made of a 2–3 mm aluminum-based ceramics protective coating which is applied over the platinum base by plasma spraying. This construction reduces the platinum loss during the crystal growth process.

For LuAP, LuYAP, LSO, and LYSO scintillation crystals the choice of the crucible is very critical since the melt is characterized by high values of density, melting point, activity, and fluidity. High temperature gradients result in overheating the crucible. The local overheating of the crucible may damage it and result in leaking of the melt. This is one of the main difficulties for growing LuAP and LSO as well as other crystals with a high temperature melting point.

5.2.6 State-of-the-Art for Crystal Growth

In spite of a high automation of the crystal growth process these technologies still remain sometimes more art than science. The state-of-the-art of these technologies determines both the efficiency of the production and the quality of the scintillators. Figure 5.22 shows PWO crystals of different dimensions grown by the Czochralski method with platinum crucible of 130 to 150 mm diameter.

One of the examples of this symbiosis between art and science is the growth of highly transparent single crystals which requires not only a good knowledge of fundamental principles but also a long trial and error experience. It is evident that crystal properties are to a large extent related to the level of impurities which are introduced in the crystal from the melt. These impurities can be either uncontrolled or introduced on purpose in the crystal during the process. But in both cases it is necessary to consider the heat transfer and the diffusion process together. When growing a crystal with a speed different from zero, the concentration of impurities in the melt is a

Fig. 5.22. PWO single crystal grown by the Czochralski method

dynamic process. The corresponding inhomogeneity of the impurity distribution is determined by the diffusion speed and by the limited efficiency of hydrodynamic mixing. Figure 5.23 illustrates the effect of overcooling by excess of impurity concentration. The temperature of crystallization depends on the impurity concentration. The balanced liquidus temperature (crystallization temperature) T_l and the actual temperature gradient (determined by the equipment) can be rather different. If the actual temperature gradient crosses the solidification temperatures line (gradient I in Fig. 5.23), the melt on the crystallization front appears to be overcooled. It creates the conditions for multicrystallization and polycrystal growing centers appear. This is called the effect of "concentration overcooling." The crystallization front loses its stability.

To avoid the negative influence of concentration overcooling the temperature gradient $\mathrm{d}T/\mathrm{d}X$ must lie higher than the liquidus temperature curve, i.e. $\mathrm{d}T/\mathrm{d}X \geq (\mathrm{d}T/\mathrm{d}X)_{X=0}$. This defines the following condition:

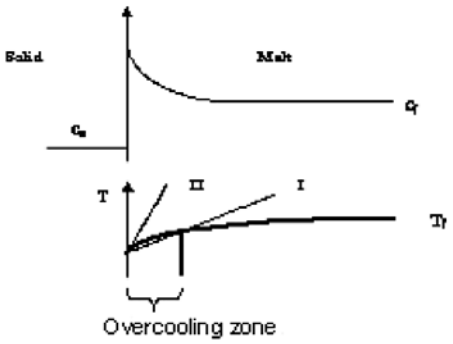

Fig. 5.23. The distribution of impurity C_l and temperature T_l at the crystallization front for the case $k_0 < 1$

$$\frac{\mathrm{d}T}{\mathrm{d}X} \geq m\frac{c_\mathrm{s}V(1-k_0)}{k_0 D}\ , \tag{5.8}$$

where k_0 is the segregation coefficient, D is the diffusion coefficient, and m is the coefficient of melting temperature decrease as a function of impurity concentration (linear approximation).

The typical signature of such instabilities (concentration overcooling) is

- a cellular growth, i.e. the phenomenon when the smooth surface of the crystallization front is broken into separate fragments and
- the probability of impurity trapping, forming a striation structure.

Figure 5.24 shows an example of such a kind of micro striation, visualized by the scattering of light by the entrapped particles.

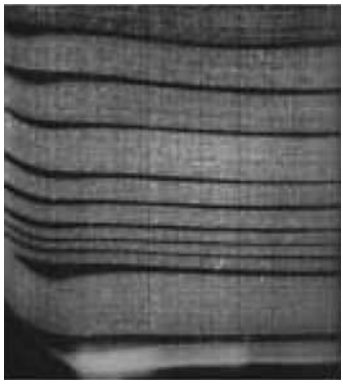

Fig. 5.24. Striation picture in grown crystals [30]

Naturally such kinds of artifacts influence the light propagation inside the crystal and at the end reduces the scintillation efficiency of the material.

There are very few descriptions of the state-of-the-art recipes for scintillation crystal growth. A few reviews related to the industrial approaches for LSO growth are for example given in [31, 32].

5.3 Activator Distribution in a Single Crystal

As was mentioned in previous chapters the scintillation mechanism in several scintillating crystals involves activator ions which are introduced as doping ions in the lattice. To manage an optimal activator concentration in the crystal the understanding of the impurity distribution process in the crystal ingot is therefore important.

Even small changes in the conditions of crystallization can induce large doping concentration variations in the crystal and result in nonuniform scintillation characteristics of the material. This problem is typical for all activated scintillators growth techniques and impose a great care on impurity selection, crystal doping conditions, and concentration control methods.

In the case of Czochralski growth, for one doping ion with a segregation coefficient $k_0 < 1$, a low evaporation rate, no pollution problems and with a diffusion rate in the liquid phase much higher than the crystallization rate, the impurity distribution is adequately represented by the Pfann (5.9) [14]. For a simple crystallization model without continuous feeding of the dopant the concentration profile is shown in Fig. 5.25.

$$C_\mathrm{s} = \frac{\kappa_0 C_0}{1-(1-\kappa_0)g} \,, \tag{5.9}$$

where g is the crystallized melt share, C_s is the impurity concentration in the melt at some point, C_0 is the initial impurity concentration in the melt, and k_0 is the segregation coefficient.

If the technical requirements impose a limit on the impurity nonuniformity along the length of a crystal,

$$\frac{c_\mathrm{bottom}}{c_\mathrm{top}} \leq \alpha \,, \tag{5.10}$$

provided that the crystallization interface is flat and that the weight of the initial cone weight is small as compared to the weight of the cylindrical part of the ingot, the optimum crystal dimensions are

$$L_\mathrm{c} d^2 = \frac{4M_0}{\pi \rho_\mathrm{s}} (1 - \sqrt[k_0 - 1]{\alpha}) \,, \tag{5.11}$$

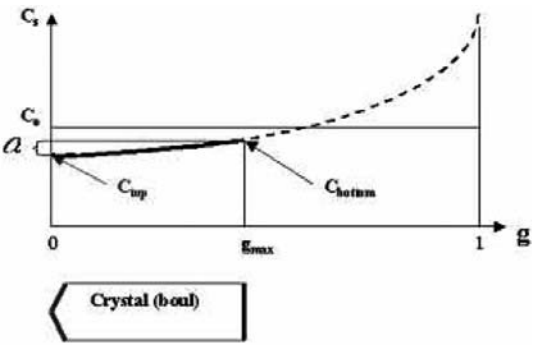

Fig. 5.25. Impurity distribution along the length of a crystal ingot

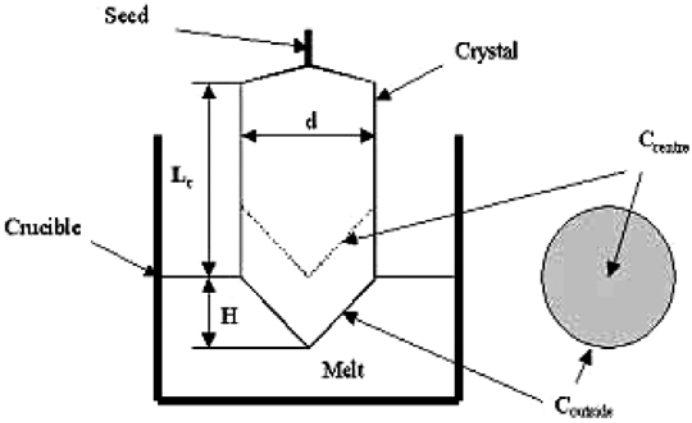

Fig. 5.26. Impurity distribution along the crystal cross-section

where L_c is the length of the crystal cylindrical part, d is the diameter of the crystal cylindrical part, M_0 is the weight of the initial melt, ρ_s is the crystal density.

However, as shown in Fig. 5.26, impurity segregation occurs not only along the length, but also along the cross-section of the crystal. If the crystallization interface is not flat the concentration profile along the crystal cross-section will depend on its curvature as well as on the crystal length and diameter.

If the technical requirements impose a limit on the impurity nonuniformity across the crystal,

$$\frac{c_{\text{outside}}}{c_{\text{center}}} \leq \beta \, . \tag{5.12}$$

In this case the ratio of the optimum crystal length, diameter and height of the crystallization interface convexity will be as follows:

$$L_c = \frac{4M_0}{\pi \rho_s d^2} - H\left(\frac{1}{1 - \sqrt[k_0 - 1]{\beta}} - \frac{2}{3}\right) \, . \tag{5.13}$$

The best solution to obtain a uniform activator distribution is therefore activator feeding during the growth process. Continuous growth allows us to control the impurity content in the melt thereby giving an opportunity to obtain scintillators with a uniform activator distribution in the whole ingot. The Tl distribution uniformity in grown CsI(Tl) crystals does not exceed $\pm$ 6% [2]. This is also a good way to compensate the evaporation from the melt in the case it is important, as it is for Tl in NaI(Tl) and CsI(Tl) crystals [2].

With this procedure of continuous growth with feeding it is possible to obtain single crystals of very large size with a good uniformity of the scintillation parameters.

5.4 Raw Material Preparation for Scintillator Crystal Growth

As was mentioned in Sect. 5.2.5 the quality and the preparation of the raw material play a very important role for the growth of oxide crystals for scintillator applications. This is even more important for alkali-halide scintillators. Many factors need to be considered to define the specifications and the conditions of scintillation single crystals growth. Using the example of the alkali-halide materials technology we discuss here the main factors influencing the crystal quality.

5.4.1 Raw Material Purity

As a rule, the criteria on the raw material purity are the first being discussed at the initial stage of the scintillator production technique development. Undoubtedly, the striving for the best purity of the initial components is important, but it does not necessarily guarantee, however, the final material quality. The raw material cost should also be taken into account. An improvement in purity by a factor of 10 (99.999% to 99.9999% for instance) corresponds to an increase in the cost by one order of magnitude.

As was shown in Chap. 5 some impurities and imperfections present in a crystal at the level of a few ppm may influence the optical quality, decrease the radiation hardness, and increase the afterglow. Therefore, the criteria for uncontrolled impurities and for an appropriate raw material specification have to be considered for each crystal specifically. The initial raw material requirements for optimal PWO crystals growth are mentioned in Sect. 5.2.5.

5.4.2 Raw Material Treatment and Preparation for the Crystal Growth

Interesting examples of raw material preparation methods concern fluoride scintillation crystals. Such materials are not only influenced by the initial component purity but also by the possible occurrence of salt hydrolysis during the storage, the preparation for crystal growth and single crystal growth itself. It is therefore necessary to purify the raw material and to control the atmosphere at the pregrowing and growing stages.

The fluoride hydrolysis of alkaline and alkali-metal (M) elements under the influence of atmosphere and adsorbed moisture can be described by the reaction

$$2\mathrm{MeF} + \mathrm{H_2O} \rightarrow \mathrm{Me_2O} + 2\mathrm{HF}\ ,$$
$$\mathrm{MeF_2} + \mathrm{H_2O} \rightarrow \mathrm{MeO} + 2\mathrm{HF}\ .$$

The resulting oxides are not isomorphic with the basic material and their traces in the crystal generally decrease its transparency and increase its sensitivity to radiation. Moreover they are often a source of strong afterglow [33].

Another example is the family of the most commonly used halide scintillators based on alkali-metal iodides. This material is highly hygroscopic and is subject to different reactions with atmosphere components. At least 17 chemical reactions describing different interactions with water, oxygen, carbonates, etc. have been analyzed so far [2]. Some examples of such reaction were referred in Chap. 5.

The products of these reactions lead to the contamination of the scintillation crystals both at the initial raw material synthesis stage and during the single crystal growth process. Therefore the methods of preparing the raw materials play a very important role and constitute a large part of the producer's "know-how."

5.4.3 Special Atmosphere for the Crystal Growth

Pregrowth raw material treatment is however not a sufficient condition to guarantee the optimal scintillator performance. Therefore these crystals are always grown in very specific atmospheric conditions. The atmosphere includes various fluorinating agents providing different recovery reactions, for example,

$$\begin{aligned}
\mathrm{MeO} + 2\mathrm{HF} &\rightarrow \mathrm{MeF_2} + \mathrm{H_2O}\ , \\
2\mathrm{MeO} + \mathrm{C_2F_4} &\rightarrow 2\mathrm{MeF_2} + 2\mathrm{CO}\ , \\
2\mathrm{MeO} + \mathrm{CF_4} &\rightarrow 2\mathrm{MeF_2} + \mathrm{CO_2}\ , \\
2\mathrm{MeO} + 2\mathrm{F_2} &\rightarrow 2\mathrm{MeF_2} + \mathrm{O_2}\ , \\
\mathrm{MeO} + \mathrm{CF_4} &\rightarrow \mathrm{MeF_2} + \mathrm{CO} + \mathrm{F_2}\ , \\
\mathrm{MeO} + \mathrm{F_2} + \mathrm{CO} &\rightarrow \mathrm{MeF_2} + \mathrm{CO_2}\ .
\end{aligned}$$

As a result, oxides are partly decomposed, and the remaining gas components are removed from the growing furnace by pump-out.

Recently, this problem has been highlighted by the growing interest for complex fluoride compounds such as $\mathrm{LiBaF_3}$:Ce, $\mathrm{LiCaAlF_6}$:Ce, $\mathrm{LiYF_4}$:Ce. Water and air components are the main contaminants for all these crystals [34]. Oxygen is commonly produced from OH ions and is an impurity. When such impurities are present, they can form oxy-complex such as $\mathrm{Me(OH)_2}$ [35]. Practical recommendations to eliminate or to at least minimize these impurities include for instance the raw material treatment for several hours in $\mathrm{CF_4}$ atmosphere [36]:

$$\mathrm{CF_4} + 2\mathrm{H_2O} \rightarrow 4\mathrm{HF} + \mathrm{CO_2}\ .$$

The use of $\mathrm{CF_4}$ atmosphere has a double effect on the purification. First, this is the way to eliminate the moisture even in trace quantities. Second, the slight enrichment in HF allows the reaction with $\mathrm{M(OH^-)}$ and $(\mathrm{MO^{2-}})$ complexes present in the melt.

In the case of industrial large-size crystal growth, reactive atmosphere treatment is possible at the stage of preliminary melt preparation (see [17]). Then the melt is supplied to a conical crucible located directly in the growth chamber, where the ingress of oxygen-containing components into the growing crystal is minimized by the choice of the gas atmosphere.

5.4.4 Additional Melt Purification

It must be noted that the melt treatment can also be efficient for single crystal purification. For example, PbF_2 doping is used for the CaF_2 single crystal growth. In this case, during lead fluoride smelting (temperature 1,097 K which is lower than the temperature of calcium fluoride smelting 1,673 K), its melt reacts with calcium oxide:

$$PbF_2 + CaO \rightarrow CaF_2 + PbO \uparrow$$

resulting in volatile lead oxide formation. Thus it is possible by this way to improve the optical transparency of the material, widely used for transparent UV windows.

5.4.5 Nonstoichiometry

Another group of structure imperfections radically influencing the single crystal scintillation characteristics is connected to the presence of nonstoichiometric defects in the crystal. This is typical for halide and oxide multicomponent scintillators.

The difference in the vapor pressure of the various components leads to a progressive deviation of the stoichiometry of the melt during the growth process. A compensation for the more volatile substance needs therefore to be applied for such crystals. For the $LiYF_4$:Ce crystal for instance the initial ratio has to be 50.5% LiF : 49.5% YF_3 [37]; for $LiBaF_3$:Ce this ratio needs to be even higher 57% LiF : 43% BaF_2 [38]. In typical oxide scintillators, $Bi_4Si_3O_{12}$ for example, an extra 1–5% of Bi_2O_3 is usually used [29,39]. Nonstoichiometry is the main reason for the radiation damage level increase. It is not so easy in practice to check the crystal stoichiometry. That is why this is usually done indirectly through the measurement of the radiation hardness as it is illustrated for BGO in [39].

5.5 Light Collection

Once a scintillating crystal with properties satisfying the user's requirements has been grown, there is still a problem of designing the detector itself in such a way as to ensure the detection of the maximum number of photons. In most applications the fraction of the photons produced in the crystal converting in

the photodetector (photomultiplier, PIN diode, avalanche photodiode) can be as low as 25–30%. The light collection optimization is therefore an important part of the scintillator detector optimization.

The number of photons extracted from a scintillator is given by

$$\eta = \alpha Y \tag{5.14}$$

where α is the light collection coefficient and Y is the yield of scintillation.

Once the crystal has been optimized with the best optical transparency in the spectral range of the scintillation light the light collection efficiency is mainly determined by the number of internal reflections of the photons inside the crystal and by the coupling interface between the crystal and the photodetector. The important parameters are

- the form and dimensions of the scintillation crystal,
- the specific features of the crystal surface treatment,
- the reflecting materials, and
- the adhesive bond "scintillator–photoreceiver."

Since the number of different types of material and surface treatment is very large it is impossible to determine a priori the optimal combination of parameters.

The theory and practice of scintillation detector engineering show that the light collection optimization is very user dependent and has to be made on a case by case basis.

Ultimately a good light collection scheme should answer two problems:

- maximize the number of photons extracted from the scintillator and
- keep a good linearity of the response as a function of the incident energy deposited in the scintillator wherever the conversion took place.

In fact the problem of light collection was already formulated long time ago [40, 41]. It was initially solved by the use of integrating spheres [40].

5.5.1 Simulations

The peculiarity of the light collection is the fact that the multiple reflections on the crystal surfaces influence the angular distribution of the reflected light as a function of the surface treatment (mainly its roughness). If in general the profile of reflection (indicatrix) has, as a rule, a pronounced maximum for a reflection angle equal to the angle of the light incidence, the features of this profile are determined by the material and by its surface treatment. The efficiency of the transfer as a function of the incident angle is also very complex. However, some approximation can be made. In particular in [40, 42, 43] the calculation of light transfer with a diffuse reflector was carried out in the so-called cosine approximation. In this case the reflection indicatrix is described by the equation

$$\Psi(\theta) = \pi^{-1} \cos\theta \, . \tag{5.15}$$

There are also some other known approximations and algorithms for light collection simulation by analytical methods.

In the recent years calculations of light collection and light propagation by statistical methods (Monte Carlo technique) [42–45] have become more and more reliable. The trajectories of all the photons produced in the scintillator bulk are calculated. Monte Carlo techniques consider the random character of the light diffusion process and in particular the differences in crystal surface treatment and in the specificity of the reflecting coating.

However, statistical methods are not free from some drawbacks, such as the poor modelization of certain surface states leading to a rather wide spread of some results and the difficulty to introduce the specific structure of the light diffusion indicatrix to simplify the algorithm and to minimize the calculation time which is still very long. However, computer development and increased calculation speed allow Monte Carlo techniques to gradually take over other approaches for light collection calculations. Moreover, the existing standard programs of DETEC type convert a scientific problem into a purely technical task [46].

In practice the critical point of these methods lies on the accuracy to simulate the behavior of the reflecting surface. In general two extreme cases are considered. In the first one the light collection is considered for a scintillator with mirror-like reflecting surfaces. This is also the simplest type of surface treatment and it is easily reproducible. In the case of scintillators with a regular geometrical form and without considering the light absorption in the crystal bulk, the value α is determined by the relationship [40]

$$\alpha_{a0} = \frac{1}{2}(1 - \cos\theta_1) = \frac{1}{2}\left(1 - \sqrt{1 - \frac{n_1^2}{n_2^2}}\right) \, , \tag{5.16}$$

where n is the refraction index of the crystal.

As follows from the equation a fraction of the light cannot escape the detector [43, 47, 48] which obviously limits the light collection efficiency. In order to improve this situation the geometry of the detector or the surface state must be modified.

Calculations have been made [42, 49] demsonstrating the importance of the shape (for BGO crystals). They show that crystals with a right-angle prism shape capture more than half of the photons.

Different ways have been considered to increase the light output from a scintillator: (a) the use of a photomultiplier tube (PMT) with a window refractive index matching as closely as possible the one of the crystal, (b) the production of scattering centers inside the crystal (for example, small gas bubbles), (c) the modification of the crystal shape and, finally, the coating of the crystal with diffusion reflector [43].

The use of diffusing materials at the surfaces allows us to significantly increase the light collection on small-size detectors with an aspect ratio close to 1. Moreover, the absence of predominant directions in the light propagation helps uniformize the light output within the whole scintillator bulk.

On the other hand, numerous calculations and several applications have shown that the mirror-reflecting surfaces are more efficient for long detectors with a bad aspect ratio or when the scintillator is in the shape of a plate with the receiver mounted on a side surface.

In the recent years a lot of experimental data have been accumulated which helped better tune the simulation programs. The discordances between calculations and experiments for "standard"-shaped detectors are now minimal [44, 45]. It gives some hope to make good predictions for new and more difficult shapes of crystals.

High energy physics has spent a large effort in light collection modeling in scintillators of various shapes [45] as shown in Fig. 5.27. These calculations were verified by the experimental data in CsI(Tl) scintillators for the BELLE and BaBar [50, 51] experiments.

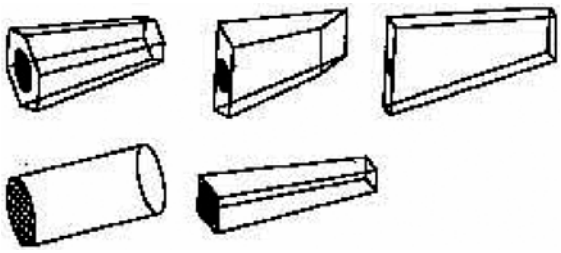

Fig. 5.27. Different shapes for HEP detectors simulated in [45]

The optimization of the light output in the 23 cm long PWO crystals for the CMS calorimeter was considered in [52]. It was shown that better light yield uniformity is achieved when one of the crystal surfaces is grinded with a specified roughness.

Scintillators for PET systems, although much smaller in size, require a precise optimization of the light collection and have been the subject of mathematical modeling [48]. Calculation by Monte Carlo technique showed that a better homogeneity of the light output can be obtained by the use of diffusion reflector with a high index of refraction and by matting the crystal face opposite to the light receiver.

The public version of the DETEC program [46] offers four different options for scintillation light collection modeling. In the METAL model, the surface is assumed to be smooth and covered by metalized coating. The PAINT model simulates diffuse reflecting surface. The POLISH and GROUND models represent surfaces that can be optically matched with other material.

Such relatively simple and available software allows us to simulate the light collection peculiarities for new scintillator configurations.

Several other simulation programs have been developed and tuned on real cases. The most complete overview of up-to-date calculation methods for light collection and typical examples of light collection simulations in scintillation detectors are presented in [44].

5.5.2 Detector Shaping

In the previous examples each crystal was considered as a single pixel which defines the coordinates of the incoming particle or γ-ray to be detected. For some applications large-size crystals are used and shaped in such a way as to provide a good uniformity of the response as well as a determination of the coordinates of the conversion point.

The idea of shaping the surface to influence the light output distribution was born 30 years ago [53]. The scheme of this light collection method is shown in Fig. 5.28.

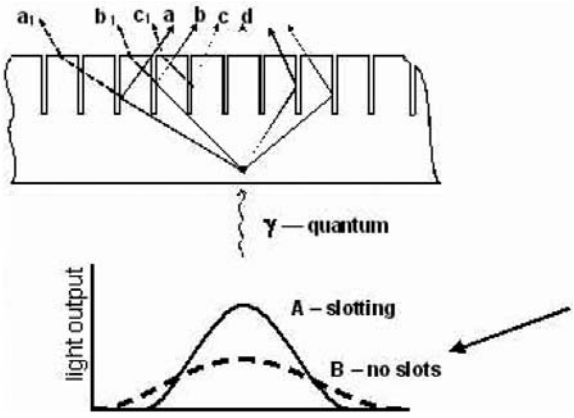

Fig. 5.28. Light collection in a slotted scintillator

The surface of the crystal is machined with slots in order to modify the conditions of light reflection at the surface. The geometry of the slots (the depth, spacing, slot filling material, etc.) is defined in order to optimize the performances for every specific application.

In [54] one-dimensional slots were cut into the entrance side of a $1''$ NaI(Tl) detector and the measurements demonstrated an improved spatial resolution. The study described in [55] showed that slots in the surface near the edge of the crystal resulted in a narrow light spread function and improved the resolution near the detector edge, thus increasing the useful area of the NaI(Tl) detector.

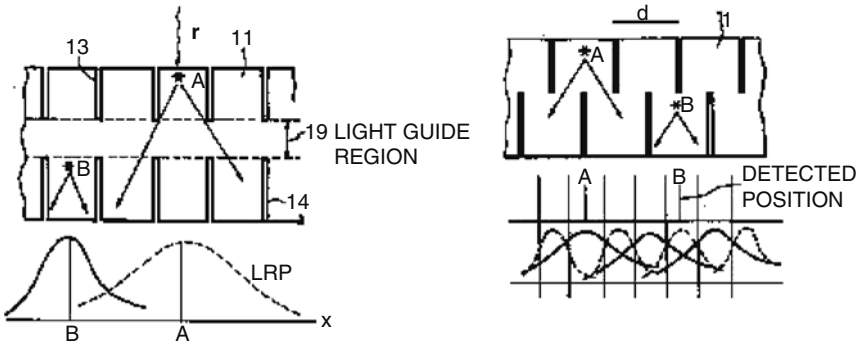

Fig. 5.29. Two surface slotting for light collection modification [57]. The bottom figures show light response functions for different scintillation flash positions

This idea found a very good application at the end of the 1990s in nuclear medicine in dual mode (SPECT-PET) systems. The StarBrite^{TM} detector from Saint Gobain with slots on the exit surface was able to produce the same light distribution in the whole energy range of the incoming γ-rays from 80 to 511 keV. Moreover, this light distribution is the same as for the conventional SPECT detectors of 9.5 mm thickness. The same readout technique as for conventional SPECT cameras is therefore directly applicable to the thick (25 mm) scintillator used for the dual mode cameras.

Figure 5.29 illustrates the influence of the slots depth and position on the light output distribution. It is interesting to notice that the slots not only collimate the light produced in the scintillator in the direction of the photomultipliers but, as a consequence of this collimation, also increase the amount of light extracted from the crystal.

Several variations of this technique have been applied. For instance, in [56] the slots were machined at the entrance surface of the scintillator. In [57] (see Fig. 5.30) the slots network was machined on both surfaces in order to give an additional information on the depth of interaction in the crystal.

The idea of the light output modification by means of surface slots has also been widely used in PET systems. The initial design based on direct coupling of the matrix detector with a PMT [58] was gradually modified by the introduction of a slotted light guide, the so-called light sharing scheme [59, 60] (see Fig. 5.30), being used in several PET systems. The individual elements have $5.8 \times 2.8\,\text{mm}^2$ cross section and 0.5 mm gap filled with reflective material.

Another example of shaping the scintillator surface for regulating the light output and improving the spatial resolution of the detector is the use of a retro-reflector. This technique can make use of a specific coating [61] or be applied directly on the crystal surface [62]. In these cases the surface of the crystal or reflector is machined to form small pyramids as in a catadioptr (therefore such type of light collection is called "retro-reflecting" [61]). The

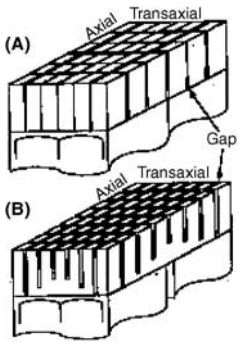

Fig. 5.30. Matrix and pseudo-discrete BGO PET block detector [59]

interest of this method is to significantly improve the light yield without decreasing the spatial resolution as would be the case with the use of a standard reflector on the back surface of the crystal (see Fig. 5.29). Such detector design allows us to reduce the influence of edge effects and to broaden the gamma camera useful field of view [62].

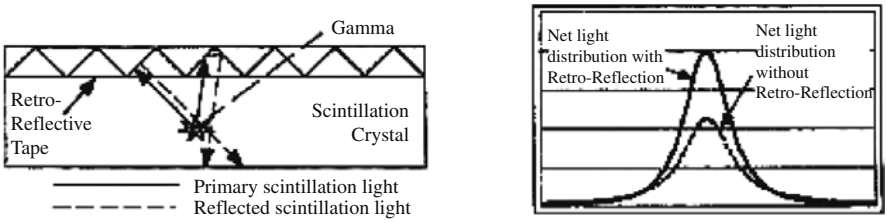

Fig. 5.31. Reflections and profiles of the light output intensity at the interface of PMT and crystal plate [61]

These examples show that the light collection optimization is one of the most important problems for scintillation detector engineering. There is a large variety of methods which have been developed for different applications on a case by case basis as the efficiency of the method is always a compromise between the choice of the scintillator material, its shape, and the technology applied for the light collection.

5.5.3 Optical Guide

The light collection optimization requires sometimes the use of a transition material between the scintillating crystal and the photodetector. In some cases the detector design does not allow us to optimally match the geometry of the scintillator with the entrances window of the photodetector. There are

in practice frequent situations of square scintillation assemblies with round cross-section PMT registration. In this case light guides are used to collect the maximum of light from the crystal and to guide it to the photodetector entrance window. Optical quartz windows are usually used as light guides particularly for near UV emitting scintillators.

Another motivation for the use of light guides is to move away the photodetector from the scintillating crystal array for position-sensitive devices. This is mandatory in the case of PMT readout in a magnetic field, or to allow a more compact design of the detection head and suppress the dead space introduced by the packaging of the photodetector.

5.5.4 Wavelength Shifters

Once the maximum number of scintillation photons have been guided to the photodetector, they still need to be converted into electrons to produce an electric signal to be processed by the readout electronics. This is the last stage of the scintillation detector optimization. In particular, the spectral sensitivity of a photodetector needs to be adjusted to the spectral range of the scintillation light. There is a large variety of PMT with different spectral sensitivities; however, a perfect matching is not always possible particularly for fast UV emitting scintillators.

One possible technique to overcome this problem is the use of wavelength shifters. It has been used to optimize the light collection in pure CsI [63]. The luminescence spectrum of such crystals is in the UV region (300–310 nm), where the sensitivity of PMT and photodiodes is very low. Usually such photodetectors have a maximum quantum efficiency in the blue or in the red spectral range. The shifters convert the UV scintillation from the crystal into visible light by the use of organic dyes (15–20 μm thick films) deposited on the crystal surface or on the photodetector entrance window. The role of the shifter is to absorb the light in the short wavelength region and to spontaneously re-emit it at a longer wavelength. The quantum efficiency of such a process may reach 90% or even more. The decay time of organic media can be very short, of the order of 1 ns, not compromising the timing performance of the scintillator. The efficiency loss resulting from this transformation can therefore be negligible as compared to the much higher losses induced by the spectral mismatch of the scintillator and the photodetector. As a result the conversion of UV luminescence into blue light can increase the overall efficiency of the detector. In [63], 10 types of scintillation dopants for polymethylphenylsioxane resins are presented to shift emissions in the 305–410 nm spectral range to the 360–550 nm range.

Figure 5.32 shows the luminescence spectrum of a CsI sample before and after coating with a wavelength shifter. Curve 3 represents the transmission of the film itself. The fast UV intrinsic luminescence of CsI (see curve 1) is absorbed by the film and shifted by about 100 nm to the region of 400 nm. Such experiments with at least five different types of wavelength shifters

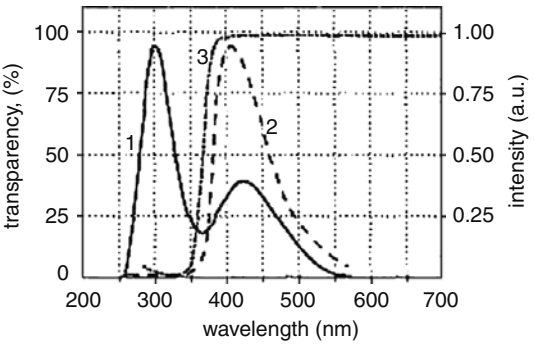

Fig. 5.32. Radioluminescence spectra of 5 mm thick, 30 mm diameter CsI sample before (*1*) and after (*2*) shifter. (*3*) Transmission spectrum of the film itself [63]

demonstrated a light output increase by a factor 1.7 to 1.8. At the same time an increase of the fast component contribution of the light from 0.6–0.7 up to 0.8–0.85 was obtained.

Such techniques are also efficient for more standard material such as CsI(Tl), in spite of, it would seem, quite well coincidence of luminescence spectrum and spectral sensitivity Si-photodiodes. The luminescence of CsI(Tl) consists of two main bands: the first one is complex and consists of several overlapped bands at 400–440 nm related to vacancy-based luminescence [65]). The main band (more intense) is at 560 nm and is caused by the exciton localization near Tl^+ ions [64]. The ratio between these bands depends on the concentration of Tl^+ ions (the blue emission more intense for a low Tl^+ contents). The use of "blue–green" shifter film (as is shown in Fig. 5.33) allows

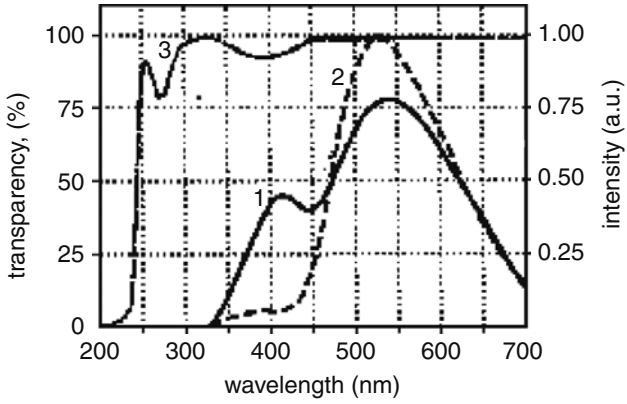

Fig. 5.33. Radioluminescence spectra of 5 mm thick, 30 mm diameter CsI sample before (*1*) and after (*2*) coating with shifter. (*3*) Transmission spectrum of the film itself. The content of Tl is 0.04 mass%

us to convert the blue emission into the green one and to increase the total light yield up to 35–40%. Such shifting is efficient for long scintillators due to a better transparency in the green than in the blue and particularly when small-size photodetectors (such as photodiodes) are used.

References

1. (a). Urusov VS (1987) Theoretical Chemistry of Crystals. Nauka, Moscow (in Russian)
   (b). Kroger FA (1964) The Chemistry of Imperfect Crystals. North-Holland, Amsterdam
2. Crystal Growth. Alkali Halides (2002) Acta, Kharkov (in Russian)
3. Kaposi O, Benese L, Zuravleva LV (1986) Determination of the thermodynamic activities by mass-spectrometry. J. Chem. Thermodyn. 18: 635–645
4. Iliasov II, Bergman AG (1966) The system Na^+, K^+, Cs^+ I^-. Inorg. Chem. B 3: 681–683 (in Russian)
5. Mahosoev MV, Alekseev FP, Lutsik VI (1978) Phase Diagram for Tungstates. Nauka, Novosibirsk (in Russian)
6. Patents of Russian Federation no 2132417, no 2164562
7. Moses WW, Derenzo SE, Fedorov A et al. (1995) $LuAlO_3$:Ce – a high density, speed scintillation for gamma detection. IEEE Trans. Nucl. Sci. 42: 275–279
8. Trower WP, Korzhik MV, Fedorov AA et al. (1996) Cerium doped luthetium-based single crystal scintillator. In: Dorenbos P, van Eijk CWE (Eds). Proc. Int. Conf. on Inorganic Scintillators and Their Applications, SCINT'95. Delft University Press, The Netherlands, pp 355–358
9. Smirnova SA, Korzhik MV (1996) Growth of crystals yttrium-aluminium perovskites with rare earth elements. In: Dorenbos P, van Eijk CWE (Eds). Proc. Int. Conf. on Inorganic Scintillators and Their Applications, SCINT'95. Delft University Press, The Netherlands, pp 495–497
10. Patent of the Russian Federation no 2233916
11. Lodis R, Parker R (1974) Crystal Growth. Rus. ed., Mir, Moscow, pp 176–183
12. von Wilke K-Th (1973) Kristallzuchtung. Wilke unter Mitarbeit von J. Bohm. VEB Deutsher Verlag der Wissenschaften, Berlin
13. Gektin AV, Zaslavsky BG (2003) Halogenide scintillators: growth and performance. In: Scheel H, Fukuda T (Eds.) Crystal Growth Technology. Wiley, New York, pp 511–536
14. US Patent 2,214,967
15. Stockbarger DC (1936) The production of large single crystals. Rev. Sci. Instrum. 7: 133–136
16. Kyropolos S, Zeits F (1926) Ein Verfahren zur Herstellung grosser Kristalls. Anorg u. allgem Chem. 154: 308–313
17. Czochralski J (1918) Ein newes Verfahren zur Messung der Kristallisatinosgeschwindigkeit der Metalle. Z. Phys. Chem. 92: 219–224
18. (a). Tanji K, Ishii M, Usuki Y et al. (1999) Crystal growth of $PbWO_4$ by the vertical Bridgman method: effect of crucible thickness and melt composition. J. Cryst. Growth 204: 505–511
    (b). Ishii M, Harada K, Hirose Y et al. (2002) Development of BSO ($Bi_4Si_3O_{12}$) crystal for radiation detector. Opt. Mater. 19: 201–212

(c). Ishii M, Kuwano Y, Asai T, Senguttuvan N et al. (2003) Growth of Cu-doped $Li_2B_4O_7$ single crystals by vertical Bridgman method and their characterization. J.Cryst. Growth 257: 169–176
19. Pfann W.G. (1966) Zone Melting. Wiley New York and London
20. Tatarchenko VA (1988) Stable Crystal Growth. Nauka, Moscow (in Russian)
21. Gektin AV (2000) Halide scintillators: present status and prospects. In: Mikhailin VV (Ed). Proc. of the Fifth Int. Conf. on Inorganic Scintillators and Their Applications, SCINT99. Moscow State University, Moscow, pp 79–88
22. U.S. Patent 4,834,832
23. U.S. Patent 4,036,595
24. Eidel'man LG, Goriletsky VI, Nemenov VA et al. (1985) Automated growing of large single controlled by melt level sensor. Cryst. Res. Technol. 20(2): 167–172
25. Zaslavsky B (1999) Automated pulling of large-diameter alkali halide scintillation single crystals from the melt. J. Cryst. Growth 200: 476–482
26. Smet F, van Enckervort WJP (1988) On the distribution of point defects in large sized bismuth germanate crystals. J. Cryst. Growth 88: 169–179
27. Borolev YuA, Ivannikova NV, Shlegel VN et al. (2001) Progress in growth of large sized BGO crystals by the low-thermal-gradient Czochralski technique. J. Cryst. Growth 229: 305–311
28. Shlegel VN, Shubin YuV, Ivannikova NV (2003) BGO crystal growth, J. Korean Cryst. Growth Cryst. Technol. 13: 1–4
29. Atroshenko L, Burachas S, Galchinetsky L et al. (1998) Scintillation crystals and radiation detectors on its base, Kiev (in Russian)
30. Gektin AV (2000) Growth and characterization of scintillation and storage materials, In: Fukuda T (Ed). Second Int. School on Crystal Growth Techn (Book of lectures), Japan, pp 304–327
31. Garmash VM, Beloglovski SYa, Lubetsi SL (2002) Industrial manufacturing of cerium-doped lutetium silicate crystals on enterprise joint-stock-company "North Crystal". Nucl Instrum. Methods Phys. Res. A 486: 106–110
32. Melcher CL, Schweitzer JS, Peterson CA et al. (1996) Crystal growth and scintilation properties of the rare earth oxyorthosilicates. In: Dorenbos P, van Eijk CWE (Eds). Proc. Int. Conf. on Inorganic Scintillators and Their Applications, SCINT'95. Delft University Press, The Netherlands, pp 309–316
33. Weller PF, Scardefield JE (1964) Doping of alkaline earth halide single crystals. J. Electorochem. Soc. 111(8): 1009–1011
34. Pastor RC (1999) Crystal growth of metal fluorides for CO_2 laser operation: I. The necessity of the RAP approach. J. Cryst. Growth 200: 510–514
35. Ranieri IM, Morato SP, Bressiani AHA et al. (2002) Growth of $LiYLuF_4$ crystals under CF_4 atmosphere. J. Alloys Compd. 344: 203–206
36. Belt R, Uhrin R (1991) Top seeded solution growth of Cr^{3+}: $LiCaAlF_6$ in HF atmosphere. J. Cryst. Growth 109: 334–339
37. Raineri I, Baldochi S, Santo A (1996) Growth of $LiYF_4$ crystals doped with holmium, erbium and thulium. J. Cryst. Growth, 166: 423–428
38. Baldochi S, Shimamura K, Nakano K et al. (1999) Growth and optical characteristics of Ce-doped and Ce:Na-codoped $BaLiF_3$ single crystals. J. Cryst. Growth 200: 521–526
39. (a) Shulgin BV, Polupanova TI, Kruzalov AV, Skorikov VM (1992) Bithmut Orthogermanate Ecaterinburg, p 170 (In Russian)

(b) Gusev VA, Kupriyanov IN, Antsygin VD et al. (2001) Features of radiation damage of BGO crystals grown by the low-thermal-gradient Czochralski technique. Nucl. Instrum. Methods Phys. Res. A 460: 457–464
40. Tsirlin YuA. (1975) Light Collection in the Scintillation Counters. Atomizdat, Moscow (in Russian)
41. Tsirlin YuA, Globus ME, Sysoeva EP (1991) Optimization of Gamma Detection in Scintillation Crystals. Energoatomizdat, Moscow (in Russian)
42. Derenzo SE, Rilers JK (1982) Monte-Carlo calculations of the optical coupling between bismuth-germanate crystals and photomultiplier Tubes. IEEE Trans. Nucl. Sci. 29: 191–194
43. Carrier C, Lecomte R (1990) Theoretical modelling of light transport in rectangular parallelepipedic scintillators. Nucl. Instrum. Methods Phys. Res. 292(3): 685–692
44. Globus ME, Grinyov BV (2001) Inorganic new and conventional scintillators. Acta, Kharkov (in Russian)
45. Gavriluk VP, Vinograd EL, Grinyov BV et al. (1997) Effect of surface conditions on the light collection in scintillation detectors. Search for optimum light collection conditions in cylindric scintillation detectors. Funct. Mater. 4: 572–583
46. Knoll GF, Knoll TF, Henderson TM (1988) Light collection in scintillation detector composites for neutron detection. IEEE Trans. Nucl. Sci. 35: 872–875
47. Carrier C, Lecomte R (1989) Trapping of fluorescent light in cylindrical scintillators. Nucl. Instrum. Methods Phys. Res. A 288(2): 622–624
48. Carrier C, Lecomte R (199) Effect of geometrical modifications and crystal shapes on light collection in ideal rectangular parallelepipedic BGO scintillators. Nucl. Instrum. Meth Phys. Res. A 294(1–2): 355–364
49. Derenzo SE (1984) Gamma-ray spectroscopy using small, cooled bismuth germinate scintillators and silicon photodiods. Nucl. Instrum. Methods Phys. Res. 219: 117–122
50. BaBar Collaboration, BaBar Technical Design Report, SLAC-R-95-457
51. Gektin AV, Gavrylyk V, Zosim D, Yankelevich V, (2000) Long length scintillators for the position sensitive radiation detection IEEE NSS/MIC Abstracts 58
52. Auffray E., Lecoq P., Schneegans M. et al. (2002) Crystal conditioning for high-energy physics detectors. Nucl. Instrum. Meth. Phys. Res. A 486: 22–34
53. Patent France 2,237,206.
54. Freifelder R, Haigh AT, Karp JS (1993) Reducing edge effects and improving position resolution in position sensitive NaI(TI) detectors. IEEE Trans. Nucl. Sci. 40: 208–213
55. Yu DC (1997) Light output distribution in slotted crystal. IEEE MIC Conf. Rec. Paper M10-24
56. Surti S, Freifelder R, Karp JS (2001) Slotted surface treatment of position-sensitive NaI(Tl) detectors to improve detectors performance. IEEE Trans. Nucl. Sci. 48: 2418–2423
57. U.S. Patent 4,831,263
58. U.S. Patent 5,091,650
59. Tornai MP, Germano G, Hoffman E (1994) Positioning and energy response of PET block detectors with different light sharing schemes. IEEE Trans. Nucl. Sci. 41: 1458–1463

60. Rogers JP, Taylor AJ, Rahimi MF et al. (1992) An improved multicrystal 2-D BGO detector for PET. IEEE Trans. Nucl. Sci. 39(4): 1063–1068
61. McElroy DP, Sung-Cheng Huang, Hoffman EJ (2002) The use of retro-reflective tape for improving spatial resolution of scintillation detectors**.** IEEE Trans Nucl Sci 49: 165–171
62. U.S. Patent 5,861,628
63. (a) Andryushenko LA, Vinograd EL, Gavriliuk VP et al. (1997) An influence of surface conditions on the scintillation properties of CsI crystals. IET 4: 19–21 (in Russian)
(b) Andryushenko LA, Kudin AM, Goriletsky VI et al. (2002) Functional possibilities of organosilicon coatings on the surface of CsI-based scintillators. Nucl. Instrum. Methods Phys. Res. A 486: 40–47
64. Zazubovich S, Karner T, Nagirnyi V et al. (1996) Exciton luminescence in Tl^{+} and Pb^{2+} doped cesium halides. In: Shreiber M (Ed). Extonic Process in Condensed Matter, Dresden University Press, pp 235–238
65. Bates CW Jr, Schneider I, Salau A et al. (1976) X-ray diffraction measurement of the Jahn–Teller distortion in $TmVO_4$. Solid State Commum. 15: 101–104

6 Two Examples of Recent Crystal Development

Abstract. Two examples of recent scintillator development are given in this chapter. They have been chosen in two different areas of applications to illustrate the common strategies, but also the differences in the approach. Lead tungstate illustrates particularly well how large and very challenging fundamental research projects are instrumental in pushing the limits of detector performances to meet an ambitious scientific goal. On the other hand, Lutetium perovskite crystals, although developed up to mass scale production by an acamedic consortium (the Crystal Clear Collaboration), is a crystal to be used mainly in commercial systems like medical imaging devices. It is therefore constrained not only by technical considerations but also by a severe competition environment, as any new commercial product.

6.1 Example of Lead Tungstate Development for High Energy Physics Experiments

6.1.1 Introduction

High energy physics is a driving force in the development of new scintillators because of the high level of performance required in particle physics detectors and of the large volumes needed.

The first example of a well organized R&D effort for the development and mass production of scintillating crystals for a large high energy physics experiment is the L3 experiment [2] at the CERN Large Electron Positron collider in the 1980s. More than 12,000 bismuth germanate (BGO) crystals were produced at the Shanghai Institute of Ceramics (China) for this experiment (Fig. 6.1). Through the example of the CMS electromagnetic calorimeter being built at CERN in the frame of its Large Hadron Collider program this chapter describes the strategies developed for the R&D and the procurement of nearly 100 tons of lead tungstate scintillating crystals in a period of about 10 years. This project is now well under way as more than one half of the crystals have been produced so far (2005) and the detector is in its assembly phase.

The CMS experiment (Compact Muon Solenoid) [3] to be installed at the future Large Hadron Collider (LHC) at CERN has proposed the construction of a scintillator-based high-resolution homogeneous calorimeter, to meet the

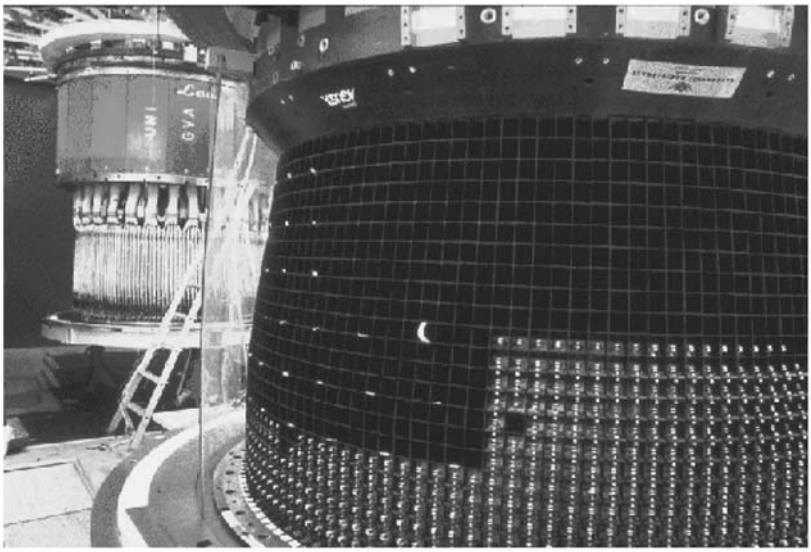

Fig. 6.1. BGO scintillation cells in the L3 Collaboration Electromagnetic calorimeter. An assembling phase

performance criteria for the discovery of an intermediate mass Higgs boson in its 2γ decay mode. The choice of lead tungstate crystals ($PbWO_4$) has been made in 1994 because of its high density, fast luminescence, and reasonable light yield and radiation resistance. It has also been decided to build a $PbWO_4$ electromagnetic calorimeter for the ALICE experiment [4] to take advantage of the very fine granularity allowed by the high density of this material, in order to resolve the high multiplicity events generated by heavy ions collisions at LHC. CMS will require 61,200 barrel crystals of trapezoidal shape divided into 17 types with average dimensions $(2.2 \times 2.2) \times (2.6 \times 2.6) \times 23$ cm^3 and 15,000 endcap crystal (one type) $(2.8 \times 2.8) \times (3 \times 3) \times 22\,\text{cm}^3$ for a total volume of $11\,\text{m}^3$ and a weight of 90 tons (Fig. 6.2).

The difficult physics constraints and harsh experimental conditions impose very tight specifications to modern detectors. The size of the experiments and the high quantitative demand allowed us to organize the R&D effort and production on a large scale (Table 6.1). This has been particularly illustrated by the work of the Crystal Clear Collaboration [1] which was able to create a multidisciplinary effort to make the best use of cross-fertilization between different categories of experts and industry to develop suitable scintillators at an industrial scale. In the case of the LHC program at CERN the possibility of making use of the large production infrastructure installed during the cold

Fig. 6.2. Some of the 80,000 CMS crystals on the automatic certification device

Table 6.1. Crystal calorimeters in the world

	Crystal Ball	Cleo II	L3	Babar	Belle LoI	L* EoI	GEM EoI	L3P	ALICE	CMS
Where	SPEAR	CESR	LEP	SLAC	KEK	SSC	SSC	LHC	LHC	LHC
When	1972	Late	1980s	1999					2007	2007
Beam	e^+e^-	e^+e^-	e^+e^-	e^+e^-	e^+e^-	pp	pp	pp	ion–ion	pp
Energy (Gev)	4	6	100	$9+3.1$	$8+3.5$	20	8,000	8,000	5.500	7,000
Crystal	NaI:Tl	CsI:Tl	BGO	CsI:Tl	CsI:Tl	BaF_2	BaF_2	CeF_3	$PbWO_4$	$PbWO_4$
Number (k)	0.7	7.8	11.4	6.8	8.8	26	45	100	18	77
Length (X_0)	16	16	21.5	16	16	24.5	25	25	22	25
Photodetector	PMT	SiPD	SiPD	SiPD	SiPD	V4T	SiPD	VPD	SiPD	APD/V3T
B(T)	0	1.5	0.5	1	1	0.75	4	1	0.5	4
f_{BC} (MHz)	1.3	2.8	0.091	2.38	10	60	67	67	8	40

war in former Soviet Union has been a key to the success. This has motivated the collaboration of physicists with the International Science and Technology Center (ISTC) [5] for the conversion of the Bogoroditsk Techno-Chemical Plant in Russia for the production of a large fraction >90% of the 80,000 lead tungstate crystals for the CMS experiment at CERN. The rest of the crystals are produced by the Shanghai Institute of Ceramics in China.

6.1.2 The Conditions of Scintillator Development for High Energy Physics (HEP)

The context of scintillator development for HEP is rather difficult. The market cannot be stabilized because of the rapidly evolving demand at each generation of experiment. The very large size of the projects imposes a strong effort of development and production in a relatively short period of time. Unfortunately the benefit of these efforts is very often lost if the next experiment requires another scintillator with improved performances. For a long time NaI(Tl) was the only candidate because the most important parameter was a high light yield to be able to read out the signals from low energy particles with standard electronics. Then, the increasing size of the experiments and the necessity of having a good granularity of the detectors opened the research toward higher density materials. That was the era of BGO with a very high density of 7.13 but a rather moderate light yield and CsI with a smaller density of 4.51 but a much higher light yield, which seems to have been a good compromise, as it is the only scintillator to have been used in at least five large size detectors so far. Unfortunately the hunt for very rare events imposed to build accelerators of higher luminosity, putting new constraints for short decay time of the scintillators. The requirements for high density have been further increased, whereas the one for high light yields has been somehow reduced because of the increased energy of incoming particles and of the emergence of new type of photodetectors such as avalanche photodiodes. These new requirements triggered a strong R&D effort on BaF_2, CeF_3, and $PbWO_4$.

Another difficulty for this activity is the complexity of the decision mechanisms in HEP. As new technologies are needed for every new generation of experiment, an important R&D effort has to be made for a proof of feasibility and a good understanding of cost issues, before any approval can be made. This takes usually several years during which no firm commitments can be made and some conditions can change. At least two difficult cases were experienced in the recent past:

- The large effort of several years for the development of large size radiation hard blocks of BaF_2 crystals was suddenly stopped by the decision to stop the SSC program in the USA.
- Similarly, the spectacular developments of avalanche photodiodes have led the CMS collaboration to finally prefer lead tungstate crystals with a lower light yield but higher density, to the higher light yield cerium fluoride CeF_3, in order to build a more compact and less expensive detector.

The uncertainty of future markets for these new scintillators is another problem for the crystal producers. At least in the first phases of the development the prospects for other applications than physics experiments are not well known. Although the situation has been rather good for BGO in the scientific, industrial, and medical domains, reasonably good for CsI with

several physics experiments and some commercial applications, it is still very unclear for BaF_2, CeF_3, and $PbWO_4$.

On top of these difficulties, the more and more severe budgetary constraints impose strong limits on the production costs of the scintillators which are only partially compensated by the financial support during the R&D phase.

Keeping in mind all these difficulties, a proper strategy has been set up for the development and production of the large quantity of lead tungstate crystals of the CMS electromagnetic calorimeter.

6.1.3 Strategy for the CMS Calorimeter

6.1.3.1 General Considerations

The first and probably most important action in the beginning of such a challenging project is to clearly define the objectives. This includes a strict definition of a list of realistic specifications to be reached by the crystal, in order to guarantee the physics performance of the detector without overdesigning. The understanding of the cost-driving factors and the study of the methods to reduce their impact on the final cost has to be included in the R&D program at the same level as the fight for improved technical parameters. Finally, the preparation of the production infrastructure must be included in the overall program with a detailed analysis of all the production aspects: procurement of raw materials, equipment, manpower, and safety. In the case of CMS a program has been set up in three phases with 3 years' R&D, 2 years' preproduction, and about 5 years' production periods.

A proper funding must be defined for each phase in full agreement with the crystal producers. It is important that the losses are minimized in the case of a modification or even a stop at any stage of the program. For the first time in the history of high energy physics, CMS has organized a well-defined support during the R&D and the preproduction phase funded by CERN with the help of the International Science and Technology Center (ISTC) in Russia. ISTC is an intergovernmental organization to bridge between Russian institutes and the world market and to promote their conversion from military to civil applications. This long-term effort associated with a nonnegligible risk must be shared with well-selected industrial partners. The possibility of making use of the large production infrastructure installed during the cold war for the growth of nonlinear crystals for military applications has played an important role in the selection of the Bogoroditsk Techno-Chemical Plant (BTCP) in Russia.

The traditional client–producer relationship must be replaced by a more effective spirit of collaboration. A mutual understanding of the different constraints on both sides has to be built in the necessary respect of a certain level of confidentiality to protect the long-term interests of the producers. This sociological aspect is very important and although it takes generally

several years to be fully integrated, it contributes to a large extent to the success of the operation. Such challenging projects cannot be successfully realized without solving the difficult equation of maximization of happiness on both sides: best performances for lowest cost on the client side, versus best profit and possibility of attracting other clients on the producer side.

6.1.3.2 Organization of the R&D

An important characteristic in the field of material science is that it requires a multidisciplinary approach. The users (in our case high energy physicists) define a set of desired performances which determine the goal to be reached. The crystal producers bring the technology and their experience in organizing mass production with maximum yield and optimized cost. A group of experts are also needed in different fields such as solid state physics, spectroscopy, chemistry, and trace element analysis, to help producers to reach the specifications set by the users. Some of the required expertise may exist in the production centers, but in most of the cases one has to open the collaboration to outside laboratories. One difficulty is to select these groups not only for their expertise but also for their ability to understand the specific spirit of their contribution. They have on the one hand to understand the user's requirements and on the other hand to help solving problems in an industrial context and not only for their academic interest. This is a long-term work, and the experience gained in previous large projects as well as R&D efforts in the frame of officially supported groups such as the Crystal Clear collaboration at CERN [1] plays a crucial role in organizing these contacts.

Another problem comes from the difficulty of the measurements in the field of material sciences, which require very often heavy equipment with scheduled access spread in different parts of the world. This is the case for synchrotron radiation sources, radiation facilities, EPR systems, and to a lesser extent for thermo-luminescence and elaborated spectroscopic devices. The time needed to perform and analyze the results of the experiments is long. This is why a specific organization had to be made in order to reduce the feedback loop with the producer. For each problem (radiation hardness), or quantity to be improved (light yield), experts are asked to propose a few tests to identify the parameters involved in this problem. Once these parameters are known, they are systematically scanned by the producer in order to find the best optimization. At this stage, a two-level feedback loop is organized, one with a few simple tests made in the vicinity of the production center to allow quick reactions, and another one with more indepth studies in specialized laboratories for a full control and understanding of the process. Once a significant improvement seems to have been made, it has to be confirmed on a statistical basis on a set of at least 10 full-size crystals in the conditions of mass production. This approach reduces as much as possible the time needed to solve a problem. However, one has to count about 1 year for each important step in the development of a new material. This is the time

it took the CMS collaboration to grow crystals of the required dimensions in 1994, to suppress slow components at the end of 1995, and more recently to make significant progress in radiation hardness of lead tungstate crystals [6].

6.1.3.3 Cost Optimization

One important aspect of these developments is the cost optimization. All the R&D effort must be driven by cost considerations. It is not sufficient to solve a problem with nonaffordable solutions. This is why the R&D as well as the production strategy is developed as a function of the existing infrastructure in the production centers. It is cheaper to extract specified impurities in 5N raw materials than to have to buy 6N pure components. Optimizing the orientation of the crystal and the annealing procedure is certainly cheaper than developing specific machines for cutting fragile crystals. The maximization of the yields at each stage of the production is one of the key objectives of the R&D.

As potential future markets are uncertain, the production infrastructure has to be organized as much as possible with R&D funds, in order to not impinge too much on the production cost of the crystals. This is also the role of the R&D to develop production technologies as simple as possible, minimizing the power consumption, and with a high degree of automatization in order to reduce manpower costs.

6.1.4 Progress on Lead Tungstate

This systematic approach has been followed for the development of Lead Tungstate crystals for the CMS experiment at CERN.

The very specific requirements of the scintillating crystals for the Electromagnetic Calorimeter at the CERN Large Hadron Collider CMS experiment have been the subject of intensive research and development for about ten years. At the start of these studies it was by no means clear that the very high purity of raw material, nor the special and harsh requirements regarding the radiation hardness of these crystals could be met at all. None of the most experienced manufacturers in the field was at that time anywhere close to being able to deliver the quality of crystals needed. An intensive long-term R&D effort was therefore undertaken by a scientific research consortium including the international CRYSTAL CLEAR Collaboration [1], members of the CERN-CMS experiment, the Institute of Nuclear Problems from Minsk and the Bogoroditsk Techno-Chemical Plant from Russia. It operated under the umbrella and with the active help of the ISTC and with generous financial support from the European Union as one of the major founding Parties to the ISTC Programs. A large development effort has also been undertaken with the Shanghai Institute of Ceramics in China.

Systematic studies from this large community as well as from others groups who jointed the PWO R&D effort at different stages have led to

several important results. They allowed to improve significantly the quality of the crystals and to prepare the final specifications for the production of nearly 80,000 PWO crystals, which have to remain stable and well calibrated under the harsh running conditions of the LHC. Most of these results have been obtained in a relatively short period of time (3 to 4 years). The most significant ones are listed below:

6.1.4.1 Crystal Growth Orientation

At the first stage of the R&D the crystal growth conditions have been optimized. The natural direction of the crystal growth is along the c-crystallographic axis. However the bi-refrigency of the crystal is a critical issue for obtaining a uniform light yield in the $25X_0$ long scintillation elements. It was found that under specific conditions the crystals could be successfully grown along the a-crystallographic axis. Moreover this crystal growth orientation produced an elliptic cross-section of the ingot. which improved the crystal/ingot volume ratio at the machining stage. With this approach, and after a long optimization of all the growth parameters the yield of barrel and endcap growth and annealing could reach the impressive value of 95%.

6.1.4.2 Improvement of the Crystal Transparency

One of the problems which has been successfully resolved is the suppression of the yellow color of lead tungstate crystals. This is a common problem for the tungstate and molybdate crystal families, which was successfully resolved for the first time. This yellow color results from two wide absorption bands with maxima near 420 and 370 nm. It was found that the origin of the 420 nm band is due to a charge transfer transition on a trivalent lead ion state about 1 eV below the bottom of the conduction band. Changing the atmosphere of the crystal growth to a neutral gas purified from oxygen and water immediately suppressed the coloration and resulted in the production of very transparent lead tungstate crystals. This important progress is illustrated in Fig. 6.3. The second band at 350–370 nm is usually present in crystals grown in not optimal conditions. The intensity of this band is well correlated with the intensity of radiation induced absorption in the scintillation region. This band is annealed in air at a temperature close to the melting point. The center responsible for this band is converted under UV irradiation to another center with maximum of absorption near 410 nm. The origin of this center has been identified as an irregular anionic tungstate complex distorted by a Frenkel defect. Following this interpretation both the 420 and the 370 nm bands have been simultaneously suppressed by trivalent rare earth doping of the crystals. The resulting improvement of the crystal transparency had also a positive impact in reducing the light dispersion of the crystals.

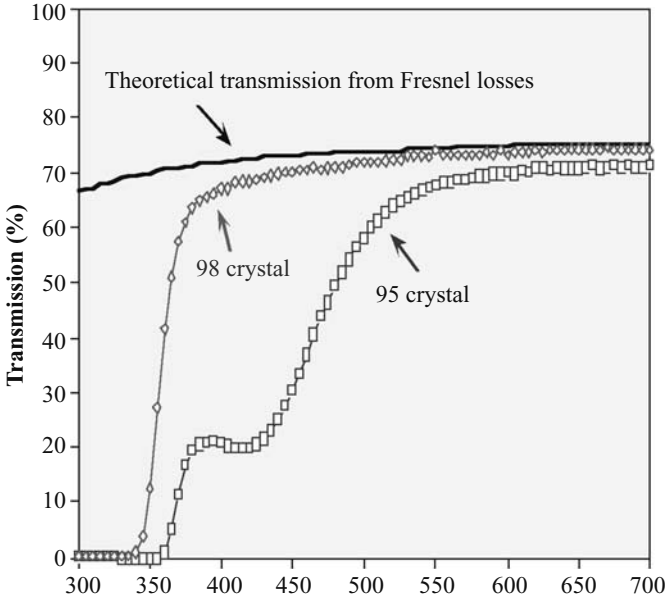

Fig. 6.3. Progress on longitudinal optical transparency of lead tungstate crystals of 23 cm length

6.1.4.3 Origin of Scintillation

Systematic spectroscopic studies carried out on many samples grown in different conditions gave us strong arguments that lead tungstate luminescence is produced by charge transfer transitions in anionic molecular complexes. Both regular WO_4^{2-} and irregular WO_3. tungstate groups are luminescent centers. The WO_4^{2-} blue luminescence (23 800 cm^{-1}) is caused by radiating transitions from triplet levels $^3T_1$, $^3T_2 \rightarrow {}^1A_1$. When an oxygen vacancy appears in a WO_4^{2-}anionic complex the local symmetry of the new WO_3 complex is reduced to C_{3v}. An additional low-symmetry component of the crystalline field splits triplet levels in (A+E) components, producing a shift of the luminescence maximum and causing the green (20 400 cm^{-1}) luminescence at room temperature. Another luminescent center in undoped PWO crystals is associated with the red (15 400 cm^1) luminescence. If the oxygen ion does not escape the crystal but is simply displaced a Frenkel defect is created. This Frenkel defect lowers furthermore the local symmetry of the WO_3 tungsten complex toward a C_3, local symmetry or even lower, thus creating an additional shift and the splitting of the original excited energy terms. Such distorted tungsten anionic complex is responsible for the red luminescence in PWO crystals. In fact, all the mentioned centers contribute to scintillation. However the regular anionic complex blue luminescence is the dominating one

at room temperature for crystals grown in optimal conditions, with specified raw material and appropriate doping.

6.1.4.4 Light Yield Temperature Dependence

Lead tungstate is a crystal of the tungstate family which counts several high light yield but slow scintillators and luminophores like $CdWO_4$, $ZnWO_4$ and $CaWO_4$. The reason for the fast decay tgime of lead tungstate is a strong thermal quenching at room temperature, which also results in a relatively low scintillation light yield. The properties of this crystal make $PbWO_4$ a good compromise between cost and performance for high resolution electromagnetic calorimetry at high energy, where a low light yield is not too much a problem. PWO scintillators have a relatively high temperature dependence of the light yield due to the origin of the radiating centres and the strong thermal quenching. The temperature dependence of the light yield around 20°C is −1.98%/°C. It requires a high precision temperature stabilization of the detecting units. For CMS a complex cooling system maintaining the crystal temperature at 18°C ± 0.1°C had to be designed to guarantee the required precision of 0.5% of the calorimeter at high energy.

6.1.4.5 Slow Scintillation Component

An impressive achievement has been the suppression of slow components in the scintillation of $PbWO_4$. It was observed in 1995 that the optimization for a higher light yield had very often the consequence to produce slow components at a few percent level in the crystals. The slow components in the scintillation related to irregular anionic complexes can be easily suppressed in the crystal by a fine tuning of the stoechiometry of the melt during the crystal growth. However another center was discovered, giving rise to slow components in the scintillation in the microsecond range. It is related to a MoO_4^{2-}anion complex, which is a stableelectron trap center. Molybdenum is an impurity associated to Tungsten. Although raw material is cleaned especially from molybdenum before the crystal growth, the molybdenum ion is chemically very close to the tungsten ion and is rather hard to separate at the raw material production level. In order to suppress this slow component contamination we had to specify a molybdenum impurity concentration in the crystal at the level of less than 1 ppm.

6.1.4.6 Improvement of the Crystal Radiation Hardness

A very critical parameter for Lead Tungstate crystals is their ability to survive in the high radiation environment of the Large Hadron Collider (LHC) in the CMS experiment. A very good stability of the light yield over time is requested to achieve a good resolution of the calorimeter. This problem is

difficult to solve, as it implies a perfect simulation of the radiation conditions in the LHC machine, and a very good understanding of the chemistry of defects in this crystal.

All these aspects have been systematically investigated and impressive progress has been made. Through intensive study of the crystals by different methods the majority of the electron and hole centers in PWO have been identified. Lead Tungstate is characterized by very different vapour pressures for the two components of the melt, Lead and Tungsten oxydes. During the growth process, even from perfectly stoechiometric raw material and whatever the technology used, a dominating leakage of lead takes place from the melt leading to the creation of cation vacancies V_c on the lead site in the host. The charge balance in the crystal impose the concomitant creation of oxygen vacancies. Intrinsic defects based on electron/hole capture by anion or cation vacancies with paramagnetic ground state have never been detected in PWO crystals. This indicates that simple centers like F^+ (anion vacancy V_o + e) and O^- (O^{2-} + h) have no energy levels in the forbidden band or are delocalized in the conduction and valence bands. Therefore the only candidates for metastable color centers in irradiated PWO crystals are cation vacancies capturing two holes of the type $O^-V_cO^-$ or oxygen vacancies capturing even amounts of electrons. Such electronic centers are deep and they are filled mostly through tunneling mechanisms. Very shallow characteristic electron centers have been identified by EPR methods whereas deep ones by TSL and other spectroscopic methods. Through several years of R&D we stated that the scintillation mechanism is not damaged in PWO crystals grown in optimized conditions. This property is as a matter of fact the result of a unique combination of the following crystal features: First, the regular anionic tungstate group is stable under ionizing radiation, second, as follows from our measurements, deep color centers in the crystal do not release electrons in the conduction band when they spontaneously decay. Due to these reasons the scintillation kinetics of the regular emitting centres does not depend on the accumulated dose .However some afterglow can be observed and be dependent on irradiation dose rate if the concentration of V_0 based defects or Mo impurity is large enough in the crystal. The observed radiation damage results therefore only from the transmission degradation resulting from the creation of color centres. The suppression of these color centers has been successfully achieved by a compensation of lead deficiency by additional doping with trivalent ions having a stable valence state like Y or La.

The very promising results of the first phase of the R & D program (1996-1998) induced the collaborating Institutes to continue the ISTC program and to further develop the necessary technologies, including the implementation of stringent quality control methods and special automated measuring equipment. This second R&D phase, financially supported on a 50/50 basis by the European Union and CERN-CMS, has led to excellent results and has set the grounds for the mass production phase, in which the quality of the

mass production technologies is being demonstrated on a large scale. This has been also the opportunity to work on several other aspects: reliability of the production, training of the staff, good managerial structure, quality insurance policy, installation of a modern communication system, development of a network of commercial contacts.

We are now (in 2005) in the last phase of this program which has to be completed for the beginning of 2007. In spite of the fact that more than 150 Czochralski ovens are involved in this production, a large effort had to be developed to increase the productivity in order to reach this goal. In order to build a safety margin in the production a specific development has been made to progressively increase the diameter of the ingots from 38 mm to 65 mm and finally 85 mm (Fig. 6.4). However the implementation of this technology still requires efforts to optimize the cutting and mechanical treatment technology of these large diameter ingots.

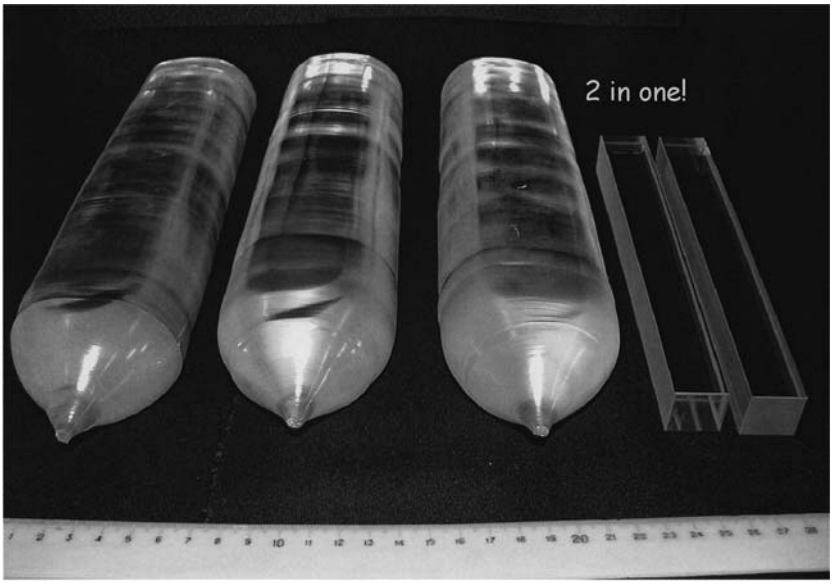

Fig. 6.4. 65 mm ingots with two CMS barrel crystals cut per ingot

6.1.5 Other Experiments Using Lead Tungstate

The large and successful effort placed by CMS on the development of lead tungstate crystals has led several other experiments to choose this crystal for their detector. One can state that lead tungstate has become the most popular scintillation material for HEP applications in the last decade.

The ALICE experiment at CERN is a dedicated heavy-ion experiment at LHC for the study of the initial phase of the collision of heavy nuclei via the direct production of single photons and di-photons. It will also look for signals of chiral-symmetry restoration and jet-quenching as a probe of deconfinement.

The ALICE PHOS calorimeter consists of 17,920 PWO crystals $22 \times 22 \times 180\,\mathrm{mm}^3$ organized in five modules of 3,584 crystals each. Special production facilities have been installed in Apatity, Russia, for the procurement of these crystals grown by the Czochralski method. The detector will be operated at -25°C and read out with avalanche photodiodes [4].

The BTeV experiment at FermiLab is a fixed target experiment to study quark flavor physics, in particular the rare decays of b-flavored particles as the source of CP violation. About 10,000 slightly tapered crystals, with dimensions $(27-28) \times (27-28) \times 220\,\mathrm{mm}^3$ will be assembled in a wall perpendicular to the beam axis. The potential production sites are in Russia and China. The production is expected to take place in the 2006–2008 period [7].

MECO will be installed on the AGS at Brookaven National Laboratory. It is a high sensitivity experiment (2×10^{-17}) which will address rare symmetry-violating process by looking at muons converting to electrons in the field of a nucleus. About 2,300 PWO crystals, with dimensions $30 \times 30 \times 120$ mm^3, will be used for this experiment [8].

The PrimEx experiment at Jefferson Laboratory will use a wall of 1,200 PWO crystals, with dimensions $20.5 \times 20.5 \times 180\,\mathrm{mm}^3$, read out by PMT for a precision measurement of the π° lifetime via the Primakov effect [9].

The photon ball is to be installed into the ANKE magnetic spectrometer at COSY, Jülich. It will study the nucleon structure via the direct measurement of neutral mesons. It is a compact hermetic ball of 876 to 1,100 tapered PWO blocks of 120 mm length read out by the 15 mm quartz light guide and fine mesh Hamamatsu 5505 PMT [10].

The PANDA experiment is a multipurpose detector for the antiproton storage ring at GSI. It will study charmonium, glueball, strangeness, and hypernuclei spectroscopy. The favored technical option so far is based on 7,200 PWO crystals, with dimensions $35 \times 35 \times 150\,\mathrm{mm}^3$, read out by avalanche photodiodes.

6.2 Development of Ce^{3+}-Doped Lutetium-Yttrium Aluminum Perovskite Crystals for Medical Imaging Applications

6.2.1 Introduction

Positron emission tomographs (PET scanners) are more and more recognized as very powerful functional imaging tools in a variety of domains such as basic research in cognitive sciences, clinical oncology, and kinetic pharmaceutical

studies, just to mention a few. Their working principle is based on the reconstruction of the product decay (two γ-rays) of an e^+ labeled tracer injected into the patient. More details are given in Chap. 3. Detection of the two 511 keV gamma rays produced in the electron–positron annihilation allows the in vivo reconstruction of the three-dimensional distribution of the isotope in the body. The detection of the two gamma rays in coincidence requires the use of scintillation detectors. Scintillators used in PET must be dense to optimize detection efficiency, fast to limit number of random coincidences, and have sufficient energy resolution to reject scattered coincidences. State-of-the-art commercial PET scanners are usually based on BGO detector blocks which have a good detection efficiency, but are quite slow (scintillation decay constant 300 ns). Consequently, these scanners operate at a sensitivity of about 1,000 kcps/μCi/ml with a coincidence time window of about 10 ns and a scatter fraction above 30–45%. Next-generation PET scanners need faster scintillators as well as depth-of-interaction encoding, which can be provided by the combination of scintillators with similar density and light yield but different decay time or emission wavelength. This demand has triggered a large effort worldwide in the last decade to explore a variety of crystals for this application.

Lutetium complex structure compounds have rapidly emerged as a natural choice because of the high atomic weight of the lutetium ion, of the good scintillation properties of other rare-earth-based materials such as YAP:Ce and GSO:Ce, and of the possibility of creating a variety of high density crystalline compounds using different ligands. A number of lutetium oxide scintillators doped with trivalent Ce ions have recently been developed, including lutetium orthosilicate LSO (Lu_2SiO_5) [11], lutetium orthophosphate LOP ($LuPO_4$:Ce) [12], lutetium aluminum garnet LuAG ($Lu_3Al_5O_{12}$:Ce) [13, 14], lutetium aluminum perovskite LuAP ($LuAlO_3$:Ce) [15–17], and lutetium pyrosilicate LPS ($Lu_2Si_2O_7$) [18]. These materials tend to exhibit three qualities most desired for gamma detection scintillators: high density and effective atomic number, high scintillation light yield, and short decay time. Although all these crystals have been under investigation for about one decade, only LSO has become a widely used commercially available scintillator so far. Among the others LuAP seems to be the most promising scintillator, with the highest density and the fastest light emission, which make it quite attractive as a gamma detection material. Its density of 8.34 g cm^{-3} is higher than that of LSO (7.34 g cm^{-3}), LuAG (6.9 g cm^{-3}), LPS (6.23 g cm^{-3}), or LOP (6.2 g cm^{-3}). Its attenuation length and photoelectric interaction fraction for 511 keV gamma rays are 1.1 cm and 32%, respectively. It is not hygroscopic and mechanically hard (8.5 Mho), free of cleavage planes, and is therefore relatively easy to cut and polish. Its melting point is below 2,000°C and close to that of LOP (1,947°C) and significantly lower than that of LSO (2,150°C). This is a significant advantage as it can be grown in molybdenum crucibles similar to the well-known $YAlO_3$ (YAP) [19–22]. However, the

growth of this crystal is complicated by phase instability problems between the wanted perovskite phase and a garnet, $Lu_3Al_5O_{12}$, and a monoclinic, $Lu_4Al_2O_9$, phase [23] which compete in a very small temperature domain of the phase diagram. Nevertheless several teams and companies are now consistently producing high quality spontaneously seeded large volume LuAP:Ce ingots.

In order to increase the crystal structure stability heavy co-doping with Y has been proposed [24]. The choice of a solid solution of the type $(Lu_{1-x}$-$Y_x)AlO_3$:Ce, was motivated by several reasons. Yttrium aluminum perovskite has a wider stability region in the Y_2O_3-Al_2O_3 phase diagram than LuAP. The Y^{3+} ion radius is very close to the one of lutetium. Both perovskites have close melting points and can easily create a solid solution. The Czochralski production technology of seeded $(Lu_{1-x}$-$Y_x)AlO_3$:Ce large volume ingots with $x = 0.3, 0.5$ is developed through a joint effort of the Bogoroditsk Techno Chemical Plant (BTCP) from Russia and experts of Crystal Clear Collaboration, CERN, Switzerland. The crystals with $x = 0.7$ can also be produced by horizontally oriented crystallization method similar to $YAlO_3$ crystals.

6.2.2 $(Lu_{1-x}$-$Y_x)AlO_3$:Ce Production Technology

$(Lu_{1-x}$-$Y_x)AlO_3$:Ce crystals have been produced by the Czochralski method using modified equipment of the "Crystal 3M" type. A view of the lutetium-yttrium perovskite production line at BTCP is shown in Fig. 6.5.

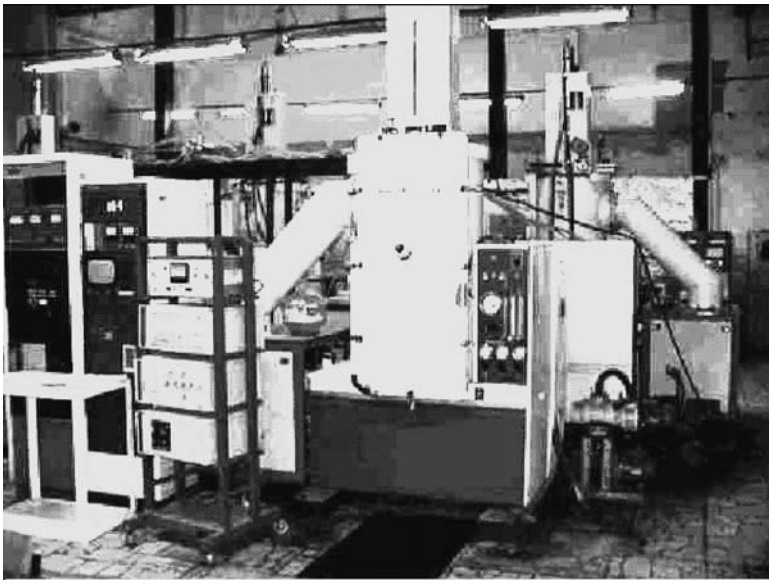

Fig. 6.5. $(Lu_{1-x}$-$Y_x)AlO_3$:Ce crystal production facilities at BTCP

The process of the crystal growth is carried out in an isolated chamber in neutral gas atmosphere. The pulling and rotation speed during the crystal growth can be varied to adjust the ingot diameter at the required value. Before mechanical treatment, the crystal ingots are annealed in low-gradient industrial ovens to reduce the stresses. An open crystallization chamber is shown in Fig. 6.6 with its modernized puller and the induction heating element. A long ingot of the grown $(Lu_{0.7}\text{-}Y_{0.3})AlO_3$:Ce single crystal is also visible.

Crystals of up to 30 mm diameter and 250 mm length with reproducible scintillation parameters have been grown from certified raw materials. Raw material production facilities have been installed which can produce more than 500 kg/year of the specified stoichiometric mixture in powdered form. Tablet compressing machines and preliminary smelting of the raw materials are used to increase the density of the starting material.

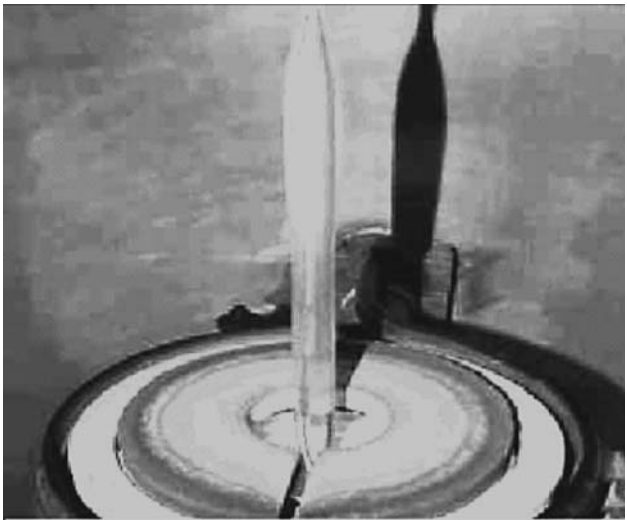

Fig. 6.6. A crystallization chamber with pulled $(Lu_{0.7}\text{-}Y_{0.3})AlO_3$:Ce crystal

More than 500 pixels ($2 \times 2 \times 10\,mm^3$) for the ClearPET® small animal PET scanner [25] can be produced from such an ingot. Work is in progress to progressively increase the ingot diameter up to at least 2 in. The 1 in. diameter scintillation elements for ionizing radiation detectors can be directly produced from the presently grown ingots. One of the scintillation elements cut from a $(Lu_{0.7}\text{-}Y_{0.3})AlO_3$:Ce ingot is shown in Fig. 6.7. LuYAP material is rather hard and not fragile, so standard mechanical treatment technology using diamond powder is applicable.

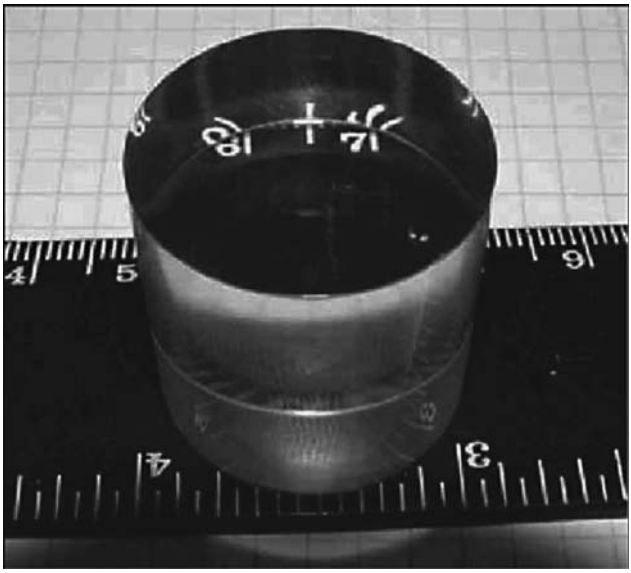

Fig. 6.7. A 1 in $(Lu_{0.7}\text{-}Y_{0.3})AlO_3$:Ce scintillation crystal for spectrometry applications

6.2.3 $(Lu_{1-x}\text{-}Y_x)AlO_3$:Ce Scintillation Properties

The tuning of the Y content in the crystal $(Lu_{1-x}\text{-}Y_x)AlO_3$:Ce allows some flexibility to optimize the optical, chemical, and physical parameters for different applications such as γ-quanta detection, positron emission tomography, and extreme applications such as well logging and hot industrial process control. $(Lu_{1-x}\text{-}Y_x)AlO_3$:Ce crystals have an intermediate position between the well-known $YAlO_3$:Ce and $LuAlO_3$:Ce and their detecting properties, especially density, stopping power, and scintillation kinetics can be adjusted to the specificity of the application. Figures 6.8 and 6.9 show the change of the crystal density and photoelectric linear attenuation coefficient as a function of the Y amount substituted to Lu.

One important aspect of the development strategy for this crystal has been to capitalize on the large amount of efforts made by the CMS collaboration at CERN and at the BTCP plant for the mass production of lead tungstate crystals (see Sect. 6.1). In spite of a tight schedule for the PWO crystals production an intensive R&D program was carried out by the BTCP experts in cooperation with the Crystal Clear Collaboration members with the support of CERN and ISTC.

The first objective was the development of an industrial production chain for the production of crystals with reproducible parameters. For this purpose three different compositions of $(Lu_{1-x}\text{-}Y_x)AlO_3$:Ce with $x = 0.8, 0.5, 0.3$ were selected for the production, starting from the well-known YAP:Ce. The choice

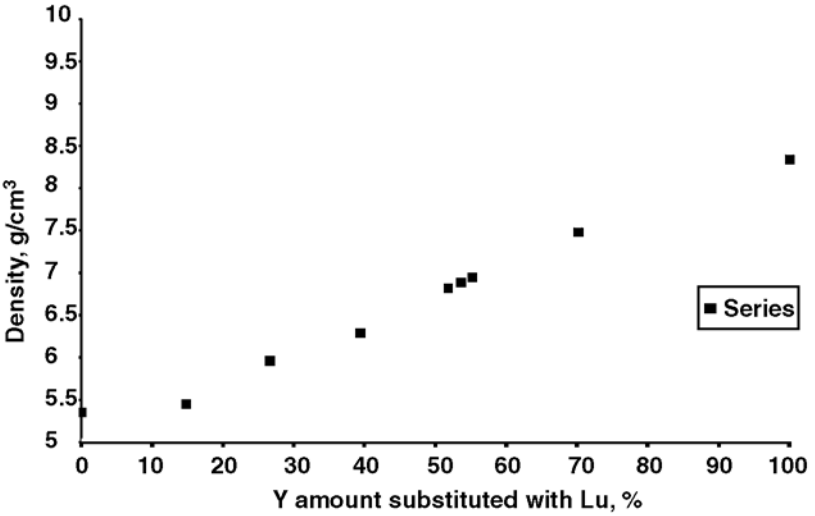

Fig. 6.8. The $(Lu_{1-x}\text{-}Y_x)AlO_3$:Ce crystal density versus the Y amount substituted to Lu

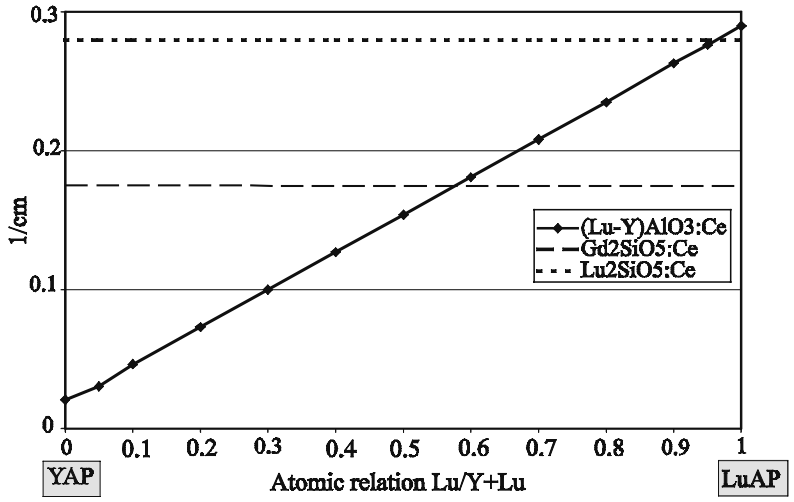

Fig. 6.9. Photoelectric linear attenuation coefficient at 511 keV of $(Lu_x\text{-}Y_{1-x})AlO_3$:Ce as a function of the Lu contents. Values for Lu_2SiO_5:Ce (LSO:Ce) and Gd_2SiO_5:Ce (GSO:Ce) are given for comparison

Table 6.2. Comparison of scintillation and physical properties of $YAlO_3$:Ce and several $(Lu_{1-x}\text{-}Y_x)AlO_3$:Ce crystals

Material	$YAlO_3$:Ce	$(Lu_{0.2}\text{-}Y_{0.8})$ AlO_3:Ce	$(Lu_{0.5}\text{-}Y_{0.5})$ AlO_3:Ce	$(Lu_{0.7}\text{-}Y_{0.3})$ AlO_3:Ce
Density (g cm^{-3})	5.35	5.9	6.5	7.2
λ_{max} emission, (nm)	347	360	375	375
Decay time (fraction in kinetics), ns (%)	30	22 (93) 85 (7)	21 (60) 85 (20) 400 (20)	17 (40) 70 (35) 400 (25)
Light yield (ph MeV^{-1})	16,000	14,000–16,000	12,000–14,000	12,000–14,000
Photoelectric fraction, % at 511 keV	4.4	13.6	22.5	27.1
Attenuation length, cm at 511 keV	2.16	1.88	1.48	1.35

was made as a function of the attenuation coefficient for γ-rays (Fig. 6.9) in order to cover different applications. A comparison of their scintillation and physical properties is shown in Table 6.2.

The crystal with 20% of Y substituted to Lu has a light yield, close to the one of YAP:Ce, a fast scintillation with a very small contribution of slow component and a relatively high density very close to 6 g cm^{-3}. It is a good candidate to be used in medical imaging devices for the detection of soft γ-rays.

The crystal with an equal amount of Lu and Y is in the same range of density and photoelectric fraction at 511 keV as GSO:Ce, but with much better mechanical and temperature properties. It is therefore a better alternative to this crystal.

The last crystal with 70% of Lu is a good candidate to be applied in PET scanners together with LSO:Ce as described in Chap. 5. This crystal has been selected for the ClearPET® scanner, a new generation PET scanner for small animals.

More than 9,000 scintillation pixels with dimensions $2 \times 2 \times 10\,mm^3$ were manufactured for the construction of ClearPET® prototypes. These crystals are used in combination with LYSO:Ce crystals in a phoswich configuration in order to allow depth of interaction measurement by identification of the crystals through their different decay times. A good homogeneity of scintillation characteristics of the crystals grown in different ovens was obtained. The mean value of the light yield is 35% relative to NaT(Tl), i.e. about 12,000 photons MeV^{-1}. The light yield of some of the grown crystals is already close to the theoretical limit which is 50% of NaT(Tl) at room temperature. The study of the temperature dependence of the energy resolution of $(Lu_{0.7}\text{-}Y_{0.3})AlO_3$:Ce pixels shows a progressive improvement when the temperature increases from 300 to 350 K. In the same temperature range the

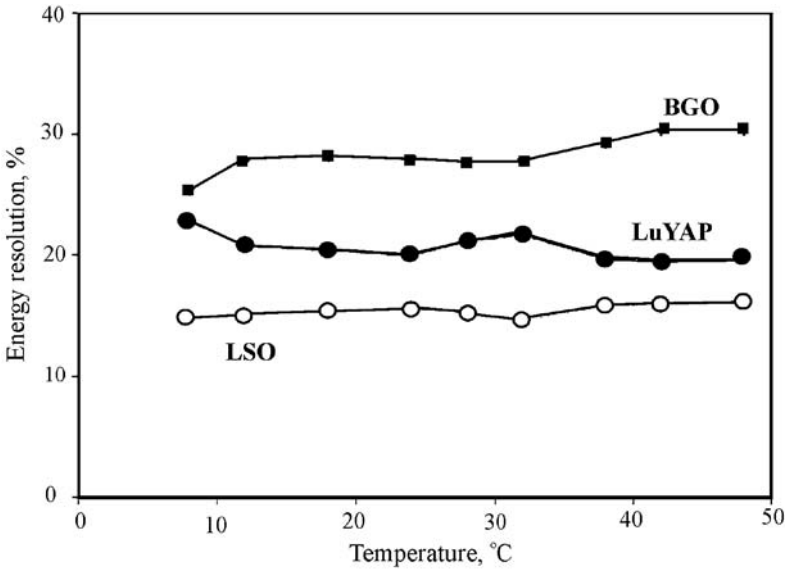

Fig. 6.10. Variation of the energy resolution for 511 keV γ-rays measured with $2 \times 2 \times 10\,\mathrm{mm}^3$ samples of $Lu_{0.7}Y_{0.3}AP$, LSO:Ce, and BGO as a function of temperature (Courtesy of E. Weber and K. Ziemons)

energy resolution of BGO and LSO:Ce degrades [26] as seen in Fig. 6.10. This variation of the energy resolution results from opposite temperature coefficients of the scintillation yield as shown in Fig. 6.11.

The consistency of the crystal quality within the ingot and in particular a small nonuniformity of the light yield and energy resolution along the crystal growth axis are mandatory for an industrial production. The typical variation of the light yield along the crystal growth axis was found to be not more than 5%. It confirms a uniform distribution of the activator along the crystal growth axis. The concentration of the activator in the crystal is well controlled by means of optical absorption spectroscopy. The optical absorption spectrum of the $(Lu_{0.7}\text{-}Y_{0.3})AlO_3$:Ce crystal and its comparison with absorption of the mass produced $YAlO_3$:Ce crystal is shown in Fig. 6.12. As shown in this figure LuYAP still has a large optical absorption in the UV range, extending to the spectral range of the scintillation. This band is attributed to charge transfer transitions $O^{2-} \rightarrow Ce^{4+}$. A large amount of efforts is presently focused on the suppression of this absorption band in the scintillation spectral region, from which one can expect a better light collection uniformity in long pixels and an improved light yield.

The light yield distribution of the grown $(Lu_{0.7}\text{-}Y_{0.3})AlO_3$:Ce crystal ingots produced in the year 2003 is shown in Fig. 6.13. The mean value of the light yield of 1 mm thick plates is 35% of that of NaI(Tl), i.e. about 12,000 photons MeV^{-1}. Some crystals had lower light yield due to macrodefects in-

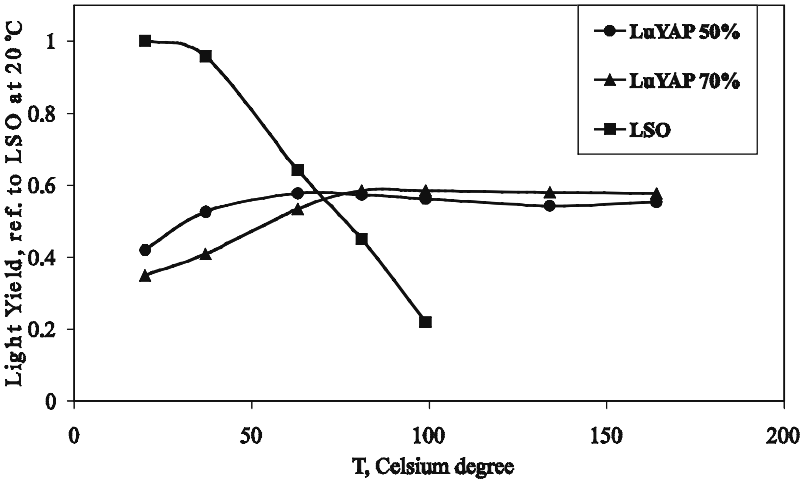

Fig. 6.11. Temperature dependence of LuYAP and LSO light yield

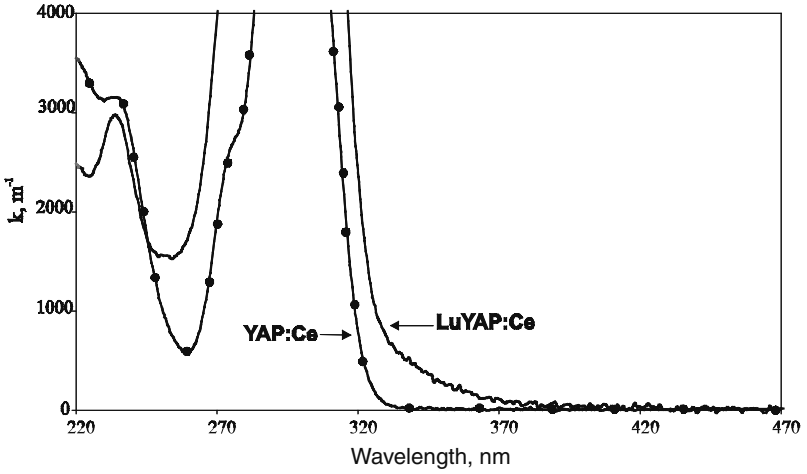

Fig. 6.12. Comparison of the optical absorption of the $(Lu_{0.7}\text{-}Y_{0.3})AlO_3$:Ce and $YAlO_3$:Ce crystals in the region of the first allowed $f \rightarrow d$ transition of the Ce^{3+} ion at 300 K

side the crystals. They were usually cut from bad quality ingots grown after several crystallization cycles in which light scattering centers such as twins and gas bubbles were clearly visible.

The scintillation decay of the grown $(Lu_{0.7}\text{-}Y_{0.3})AlO_3$:Ce crystals can be fitted by three-exponential components with the following time constants and normalized amplitudes: 17 ns—86%, 70 ns—12%, 400 ns—2%. The scintillation pulse shape of crystals with crystallization numbers ranging from 4 to 11 is shown in Fig. 6.14 and compared to LSO:Ce. The crystallization numbers

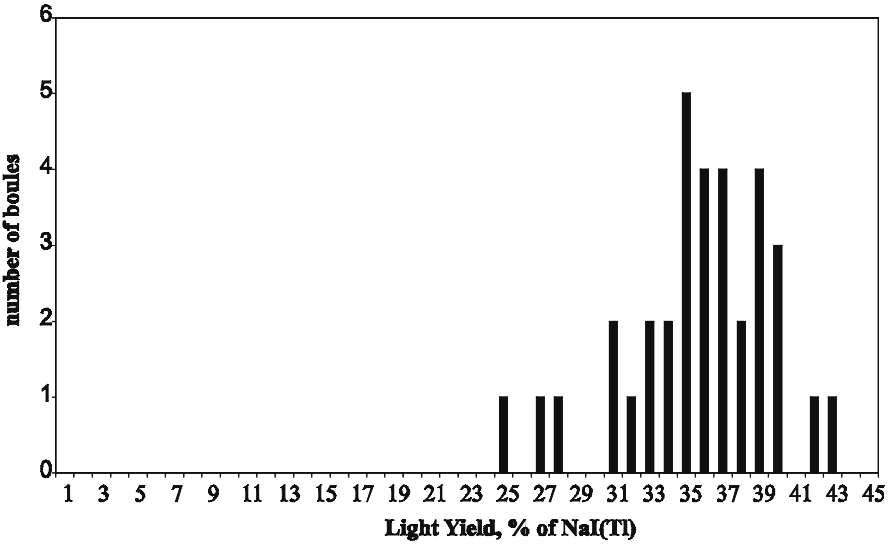

Fig. 6.13. Light yield distribution of $(Lu_{0.7}\text{-}Y_{0.3})AlO_3$:Ce crystals. The light yield of samples cut from the top part of the ingots with thickness 1 mm is compared with $\emptyset 25 \times 1\,mm^3$ NaI(Tl) detector as reference at 300 K

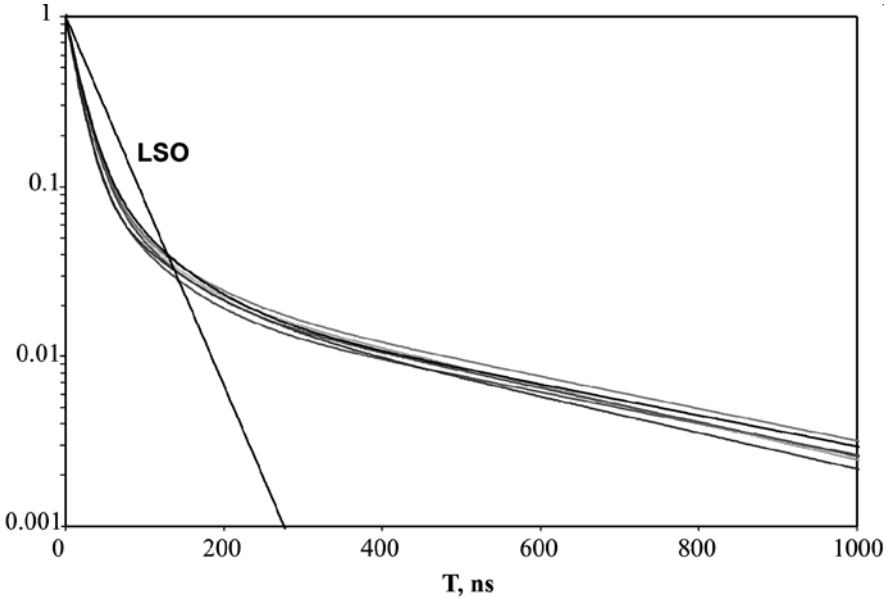

Fig. 6.14. Shape of the $(Lu_{0.7}\text{-}Y_{0.3})AlO_3$:Ce scintillation pulse for crystallization numbers 4–11 compared to that of LSO:Ce at 300 K

are not indicated since there is no correlation between the scintillation pulse shape and the crystallization number. However, for crystallization numbers lower than 3 and greater than 13 some increase of the slow decay component was observed.

The stability of the shape of the LuYAP scintillation pulse and the rather narrow light yield distribution of the grown ingots testify the good quality of raw materials and the reproducibility of the growing process. Effective LSO/LuYAP pulse shape discrimination can be realized on the basis of either the fast or the slow decay component of $(Lu_{0.7}\text{-}Y_{0.3})AlO_3$:Ce.

The influence of the additional optical absorption band on the light collection in $(Lu_{0.7}\text{-}Y_{0.3})AlO_3$:Ce pixels is estimated through the measurement of the light yield of standard $2 \times 2 \times 10\,\text{mm}^3$ pixels in vertical and horizontal positions. Figure 6.15 represents the pulse height spectrum of a Na-22 source measured when the $2 \times 10\,\text{mm}^2$ or the $2 \times 2\,\text{mm}^2$ pixel surface is coupled to the PMT window ("horizontal" and "vertical" geometry). The light yield ratio obtained for LuYAP pixel from these spectra is a good estimator of this absorption band intensity. The ratio LY_{hor}/LY_{vert} is about 2.2 for LuYAP to be compared to 1.85 for LSO pixels as a direct result of a better optical transparency of the LSO crystal in its emission region.

The width of the light yield distribution of $(Lu_{0.7}\text{-}Y_{0.3})AlO_3$:Ce pixels was found to be very close to that of LuYAP boules used for pixel production. The typical light yield distribution of $2 \times 2 \times 10\,\text{mm}^3$ pixels of LuYAP is shown in Fig. 6.16. A subset of 100 samples was randomly taken from a batch of 1,500 pixels. Each pixel was wrapped in two layers of TYVEK reflecting material and the $2 \times 2\,\text{mm}^2$ pixel surface was coupled to the PMT window with Dow Corning Q2-3067 optical grease. A $2 \times 2 \times 10\,\text{mm}^3$ LSO pixel was used as a reference with the same conditions of wrapping and coupling.

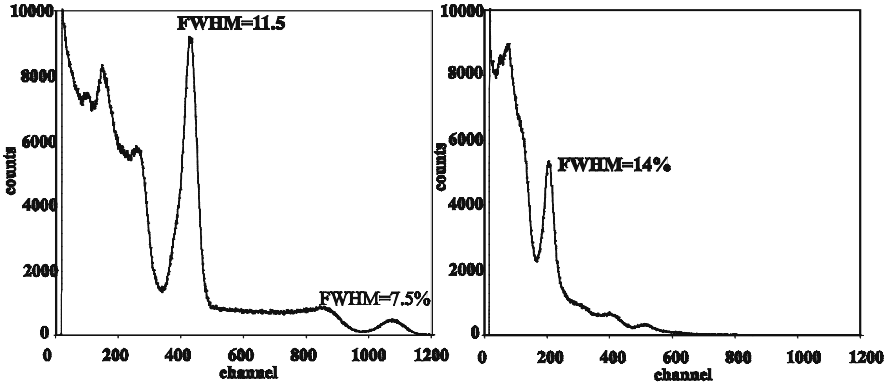

Fig. 6.15. The pulse height spectrum of a Na-22 source measured with the $2 \times 2 \times 10\,\text{mm}^3$ LuYAP pixel. The surface coupled to the PMT window is $2 \times 10\,\text{mm}$ (*left*) and $2 \times 2\,\text{mm}$ (*right*)

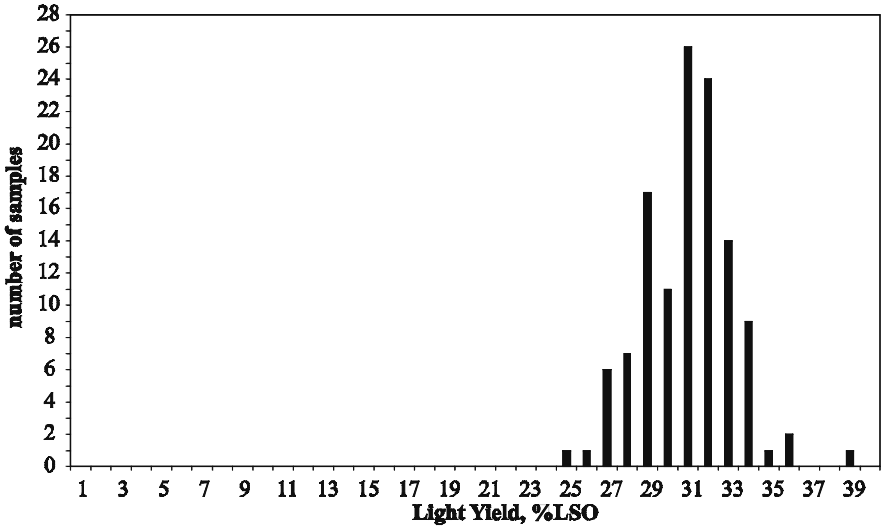

Fig. 6.16. Light yield distribution of $2 \times 2 \times 10\,\mathrm{mm}^3$ pixels of $(Lu_{0.7}\text{-}Y_{0.3})AlO_3$:Ce

After several years of academic work to understand the basic properties of $(Lu_{1-x}\text{-}Y_x)AlO_3$:Ce, impressive progress on the industrial development of this crystal has been made which makes it a very serious candidate for several applications in the low γ-quanta energy registration domain, and particularly medical imaging devices (because of its excellent linearity at low energy and good resulting energy resolution) and well-oil logging (because of its very good properties at high temperature). Moreover, a large potential of improvement exists in light yield and energy resolution through the suppression of the absorption band tail at 360 nm, as well as in decay time when the traps responsible for the slow components will be identified and suppressed.

Besides the $PbWO_4$ scintillator development and industrial implementation, the case of LuYAP:Ce has been another good example in the recent years showing how fundamental research can drive well-organized multidisciplinary collaborations of experts to develop products of high value for the society.

References

1. R&D Proposal for the study of new fast and radiation hard scintillators for calorimetry at LHC: Crystal Clear Collaboration, CERN/DRDC P27/91-15, project RD-18
2. Adeva B, Aguilar-Benitez M, Akbari H et al. (1990) The construction of the L3 experiment. Nucl. Instrum. Methods Phys. Res. A 289: 35–100
3. CMS Technical Proposal, CERN/LHCC 94-38, December 1994
4. ALICE Collaboration Technical Proposal, CERN/LHCC/95-71
5. ISTC: International Science and Technology Center. www.istc.ru

6. Annenkov A, Auffray E, Borisevich A et al. (1999) Suppression of the radiation damage in lead tungstate scintillation crystal. Nucl. Instrum. Methods Phys. Res. A 426: 486–490
7. The BteV proposal, March 2002, BteV-doc-316
8. MECO Collaboration (1999) A proposal to the National Science Foundation to construct the MECO and KORPIO experiments http://meco.ps.uci.edu
9. PrimEx Conceptual Design Report. A precision measurement of the neutral pion lifetime via the Primakof effect. Jefferson Lab, March 3, 2000
10. Barsov S, Bechstedt U, Bothe W et al. (2001) ANKE, a new facility for medium energy hadron physics at COSY-Jülich. Nucl. Instrum. Methods Phys. Res. A 462: 364–381
11. Melcher CL, Schweitzer JS (1992) Cerium-doped lutetium orthosilicate: a fast, efficient new scintillator. IEEE Trans. Nucl. Sci. 39: 502–505
12. Lempicki A, Berman E, Wojtowicz AJ et al. (1993) Cerium-doped orthophosphates: new promising scintillators. IEEE Trans. Nucl. Sci. 40: 384–387
13. Van Eijk CWE, Andriessen J, Dorenbos P et al. (1994) Ce^{3+} doped inorganic scintillators. IEEE Trans. Nucl. Sci. A 348: 546–550
14. Ryskin NN, Dorenbos P, Van Eijk CWE et al. (1994) Scintillation properties of $Lu_3Al_{5-x}Sc_xO_{12}$ crystals. J. Phys.: Condens. Matter 6: 10423–10434
15. Moses WW, Derenzo SE, Fyodorov A et al. (1995) $LuAlO_3$:Ce—a high density, high speed scintillator for gamma detection. IEEE Trans. Nucl. Sci. 42: 275–279
16. Minkov BI (1994) Promising new lutetium based single crystals for fast scintillators. Funct. Mater. 1: 103–105
17. Lempicki A, Randles MH, Wisniewski D et al. (1995) $LuAlO_3$:Ce and other aluminate scintillators. IEEE Trans. Nucl. Sci. 42: 280–284
18. Pauwels D, Le Masson N, Viana B et al. (2000) A novel inorganic scintillator: $Lu_2Si_2O_7$:Ce^{3+} (LPS). IEEE Trans. Nucl. Sci. 47: 1787–1790
19. Weber MJ (1973) Optical spectra of Ce^{3+} sensitized fluorescence in $YAlO_3$. J. Appl. Phys. 44: 3205–3208
20. Autrata R, Schouer P, Kvapil Jiri et al. (1983) A single crystal of $YAlO_3$:Ce^{3+} as fast scintillator in SEM. Scanning 5: 91–96
21. Baryshevsky VG, Korzhik MV, Moroz VI et al.(1991) $YAlO_3$:Ce—fast-acting scintillators for detection of ionizing radiation. Nucl. Instrum. Methods Phys. Res. B 58: 291–293
22. Korzhik MV, Misevich OV, Fyodorov AA (1999) $YAlO_3$:Ce scintillators: application for X- and soft γ-ray detection. Nucl. Instrum. Methods Phys. Res. B 72: 499–501.
23. Smirnova SA, Korzhik MV (1996) Growth of crystals yttrium-aluminum perovskites with rare earth elements. In: Dorenbos P, van Eijk CWE (Eds). Proc. Int. Conf. on Inorganic Scintillators and Their Applications, SCINT'95. Delft University Press, The Netherlands, pp 495–497
24. Trower WP, Korzhik MV, Fedorov AA et al. (1996) Cerium doped luthetium-based single crystal scintillator. In: Dorenbos P, van Eijk CWE (Eds). Proc. Int. Conf. on Inorganic Scintillators and Their Applications, SCINT'95. Delft University Press, The Netherlands, pp 355–358
25. A PET scanner. Patent WO03/001242A1
26. Weber S, Christ D, Kurzeja M et al. (2003) Comparison of LuYAP, LSO, and BGO as scintillators for high resolution PET detectors. IEEE Trans. Nucl. Sci. 50: 1370–1372

Conclusion

We hope that this book will be useful for a wide community of people who are, directly or indirectly, involved in the development and applications of detectors for ionizing radiation as well as for teachers and students in physics instrumentation. In writing the book we have obviously capitalized on our own knowledge on the subject and we would like to make a few remarks related to further progress in this field.

The development and engineering of new inorganic scintillators is a multidisciplinary activity and further progress will be driven mostly by wide collaborations of scientists and technologists. Moreover the development of a new material requires more and more investments in a relatively short time. The market being dominated by applications in civil institutions (physics research, medicine) a combination of efforts from both governmental and intergovernmental funding agencies and from private business resources is the most realistic approach. The experience of the Crystal Clear Collaboration for the development of lead tungstate and of Ce^{3+}-doped perovskite scintillation materials is a good example which demonstrates that a well-organized structure can manage all stages of the development of inorganic crystalline materials, from the fundamental research and development to the installation of large production facilities.

We believe that experimental high energy physics and medical imaging will continue to be the main driving force in the development of new scintillation materials, although the demand for security systems is increasing significantly. The CERN Large Hadron Collider (LHC) is not yet commissioned but plans already exist for a luminosity upgrade of the accelerator. It may require new and even more radiation hard materials. But this is certainly a very fast development of the medial imaging instrumentation with a high demand for high light yield, good response proportionality and excellent timing resolution, which will highly motivate the development of new materials in the near future.

Of course, we have to be open to spontaneous discoveries of new materials with exciting properties, but the main vector of the success will be the systematic study of the material fundamental properties. The progress of the computing combinatorial methods will certainly offer new possibilities of virtually producing new compounds and predicting their properties. New

technological approaches based on the progress of nanotechnologies will also have an impact at least at two levels. The first one concerns the possibility of producing highly transparent ceramics, which at some point may compete with a single crystal structure. The other possible more fundamental perspective offered by nanotechnologies is to give access to new extremely fast scintillation mechanisms in nanostructured systems where quantum physics effects dominate.

Finally we should not forget the continuous progress in crystal growth technologies with interesting perspectives to produce, for instance, very large ingots of excellent quality or crystals grown in shape at high speed. Through all these developments and the pressure from the increase and diversification of the market, the contribution of scintillating materials to the price of detection systems is likely to progressively go down in the future.

Glossary

Eg	energy width of the forbidden zone in a dielectric medium
τ_r	radiating time of the luminescence transition
ω_{int}	frequency of interaction between primary and secondary luminescent centers in the medium
Y	scintillation light yield
E_γ	energy of γ-quantum
β	conversion efficiency of the dielectric medium
S	efficiency of the energy transfer of thermalised pairs to the excited states of luminescent centers.
Q	quantum yield of the intra-center luminescence
Y_e	energy efficiency of scintillation
E_f	average energy of scintillation photons
I(t)	the kinetics of scintillation
τ_{sc}	decay constant of scintillation kinetics
$\lambda_{sc(max)}$	wavelength of scintillation band maximum
ν_{sc}	frequency of scintillation band maximum
$\Delta\lambda_{sc}$ ($\Delta\nu_{sc}$)	width of the scintillation band
e	electron
h	hole in an electron shell
A	activator ion
A^*	activator ion in excited state
$h\nu$	luminescence quantum
ex	exciton
E_r	energy of the radiating state of the activating ion
τ_d	delocalization time
k	Boltzman constant
T	temperature (K)
n	refraction index
C_{DA}	parameter of donor-acceptor dipole-dipole interaction
ρ	density
Z_{eff}	effective charge of the dielectric medium
X_0	radiation length of the medium
R_M	Moliere radius of the medium
a	the statistical term in the energy resolution equation
b	the noise term in the energy resolution equation

c	the noise term in the energy resolution equation
CT	computed tomography
PET	positron emission tomography
SPECT	Single Photon Emission Computed Tomography
R	energy resolution of the low energy detector
RE	rare earth ion
STE	self trapped exciton
STH	self trapped hole
VUV	vacuum ultra violet light
E_{TA}	thermo-activation energy
TSL	thermo-stimulated luminescence
EPR	electron paramagnetic resonance
SCC	single-configurational coordinate model in the electronic energy level description
Q_g	configurational coordinate of the electron ground state
Q_e	configurational coordinate of the electron excited state
CTS	charge transfer states
V_o	oxygen vacancy
V_c	cation vacancy
F^+	oxygen vacancy capturing one electron
F	oxygen vacancy capturing two electrons
F	halide vacancy capturing one electron
LHC	Lage Hadron Collider
CMS	Compact muon Solenoid Collaboration Experiment at LHC
R&D	research and development program
PMT	photomultiplier
HEP	High Energy Physics
BGO	Bismuth Germanate ($Bi_4Ge_3O_{12}$)
LSO	Lutetium orthosilicate (Lu_2SiO_5)
GSO	Gadolinium silicate (Gd_2SiO_5)
LuAP	Luthetium perovskite ($LuAlO_3$)
YAP	Yttrium perovskite ($YAlO_3$)
PWO	lead tungstate ($PbWO_4$)

Index

Printing: Krips bv, Meppel
Binding: Stürtz, Würzburg